Mechanistic Insight Into the Aggregation Pathways of the hLL-$37_{17\text{-}29}$ Peptide and the Effect of These Aggregates on Model Membranes

A Thesis Submitted
in Partial Fulfilment of the Requirements
for the Degree of
DOCTOR OF PHILOSOPHY

by

Aritra Mitra

Under the Supervision of

Prof. Sandip Paul

Department of Chemistry
Indian Institute of Technology Guwahati
2025

To Ma, Baba and Avipsa,
The Three Pillars of my Life ...

Declaration

I, **Aritra Mitra**, hereby declare that this thesis titled, "**Mechanistic Insight Into the Aggregation Pathways of the hLL-37$_{17\text{-}29}$ Peptide and the Effect of These Aggregates on Model Membranes**" and the work presented in it are my own. I confirm that:

- This complete work was carried out during candidature for a **Ph.D.** degree at IIT Guwahati under the supervision of Prof. Sandip Paul.
- The research was executed in keeping with the general and ethical practices of doing science and reporting scientific observations.
- The research was substantiated and verified with previously reported literature and all the sources were properly cited and acknowledged.
- The computer codes used in this work were self-written or adapted from various sources that have been appropriately cited.

Aritra Mitra

.....

(Signature)

Date:24.11.2025

Aritra Mitra

Place: IIT Guwahati

Roll No: 186122003

DEPARTMENT OF CHEMISTRY
INDIAN INSTITUTE OF TECHNOLOGY GUWAHATI

Certificate

It is certified that the work contained in this thesis entitled "**Mechanistic Insight Into the Aggregation Pathways of the hLL-37$_{17\text{-}29}$ Peptide and the Effect of These Aggregates on Model Membranes**", submitted by **Aritra Mitra**, bearing Roll No. **186122003**, for the award of **Doctorate of Philosophy** in Chemistry is completely based on his own work carried out under my supervision and the same has not been submitted elsewhere for a degree.

Prof. Sandip Paul
Project Supervisor
Department of Chemistry
Indian Institute of Technology Guwahati

Acknowledgements

A Ph.D. is a challenging journey - often painstakingly long - that pushes the limits of your knowledge and perseverance. There are days when you wake up full of excitement, scribble down a to-do list, rush to the lab with a brilliant idea, and dive right into testing it. These are the bright, sunny days. On these days, you feel unstoppable, like you're on top of the world. And then there are those days - when your simulations yield nothing of value, your code throws up a hundred baffling syntax errors, and your project hits a wall so hard you start questioning if it's even worth continuing. These are the cold, rainy days.

Anyone who's walked this path will tell you: the sunny days are precious and few. The rainy ones? There are many, much like the weather here in Guwahati. The trick is to wait out the storm and enjoy those rare few sunny days like your life depends on it. But you can't wait out the storm alone. You need people to help you out of it at times. I take this opportunity to thank those precious few without whom this journey would not have been possible.

First and foremost, I would like to express my deepest gratitude to my supervisor, Prof. Sandip Paul, whose unwavering support and insight have guided me throughout this journey. I am especially thankful for the freedom he gave me to pursue my own ideas—an experience that proved invaluable. It was through that freedom, and the inevitable challenges that accompanied it, that I grew as a researcher. Yet, whenever I found myself stuck, his timely guidance—and, when needed, a firm nudge—helped me regain clarity and direction. Beyond research, he consistently encouraged me to apply for projects and attend conferences that have broadened my exposure to science and shaped my career and perspective. I can say with sincere humility that I would not be the researcher I am today without his mentorship.

Next, I would like to thank my doctoral committee members, Prof. Bhubaneshwar Mondal (Chairperson), Prof. Sunanda Chatterjee, and Prof. P.K. Padmanabhan, for periodically reviewing my work and offering valuable suggestions that helped shape my research. I am also sincerely grateful to all the faculty members in the department for their kind support at various stages of my doctoral journey. I acknowledge the Ministry of Education (MOE), India, for providing financial support, and IIT Guwahati for offering the research infrastructure necessary for carrying out my work. In particular, I am thankful for the

supercomputing facilities at IIT Guwahati - Param Ishan and Param Kamrupa - the two workhorses that handled the heavy simulation load of my research. I would also like to acknowledge the Department of Biotechnology (DBT), India, for funding my project on antimicrobial peptides.

A significant part of my PhD journey was spent in my lab (CHEL-103) - especially, the desk at the far end of the room - which will always hold a special place in my heart. It was here that I met some wonderful people, with whom I had the privilege of working and discussing science that left a lasting impact on me. First and foremost, I would like to thank Srijita Di and Ritu Di, two lovely seniors who became dear friends and continue to be my go-to people whenever I need advice. I'm also grateful to Krishna Da, Saikat Da, and Rabi Da for their guidance during the early days of my PhD, when the world of molecular dynamics simulations was still new and unfamiliar to me. A heartfelt thank you to Madhusmita, with whom I shared this seven-year-long PhD journey—and occasionally, some much-needed tea breaks at Core-3 whenever the science became too overwhelming. I'm equally thankful to my kind and supportive juniors—Rimjhim, Sanjib, Mira, Anandita, Vanneikima, Balaram, and Srimila—whose discussions on various projects not only enriched my understanding but also brought great clarity to my own work. A special word of thanks to Mira, Balaram, and Srimila for painstakingly proofreading my thesis and helping me ensure it was free of typos. I would also like to acknowledge two of my wonderful interns, Viswas and Subhamoy, whom I had the privilege of mentoring during my PhD. And lastly, a big thanks to Sushil Da from the Core-3 canteen for the endless cups of tea that kept my brain from crashing under the workload.

I am deeply grateful to my hostelmates—Anindya, Anjishnu, Arin, Surajit, Anik, Sanket, Jyotirmoy, Argha, Alik, Partha, Santanu, Tanay, Adri, and Aritra—who made my hostel life an unforgettable experience. Our routine of sitting together for dinner in the hostel mess, engaging in hearty discussions over meals, and then taking long walks around the campus before retiring to our rooms is among my most cherished memories. I would like to make special mention of Anindya for always being there in my times of need, Anjishnu and Anik for being patient and thoughtful listeners, Surajit for his valuable advice, and Arin for his unwavering loyalty. I am also grateful to my dear friend Suchetana, who became one of my "bros" during this journey. A special note of appreciation goes to my juniors Argha and Jyotirmoy, with whom I shared some of the funniest and most joyful moments in the hostel. Some of my fondest memories include the cooking sessions where

we all pitched in to create delicacies together and the countless tea and adda sessions at Khoka that brought us closer as friends.

I owe my PhD journey to the unwavering support of my family—without them, this degree would simply not have been possible. First and foremost, I am deeply grateful to my grandparents, who first recognized my potential as a student and continually encouraged me to pursue academics with dedication. I am also indebted to my in-laws, whose constant motivation and gentle pushes kept me going through the most challenging phases. A very large share of my gratitude goes to my parents. Their years of hard work, sacrifice, and belief in me have been the foundation of my resilience and the reason I could take on this long and demanding path.

I would like to dedicate a very special note of thanks to my wife, Avipsa. She has been my strongest pillar throughout this journey. Being a researcher herself, she has been a sounding board for ideas, a partner in long scientific discussions, and an endless source of encouragement. During the early years of my PhD, when my project seemed to be going nowhere and I often felt like quitting, it was her confidence in me that convinced me to persist. The eventual success of this work is as much hers as it is mine. Without her, I might have taken a very different path in life and missed out on this extraordinary experience.

And finally, I want to thank myself—a small but necessary acknowledgement—for showing up to the lab on days when I least wanted to, for pushing through every frustrating error in my codes, and for wrestling with the daunting task of scientific writing, one slow sentence at a time.

Contents

List of Figures

List of Tables

"The present is theirs; the future, for which I really worked, is mine"

Nikola Tesla

Chapter 1

Introduction

1.1 An overview of antimicrobial resistance

1.1.1 What is antimicrobial resistance?

Antimicrobial resistance (AMR) is a trait that enables microbes to survive and proliferate under conditions lethal to them. One such condition occurs in the presence of drugs, particularly antibiotics, that are commonly used to treat infections. Microbes develop resistance to these drugs as an inevitable coping mechanism to withstand their selection pressure . As a result, infections caused by resistant microbes get notoriously challenging to treat, and in many cases, can be life-threatening [1].

The increased use of antibiotics, particularly in developing countries, allows bacteria to build AMR, increasing morbidity and mortality per year [2–4]. The World Health Organization (WHO) has attributed AMR as the third leading cause of death worldwide, with 1.27 million deaths occurring in 2019 alone [5]. In 2022, roughly 5 million casualties were indirectly linked to drug-resistant infections, with this number projected to increase to 40 million yearly by 2050 [6]. Thus, AMR negatively impacts preventive and therapeutic health care and requires urgent attention [7–9]. Figure 1.1 illustrates the rise in AMR-related deaths caused by resistant pathogens from 1990 to 2021 for two different

age groups (below and above 5 years). The current demand for novel antibiotics fails to keep up with the ever-increasing categories of resistant strains [10]. Since the last developed broad-spectrum antibiotic, Fluoroquinolone, few are in the pipeline [11]. Focus has instead shifted to preserving the efficacy of the existing ones through proper consumption practices.

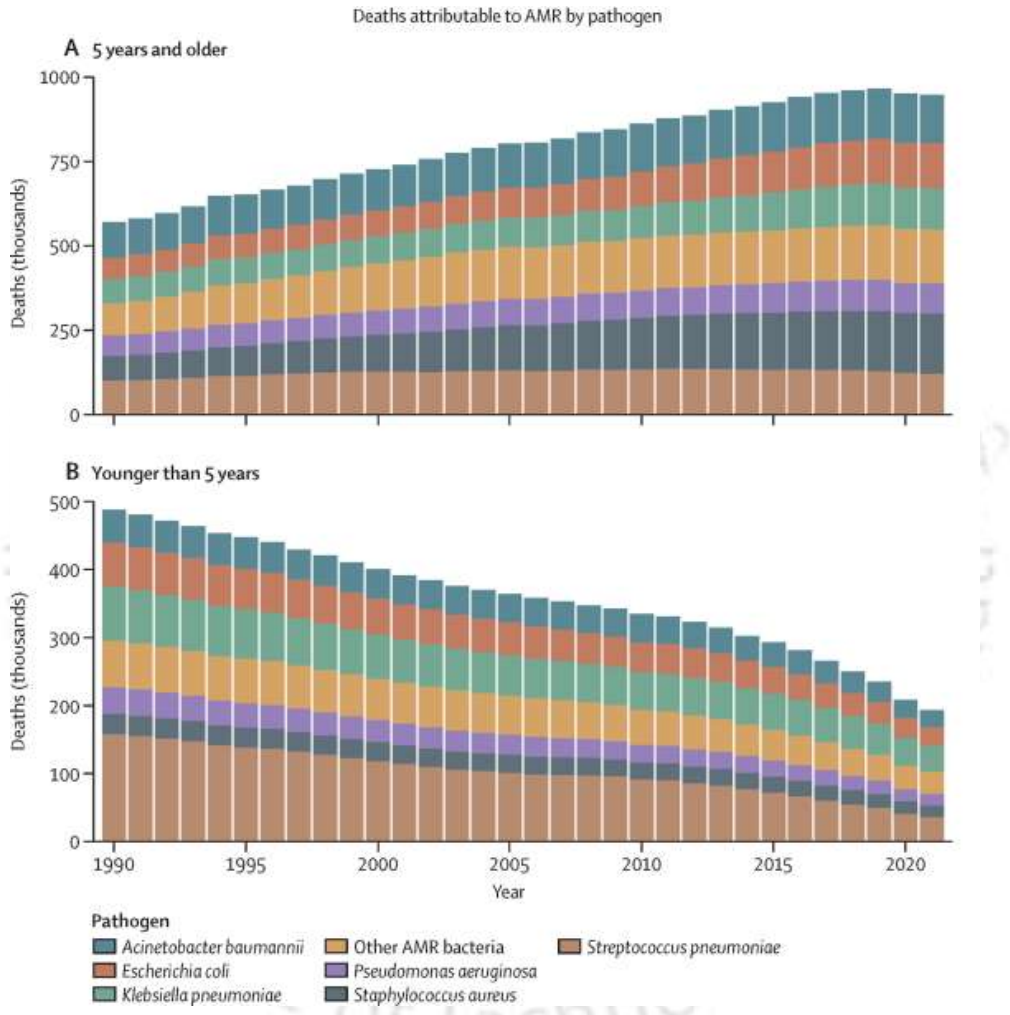

FIGURE 1.1: Increase in AMR-related mortalities in individuals belonging to two different age groups: (A) younger than 5 years, and (B) 5 years or older. Figure reproduced from Ref. 12 under the terms of the Creative Commons CC-BY license.

1.1.2 History of AMR development

The discovery of Penicillin in 1928 by Sir Alexander Fleming initiated an era of antibiotic discovery and innovation that continued till the early 1960s. The antibiotics we commonly

use today were developed during this "Golden Age" of antibiotic research. Following this, antibiotic innovation gradually declined due to the emergence of drug-resistant pathogens. The earliest microbes reported to develop resistance were bacteria [11]. A penicillin-resistant *Staphylococcus* strain was reported, even before the drug was marketed in 1940. A penicillinase-resistant variant of methicillin was introduced in 1959, naturally resulting in a methicillin-resistant strain in the following year [13]. In 1958, a glycopeptide-based antibiotic, vancomycin, was introduced to combat methicillin-resistant strains, but again, several vancomycin-resistant strains emerged as a response [14]. As an alternative, β-lactam based antibiotics like cephalosporin were initially prescribed to treat penicillin-resistant cases, which led to multiple generations of the drug being developed. Until recently, a fifth-generation cephalosporin was put into the pipeline as the previous four generations of the drug developed significant resistance. Similarly, carbapenem, another β-lactam based antibiotic was introduced to treat cephalosporin-resistant cases. However, several carbapenem-resistant enterobacterales (CRE) were reported since 2006 following the extensive prescription of these drugs during the 1990s to 2000s [15]. This tug-of-war between newly developed antibiotics and the emergence of resistant strains as a response has continued since the inception of this drug, which has led to genuine concerns: Are we heading into a post-antibiotic era where we have no treatment for bacterial infections?

Amidst these developments, a new category of pathogens exhibits extensive drug resistance. The term "superbugs" was first coined to refer to multidrug or pan-drug resistant microbes resistant to all known antibiotics. Currently reported superbugs include *Enterobacterales*, *Staphylococcus aureus*, *Klebsiella pneumoniae*, *Acinetobacter baumannii*, *Pseudomonas aeruginosa*, and *Enterobacter* (bearing the acronym "ESKAPE"), along with carbapenem-resistant Enterobaterales (CRE), cabapenem-resistant *Klebsiella pneumoniae*, methicillin-resistant *Staphylococcus aureus* (MRSA), vancomycin-resistant *Enterococcus* (VRE) and multi-drug resistant *Acinetobacter* [16].

1.1.3 How bacteria develop AMR

Resistance to antibiotics arises from a natural coping mechanism, where resistant microbes have a survival advantage over non-resistant ones. Microbes, particularly bacteria, develop AMR through changes in their genetic framework either through 1) mutations or 2) incorporation of foreign DNA through horizontal gene transfer (HGT). The modifications generally occur in genes that code for receptors of the antibiotic, their transporters, or regulators that inhibit transporter synthesis. Evidence suggests that commensal or environmental bacteria are particularly responsible for promoting resistance in pathogenic bacteria through HGT [17]. These bacteria produce certain toxins that help them fight against invading pathogens. However, they are equipped with antibiotic-resistant genes that prevent them from dying from their toxins [18]. Figure 1.2 illustrates how AMR develops and spreads among bacteria. Bacteria acquire resistance primarily through the

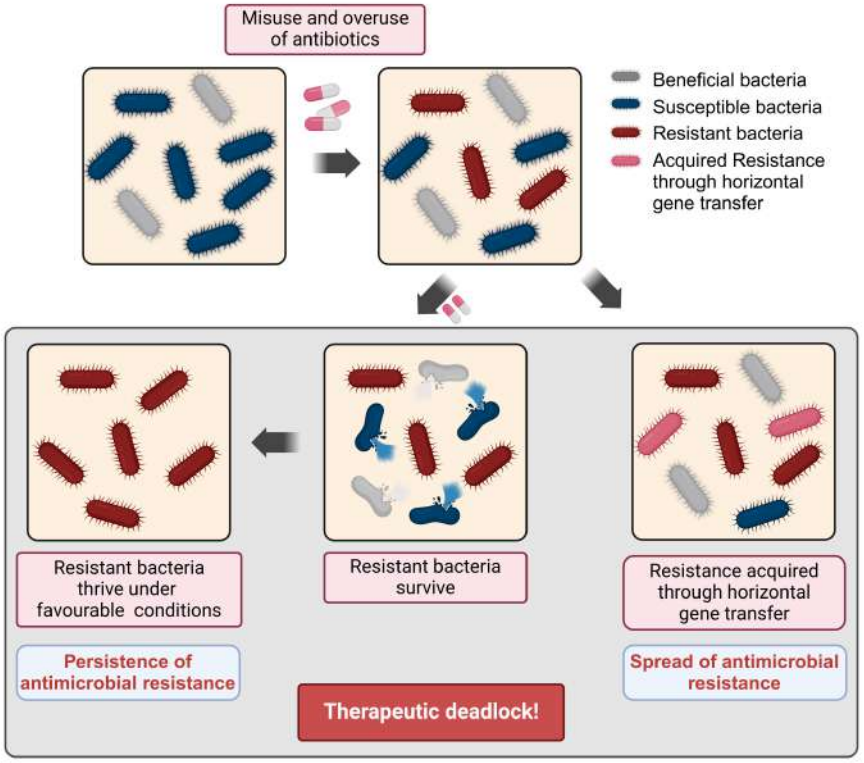

FIGURE 1.2: Mechanism by which AMR develops and spreads in bacteria.

following three pathways:

- **Intrinsic resistance**: The inherent capability by which bacteria produce countermeasures to antibiotics through genes present in their natural chromosome without the need for mutations or foreign DNA [19, 20].
- **Acquired resistance**: The evolutionary pathway by which previously susceptible bacteria acquire resistance through mutations in their genetic structure or by including exogenous genetic material via HGT [21, 22].
- **Adaptive resistance**: This is the response to selection pressure at sub-inhibitory antibiotic concentration, which also depends on other environmental stimuli (for ex, pH, ionic strength, stress, etc). Unlike the other two, adaptive resistance is often transient and ceases to exist when the selection pressure is removed [23, 24].

1.1.4 How AMR protects bacteria against antibiotics

Once the bacteria develop resistance, it renders antibiotics ineffective by the following mechanisms:

- **Reduced uptake of drugs**: The lipopolysaccharides (LPS) present in the outer membrane of gram-negative bacteria act as a natural barrier to chemicals, including antibiotics, and limit the uptake of the drug. Also, outer membrane proteins such as porins act as the gateway for antibiotics. So, the quantity or type of porin proteins is often regulated to limit the drug uptake. Specific resistance mechanisms regulate porin expression or induce changes in its structure, due to which its druggability decreases [25]. Few bacterial species have been reported to form biofilms that also reduce drug permeability [26, 27].
- **Changes in the drug receptor**: Spontaneous mutations in the genetic structure often modify the antibiotic receptor, which is why its binding is either prevented or reduced. Certain mutations can produce competing proteins that can bind to the drug and render it ineffective [28–31].

- **Chemical modification of the drug**: Antibiotics are chemically degraded through hydrolysis or modified by adding a functional group (acetyl, phosphoryl, adenyl, etc.) by certain bacterial enzymes. The modified product fails to bind to the protein receptor and thus is rendered ineffective [32].

- **Drug elimination through efflux**: Efflux pumps located in the plasma membrane help bacteria eliminate harmful compounds (antibiotics, metabolites, and signal molecules) from the cell interior. Substrate-specific pumps that selectively flush out antibiotics, may develop in resistant bacteria from exogenous genes [32–34].

1.1.5 Factors contributing to AMR

The rise and spread of AMR have been traced back to multiple sources that have been broadly categorized into (i) environmental factors, (ii) drug related factors, (iii) negligence in part of the patients and (iv) poor practices by physicians. Following are few specific drivers for AMR:

- **Misuse and overuse of antibiotics**: AMR is accelerated by misuse and overuse of antibiotics in humans and animals as revealed by epidemiological studies [35]. The primary reason for misuse is the use without indication of bacterial infection. Lack of knowledge in patients often leads to misconceptions about antibiotics, for example, using them to treat viral infections like the common cold and flu, or discontinuing the dosage before the prescribed duration is completed. The worst contributor to AMR is the easy availability of antibiotics as over-the-counter (OTC) drugs, which often leads to over-prescription by healthcare workers, pharmacists, and veterinarians. Often, physicians misuse antibiotics to gain unethical incentives from pharmaceutical companies for prescription [35–37].

- **Improvement in standard of living**: The overall increase in gross domestic product (GDP) globally has improved the standard of living, particularly in low and

middle-income countries (LMICs), which has increased the affordability of OTC antibiotics and their usage. Additionally, better income has led to increased consumption of animal proteins, which has increased transmission of AMR from livestock to humans [38].

- **Inappropriate antibiotic prescription**: Inappropriate prescription by physicians includes using the wrong drug for treating infections, prescribing the incorrect dosage or duration of consumption, or using antibiotics where they are unnecessary. Ideally, bacteria should be isolated and their specificity should be tested before prescription. However, a report published by the CDC (Centers for Disease Control and Prevention) in 2017 revealed a staggering 75% of cases where antibiotics were prescribed without due diligence [39–41].

- **Lack of innovation in antibiotics**: Over the past few decades, pharma companies have gradually declined in formulating novel antibiotics. The newly developed drugs are minor modifications of the existing ones and run the risk of developing resistance within a few years. This lack of interest stems from strict regulations from the FDA (Food and Drug Administration) in drug testing and marketing, as well as the associated costs of research and synthesis. Pharma companies have, instead, shifted their focus on drugs for chronic because of profitability [42, 43].

- **Use of antibiotics in farming and agriculture**: To meet the growing demands of human consumption, farming practices now rely heavily on antibiotics to improve feed quality, treat infections, and prevent diseases in livestock. A residual amount of these drugs finds its way into the human diet via livestock-derived products (for example, eggs, milk, protein, fat, etc.) and results in AMR. This misuse is rampant due to a lack of regulatory bodies in veterinary practices [44, 45].

- **Ease of travel**: Development in commute routes among nations has made traveling and exporting convenient. The resistant-bacterial strains endemic in one country are often unknowingly carried by humans and livestock to other countries where they were non-existent previously, leading to the spread of AMR [46, 47].

1.2 Ways to tackle AMR

The following preventive measures have been adopted to tackle AMR in recent times:

- **Prevention of Infections**: Efforts are underway to improve healthcare facilities (sanitation, drinking water, and hygiene) as preventive measures to mitigate AMR transmission. A combined effect of these factors alone can prevent more than 337000 AMR-related deaths per year. Another option is to formulate vaccines specific to resistant strains. Vaccines offer a preventive alternative to antibiotics, reducing healthcare pressure from infection-related hospitalizations. Unlike antibiotics, which are typically prescribed post-infection, vaccines are administered as a prophylactic measure. They function by activating the host immune system, which can identify future infections and kill the microbes in their entirety. This prevents the emergence of resistant strains, making them an effective tool in curbing the spread of infections [48–50].

- **Regulating Antibiotic Access**: Strict policies are being implemented to limit the availability of antibiotics as over-the-counter (OTC) medications and prevent their misuse. The World Health Organization's Access, Watch, and Reserve (AWaRe) program advocates the use of narrow-spectrum antibiotics (with a lower risk of causing AMR) for minor infections, recommends antibiotics in the Watch category to treat severe cases, and Reserves last-resort antibiotics for diseases caused by multidrug-resistant pathogens [51, 52].

- **Taking stewardship for antibiotics**: Strategies targeting the misuse of antibiotics involve awareness programs that educate the masses regarding the risks of AMR, promoting clarity in patient-doctor communication, and taking accountability for the antibiotic reserve for proper usage. For example, local guidelines can be implemented to prescribe antibiotics for hospital-acquired (nosocomial) infections [53, 54].

- **Increasing AMR surveillance**: The WHO has initiated multiple global collaborations for AMR surveillance, which keeps the rise and spread of resistant strains in check. The surveillance programs entail the collection and sharing of data between nations, which helps curate evidence-based plans for prescribing antibiotics, optimizing outcomes, and cutting down healthcare costs. AMR surveillance often includes sequencing the whole pathogen genome, which can detect resistant traits early [55–59].

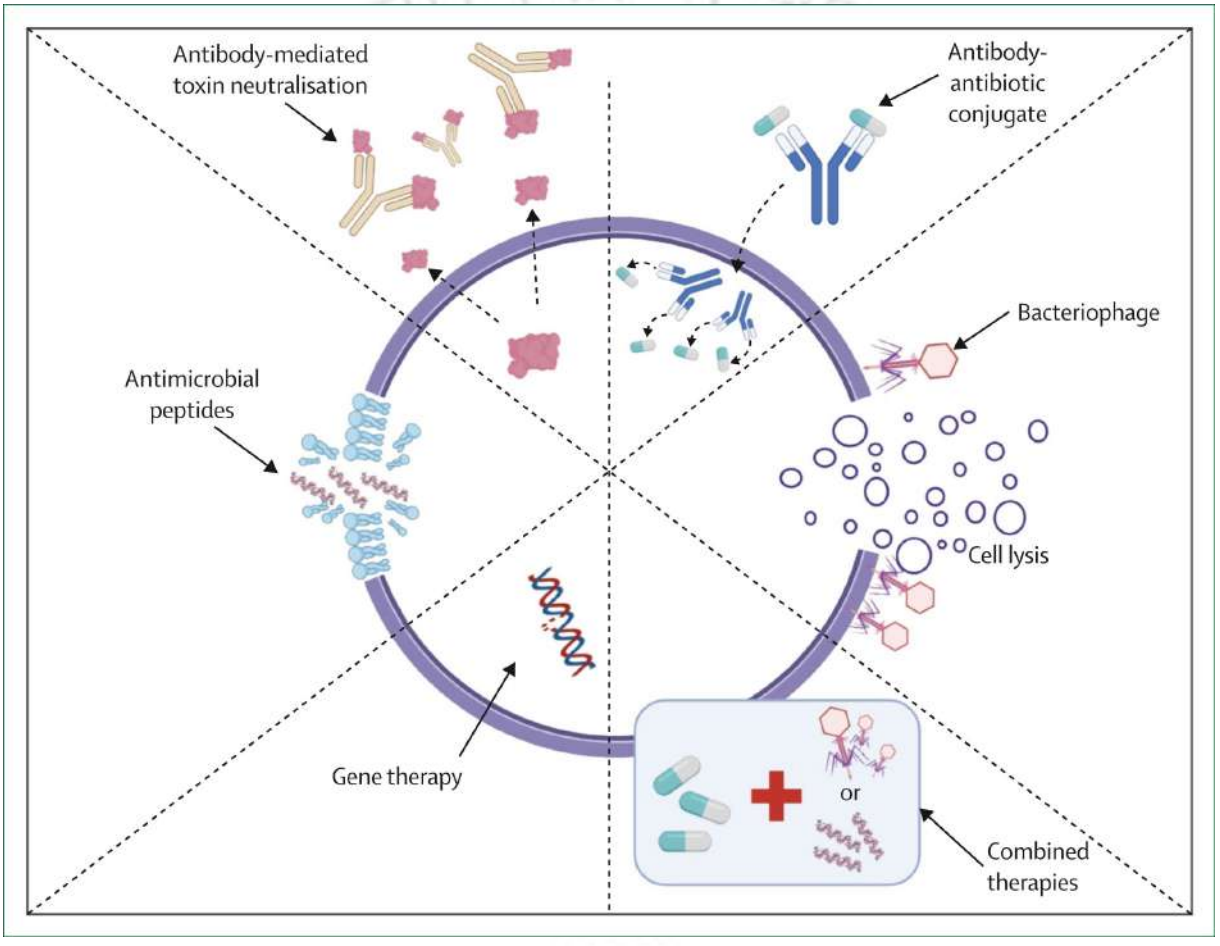

FIGURE 1.3: Therapeutic alternatives to antibiotics currently being explored. Reproduced from Ref. 60 under the terms of the Creative Commons CC-BY license.

- **Resorting to non-antibiotic-based treatments**: Alternatives to antibiotics are currently being explored as summarized in Figure 1.3. These include:

  - ◇ **Antibodies**: Human monoclonal antibodies (HMAs) can either kill the pathogens directly, neutralize their toxins, or bind to them to be easily identified by the

immune system. MHAs have been used earlier in the treatment of cancer and autoimmune disorders, and very recently, in the COVID-19 pandemic. They are highly specific to pathogens and preserve the natural microbiota [60–63].

- ◇ **Antibody-antibiotic conjugates**: A related strategy is to conjugate antibiotics to monoclonal antibodies that specifically bind to pathogens and release the drug molecules at the site of infection. These conjugated systems can narrow broad-spectrum antibiotics to site-specific or pathogen-specific drugs, promoting efficiency while preserving the commensal population [64, 65].
- ◇ **Gene Therapy**: The advent of the CRISPR-Cas9 technique has enabled us to edit the bacterial genome with high precision. This method uses CRISPR-Cas9 nucleases to introduce irreversible lesions to the bacterial chromosome, which ultimately lead to cell death. Additionally, these nucleases can be programmed to target selective bacterial species, which can help eliminate resistant strains from a mixed population [66, 67].
- ◇ **Bacteriophages**: An invasive technique to tackle resistant bacteria involves bacteriophages or viruses; they infect the bacterial cells and create multiple copies of themselves, ultimately leading to host lysis. Their action can be limited to the target bacteria and thus very specific, like the previous techniques. They can be administered in synergy with antibiotics and can produce enzymes that prevent biofilm formation. In addition, they can be trained to recognize their target cells in vitro, before they are administered in vivo [68–72].
- ◇ **Antimicrobial peptides (AMPs)**: These constitute short cationic peptides that are at the forefront of the immune system and provide the first layer of defense to invading pathogens. These peptides either disrupt the membrane integrity or act through membrane-independent pathways. In addition, they can modulate immunity and have antiviral and anticancer properties. Few antimicrobial peptides have been put to clinical trials and have shown better efficiency in synergy with antibiotics. Currently, research is focused on the delivery of these peptides to the target site through nanoparticles, hydrogels, and DNA/RNA-based carriers [73–82].

1.3 How antimicrobial peptides can help fight AMR

To understand how AMPs can be used against drug-resistant bacteria, we must first understand how they function. Such functional insights are crucial for the synthesis and design of drugs that optimize therapeutic strategies and mitigate harmful side effects. Broadly, AMPs operate either via membrane disruption or through non-disruptive pathways [83].

1.3.1 Membrane-dependent pathways

The interaction between AMPs and bacterial membranes is a complex and unique process driven primarily by molecular interactions. Generally, AMPs are amphipathic in nature, having both charged and hydrophobic residues on the surface. The positively charged residues adhere to the negatively charged phospholipid headgroups in the membrane (via electrostatic interactions). The hydrophobic groups, on the other hand, insert into the membrane and interact with the long hydrocarbon chain of the lipids. Beyond a critical concentration, AMPs aggregate among themselves and alter the mechanical properties of the membrane, leading to membrane thinning or pore formation. Such alterations disrupt the membrane barrier function and cause an imbalance of ions across the membrane that inhibits bacterial growth. Based on the sequence of events that lead to membrane disruption, the following mechanisms have been proposed (Figure 1.4):

- **Barrel-stave mechanism**: In this model, the AMPs aggregate into a polypeptide when they cross a certain threshold concentration and insert across the membrane vertically. The hydrophobic residues of the polypeptide interact with the hydrophobic tails of the lipid. The hydrophilic residues occupy the interior and create a transmembrane channel through which water molecules and ions can pass. Such transmembrane channels disturb the ion gradient and cause efflux of materials from the cell. The amphipathic structure of the peptides often develops post-aggregation but prior to insertion. The only caveat for this mechanism is the length of the peptides, which should be of the dimension of the membrane [84–86].

- **Toroidal-pore model**: In this model, peptides remain attached to the lipid headgroups and induce a tilt away from their lamellar normal during membrane invasion. This deformation results in toroid-like structures, where the lipid headgroups in the upper leaflet curve inward and merge with those in the lower leaflet, forming pores lined by both lipids and peptides. The hydrophobic residues of the peptide interact with the acyl chains, while the cationic residues are masked by the arched lipid headgroups. These pores are distinct from the barrel-stave pores, where the lipid headgroups retain their orientation and the peptides alone constitute the pore lining [86–89].

- **Carpet model**: In this mechanism, AMPs accumulate on the membrane surface like a carpet but fail to invade the hydrophobic core. Instead, the aggregate alters the membrane curvature leading to inward dissolution of the membrane into micelles similar to what we observe in detergents. This model is independent of interactions among AMPs and also independent of AMP interaction with the hydrophobic membrane core. Thus, peptides that show antimicrobial activity irrespective of their amino acid sequence and length operate via the carpet model [90–92].

1.3.2 Membrane-independent pathways

- **AMPs target cell walls**: AMPs either inhibit the formation of the cell wall or increase its permeability. There are two ways by which cell wall synthesis can be arrested. One involves AMPs that suppress the synthesis of Lipid II, an important precursor of the peptidoglycans N-acetylglucosamine (NAG) and N-acetylmuramic acid (NAM), which are essential components of the cell wall [94–97]. The deficiency in these components reduces the extent of cross-linking, thereby weakening the cell wall integrity. Another pathway involves AMPs that can choke bacterial respiration and reduce the production of ATP. Since cell wall formation is an active process, reduced ATP hinders its synthesis [98, 99]. AMPs can also activate enzymes or signalling pathways that release autolysin from bacteria and increase the permeability of the cell wall [100, 101].

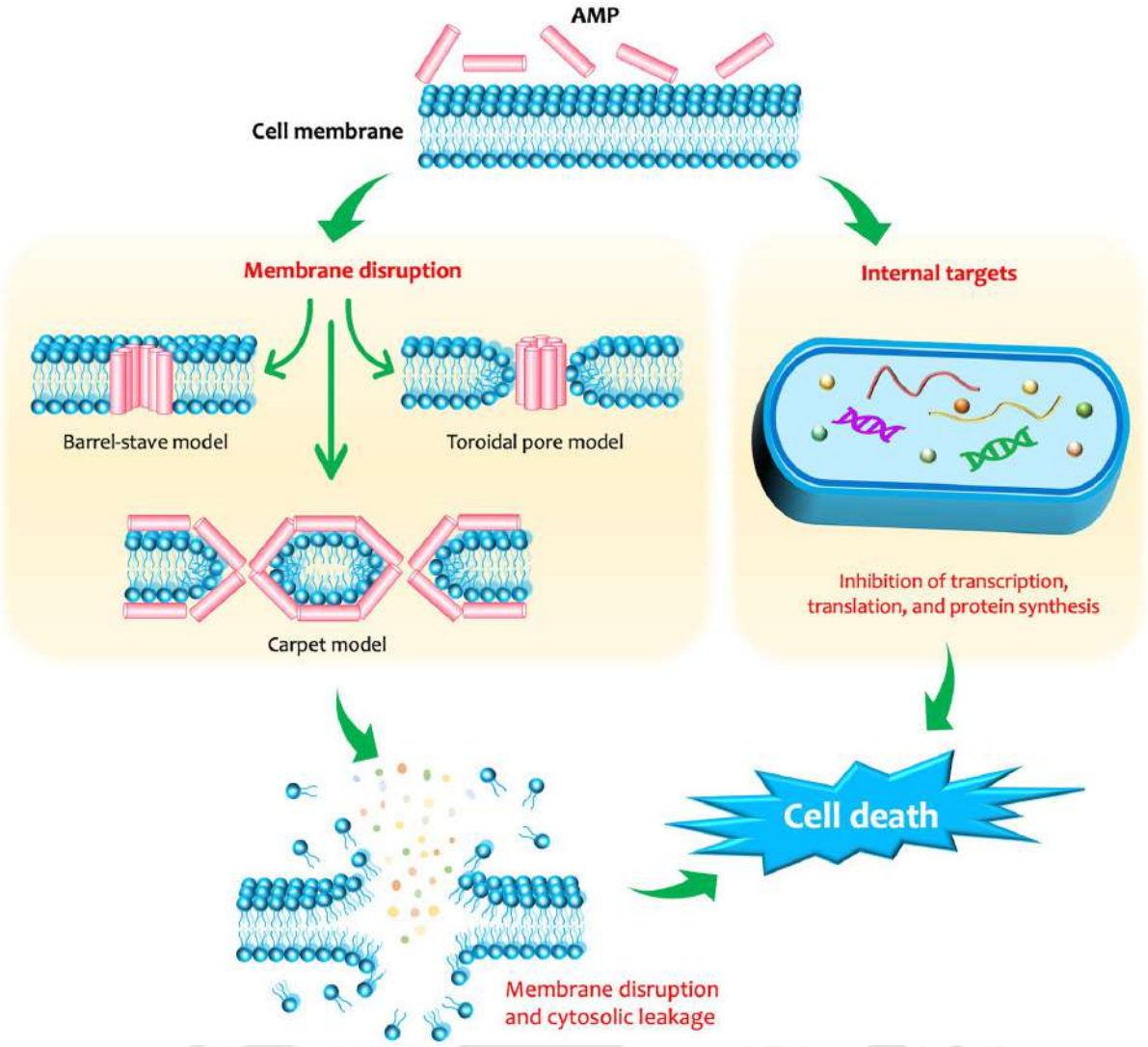

FIGURE 1.4: Models explaining how antimicrobial peptides exert their bactericidal activity, either by targeting intracellular components or by disrupting the cell membrane. Membrane disruption occur typically through one of three main pathways: the barrel-stave model, the toroidal-pore model, or the carpet model. Reproduced from Ref. 93 under the terms of the Creative Commons CC-BY license.

- **AMPs target intracellular components**: AMPs can bind to intracellular proteins and nucleic acids and interfere with the normal functioning of the cell. For instance, certain AMPs inhibit the replication of the genetic material while others cause degradation of DNA and RNA [102, 103]. In a few cases, AMPs also inhibit cell division and break the cell cycle [104, 105]. DNA repair is another important process that can be affected by certain AMPs, which leads to genetic disorders and cell death [106]. Besides, certain AMPs can target proteins that are responsible

for cellular metabolism, repair, and defense. In particular, they inhibit the electron uptake capability of intracellular enzymes and reduce the formation of ATP. Often, enzymes that break down metabolites are suppressed, which leads to the accumulation of toxic materials and loss of homeostasis inside the cell [107, 108].

- **AMPs target bacterial biofilms**: Biofilms are bacterial colonies embedded in an extracellular matrix that cooperate among themselves and function as a community. Numerous AMPs have been reported to disrupt biofilm formation and protect against infections. In a few cases, AMPs increased ciliary growth, leading to higher mobility of cells, thus preventing their adhesion to a surface [109, 110]. In other cases, they either blocked the sensing towards biofilm population or increased stress response, which prevented bacteria from coming together [111–113]. The extracellular matrix, which is composed of lipids, polysaccharides, proteins, and nucleic acids, can be degraded by a few AMPs, which also hinder biofilm formation [114–116].

- **AMPs modulate immunity**: AMPs play a crucial role in both innate and adaptive immunity. During pathogenic invasion, AMPs can either invoke or regulate immune responses. In particular, they regulate immune responses by influencing apoptosis in immune cells. This is crucial to determine the extent and period of the immune response while preventing tissue damage from uncontrolled immune reactions [117, 118]. In some instances, they also direct epithelial and immune cells to the site of injury and promote healing and regeneration of blood vessels [119].

1.4 The LL-37 peptide and its fragments

The human LL-37 (hLL-37) is a 37-residue antimicrobial peptide derived from the cathelicidin family of proteins [120–123]. The cathelicidin precursor has three distinct regions: (i) the N-terminal signal sequence, (ii) the highly conserved “cathelin” domain, and (iii) the C-terminal domain, which contains the antimicrobial segment [124–127]. Cathelicidin undergoes multiple stages of proteolytic cleavage and modifications to produce the LL-37

peptide, which is unstructured in solution but adopts an α-helical structure in the presence of membranes or at high peptide and salt concentrations [128–131]. hLL-37 plays a pleiotropic role in the immune system as it has antimicrobial and antiviral properties and shows promise as an alternative to conventional antibiotics [132–135]. In addition, LL-37 expression has been linked to the inhibition or progression of certain types of cancers [136–140]. Besides, it can attract neutrophils to the infection site to fight microbes and, in some instances, inhibit them to keep the immune response in check [141–143]. Another essential ability of LL-37 is seen in the regeneration of blood vessels, which helps heal wounds [144]. Figure 1.5 illustrates the monomeric structure of hLL-37 determined

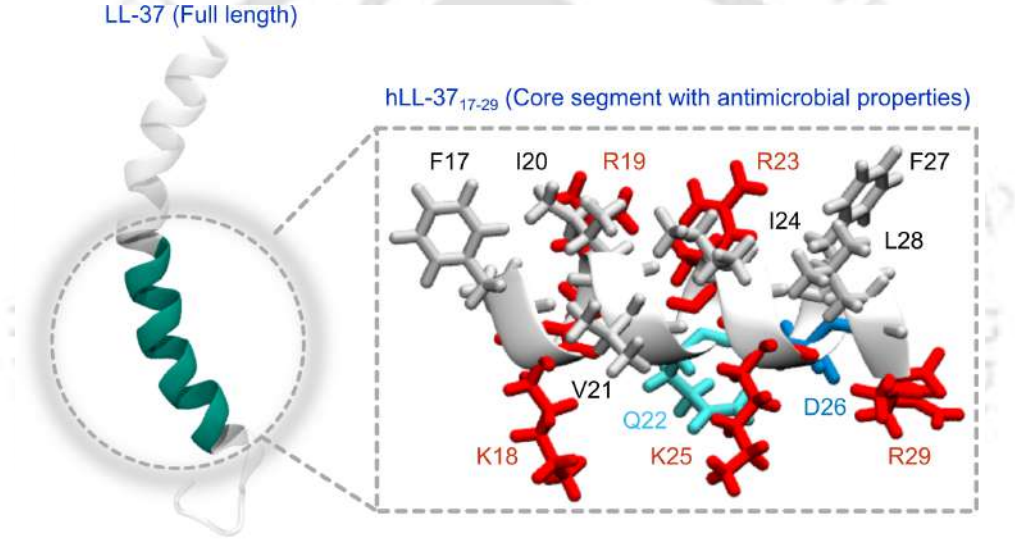

FIGURE 1.5: The hLL-37$_{17-29}$ fragment is generated from full-length LL-37 by bacterial proteases and represents the smallest segment that retains the antimicrobial activity of the parent peptide. The amino acid residues comprising this fragment are labeled. The peptide carries a net positive charge due to an abundance of cationic residues, with Asp26 (D26 in full-length LL-37) being the only negatively charged residue. In addition, a polar Gln22 (Q22) is also present.

in the presence of DPC micelles [130]. The peptide also exists in higher oligomeric structures at high concentration, protecting it from proteolytic cleavage [131, 145, 146]. The fragments derived from LL-37 are equipped with unique functionalities and provide an interesting area of research. The core segment, constituting the residues 17-29 (hLL-37$_{17-29}$), is the smallest fragment that retain the antimicrobial properties [147] of the full length peptide. This fragment adopts an α-helical structure in the presence of detergents, with

hydrophobic and hydrophilic residues occupying the opposite faces of the helix. The hydrophilic face, rich in cationic residues (Lys and Arg), can target the negatively charged bacterial membrane, while the hydrophobic face helps embed into the membrane interior. If we exclude the 17^{th} Phe residue, the residual 12-residue fragment (also known as KR-12) retains its antimicrobial property with reduced toxicity to human cells [148, 149]. The segments excluding the core region, especially 1-12 and 30-37, are generally disordered, forming short helices adjacent to turns and coils, and are associated with weak antimicrobial activity [147].

Previous studies on the hLL-$37_{17–29}$ fragment have shown that this peptide not only retains the antimicrobial activity of the full-length peptide but also exhibits a strong tendency to aggregate into supramolecular nanostructures with a characteristic cross-α amyloid architecture. The X-ray crystal structure of the resulting assembly reveals a repeating four-helix bundle motif. These studies highlight important functional roles of aggregation but also underscore key limitations: experimental approaches provide structural snapshots of the assembled state, yet they offer limited mechanistic insight into how dispersed peptides form encounter complexes, how these complexes reorganize into ordered bundles, or how physicochemical factors such as charge, hydrophobicity, and residue identity modulate these pathways. Likewise, while experiments suggest that aggregation can either enhance or inhibit antimicrobial activity, direct evidence linking sequence, aggregation propensity, and membrane interactions remains incomplete. These gaps emphasize the importance of molecular simulations, which can resolve the self-assembly process at high temporal and structural resolution and, through tools such as Markov state modeling and transition path theory, reveal the aggregation pathways, relaxation mechanisms, and membrane interactions that are difficult to access experimentally.

1.5 Thesis Overview

In the present chapter (**Chapter 1**), we have discussed the potential havoc of antimicrobial resistance and how antimicrobial peptides can be utilized to fight against it. In

particular, we have focused on the hLL-$37_{17\text{-}29}$ peptide that is known to possess antimicrobial activity and can aggregate into α-amyloids, an unique self-assembly principle reported recently. For this purpose, we have carried out molecular dynamics simulations of the hLL-$37_{17\text{-}29}$ peptide and its mutants in solution and in the presence of model membranes. We have taken this MD generated data to train unsupervised models using the framework of Markov state modelling. In **Chapter 2**, we briefly discuss the methodology of molecular dynamics simulations, the fundamentals of Markov state modelling and transition path theory. In **Chapter 3**, we study pathways via which hLL-$37_{17\text{-}29}$ peptides form encounter complexes (starting from a completely dispersed state) using semi-empirical Markov state models and transition path theory. In **Chapter 4**, we build Markov state models with finer molecular descriptors to study the pathways via which encounter complexes relax from a disordered state to an ordered state. We identify key interactions that drive this structural organization and propose a comprehensive model for α-amyloid self assembly. In **Chapter 5**, we explore how pre-formed hLL-$37_{17\text{-}29}$ fibrils interact with model membranes, ranging from bacterial to mammalian, in an effort to explain their selectivity. In **Chapter 6**, we study the effect of point mutations (at Ile24) on the aggregation property of hLL-$37_{17\text{-}29}$ to explain why these mutations can potentially reduce the antimicrobial activity of this peptide. In **Chapter 7**, we provide an overall summary based on our findings.

Chapter 2

Methodology

2.1 Molecular dynamics simulations

The phase space of the systems has been sampled using classical molecular dynamics (MD) simulations [150, 151]. Such techniques have been employed extensively to study biological systems like proteins, DNA, lipids, sugars, etc. [152]. In MD simulations, the constituent atoms of the biomolecule and the surrounding molecules (for example, water and ions) are treated as classical particles that obey Newton's laws of motion. The particles evolve in time according to:

$$m\frac{d^2\boldsymbol{r_i}}{dt^2} = \boldsymbol{F_i} \tag{2.1}$$

where $\boldsymbol{r_i}$ represent the position vector of particle i and $\boldsymbol{F_i}$ is the force acting on it. Equation 2.1 is solved numerically at time intervals of Δt (discussed later). The state of the systems (atomic positions and momenta) at time t_0 yields the state at time $t_0 + \Delta t$. The positions ($\boldsymbol{r_i}$) and velocities ($\boldsymbol{v_i}$), recorded at each timestep, are used to compute average properties that can be verified experimentally. $\boldsymbol{F_i}$ in Equation 2.1 is calculated as the gradient (∇) of the potential function, U, that describes all inter-atomic interactions in the system is a function of $\boldsymbol{r_i}$:

$$\boldsymbol{F_i} = -\nabla\ U(\boldsymbol{r_i}) \tag{2.2}$$

and can be broken down as the sum of bonded and non-bonded interactions:

$$U = U_{bonded} + U_{non-bonded} \tag{2.3}$$

where U_{bonded} can be further broken down into,

$$U_{bonded} = U_{bond} + U_{angle} + U_{dihedral} \tag{2.4}$$

and $U_{non-bonded}$ can be expanded into a sum of van der Waals and coulombic interactions:

$$U_{non-bonded} = U_{vdW} + U_{coulomb} \tag{2.5}$$

The three terms in Equation 2.4, namely, U_{bond}, U_{angle}, and $U_{dihedral}$ incorporates the energy contribution that comes from bonding between atoms, more specifically, the energy contributions arising due to distortion in the bond lengths, bond angles, and dihedral angles that occur due to the dynamic nature of the molecules. U_{bond} and U_{angle} can be expressed as a simple harmonic potential between directly bonded atoms (1-2 in case of bond lengths and 1-3 in case of angles) given as:

$$U_{bond} = \sum_{bonds} k_b(r - r_{eq})^2 \tag{2.6}$$

$$U_{angle} = \sum_{angles} k_\theta(\theta - \theta_{eq})^2 \tag{2.7}$$

where the summation runs over all bonds (Equation 2.6) and angles (Eq. 2.7) in the system; k_b and k_θ are the force constants for bond stretching and angle bending, respectively. The equilibrium bond lengths and angles are designated as r_{eq} and θ_{eq}. According to AMBER convention, $U_{dihedral}$ can be expressed as a fourier-series expansion of all torsional terms having the following functional form:

$$U_{dihedral} = \sum_{dihedrals} V_n[1 + cos(n\phi - \delta)] \tag{2.8}$$

where V_n represents the torsion barrier, δ represents the phase and n is the periodicity in the torsion angle.

The non-bonded contribution to U in Equation 2.3 arise due to van der Waals and electrostatic interactions between atoms. The van der Waals component can be modelled using a simple 6-12 Lennard-Jones (LJ) potential and the electrostatic component can be modelled using a simple Coulomb potential. While calculating the non-bonded potential, only pairwise interactions are considered (three or higher-body interactions are ignored). Mathematically, the total non-bonded potential over all i, j pairs in a systems can be expressed as:

$$U_{non-bonded} = U_{vdW} + U_{coulomb} = \sum_{i=1}^{N-1} \sum_{j=i+1}^{N} \left[\frac{A_{i,j}}{R_{ij}^{12}} - \frac{B_{i,j}}{R_{ij}^{6}} + \frac{q_i q_j}{\varepsilon R_{ij}} \right] \tag{2.9}$$

However, the relation of Equation 2.9 to a 6-12 LJ potential requires further explanation, specifically the terms, $A_{i,j}$ and $B_{i,j}$. The standard expression of LJ potential $V_{i,j}$ between atoms i and j is given as:

$$V_{i,j} = 4\varepsilon_{i,j} \left[\left(\frac{\sigma_{i,j}}{r_{i,j}} \right)^{12} - \left(\frac{\sigma_{i,j}}{r_{i,j}} \right)^{6} \right] \tag{2.10}$$

where $r_{i,j}$ is the inter-atomic separation, $\varepsilon_{i,j}$ is the depth of the LJ potential well, and $\sigma_{i,j}$ is the inter-atomic separation where the attractive and repulsive potential negate each other. $\varepsilon_{i,j}$ and $\sigma_{i,j}$ are unique for a particular atomic pair. Another form of the LJ potential, expressed in terms of the van der Waals radii, $R_{min}(i, j)$, is given as:

$$V_{i,j} = \varepsilon_{i,j} \left[\left(\frac{R_{min}(i,j)}{r_{i,j}} \right)^{12} - 2 \left(\frac{R_{min}(i,j)}{r_{i,j}} \right)^{6} \right] \tag{2.11}$$

where $R_{min}(i, j)$, expressed as a sum of R_i and R_j, is the distance between the atoms i and j where the LJ potential is at its minimum (i.e. at $V_{i,j} = -\varepsilon$). Combining Equation 2.10 and 2.11, we can relate $R_{min}(i, j)$ and $\sigma_{i,j}$ as:

$$R_{min}(i, j) = 2^{1/6} \sigma_{i,j} \tag{2.12}$$

Similarly, $A_{i,j}$ and $B_{i,j}$ are related to $R_{min}(i,j)$ as:

$$A = \varepsilon R_{min}^{12}(i,j) \quad \text{and} \quad B = 2\varepsilon R_{min}^{6}(i,j) \tag{2.13}$$

The $R_{min}(i,j)$ and $\varepsilon_{i,j}$ between the atomic pair i and j is deduced according to the Lorentz-Berthelot mixing rules where:

$$R_{min}(i,j) = 0.5[R_{min}(i) + R_{min}(j)] \quad \text{and} \quad \varepsilon_{i,j} = \sqrt{\varepsilon_{i,i} \cdot \varepsilon_{j,j}} \tag{2.14}$$

The coulomb contribution in Equation 2.3 is evaluated based on the partial charges q_i and q_j on atoms i and j. The parameters appearing in the equations above (k_b, k_θ, V_n, δ, $R_{min}(i,j)$, $\varepsilon_{i,j}$, q_i, and q_j) define the force field used in the MD simulations. For all systems examined in this thesis, these parameters were taken from the AMBER force field. Specifically, the hLL-$37_{17\text{–}29}$ peptide was modeled using the AMBER14SB force field, water molecules were modeled with TIP3P, and lipid molecules were modeled using LIPID21 available in the AMBER software suite.

With the functional form of the potential U clearly defined, the forces ($\boldsymbol{F_i}$) are evaluated according to the Equation 2.2 which gives the acceleration ($\boldsymbol{a_i}$) of the particles. Based on $\boldsymbol{a_i}$'s, Equation 2.1 is solved numerically using the leap-frog integrator as:

$$x_{t+\Delta t} = x_t + v_t \Delta t + \frac{1}{2} a_t \Delta t^2 \tag{2.15}$$

$$v_{t+\Delta t} = v_t + \frac{1}{2}(a_t + a_{t+\Delta t})\Delta t \tag{2.16}$$

where x_t, v_t, and i_t represents the position, velocity and acceleration at time t, respectively, which is used to solve for these quantities at time $t + \Delta t$. In fact, for practical purposes, a modified version of this integrator is used, that accounts for thermostat and barostat algorithms and the various constraints imposed on the system, which is beyond the scope of our discussion.

2.2 Markov state modelling

Markov state modelling is a mathematical framework that discretizes the 6N-dimensional phase space of a dynamical system into disjoint sets or metastable states. Such a decomposition transforms the time evolution of the system in the phase space into transitions between the metastable states. These transitions are captured in a count matrix $C(\tau) = [c_{ij}(\tau)]$, where $c_{ij}(\tau)$ represents the number of transitions from state i to j at lag time τ. The count matrix is transformed into the row-stochastic transition $P(\tau) = [p_{ij}(\tau)]$, where $p_{ij}(\tau)$ denotes the probability that the system is in state j at time $t + \tau$, provided it was in state i at time t. Before the trajectories can be discretized, their dimensionality is reduced by projecting them onto a low-dimensional subspace using the time-lagged independent component analysis (TICA) [153, 154]. For simulations that are carried out under equilibrium conditions, the transition matrix follows an interesting principle called the "principle of detailed balance", which can be mathematically written as,

$$\pi_i p_{ij} = \pi_j p_{ji} \tag{2.17}$$

where π_i and π_j represent the stationary state distribution (population) in state i and j, respectively. The lag time τ is the interval between MD time steps, chosen such that the Markovianity of the process is ensured while the faster processes are still preserved. One way to choose the lag time is to calculate the timescales of the processes in the underlying system. These timescales, also known as implied timescales (ITs), are evaluated as follows:

$$t_i = \frac{-\tau}{ln\,|(\lambda_i(\tau)|} \tag{2.18}$$

where $\lambda_i(\tau)$ are the eigenvalues of the transition matrix. The ITs are evaluated for a range of lag times τ_i ($\tau_i \in \{\tau_1, \tau_2, \tau_3 \cdots \tau_n\}$). The τ_i at which the ITs become invariant is chosen as the final lag time for MSM construction. Based on this τ_i, the transition matrix is constructed. The validity of this transition matrix is determined by the Chapman

Kolomogorov (CK) test. For a Markovian matrix, the CK property can be expressed as:

$$P(k\tau) = P^k(\tau) \tag{2.19}$$

where the left side is the transition matrix evaluated at time $k\tau$ ($k > 1$) and the right side is the transition matrix at τ (calculated previously) raised to the power k. The closer the values of the estimated and calculated matrix, the better is the model. The CK validated transition matrix can be decomposed into eigenvectors and eigenvalue pairs. The left eigenvector corresponding to highest eigenvalue ($\lambda_1 = 1$) represent the stationary distribution (population) of the state (π^T) according to:

$$\pi^T P(\tau) = \pi^T \tag{2.20}$$

The remaining eigenvalues ($\lambda_{i>1}$ where $\lambda_i < 1$) quantify the timescales (ITs) of the various processes in the system. These processes themselves are represented by the right eigenvectors (ψ_i) of $P(\tau)$, according to:

$$P(\tau)\psi_i = \lambda_i(\tau)\psi_i \tag{2.21}$$

2.3 Transition path theory

The entries n_{ij} in the count matrix mentioned previously quantifies the number of transitions from state i to j. Inter-state transition times were approximated according to $t_{ij} = \frac{N_i}{n_{ij}}$, where $N_i = \sum_{j \in S} n_{ij}$, represents the total residence time in state i. The Markovian generator matrix, $R = (r_{ij})_{i,j \in S}$ were evaluated from t_{ij} as follows:

$$r_{ij} = \frac{1}{t_{ij}} - \delta_{ij} \sum_{j \neq i} r_{ij} \tag{2.22}$$

where δ_{ij} denotes the Kronecker delta function. The generator matrix, R, bear the following properties [155]:

$$R = \begin{cases} r_{ij} \geqslant 0 & \forall i, j \in S, i \neq j \\ \sum_{j \in S} r_{ij} = 0 & \forall i \in S \end{cases} \tag{2.23}$$

and can be used to evaluate the population of states, π, (also known as the stationary distribution of states) based on [155]:

$$0 = \pi^T R \tag{2.24}$$

Using the stationary state population $(\pi_i)_{i \in S}$, the time-reversed generator matrix, $(\tilde{R})$, was evaluated as follows [155]:

$$\tilde{r}_{ij} = \frac{\pi_j}{\pi_i} r_{ji} \tag{2.25}$$

Next, a pair of states were singled out from S to represent the systems' initial (P) and the final (Q) aggregate states. In a trajectory, multiple transitions from P to Q may occur via an ensemble of pathways. The probability of the ith state participating in a P→Q event can be obtained from the piecewise committor functions, q_i^+ and q_i^- (Equation 2.26, 2.27). The forward committor, q_i^+, measures the probability of the system in the state i to travel to state Q, in a single step or a sequence of steps, without visiting state P on the way. Similarly, the backward committor, q_i^- measures the probability that the system, currently in state i, has traveled from state P (directly or via a sequence of steps) without visiting state Q in between. q_i^+ and q_i^- were calculated from the generator matrices (R and $\tilde{R}$) using:

$$\begin{cases} \sum_{j \in S} r_{ij} q_j^+ = 0 & \forall i \in (P \cup Q)^c, \\ q_i^+ = 0 & \forall i \in P \\ q_i^+ = 1 & \forall i \in Q \end{cases} \tag{2.26}$$

and,

$$\begin{cases} \sum_{j \in S} \tilde{r}_{ij} q_j^- = 0 & \forall i \in (P \cup Q)^c, \\ q_i^- = 1 & \forall i \in P \\ q_i^- = 0 & \forall i \in Q \end{cases} \tag{2.27}$$

The ensemble of reactive trajectories that transition from state i to j per unit time, on the way from P $\rightarrow$ Q is denoted by f_{ij}^{PQ} and computed as,

$$f_{ij}^{PQ} = \begin{cases} \pi_i q_i^- r_{ij} q_j^+ & if\ i \neq j \\ 0 & if\ i = j \end{cases} \tag{2.28}$$

To account for back transitions from j to i, that reduces the overall contribution to the pathway P $\rightarrow$ Q, the net flux f_{ij}^+ (also called flux current) is considered, where,

$$f_{ij}^+ = max(f_{ij}^{PQ} - f_{ji}^{PQ}, 0) \tag{2.29}$$

Weighted graphs were constructed based on the population of states (π)and the net transition fluxes (f_{ij}^+)- represented as $G(V, E)$, where vertices V represent the states in S (i.e., $V \in S$) and the edges E are measured by the flux current among the states ($E = \{f_{ij}^+\}$). G was depicted as a transition network using the Networkx package in Python. All P $\rightarrow$ Q events in the conformational space S are denoted as pathways χ in $G(V, E)$, where $\chi = (v_0, v1, v2, \cdots v_n) : v_0 \in P, v_n \in Q$. Connected pathways($\chi$) were obtained using the depth-first search (DFS) algorithm [156]. For a particular χ, the rate at which P $\rightarrow$ Q occurs is limited by the minimum flux current ($f_{ij,min}^+$) in the pathway. The dominant pathway was determined based on the maximum value of ($f_{ij,min}^+$) in $G(V, E)$ using a binary search approach. This flux was subtracted from $G(V, E)$, and the resulting graph was used to determine the next important pathway. A stepwise implementation of the theory was accomplished using the PyEMMA library in Python [157].

Chapter 3

Pathways of hLL-$37_{17\text{-}29}$ Aggregation Give Insight into the Mechanism of α-Amyloid Formation

Overview

α-amyloids present a novel self-assembly principle that can be utilized to prepare functional biomaterials. Evidence of α-amyloid formation in the active core of the human LL-37 protein (comprising residues 17 to 29) was associated with this peptide's membranolytic property. Though mechanistic pathways of β-amyloid formation are known, such studies are scarce in α-amyloids. Modern computational techniques allow such mechanistic studies in molecular detail. Here, we propose aggregation pathways in hLL-$37_{17\text{-}29}$ through molecular dynamics simulations. We first identified oligomers among peptides based on a distance criterion. The distribution of oligomers were then used to build Markov state models from which pathways were obtained using the framework of transition path theory. We checked the structural stability of the peptides during oligomerization which is crucial from their functional point of view. We also investigated the key residues that participate in oligomer formation, the interactions between them, and the effect of residue mutations on the binding free energy of the peptides. Our findings suggest that larger oligomers are produced from the association of smaller and intermediate oligomers. The peptides retain their helical structure during aggregation with transient occurrences of 3-10 helix and turns. Hydrophobic interactions are vital in the aggregation of these peptides with I24 playing a crucial role. Mutation of this residue to Ala decreases the peptides' binding free energy, resulting in reduced aggregation tendency.

3.1 Introduction

Amyloids refer to the organized self-assembly of proteins that adopt various structural features ranging from water-soluble aggregates to insoluble plaque-like deposits [158, 159]. Depending on the secondary structure of the constituent protein monomer, amyloids can be broadly classified into two categories: α [160, 161] and β [162–165]. The domain of β-amyloids has been extensively researched and linked to numerous neurodegenerative and systemic disorders [166, 167]. On the contrary, the occurrence of α-amyloids was only recently reported by Engelberg et al. to explain the self-assembly of the cytotoxic peptide PSMα3 secreted by *Streptococcus aureus* [160]. This particular protein assembly mimics the cross-β architecture in β-amyloids [168], where individual helices stack perpendicular to the fibril axis, forming α-helix rich sheets that interact via hydrophobic interfaces to form the cross-α architecture. Owing to architectural resemblance, α-amyloids bear similar tinctorial and morphological properties as β-amyloids [160]. The α-amyloid self-assembly in PSMα3 was associated with the cytotoxic effects of *Streptococcus aureus*. The helical nature and the tendency of the peptides to undergo fibrillation jointly explained the cytotoxicity of PSMα3 [160]. Further, the presence of positively charged residues on the peptide surface was found to contribute to its cytotoxicity [161]. A combination of hydrophobic-hydrophilic residues on the peptide surface facilitates adhesion to cell membrane leading to disruption.

Both α and β-amyloids exist as unbranched fibril-like structures that can be utilized to build functional biomaterials with diverse applications [169–172]. Studies indicate that β-amyloids can catalyze reactions [173, 174] and are an excellent source of functional materials having optical, electrical, and mechanical properties [175–178]. However, the inherent toxicity of β-amyloids and their association with various pathological conditions limits their practical application. Host defense peptides, which are integral components of the immune system, show evidence of aggregation into amyloid fibrils and thus provide suitable alternatives for the design of biomaterials [179–182]. Additionally, the antimicrobial property of these peptides can be exploited to combat resistant bacterial strains that constitute a serious health risk to modern society [5].

Human LL-37 (hLL-37) is a host defense peptide cleaved from the precursor cathelicidin protein, hCAP-18 [183]. hLL-37 plays a pleiotropic role in the host immune system [184] as it: (a) provides the first level of resistance to invading pathogens [185–187], (b) directs immune cells to the location of the injury [188], (c) regulates the secretion of pro-inflammatory factors [189–191], and (d) boosts cell division for wound healing [192–195]. Loss or reduced expression of hLL-37 is associated with several diseases, viz., morbus Kostmann [196], and atopic dermatitis [197]. hLL-37 bear high sequence similarity with PSMα3 showing a tendency to aggregate into α-helical fibrils [198]. The functional role of hLL-37 as a membrane disruptor stems from its tendency to form fibrillar aggregates [186, 198]. The membranolytic property of hLL-37 also depends on the nature of the constituent lipid-forming trans-membrane pores for unsaturated lipids and supra-helical fibrillar aggregates for saturated lipids [199]. Co-complexation of hLL-37 with DNA amplifies the activation of the Toll-like receptor 9 in immune cells and modulates the immune response [200]. hLL-37 can be truncated into a plethora of fragment peptides with antibacterial [130, 201], anti-biofilm [202], antiviral [203], and anticancer [139] properties. Specific bacterial proteases degrade hLL-37 into inactive fragments as part of their virulence action [204]. The shortest region of the hLL-37 peptide comprising the residues 17-29 (^{17}FKRIVQRIKDFL^{29}R) is effective against bacterial and cancer cells [147]. Engelberg et al. [205] recently demonstrated the supra-molecular structures formed by the hLL-$37_{17\text{-}29}$ fragment via X-Ray crystallography. A wheel plot representation (Figure 3.1) of this fragment peptide reveals two faces of opposite polarity that assist in its aggregation into supramolecular nanostructures having the signature cross-α amyloid architecture. Antimicrobial property is attributed to the aggregation behaviour of the peptide and is disrupted with the incorporation of charged amino acid residues on the hydrophobic face of the peptide.

Cross-α amyloids bring forth a new self-assembly principle in nature that is omnipresent and crucial to study. Advances in technology and theory make it possible to study aggregation pathways in peptides in mechanistic detail. One such technique involves the construction of Markov State Models (MSMs) based on different intermolecular features

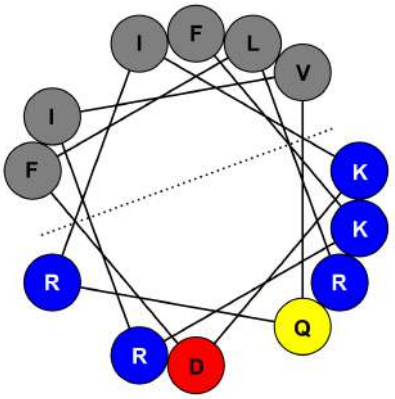

FIGURE 3.1: **Wheelplot representation of hLL-37$_{17\text{-}29}$ helix:** The dotted line divides the two faces of the helix - the hydrophobic face consisting of hydrophobic residues (gray) and the hydrophilic face consisting of polar (yellow), positively charged (blue) and negatively charged (red) residues.

that capture the aggregation process [206–211]. In particular, MSMs built on the distribution of oligomeric species in solution give us a qualitative model for peptide aggregation processes [212]. With semi-empirical MSMs as the backbone, the pathways of peptide aggregation can be acquired using the framework Transition Path Theory (TPT) [155, 213–215]. Here, we study aggregation properties of hLL-37$_{17\text{-}29}$ via all-atom molecular dynamics (MD) simulations. We first identified clusters among peptides based on a distance-cutoff and then calculated the relative abundance of each oligomer. We then constructed MSMs based on the aggregation state of the peptides and explored pathways via which peptides assemble using TPT. We also looked at the structural changes of the peptide during the aggregation process. We then figured out vital molecular interactions that promote peptide aggregation. Additionally, we quantified the energetic contribution of each residue toward the aggregate formation. Our findings reveal the presence of intermediate oligomeric states that coalesce to form higher order oligomers. We attribute hydrophobic interactions among residues as the dominant force that guide the aggregation process. In particular, I24 plays a crucial role in aggregation as a mutation in this residue alters binding among peptides remarkably.

We have structured the rest of Chapter 3 into the following Sections: (a) In Section 3.2, we discuss the specifics of the systems used in this Chapter, the various conditions employed

in the MD simulation, and a detailed description of the analyses, particularly TPT, (b) In Section 3.3, we present the results of the analyses in detail and provide physical interpretation for our observations, and (c) In Section 3.4, we conclude our overall findings in this study.

3.2 Methods

3.2.1 Preparation of hLL-37$_{17\text{-}29}$ structure

X-Ray crystal structure of the hLL-37$_{17\text{-}29}$ dimer (resolution $\approx$ 1.35 Å) was downloaded from the RCSB Protein Data Bank (PDB ID: 6s6m) [205]. Monomer coordinates were extracted from the PDB to yield the initial structure of the peptide. To prevent electrostatic interactions among the peptide terminals, acetyl (ACE for the N-terminal) and N-methyl (NME for the C-terminal) caps were added with the `tleap` module of AMBER18 [216]. Next, the protonation state of the residues at pH 7 was determined using `PROPKA 3` software [217, 218] Consequently, Arg residues at positions 3, 7, and 14 and the Lys residues at 2 and 9 were protonated. The Asp residue at the 10$^{\text{th}}$ position was deprotonated, imparting a net +4 charge to the peptide. The resulting monomer was minimized in vacuo to eliminate initial steric clashes. The peptide was modeled using the AMBERff14SB [219] force field.

3.2.2 Preparation of the systems

Two systems were prepared consisting of 4 and 8 units of hLL-37$_{17\text{-}29}$-referred henceforth as hll-4 and hll-8, respectively (Table 3.1). For hll-8, the 8 peptide units were placed at the corners of a cube of edge 40 Å. For hll-4, the 4 peptides were placed at the alternate corners of a cube of 40 Å to ensure sufficient separation between the peptides. A total of 5 and 6 replicas were generated for hll-4 and hll-8, respectively, which differ in the relative orientation of the peptides. The smaller cubes, with peptides at the corners,

were immersed in a larger water box to obtain the solvated systems. Roughly 2000 water molecules were added per peptide for the two systems. For modeling water molecules, the explicit TIP3P force field was used [220]. PACKMOL [221] software was employed to prepare the initial configuration of the systems, keeping the distance between any two atoms greater than 2 Å. At physiological pH, the protein carries a net positive charge of 4 units that were neutralized by 4 Cl^- ions using the `tleap` module of AMBER18 [216]. To set the ionic strength at 150 mM, additional Na^+ and Cl^- ions were added [222]. Monovalent ion parameters used were obtained from the works of Joung et al [223].

TABLE 3.1: Details of all the systems used in Chapter 3. N_p designate the number of peptides used in each of the systems. M_p designates the molar concentration of the peptides. The total simulation time for each of the systems are given alongside.

System	N_p	**Box length (Å)**	M_p**(M)**	**Simulation Time**
hll-4	4	≈ 65	≈ 0.025	5×500 ns
hll-8	8	≈ 80	≈ 0.025	6×1000 ns

3.2.3 MD Simulation Protocol

Systems were minimized in two consecutive stages- An initial 5000 steps of the steepest descent method followed by 5000 steps of the conjugate gradient method to eliminate bad contacts between the atoms (if any). The SANDER module of AMBER18 [216] was used to perform the minimizations. The final temperature of the systems was attained in a stepwise manner over a time duration of 400 ps in an NVT ensemble. Following this step, each system was equilibrated for 4 ns at 300 K and 1 atm pressure in an isothermal-isobaric (NPT) ensemble. The concentration of the peptides at the end of the equilibration step was approximately 0.025 M. The equilibrated systems were then subjected to a production run under NPT conditions, during which the coordinates were recorded at a time interval of 4 ps. The equations of motion were solved at intervals of 2 fs using the leap-frog algorithm. Berendsen barostat [224] (coupling constant = 2 ps) and Langevin thermostat [225] (collision frequency = 1 ps^{-1}) were utilized to maintain constant pressure and temperature throughout the NPT simulations. Covalent bonds

involving hydrogen were restrained with the SHAKE algorithm [226]. Short-ranged non-bonded interactions were computed within a cutoff distance of 10 Å. The particle mesh Ewald (PME) [227] algorithm was used to calculate electrostatic contributions from both long-range and short-range interactions. The short-range contributions were calculated in the real space (cutoff = 10 Å) and the long-range contributions were calculated in the Fourier space using Ewald summation with 1 Å grid spacing. Periodic boundary conditions were imposed along the three coordinate axes. Each replicate of hll-4 was simulated for a duration of 500 ns, whereas hll-8 replicates were simulated for 1 μs each. Long simulation times were attained using the GPU implementation of the AMBER simulation code [228].

3.2.4 Analyses

3.2.4.1 Cluster structure analysis

Oligomers among peptides were identified based on a clustering algorithm that uses the nearest-neighbour approach proposed by Stoddard [229]. In brief, a pair of peptides form a cluster if the inter-atomic distance between any two atoms is less than 4 Å [207]. The number of oligomers of each size was computed per MD frame. The changes in the oligomeric state were determined from the time evolution of the largest cluster size. The relative abundance of an oligomer, $P(n)$, was obtained using the following:

$$P(n) = \frac{\langle N(n,t) \rangle}{\sum_n \langle N(n,t) \rangle} \times 100 \tag{3.1}$$

where $N(n,t)$ represents the number of oligomers of size n at time t. The angular brackets $\langle \cdots \rangle$ denote time averages.

3.2.4.2 Transition Path Theory

For TPT, Markov State Models (MSMs) were constructed based on the dispersion state of the hLL-$37_{17\text{-}29}$ peptides in solution. Dispersion states (S) were determined using the

'identical elements grouping' method [212]. In brief, this method deduces all possible combinations ($M(n,r)$) by which n identical polypeptide chains can be distributed into r distinct oligomeric groups. Mathematically, $M(n,r)$ is given as:

$$M(n,r) = \sum_{i}^{r} M(n-r,i) \tag{3.2}$$

and obeys the following properties:

$$M(n,1) = 1 \tag{3.3}$$

$$M(n,n) = 1 \tag{3.4}$$

$$M(n+1,n) = 1 \tag{3.5}$$

Each MD frame was assigned to a particular state S according to the clustering algorithm mentioned in Section 3.2.4.1. The time evolution of the systems, at an interval of 8 ps (lag time), was monitored as stochastic jumps between the different states in S. Each transition from state i to j $(i,j \in S)$ was recorded in the form of a count matrix, $C = (n_{ij})_{i,j\in S}$, where an entry n_{ij} quantifies the number of such transitions. This count matrix forms the basis of the semi-empirical MSMs from which the pathways were extracted using transition path theory outlined in Chapter 2.

3.2.4.3 Structural Features of the oligomers

The root-mean-square deviation in atomic coordinates (relative to the energy-minimized structure) was measured considering only backbone atoms (C, C_α, N, O), as deviations in these atoms reflect the most in the overall peptide structure. Global motions (translational and rotational) were eliminated by the least-square fitting of the peptide structure to the energy-minimized configuration. The mass-weighted variation in atomic positions was calculated over the entire trajectory, considering frames at an interval of 40 ps. The rolling averages of the RMSD values over 500 frames were plotted against time. The secondary structure of the peptides was evaluated utilizing the DSSP algorithm implemented in the

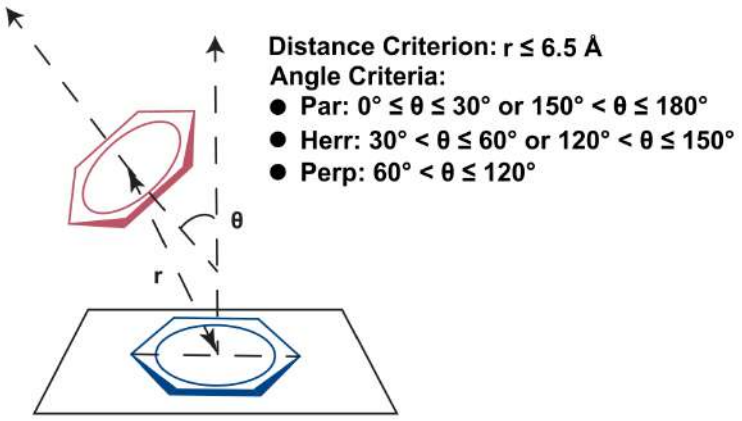

FIGURE 3.2: Schematic for π-stacking interactions among Phe rings.

CPPTRAJ [230] module of AMBER18. Salt-bridges of a system were identified between the oxygen atoms of acidic residues (Asp) and the nitrogen atoms of basic residues (Arg and Lys). A salt bridge was formed when the contact distance between these atoms was less than 3.5 Å. Even though multiple contacts are possible between a pair of residues, one was adequate for salt-bridge assignment.

3.2.4.4 Inter-residue interactions and energies

Inter-residue contact maps for each of the oligomeric states were computed next. A pair of residues were considered in contact, provided the inter-atomic distances were less than 4 Å. The contact information was stored in a matrix, where the rows and columns correspond to the peptide residues. For every contact between the ith residue of one peptide with the jth residue of another, the corresponding cell in the contact matrix was incremented by one. The contact matrix was populated based on all the replicates of the systems. The final matrix was normalized and depicted as a heat map using the Seaborn library of Python. For Phe rings having center-of-mass (COM) distances within 6.5 Å three different stacking interactions are possible based on their relative orientation: (1) 0-30°/150-180° for parallel(Par) stacking, (2) 30-60°/120-150° for herringbone (Herr) interactions and (3) 60-120° (Perp) for perpendicular stacking [231]. Figure 3.2 summarizes the geometric definition of π-stacking interactions. The effect of mutations on the binding energy of the

peptides was studied using the Alanine scanning technique implemented in the MMGBSA method of AMBER18 [232, 233] The details of the MMGBSA method used in peptide aggregation are given elsewhere [234].

3.3 Results and Discussion

3.3.1 hLL-37$_{17\text{-}29}$ peptides show tendency to aggregate into oligomers of various sizes

We captured snapshots of the systems at three different instances of the simulation: (1) post-equilibration, (2) at an intermediate timescale, and (3) at the end of the production run (Figure 3.3 and Figure 3.4). For both the systems, hLL-37$_{17\text{-}29}$ shows tendency to aggregate under the conditions we employed for our MD simulations. The final peptide concentration in the systems ($\approx$ 0.025 M) was 2.5 times higher than the experimental concentration (0.010 M) at which the peptide was crystallized. Our rationale for taking a higher concentration was to ensure that we work in the concentration range critical for peptide aggregation. Also, it is often difficult to recreate `in vitro` concentrations for peptide aggregation simulations due to the higher number of water molecules required, which increases the computational cost [235]. Besides, the local concentration of the peptides `in vitro` generally exceeds their physiological concentration in the event of an aggregation [236].

In our discussions, we have preserved the actual residue numbers of the peptide in hLL-37, i.e., the N-terminal starts at 17 and the C-terminal ends at 29. For ease of comprehension, we categorized oligomers based on size into three groups (Figure 3.4): (1) lower order oligomers, (2) intermediate oligomers, and (3) higher order oligomers. The snapshots show aggregation among the peptides for the hll-4 and hll-8 systems. Post-equilibration, we found that the peptides are mostly dispersed with rare occurrences of lower order oligomers. The tendency to form lower order aggregates is higher in the case of hll-8 systems compared to hll-4. Even though we kept the concentration of the peptides similar

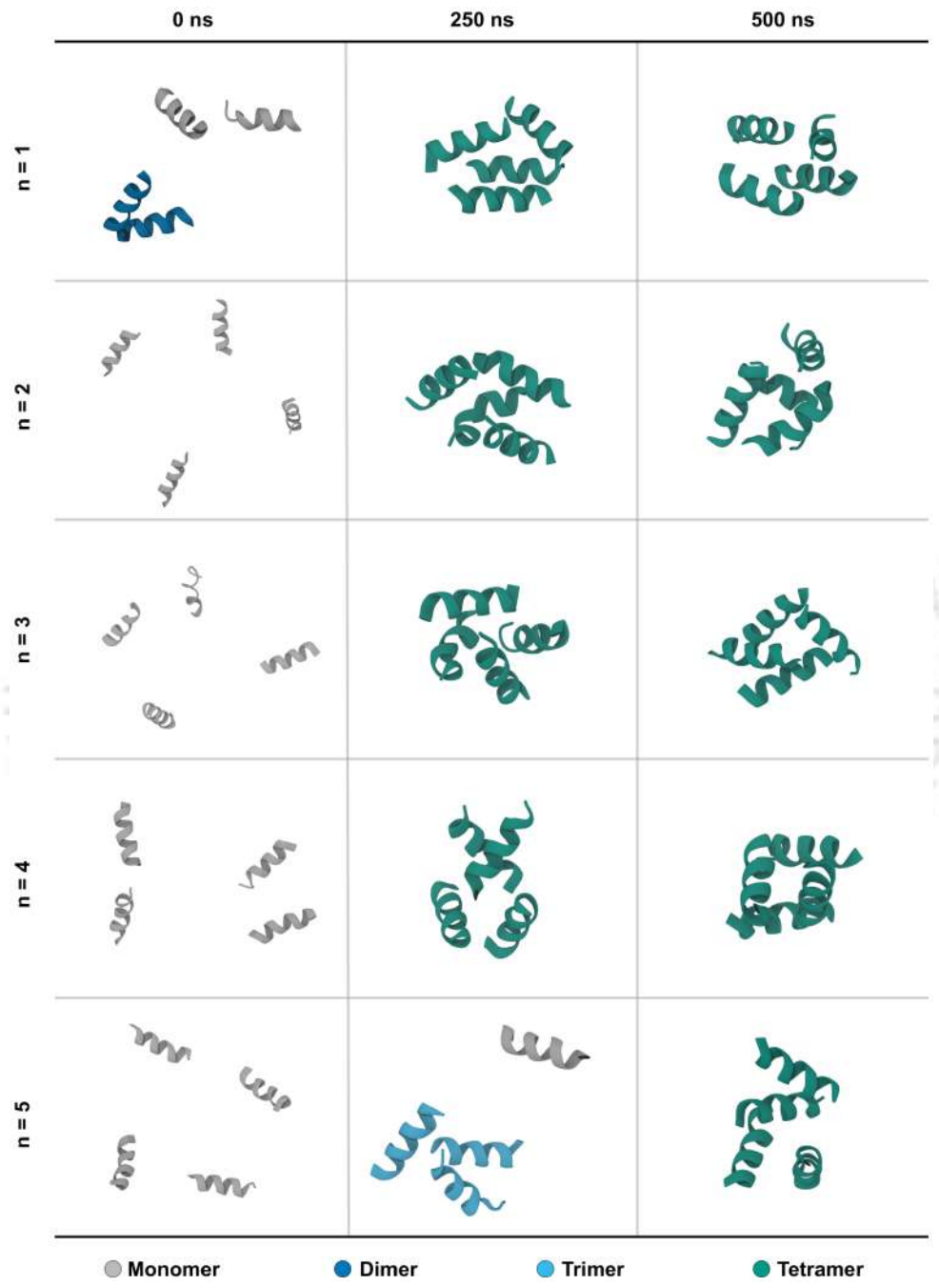

FIGURE 3.3: **Snapshots of the hll-4 systems taken at three different instances of the simulations:** at 0 ns (left), at 250 ns (middle) and at 500 ns (right). System replicas are labelled as n. The peptides are coloured based on the oligomeric state they belong to.

for the systems, a higher aggregation tendency for hll-8 is explained by the increased encounters among peptides due to the finite size of the simulation box [237]. Around 250 ns, most hll-4 replicas achieve the highest tetrameric state. Halfway through the simulation (at 500 ns), we rarely detected the octameric state in hll-8; instead, we observed an abundance of intermediate oligomeric forms.We suggest that lower-order oligomers are easily formed, and higher-order oligomers are challenging to achieve at the intermediate simulation timescales. The chances of achieving the largest aggregate size increase at the end of the production run for hll-8. 4 out of the 6 hll-8 replicas aggregate to the octameric state at the end of the 1 μs simulation. Only in rare cases do the systems remain dispersed as intermediate oligomers on completion of the production run. For hll-4 systems, the tetramers formed halfway into the simulations remain intact till the end.

3.3.2 Formation of lower and intermediate oligomers kinetically faster than higher order oligomers

The snapshots provide only static information about the systems at different instances of the MD simulations. To study the kinetics of the aggregation process, we monitored the time evolution of the largest cluster formed for hll-4 and hll-8 systems (Figure 3.5(a) and (b)). We found that hll-4 systems attain the highest possible oligomer state faster than hll-8. For hll-4 (Figure 3.5(a)), most replicates reached the tetrameric state within ≈125 ns of MD simulation. In a few cases (Figure A.1, Appendix A), the systems oscillate between the tetrameric form and lower oligomers during the initial duration of 125 ns. Once formed, the tetrameric state remains preserved for the rest of the simulation. In rare cases, we found transient breakdown of the tetramer into lower order oligomers which is quickly recovered. For hll-8 (Figure 3.5 (b)), the kinetics of oligomerization is slower compared to hll-4 as the overall oligomerization state increases progressively during the simulation. In the 1 μs simulation timescale, we recorded an average oligomerization state of 7 in hll-8 systems. On closer inspection (Figure A.2, Appendix A), we found occurrences of the octameric form in few of the replicas. Instead, the system traverses between the numerous

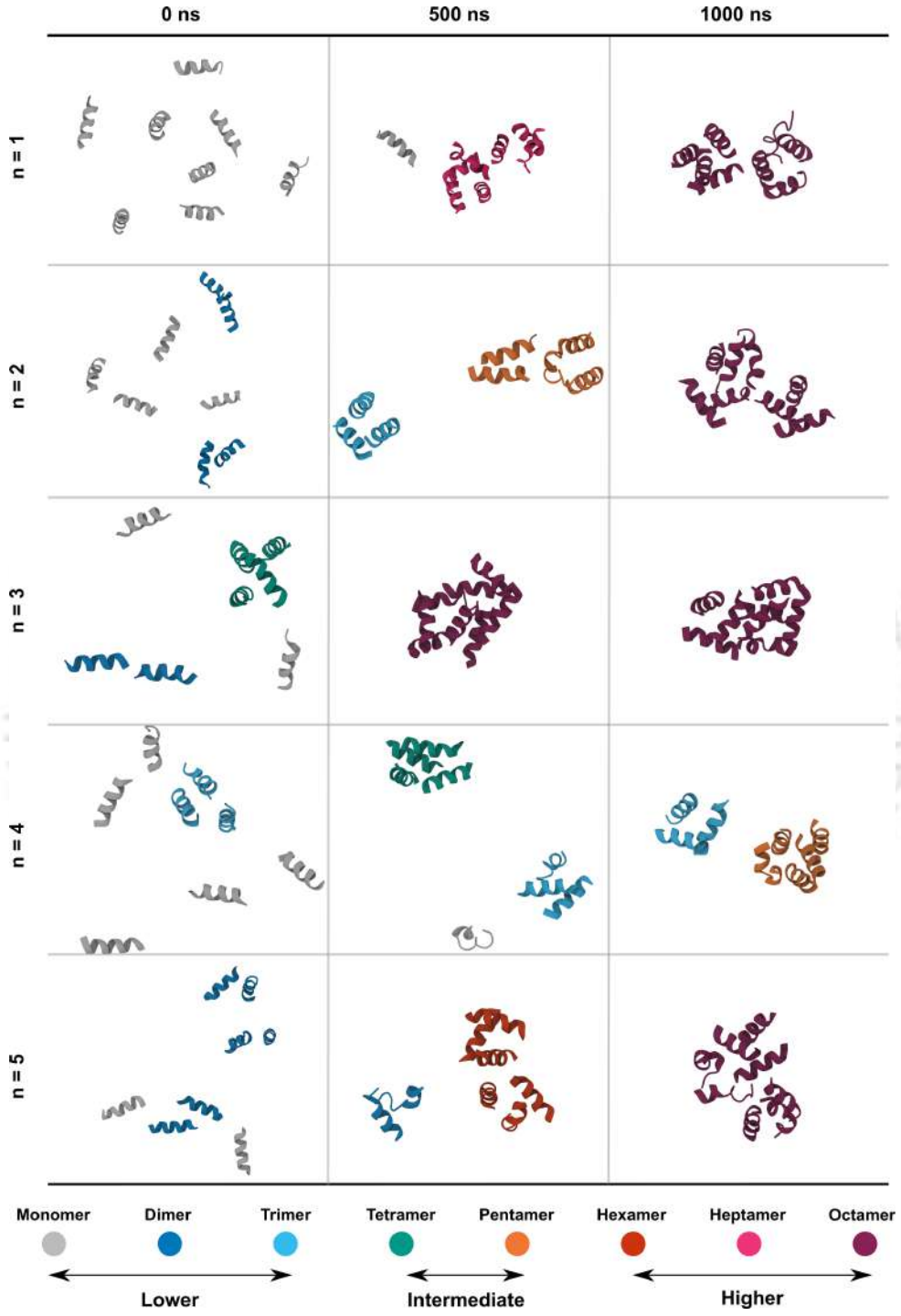

FIGURE 3.4: **Snapshots of the hll-8 systems taken at three different instances of the simulations:** at 0 ns (left) at 500 ns (middle) and 1000 ns (right). System replicas are labelled as n. The peptides are coloured based on the oligomeric state they belong to. The panel below shows the classification of the oligomers based on size. We maintain this classification for the rest of the chapter.

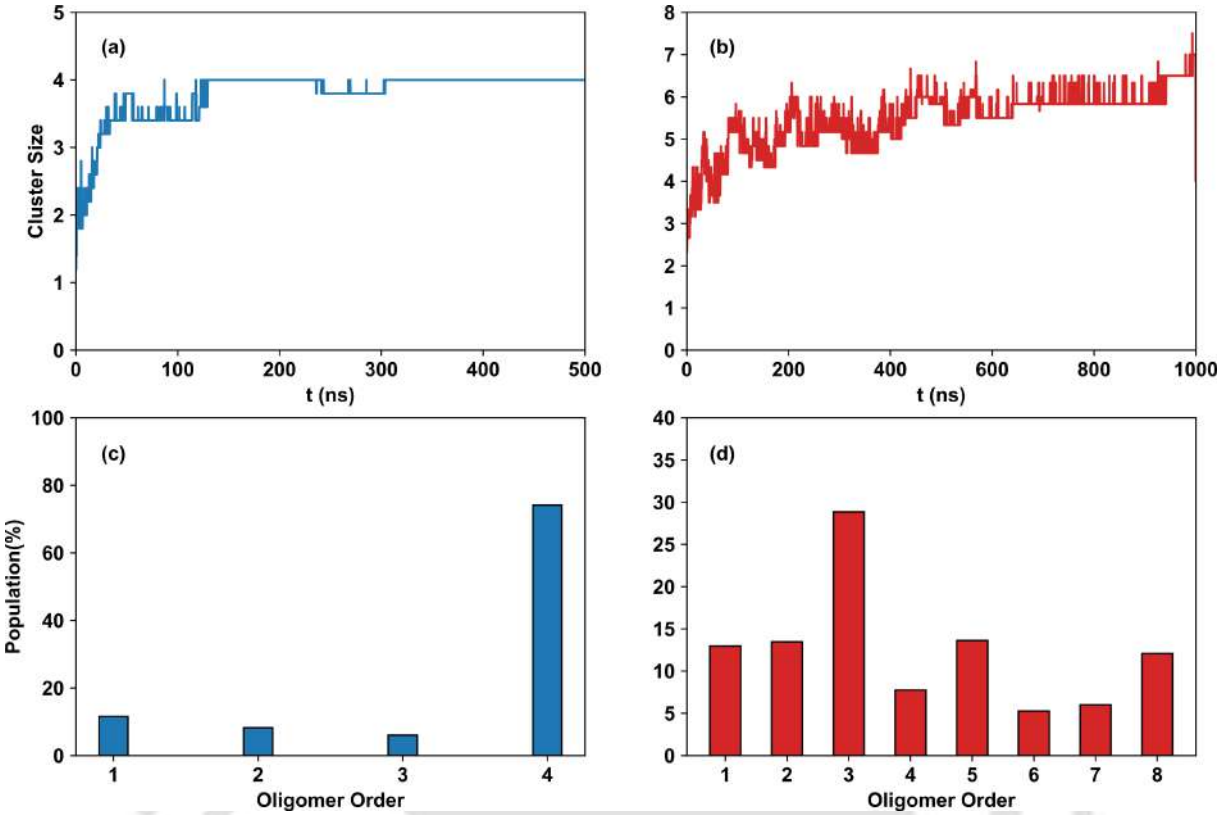

FIGURE 3.5: Time evolution of the average cluster size for (a) hll-4 and (b) hll-8 systems. Relative abundance of the oligomers for (c) hll-4 and (d) hll-8 systems. The population and the cluster size is averaged over the n replicas of the two systems reported in this Chapter. The population is expressed in percentage.

intermediate oligomeric states. The octameric state is achieved by means of encounters between intermediate and lower order oligomers. Thus, octamers are formed relatively late into the simulation and shows tendency to breakdown into smaller oligomers. For replicas not reaching their highest oligomeric state, we require further simulation for the encounter complex to stabilize. Overall, we predict that hLL-$37_{17\text{-}29}$ peptides are stabilized in their intermediate oligomeric states and gradually achieves higher oligomeric states when they coalesce with some lower order oligomer.

Since numerous oligomeric states are visited during simulation, we next calculated their probability of occurrence for hll-4 and hll-8 systems (Figure 3.5(c) and (d)). The relative abundance of the oligomers was based on the data pooled over all the replicas of the systems. For hll-4 (Figure 3.5(c)), we observe the highest abundance of tetramers compared to the rest of the oligomeric states. Our observation mirrors our previous finding

that hll-4 systems are stable as tetramers, formed during the early stages of the simulation and preserved for the rest of the duration. For hll-8 (Figure 3.5(d)), the abundance of intermediate oligomers becomes apparent, with a particularly low abundance for the higher oligomeric states. We found that hll-8 systems are dispersed chiefly as intermediate or lower oligomeric states. For hll-8, trimers are the most abundant, followed by the pentamers. Among the higher order oligomers, the octameric state is preferred to the hexamers and the heptamers. We also detected a considerable amount of monomers and dimers in hll-8 systems. Intermediate oligomeric states were previously detected in engineered helical peptides aggregating into quasiregular α-helical fibrils [238]. Recent nanopore and mass spectrometry experiments also support the preference of lower and intermediate oligomers over higher oligomers for two other hLL-37 fragments which explains the slow kinetics of octamer formation in our case [239].

3.3.3 Association of an intermediate oligomer with a lower order oligomer gives higher oligomers

Next, we explored pathways through which hLL-$37_{17\text{-}29}$ monomers aggregate into higher order oligomers using the concept of TPT. To this end, we constructed MSMs based on the dispersion state (S) of the peptides in the systems. We used the 'identical elements grouping' method to describe the dispersion states, which led to 5 and 22 states for the hll-4 and hll-8 systems, respectively. For all future discussions, we have represented the states as a collection of the different oligomers enclosed within square brackets. Thus, [1,1,1,1] and [1,1,1,1,1,1,1,1] represent the completely dispersed states in hll-4 and hll-8, respectively. Similarly, [4] and [8] represent the completely aggregated states of the two systems. The rest of the states, for instance, state in hll-4 consists of a pair of dimers. Similarly, state [2,3,3] is a collection of a dimer and a pair of trimers. Having defined the different states S, we next recorded the frequency of transitions among them as a transition matrix. The diagonal elements of this matrix signify self-transitions among states that do not contribute to any aggregation process. The off-diagonal elements, n_{ij}, represent the number of transitions from state i to j. The heat map representation of the

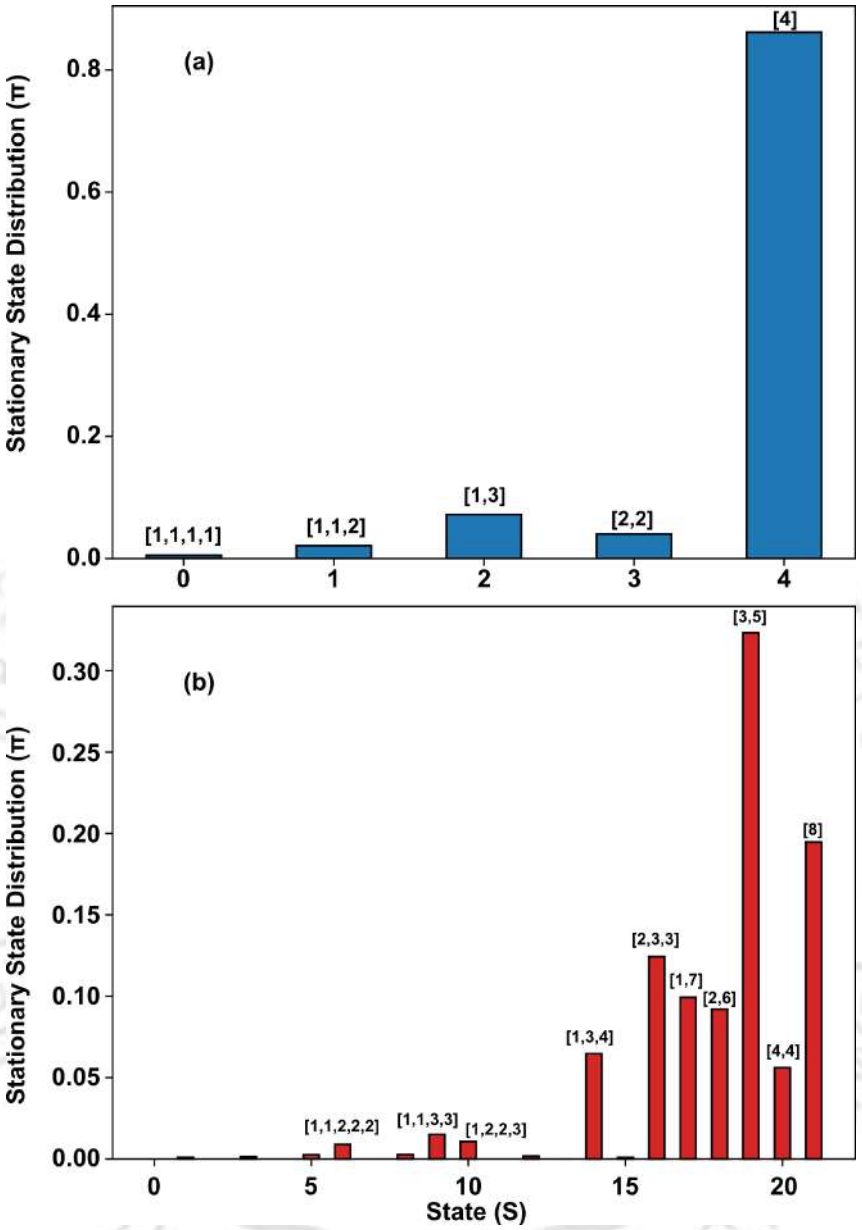

FIGURE 3.6: Stationary state distribution (π) of the dispersion states (S) of (a) hll-4 and (b) hll-8 systems. The state labels denote the distribution of the different oligomeric species in the systems.

transition matrices (Figure A.3 and Figure A.4 of Appendix A) reveals that the number of forward transitions is approximately equal to the number of backward transitions for any pair of states (i.e., $n_{ij} \approx n_{ji}$). We attribute this 'principle of detailed balance' in inter-state transitions to the reversibility in the aggregation process, typical of systems in equilibrium. Note that we refrained from forcing reversibility in our systems and arrived at it through multiple simulations of the same system. However, the principles of TPT

apply to non-reversible systems as well. We next obtained the population of the states

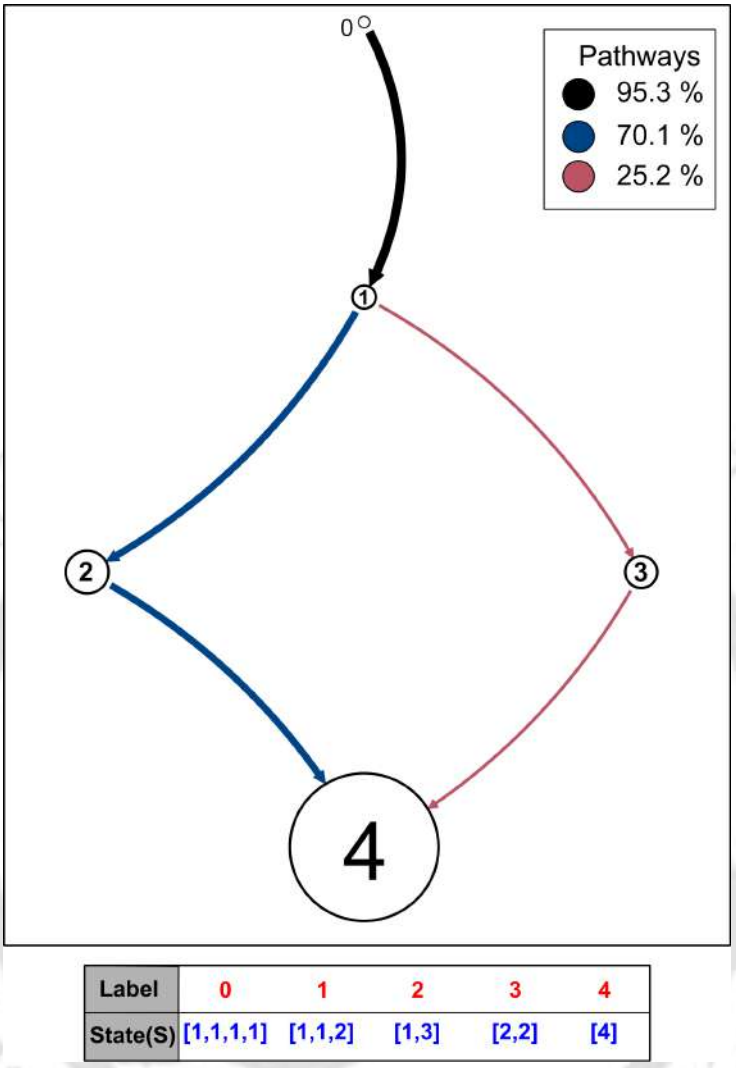

FIGURE 3.7: Transition network depicting the pathways by which systems travel from a dispersed state [1,1,2] (consisting of two monomers and a dimer) to a fully aggregated state [4] in hll-4.

(Figure 3.6) in S based on Equation 2.20. For hll-4 and hll-8, the completely dispersed state is almost absent. We also noticed a reduced abundance in states having higher number of free monomers. Consequently, dispersion states bearing intermediate or higher oligomeric forms become more probable which indicates a strong aggregation tendency among hLL-$37_{17\text{-}29}$ peptides. In hll-4, the tetrameric state is the most abundant, almost 12-fold higher than the next most prevalent state [1,3] (Figure 3.6(a)). We also observed a small but finite probability of the hll-4 systems present as a pair of dimers [2,2]. For hll-8 (Figure 3.6(b)), state [3,5] is the most abundant, followed by the completely aggregated

state [8]. Interestingly, we found that states in which oligomers comprise an odd number of peptides are more probable than oligomers with an even number of peptides. In particular, the absence of state [2,2,4], the reduced occurrence of state [4,4], and the abundance of states [2,3,3], [1,7], and [3,5], suggest a preference for oligomers with an odd number of peptide units. Such preference is not evident in the case of hll-4 systems where the tetramers dominate over other oligomeric forms. However, there is an inherent tendency of the peptides to shift to odd oligomeric species when more peptides become available.

To figure out the aggregation pathways, we defined the starting point (P) and the destination (Q) of the pathway based on the population of states (π). The abundance of the fully aggregated states-[4] in hll-4 and [8] in hll-8- make them obvious for the choice of Q. However, due to the low probability of occurrence of the completely dispersed states ([1,1,1,1] in hll-4 and [1,1,1,1,1,1,1,1] in hll-8), we chose an intermediate state as P for the systems. Accordingly, we assigned state [1,1,2] in hll-4 and state [1,1,2,2,2] in hll-8 as starting points for pathway decomposition. In the case of hll-4, we obtained two pathways by which the systems travel from state [1,1,2] to state [4] (Figure 3.7). These two pathways account for 95.3 % of the flux between [1,1,2] and [4]. The dominant pathway having an occurrence probability of 70.1 % goes via the following route : [1,1,2] $\rightarrow$ [1,3] $\rightarrow$ [4]. The next probable pathway (25.2 %) for the transition goes through the sequence, [1,1,2] $\rightarrow$ [2,2] $\rightarrow$ [4]. The mean free passage time for the system's journey from states [1,1,2] to [4] is around 2.1 ns. For hll-8 systems, numerous pathways for transition from state [1,1,2,2,2] to state [8] were obtained (Figure 3.8). We represent only the top three pathways that account for 58.3 % of the net flux current between the two states. The dominant pathway, with an occurrence probability of 25.4 % goes through the following route: [1,1,2,2,2] $\rightarrow$ [1,2,2,3] $\rightarrow$ [2,3,3] $\rightarrow$ [3,5] $\rightarrow$ [8]. A second, competing pathway having an occurrence probability of 21.4 % follows the sequence of states : [1,1,2,2,2] $\rightarrow$ [1,1,2,4] $\rightarrow$ [1,3,4] $\rightarrow$ [1,7] $\rightarrow$ [8]. The third pathway, which contributes 11.6 % of all [1,1,2,2,2] $\rightarrow$ [8] transitions, is given as:[1,1,2,2,2] $\rightarrow$ [1,2,2,3] $\rightarrow$ [1,3,4] $\rightarrow$ [3,5] $\rightarrow$ [8]. The system takes a mean passage time of 5.8 ns to travel from states [1,1,2,2,2] to [8]. With an increasing number of peptides in the systems, numerous dispersion states become available, and as a

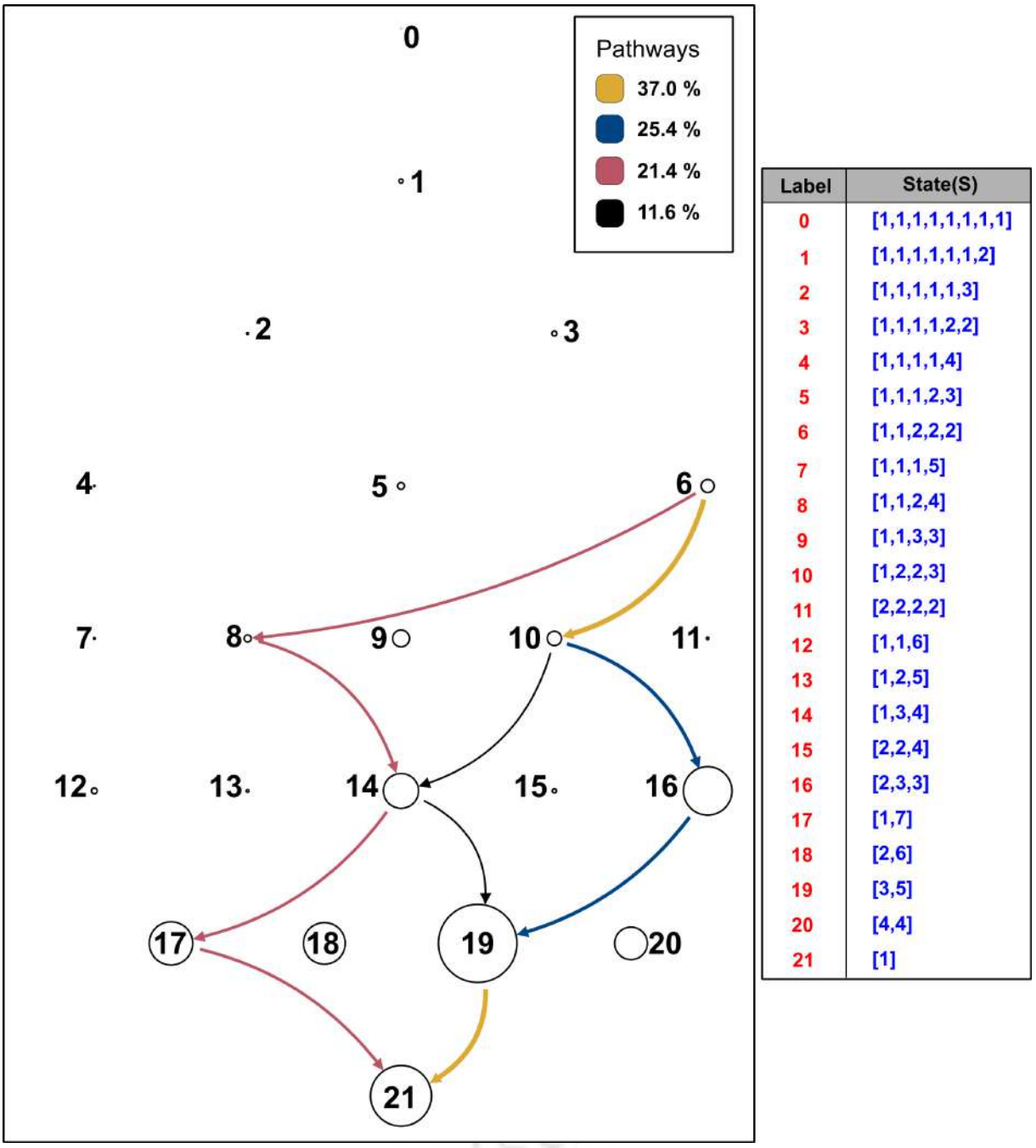

Label	State(S)
0	[1,1,1,1,1,1,1,1]
1	[1,1,1,1,1,1,2]
2	[1,1,1,1,1,3]
3	[1,1,1,1,2,2]
4	[1,1,1,1,4]
5	[1,1,1,2,3]
6	[1,1,2,2,2]
7	[1,1,1,5]
8	[1,1,2,4]
9	[1,1,3,3]
10	[1,2,2,3]
11	[2,2,2,2]
12	[1,1,6]
13	[1,2,5]
14	[1,3,4]
15	[2,2,4]
16	[2,3,3]
17	[1,7]
18	[2,6]
19	[3,5]
20	[4,4]
21	[1]

FIGURE 3.8: Transition network depicting the pathways by which systems travel from a dispersed state [1,1,2,2,2] (consisting of two monomers and three dimers) to a fully aggregated state [8] in hll-8.

result, multiple pathways become possible in hll-8 systems. Also, the individual contribution from the pathways is lower than hll-4 systems. For both hll-4 and hll-8, we found that trimers are either involved directly or transform to an intermediate oligomer on the way to the highest aggregation state. Our observation explains the abundance of the trimer

and pentamers in the hll-8 systems which coalesce into the octameric state. Contrary to the nucleation mechanisms observed in amyloid-β peptides, aggregation of hLL-$37_{17\text{-}29}$ occurs through the union of intermediate and lower oligomers, resulting in densely packed helical aggregates [240, 241]. Although similar in architecture and morphology, α and β-amyloids differ significantly based on their aggregation behaviour.

3.3.3.1 Peptides retain their helical structure during aggregation

To test the structural integrity of the peptides during aggregation, we next measured the atomic deviations as a function of time (Figure A.5 and Figure A.6, Appendix A). Any significant structural changes in the peptide would reflect in the root mean square deviation (RMSD) of the backbone atoms. For hll-4 systems, the average RMSD value ranges between 0.7-2.5 Å. For hll-8, the average RMSD varies between 0.7-2.8 Å. In rare cases, we observe deviation in the peptide structure exceeding 3 Å. Overall, the average RMSD data indicates that the peptide structure is stable during aggregation. However, fluctuation in the RMSD data over time suggests minor deviations from the native structure.

To find out the cause of this structural behaviour, we monitored the secondary structure of the peptides with time. The secondary structure of these peptides, which is exclusively α-helical, drives the aggregation process and the membranolytic property of these antimicrobial peptides [160, 205, 238]. The time evolution of the secondary structure of the peptides is plotted in Figure A.7 and Figure A.8 (Appendix A). We found that each hLL-$37_{17\text{-}29}$ unit possesses a highly preserved core (comprising residues 19 to 28 with helical tendencies close to 1.0) and a disordered N- and C-terminal. For both hll-4 and hll-8 systems, we found that the individual α-helices are preserved. However, we see occasional appearances of turn and 3-10 helix in a few of the peptides (Figure A.9 and Figure A.10, Appendix A). This explains the fluctuations in the RMSD values of the peptides, as discussed in the previous section. The region in red represents the termini, i.e., ACE and NME caps, that do not participate in any secondary structure formation. Overall, the

α-helix character predominates over the other secondary structures combined. All except one peptide, show more than 80 % α-helix content. The helical nature of hLL-$37_{17\text{-}29}$ agrees with the NMR solution structure of the peptide [147]. We also observed a tendency of the peptides to form turns via 3-10 helices.

Next, we investigated how hLL-$37_{17\text{-}29}$ peptide retains its structure during aggregation. A network of intramolecular salt-bridges could explain the structural stability of the full-length ll-37 and the active core hLL-37(17-29) peptide [199, 200]. Therefore, we calculated salt bridges among the charged residues of the peptide. The primary residues involved in salt bridges were D26 and R23/29. The other charged residue, namely Lys25, was responsible for inter-molecular salt-bridges during peptide self-assembly. We found that the dominant intramolecular salt-bridging pair are the residues Asp26-Arg29 (55.55 %) followed by Asp26-Arg23 (45.45 %), with Asp26-Lys25 (1.00 %) contributing the least. Thus, in addition to intramolecular hydrogen bonds, intramolecular salt bridges further strengthen the peptide structure, which explains the alpha-helical nature being conserved during aggregation.

3.3.4 Hydrophobic interactions dictate aggregation in hLL-$37_{17\text{-}29}$

Next, we identified residues that interact during the formation of oligomers. For this purpose, we calculated the inter-residue contact probability based on the distance cutoff we adopted for identifying clusters, i.e., we consider two residues to be in contact when the distance between any two constituent atoms is less than 4 Å. Since intermediate oligomers, namely dimers, trimers, and tetramers constitute the building blocks for higher order oligomers, we built separate contact maps for each to study the changes in inter-residue interactions with oligomer size. Irrespective of oligomer size, we observed strong contact probability among the I24 residues of the peptide chains (Figure 3.9). This particular residue also interacts to a lower extent with other hydrophobic residues, namely, I20 and F27. I20 is another residue that forms hydrophobic contact with L28 and F27. We also found a strong tendency of F27 to interact with each other and, to a lower extent, with F17. Together, I24, I20, F27, and L28 account for the critical interactions among peptides

present in an oligomer. Except for R23, the charged or polar residues, particularly K18, R19, Q22, K25, D26, and R29 fail to interact with other residues. From the electrostatic potential maps in Figure 3.9(b) and (c), we find that the charged residues reside on the oligomer surface. The build-up of charge density (especially positive charge density from Lys and Arg residues) thus facilitate oligomer interaction with the neighbouring solvent molecules and ions. The core of the oligomers, on the contrary, is composed of hydrophobic residues, mainly Ile and Phe (Figure 3.9(c) and (d)). Thus, hydrophobic contacts dominate the oligomer formation in hLL-$37_{17\text{-}29}$ fragments. Such interactions arise from the peptide structure where hydrophobic residues constitute one face of the helix, and inter-peptide contacts are created from this hydrophobic face predominantly.

We investigated the role of π-stacking interactions among the Phe residues at 17 and 27. The contact maps showed a strong interaction between two F27 residues and a weaker interaction with F17. We thus focused on the pairs F27-F27 and F27 -F17, for our calculations. We created 2d-density plots (Figure A.11, Appendix A) for the distance and angle between two Phe rings- the distances are measured from the COM of the rings and the dot product of the vector normal gives the orientation between them. Rare instances of parallel π-stacking occur for the dimer (F27-F27 having 18 % probability) and the trimer (F27-F17 with 27 % probability). The Phe rings, instead, prefer the Herr or Perp conformation. The Herr conformation involves weak interaction among the Phe rings, whereas the Perp conformation fail to contribute to stacking. Interestingly, the Perp conformation is dominant in tetramers. This might account for the higher abundance of dimers and trimers in the systems where stacking interactions provide additional stability but are almost absent in the case of tetramers. Though F27-F17 is predominantly Perp in the case of dimers, F27-F27 is favourably present in Par or Herr conformation. On the contrary, F27-F27 is predominantly Perp in trimers but compensated by the F27-F17 present in either Par or Herr conformation. The peptides attach via I24 residues and form secondary π-stacking interactions among the F27 rings at the C-terminal. As a result, there is structural ordering among the peptides in the oligomers, but we failed to observe the cross-α architecture as seen in the X-ray crystal structure of Engelberg et al [205].

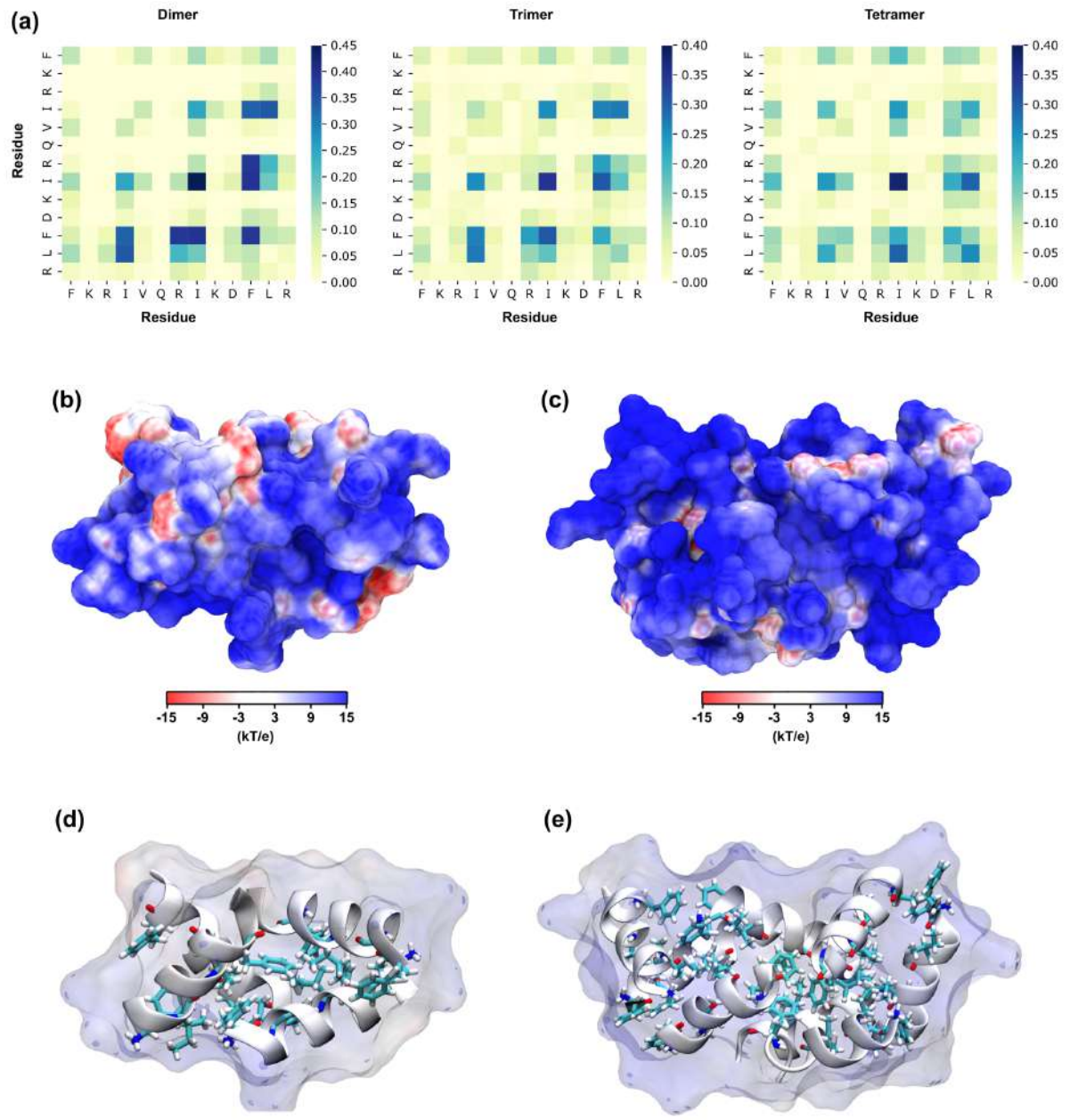

FIGURE 3.9: (a) Residue-residue contact probability for dimers, trimers and tetramers. Electrostatic potential (EP) maps depiciting the surface charge distribution in (b) tetramers and (c) octamers. Ile and Phe residues constituting the core of the (d) tetramers and (e) octamers illustrate the role of hydrophobic interactions in oligomer formation.

Next, we quantified the free energy contribution of each residue to the aggregation process. For this purpose, we mutated each residue to Ala and then measured the effect of this mutation on the binding free energy. The difference in Gibbs binding free energy of the wildtype with respect to the mutant, $\Delta(\Delta G)$, is depicted in Figure 3.10. Based

on our definition, $\Delta(\Delta G)$ can be positive, negative or 0. A negative value of $\Delta(\Delta G)$ signifies that peptide binding is more favourable in the wildtype compared to the mutant. Similarly, a positive value of $\Delta(\Delta G)$ is an evidence of the mutant interacting favourably compared to the wildtype. We observed the lowest $\Delta(\Delta G)$ for the I24A mutant, which indicates that mutation of I24 to Ala reduces the binding affinity and thus I24 is crucial for peptide aggregation. Our finding conforms with the strong Ile24-Ile24 contacts we observed previously in the contact maps. F27A is another mutant that shows an increase in binding free energy on mutation but the value is approximately half of the I24A mutant. The I20A and the F17A mutants are other notable residues that alter the binding propensity significantly. Mutation of the positively charged Lys and Arg residues at 18, 19, 25, and 29 to Ala, on the contrary, favours the binding among peptides. Similar to our findings, Engelberg et al.[205] reported that mutation of certain hLL-$37_{17\text{-}29}$ residues, particularly I24, decrease its antimicrobial property (due to increased minimum inhibitory concentration). Combining experimental and theoretical evidence, we may suggest that the antimicrobial property of this peptide is linked to its aggregation tendency.

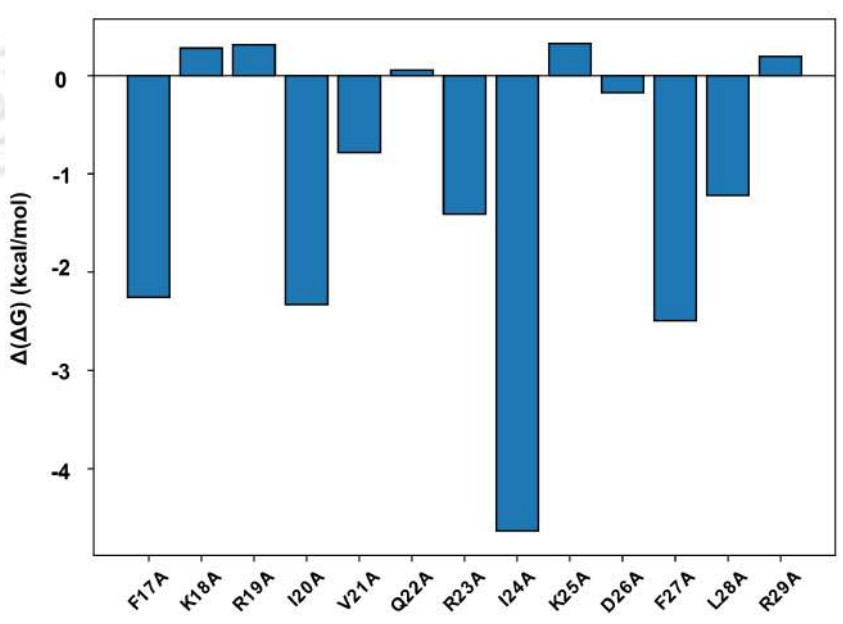

FIGURE 3.10: Change in binding free energy of the wildtype hLL-$37_{17\text{-}29}$ peptide with respect to the alanine mutants. $\Delta(\Delta\ G)$ is mathematically expressed as: $\Delta(\Delta\ G) = \Delta\ G_{WT} - \Delta\ G_{mutant}$. A negative value of $\Delta(\Delta G)$ signifies that peptide binding is more favourable in the wildtype compared to the mutant. Similarly, a positive value of $\Delta(\Delta G)$ is an evidence of the mutant interacting favourably compared to the wildtype.

3.4 Conclusions

The active core of the human LL-37 peptide (comprising residues 17 to 29) possesses antibacterial and anticancer properties and tends to aggregate into cross-α amyloid fibrils. Here, we studied the aggregation mechanism in hLL-$37_{17\text{-}29}$ based on atomistic molecular dynamics (MD) simulations. Since peptide aggregation is a stochastic process, we prepared multiple configurations of the systems consisting of 4 or 8 hLL-$37_{17\text{-}29}$ units. We subjected these systems to an extended production run under isothermal-isobaric conditions (P = 1 atm, T = 300 K). From the simulation data, we identified oligomers among peptides based on a distance cutoff and studied their time evolution and relative abundance to capture the dynamics of the aggregation process. Next, we constructed Markov State Models (MSMs), where states were defined based on the distribution of the different oligomers in the systems. With such semi-empirical MSMs as the foundation, we obtained the aggregation pathways using the transition path theory (TPT) framework. To the best of our knowledge, this Chapter provides the first mechanistic insight into the aggregation pathways of these peptides. Since the helical structure is crucial for the aggregation and membrane permeability of these peptides, we checked their structural integrity during aggregation. Next, we identified residues that participated in aggregation and studied the nature of the interactions among them. We also quantified the binding energy changes in these peptides based on alanine scanning studies. Snapshots of the systems taken at different simulation times show evidence of aggregation among the peptides. The peptides transition from an initially dispersed state to an aggregated state with variable tendencies. For systems consisting of 4 peptides (hll-4), the tetramer state is achieved early in the trajectory and remains stable during production. The octamer state in systems with 8 peptides (hll-8) is unstable and formed late into the trajectory. hll-8 systems prefer to exist in lower (trimer) or intermediate (pentamer) oligomeric forms. Rare occurrences of the octamers result from transitions of the hll-8 systems from an intermediate oligomeric state. We defined aggregation pathways between a dispersed state and a completely aggregated state. For both hll-4 and hll-8, we found that trimers are either involved directly or convert to an intermediate oligomer before transitioning to a higher-order oligomer.

The increased population of the states consisting of trimers further indicates their role in aggregation. For hll-4, two significant pathways explain the formation of tetramers from peptide monomers. For hll-8, numerous dispersion states are available, due to which multiple pathways are possible. The mean free passage time required to attain the final aggregated state of the system is higher in hll-8. Aggregation to a larger oligomer proceeds via the association of two small oligomers, notably different from the nucleation mechanisms in β-amyloid peptides. Here, we mention that pathways predicted from a semi-empirical definition of the dispersion states provide qualitative ideas about the aggregation process. MSMs built on detailed intermolecular features are required to predict the actual kinetics of the transitions. Except for transient fluctuations, the peptides retain their helical structure during aggregation. Structural deviations arise due to the conversion of the helix into 3-10 helix and turn elements. The exceptional stability of the peptides is explained by intramolecular salt bridges, particularly between the Arg residues at positions 23 and 29, with the Asp residue at 26. Hydrophobic interactions guide the aggregation process in hLL-$37_{17\text{-}29}$ peptides, with the Ile residues at 20 and 24 and the Phe residues at 17 and 27 playing a vital role. We found π-stacking interactions among the Phe residues in dimers and trimers. The peptides thus attach via the I24 residues, with additional π-stacking among the Phe residues which results in structural ordering between them. Alanine scanning studies reveal that mutation of the I24 residue decreases the binding energy of the peptides more than the Phe residues. Our observation agrees with the increased minimum inhibitory concentration (MIC) values of I24 mutants as seen experimentally. We thus propose that the aggregation among these peptides is crucial for their antimicrobial property.

To summarize, the key findings of this study include (1) Significant aggregation tendency among the hLL-$37_{17\text{-}29}$ peptides, (2) Ease of formation of lower or intermediate oligomers over higher order aggregates, (3) Association of small oligomers, particularly trimers, result in higher order aggregates (4) α-helical structure of the peptides is retained during aggregation with minor fluctuations, and (5) I24 is vital for the aggregation of these peptides.

Chapter 4

Markov State Models Reveal Relaxation Pathways Leading to Cross α-Amyloid Architecture in hLL-$37_{17\text{-}29}$ Aggregates

Overview

Self-assembly among peptides is ubiquitous and gives rise to supramolecular structures with diverse functionalities. One such example is the antimicrobial peptide hLL-$37_{17\text{-}29}$, which self-assembles into fibrillar structures characterized by a signature cross-α amyloid architecture. In our previous Chapter, we elucidated the mechanism by which dispersed peptides self-assemble into oligomers of various shapes and sizes. These studies provided insight into the pathways operating during the early stages of self-assembly. However, the relaxation processes that transform these disordered encounter complexes into a perfectly ordered arrangement remain poorly understood. In this Chapter, we constructed comprehensive Markov state models (MSMs) incorporating detailed molecular descriptors that capture these relaxation processes, even at timescales rarely achieved by conventional simulations. To this end, we performed μs-long simulations of both the tetrameric hLL-$37_{17\text{-}29}$ and the metastable trimeric state, which acts as a reactive intermediate during tetramer formation. Our models effectively cluster the conformations into metastable states between which these encounter complexes oscillate before transitioning to the next higher oligomeric form. Notably, the MSM for the tetramer reveals a highly populated metastable state that reproduces the cross-α amyloid architecture with near-crystallographic precision. This relaxation process is guided by the formation of a hydrophobic core that maximizes protein–protein interactions while keeping hydrophilic residues exposed to solvent. In addition, this study provides the first detailed characterization of the reactive trimer intermediate, a species that is difficult to probe experimentally. We also present the first kinetic evidence of self-healing in the hLL-$37_{17\text{-}29}$ tetramer, a mechanism that maintains the integrity of its hydrophobic core. Finally, the formation of well-ordered intermediates exposes specific residue patterns on the surface, which may be exploited as epitopes for immunomodulatory functions.

4.1 Introduction

Self-assembly is a natural phenomenon where disordered macromolecules organize into ordered structures, driven primarily by non-covalent interactions [242]. The reversibility of these interactions (hydrogen bonds, $\pi - \pi$, hydrophobic, electrostatic) imparts exceptional dynamism to the structures, enabling them to adapt and respond to external stimuli [243, 244]. This principle has been exploited in the field of nanotechnology and material science [245–249] to engineer self-healing materials [250–252], energy storage devices [253, 254], organic electronic devices [255], etc. However, nature remains the ultimate architect - employing self-assembly to materialize complex systems from simple components, surpassing the most sophisticated artificial materials in functionality [245, 248]. From muscle fibres and connective tissues to viral capsids, bacterial flagella, and the very structure of the ribonucleic acids [256], self-assembly is ubiquitous across all scales of biological organization.

Among these natural systems, proteins and peptides constitute a versatile class of macromolecules capable of self-assembling into nanostructures with remarkable biocompatibility and bioactivity [257, 258]. The self-assembly is guided by intrinsic [259–262] (sequence and nature of the amino acids) and extrinsic factors (temperature [263, 264], solvent [265–268], pH [269–272]), offering tunable control over their properties. Such self-assembled systems have been successfully fabricated into supercapacitors [273–276], biosensors [277–280], drug-delivery agents [281–283], etc. Moreover, these protein-based assemblies show significant promise in cancer treatment [284–289], immune regulation [290], and the synthesis of antimicrobial materials [291–295]. Of particular interest is the broad-spectrum antimicrobial activity of certain peptide assemblies, which can be leveraged to fight multidrug-resistant pathogens [296–299]. These materials are typically synthesized using antimicrobial peptides (AMPs) as the building blocks, which are innate components of the immune system and provide the first layer of resistance to pathogens [300, 301]. They destabilize the pathogenic membrane and can bypass resistance pathways commonly encountered in commercial antibiotics [302–305]. Additionally, these biomaterials are selective in their

action, can withstand proteolytic degradation, and often promote drug release over long durations [306–308].

An unique example of self-assembly is demonstrated by the hLL-$37_{17\text{-}29}$ peptide - an antimicrobial fragment cleaved from the full-length LL-37 by bacterial proteases [309]. The resulting supramolecular structure features a 3-dimensional repetition of the hLL-$37_{17\text{-}29}$ tetramer, stabilized by electrostatic and $\pi - \pi$ interactions [310]. Each tetramer

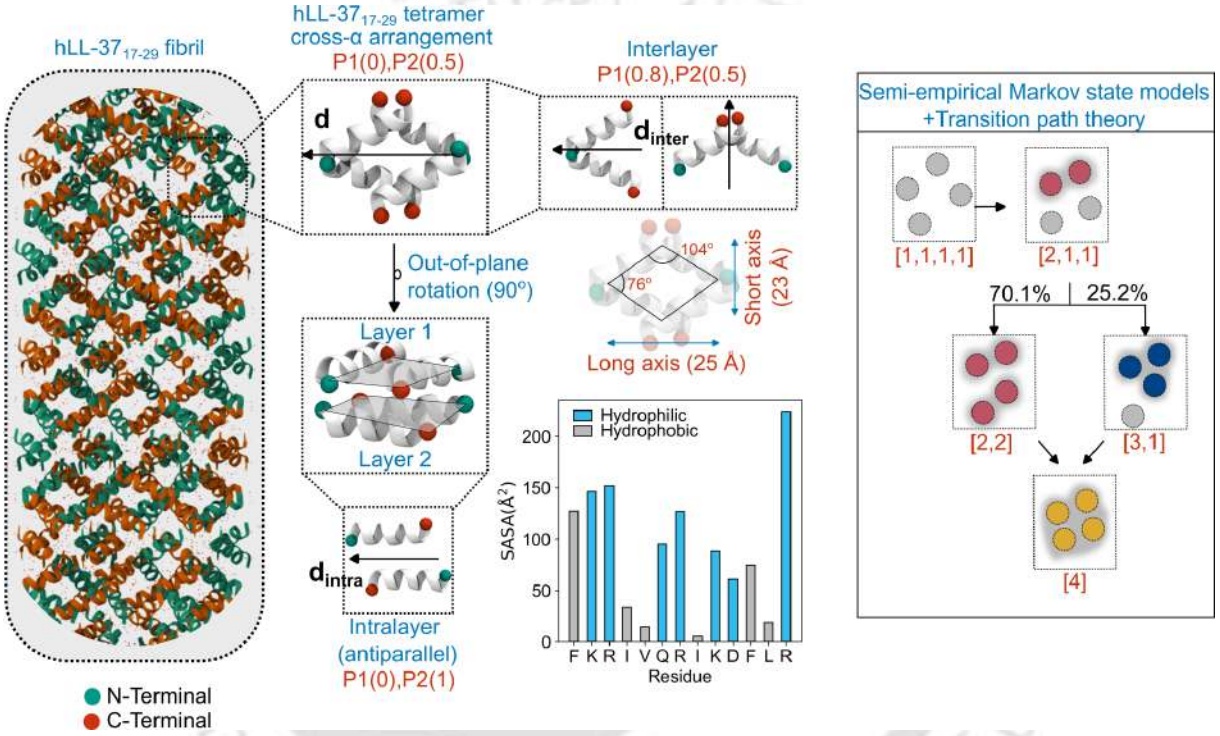

FIGURE 4.1: **Structural features of the hLL-$37_{17\text{-}29}$ tetramers:** The peptides form a 4-helix bundle (4HB) with a cross-α amyloid architecture. This specific arrangement of peptides can be described using the polar (P1) and nematic order parameters. The tetramer possesses a buried hydrophobic core with hydrophilic residues exposed, as characterized by their solvent-accessible surface areas (SASA). The tetramers arise from initially dispersed peptides through two main pathways (see Chapter 3), involving either a dimer (25.2 %) or a trimer (70.1 %) intermediate.

is a 4-helix bundle (4HB), consisting of two dimers arranged in stacked layers, in which dimers in one layer criss-cross those in the adjacent layer giving rise to a signature cross-α amyloid architecture (Figure 4.1). Within a single layer, the helices are anti-parallel, while those in adjacent layers adopt a 'V'-shaped angular (76° or 104°) orientation. The overall structure resembles a flattened rhombohedron, defined by two identical top and bottom faces and four uniform edges. The internal ordering among the peptides can be

described in terms of the polar (P1) and nematic (P2) order parameters (See Section 4.2 for details) [311, 312]. P1 measures the unidirectionality in peptide alignment, while P2 measures their orientation relative to the director vector (**d**), which lies along the long-axis (≈ 25 Å) of the tetramer. Although, the tetramer lacks unidirectionality in the peptide orientations (P1=0), the helices are consistently oriented at an angle with respect to **d** (P2=0.5). Within a given layer, the antiparallel dimers lack polarity (P1=0) but show strong alignment along $\mathbf{d_{intra}}$ (P2=1). In contrast, dimers in adjacent layers are highly unidirectional (P1=0.8) but maintain an angular orientation relative to $\mathbf{d_{inter}}$ (P2=0.5). The first known instance of such cross-α arrangement was identified in the PSMα3 peptide secreted by *Staphylococcus aureus* that was linked to its cytotoxic nature [160, 161].The cross-α motif shares morphological and tinctorial similarities with β-amyloids, yet notably lacks their neurodegenerative effects. In addition, hLL-$37_{17\text{-}29}$ also exhibits anticancer properties that elicit further research into its self-assembly behavior [309].

Molecular dynamics simulations provide insights into the self-assembly process that are difficult to achieve through experimental techniques. In our previous Chapter, we examined how initially dispersed hLL-$37_{17\text{-}29}$ peptides aggregate into a tetramer using semi-empirical Markov models and transition path theory [146]. We identified two aggregation pathways (Figure 4.1), in which a trimer intermediate is more probable (70.1 %) than a dimer pair (25.2 %). Aggregation was driven by interactions among hydrophobic residues on one face of the helix, particularly Ile24, which form a hydrophobic core. However, this semi-empirical approach could not resolve the internal arrangement of peptides during aggregation. These simulations captured the formation of encounter complexes but did not provide insight into the relaxation processes that transform these disordered complexes into ordered structures. One way to overcome this limitation is to construct Markov state models (MSMs) using molecular features in a high-dimensional space that can explore such relaxation pathways. Indeed, MSMs have been successfully applied to study self-assembly in lipids and β-amyloids [207, 313, 314].

In this chapter, we investigate how disordered encounter complexes relax into ordered structures with a cross-α amyloid architecture. We also examine the structural relaxations within the trimer, which is the major on-pathway intermediate to the tetramer.

To this end, we performed classical molecular dynamics simulations of hLL-$37_{17\text{-}29}$ peptides starting from a completely dispersed state. Unlike Chapter 1, here the encounter complexes were allowed to equilibrate on the microsecond timescale to capture the various relaxation pathways. From the MD data, we constructed Markov state models that group aggregates based on distances between hydrophobic residues of the peptide chains. We then applied transition path theory to identify transition pathways between these metastable states. To the best of our knowledge, this study provides the first evidence of such relaxation processes in hLL-$37_{17\text{-}29}$ aggregates, ultimately leading to a 4-helix bundle with the characteristic cross-α amyloid architecture.

We have organized the rest of Chapter 5 into the following sections: In Section 4.2, we briefly recapitulate the simulation protocols from our previous Chapter and outline the step-by-step construction of the Markov state models. In Section 4.3, we explore the relaxation pathways of the hLL-$37_{17\text{-}29}$ trimers and tetramers from their encounter complexes. In particular, we examine the structural features of the metastable states for each oligomeric form, reveal the kinetic aspects of their interconversions, and propose a comprehensive model for the self-assembly process that transforms initially disordered peptides into a cross-α amyloid architecture. In Section 4.4, we summarize the findings of our study.

4.2 Methods

4.2.1 MD simulation protocol

The MD simulations were performed using the AMBER20 software suite [315]. Two independent systems were prepared, consisting of three and four units of the hLL-$37_{17\text{-}29}$ peptide. The detailed simulation protocol is described in Chapter 3. Briefly, the capped peptides were randomly placed in a cubic simulation box and solvated with explicit water. The peptides and water molecules were modeled using the AMBERff14SB and TIP3P force fields, respectively [219, 220]. The systems were neutralized with Cl^- ions to balance the

positive charges of the peptides, and additional Na^+ and Cl^- ions were added to achieve a physiological ionic strength of 0.15 mM. The systems were energy-minimized to remove steric clashes introduced during packing, followed by a short heating phase to 300 K in the NVT ensemble (1.25 ns) and equilibration under NPT conditions (4 ns).

After equilibration, production simulations were performed in the NPT ensemble on the microsecond timescale. For the tetramer, five independent simulations of 10 μs each were carried out, with coordinates saved at 100 ps intervals. Similarly, for the trimer, four independent 10 μs simulations were conducted, starting from different initial coordinates and velocities. Temperature and pressure were controlled using the Langevin thermostat and the Berendsen barostat [224, 225]. Short-range non-bonded interactions (van der Waals and electrostatic) were calculated in real space with a 10 Å cutoff, while long-range electrostatics were computed in Fourier space using the particle-mesh Ewald method with a grid spacing of 1 Å[227]. Covalent bonds involving hydrogen atoms were constrained using the SHAKE algorithm to remove high-frequency motions[226]. The equations of motion were integrated with a modified leapfrog integrator using a 2 fs timestep [151]. Microsecond-long trajectories were generated with the GPU-accelerated version of AMBER20 [228], with coordinates saved every 100 ps for subsequent analyses. Periodic boundary conditions were applied to eliminate finite-size and surface effects [150].

4.2.2 Markov State Modelling

The detailed theory of Markov state modeling (MSM) is described in Chapter 2. The MSM workflow was implemented using the PyEMMA library in Python [316, 317]. To construct the feature space for the self-assembly, inter-residue distances between hydrophobic residues were selected. Since the peptides are indistinguishable, distances were evaluated by accounting for permutation symmetry using the TICAgg approach proposed by Sengupta et al. [318]. The resulting high-dimensional TICA space was projected onto a 10-dimensional subspace using time-lagged independent component analysis (TICA), which preserves the slowest dynamical processes [153, 154]. Conformations in this TICA subspace were clustered using the k-means algorithm into 'n' cluster centers [319]. Each

MD frame was then assigned to the nearest cluster center, thereby discretizing the trajectory into transitions between these microstates. These transitions were recorded in an $n \times n$ transition matrix, where the $(i, j)^{\text{th}}$ element denotes the frequency of transitions from state i to j. The transition matrix was computed at various lag times (τ) to estimate the implied timescales (ITs) of the slowest processes [320]. The final lag time was chosen at the point where the ITs plateaued, ensuring Markovian behavior. Based on this lag time, the final MSM was constructed using the maximum-likelihood estimator [319]. The 400-microstate MSM was further coarse-grained into macrostates (metastable states) using the fuzzy PCCA++ algorithm [321, 322]. Prior to deciding the number of macrostates, spectral analysis of the ITs was performed; a separation factor of 1.5 or higher between consecutive ITs was used to determine the number of macrostates, following previous studies [207]. The Markovian nature of the coarse-grained MSM was verified using the Chapman–Kolmogorov test [323]. After defining the macrostates, the interconversion kinetics were analyzed using transition path theory (TPT), as discussed in detail in Chapter 2. Briefly, TPT requires identifying a source and a sink state, with all other macrostates treated as intermediates. Each macrostate is assigned forward and backward committors, which quantify the probability of reaching the source or sink first. These macrostates are connected by edges that measure the transition flux between them. The main pathways and their contributions were extracted from these fluxes using an iterative combination of depth-first search and binary search algorithms. Based on visual inspection, the most disordered and most ordered macrostates were chosen as the source and sink, respectively.

4.2.3 Analyses

The key interactions within the metastable states were deduced using contact maps, which quantify the probability of interaction between residue pairs (Chapter 3). The secondary structure of the peptides was evaluated using the DSSP algorithm [324]. Non-bonded interaction energies (electrostatic and van der Waals) were computed using the NAMD Energy Plugin (Version 1.4) in VMD[325]. Hydrophobic contacts between residues were

identified based on a distance cutoff of 4 Å between any two atoms. The compactness of each oligomer was quantified based on its inertia tensor **I** calculated relative to the center-of-mass (COM) as:

$$\mathbf{I} = \begin{bmatrix} I_{xx} & I_{xy} & I_{xz} \\ I_{yx} & I_{yy} & I_{yz} \\ I_{zx} & I_{zy} & I_{zz} \end{bmatrix} \tag{4.1}$$

where $I_{xy} = I_{yx}$, and similarly for the other off-diagonal terms, since **I** is symmetric. The three eigenvalues of the tensor $(\lambda_1, \lambda_2, \lambda_3)$, corresponding to the moments of inertia along the principal axes (x, y, z), were ranked in ascending order ($\lambda_{\text{min}} \leq \lambda_{\text{mid}} \leq \lambda_{\text{max}}$). The compactness was defined as the ratio of the smallest to the largest moment of inertia, scaled by a factor of 10, and rounded to the nearest integer as [207]:

$$\text{Compactness} = \text{round}\left(10 \times \frac{\lambda_{\text{min}}}{\lambda_{\text{max}}}\right) \tag{4.2}$$

A compactness value of 1 corresponds to a linear, rod-like aggregate, whereas a value of 10 represents a perfect sphere. The polar and nematic order parameter (P_1 and P_2), which measures anisotropy in liquid crystals, was used to quantify structural alignment among the peptides in the oligomers [311, 312]. P_1 is evaluated according to:

$$P_1 = \frac{1}{N}\sum_{i=1}^{N} \hat{z}_i \cdot \hat{d} \tag{4.3}$$

and P_2 is evaluated as:

$$P_2 = \frac{1}{2N}\sum_{i=1}^{N} \left[3(\hat{z}_i \cdot \hat{d})^2 - 1\right] \tag{4.4}$$

where N quanitifies the number of peptides, $\hat{z}_i$ is the unit vector connecting the C_α atoms of the N and C-termini, and $\hat{d}$ represents the largest eigenvector of the ordering martix, Q, expressed as:

$$Q = \frac{1}{2N}\sum_{i=1}^{N} \left[3z_i^{(a)} z_i^{(b)} - \delta_{ab}\right] \tag{4.5}$$

where z_i^k is the k-th component of z_i an d δ_{ab} is the kronecker delta (δ_{ab}=1 for $a = b$; 0, otherwise). P1 and P2 were evaluated using in-house Python scripts. The solvent

accessible surface area of the different metastable states and the residues were calculated using the Shrake-Rupley algorithm implemented in VMD [326].

4.3 Results and discussion

4.3.1 Structural relaxations in the tetramer

4.3.1.1 hLL-37$_{17\text{-}29}$ tetramer samples 6 metastable states

We chose intermolecular C_α distances between hydrophobic residues (F17, I20, V21, I24, F27, L28) to construct the feature space for tetramer self-assembly. The feature vectors in this 216-dimensional space ($\mathbb{R}^{216}$) were projected onto a 10-dimensional subspace ($\mathbb{R}^{10}$) using time-lagged independent component analysis (TICA) [153, 154], which reduces dimensionality while retaining the kinetically slow motions in the system (Figure B.1a, b, Appendix B). We then applied the k-means algorithm to cluster conformers in the

TABLE 4.1: Population, free energy, helical content and the non-covalent interaction energies (electrostatic and van der Waals) of the 6 metastable states

State	Abundance	Free Energy (kcal/mol)	Helical propensity (%)	Electrostatic (kcal/mol)	van der Waals (kcal/mol)
Q0	0.31	3.23	74	-36.43	-97.14
Q1	1.24	2.40	79	-59.05	-108.68
Q2	7.07	1.36	75	23.14	-99.79
Q3	12.52	1.02	75	-7.54	-101.01
Q4	9.56	1.18	78	-69.04	-105.56
Q5	69.30	0.00	80	-98.71	-116.01

TICA subspace into 400 cluster centers, or microstates. The transitions between these microstates were recorded in a 400×400 transition matrix at different lag times to analyze how the implied timescales (ITs) vary with this parameter. The ITs become invariant beyond 10 ns, which serves as the lag time for the final MSM (Figure B.1c, Appendix B). Next, we performed spectral analysis to identify 6 metastable states, based on the relative separation of timescales (Figure B.1d, Appendix B). The validity of this 6-state MSM was

verified using the Chapman-Kolmogorov test, which showed good convergence between estimated and predicted values (Figure B.2, Appendix B). The 6 metastable states were grouped from the 400 micrstates using the fuzzy PCCA++ method. Finally, the transition kinetics between these states were computed within the framework of transition path theory. Table 4.1 summarizes the population of each state (Q0-Q5) along with the associated Gibbs free energy. State Q0 is the least populated, whereas Q5 has the highest population among all the states.

Figure 4.2 (top panel) shows snapshots of the six metastable states, while the transition network below illustrates the rate constants for interstate conversions. Three major pathways, accounting for 96 % of the net flux, drive the transformation of the system from the disordered state Q0 to the ordered state Q5. The key intermediates in this process are Q3 and Q4. In pathway-1, both intermediates are involved, whereas in pathways-2 and -3, only one of them participates. State Q1 does not contribute to any of the pathways and remains disconnected from the transition network, representing a detour state.

4.3.1.2 Structural features of the metastable states

We explored the changes in the peptide secondary structure during relaxation. Based on Table 4.1, the least populated Q0 is the least structured, whereas the highly populated Q5 has a very high helical content. All the other states feature between these two extremes, with Q1 and Q4 showing higher helical content than the rest (Q2 and Q3). Thus, structural reorganization among the peptides inevitably gets coupled with the changes in the peptide structure itself. The structural plasticity in peptides during self-assembly was also reported for the Aβ_{16-22} peptides [206].

The internal reordering among the peptides during tetramer relaxation can be captured using the polar and nematic order parameters. Figure 4.3a represents the distribution of these parameters for structures sampled in each metastable state. We recall that a perfect cross-α amyloid architecture has a polar order parameter of 0.0 and a nematic order parameter of 0.5. The most abundant state, Q5, displays sharp distributions centered around these values, along with exceptionally high α-helical content, which suggests that

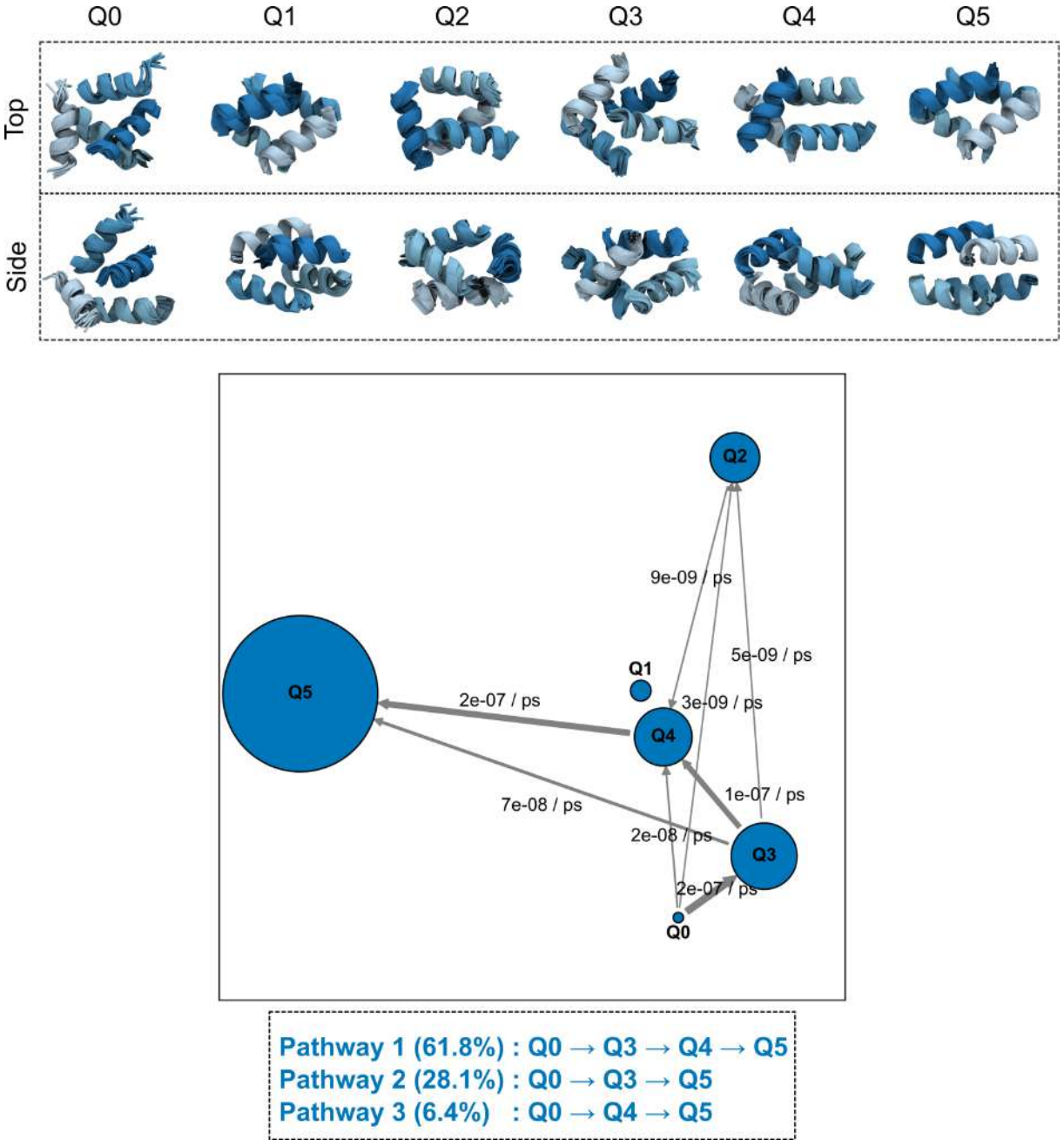

FIGURE 4.2: **Macrostates of the hLL-37$_{17\text{-}29}$ tetramer and their interconversion kinetics:** Six-state MSM with representative structures obtained from 50 μs of simulation of the hLL-37$_{17\text{-}29}$ tetramer. For each metastable state, both top and side views are shown, overlaid with 10 similar structures from the same state. The transition network illustrates the kinetics of interconversion between these states. The major pathways leading from state Q0 to Q5 are shown below.

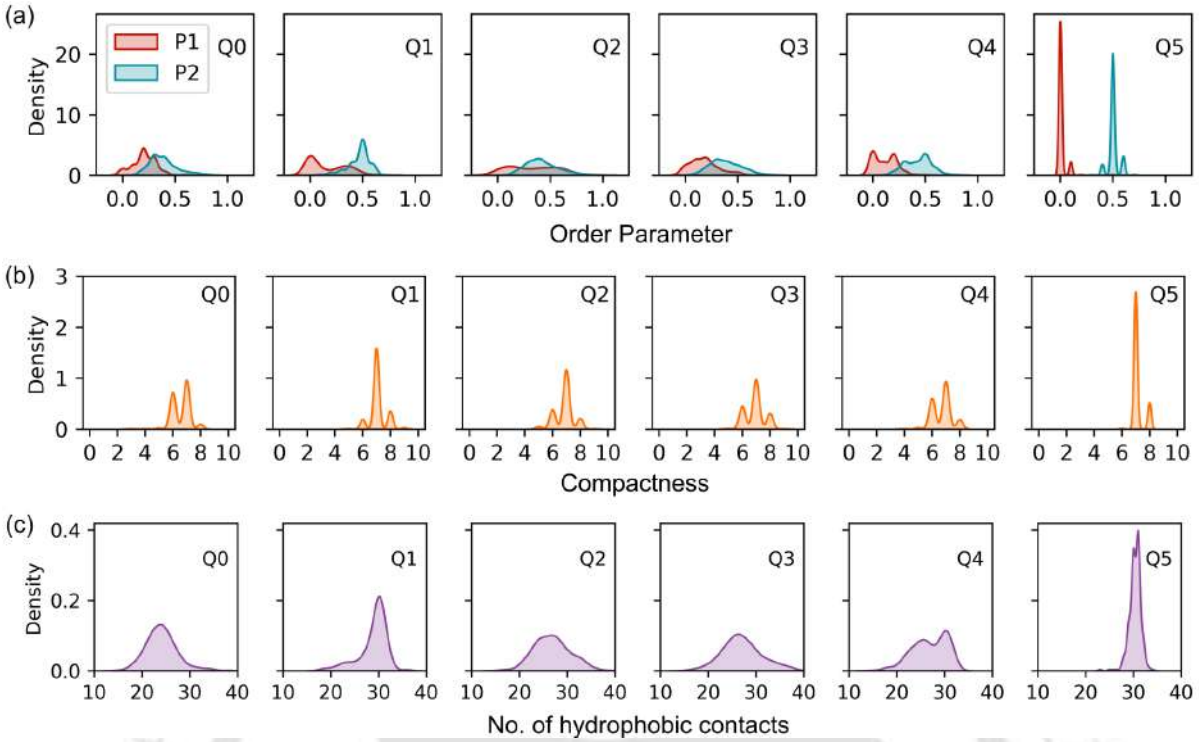

FIGURE 4.3: **Structural features of the 6 metastable states:** Distributions of (a) polar order (P1) and nematic order (P2), (b) compactness, and (c) the number of hydrophobic contacts for each metastable state. Each distribution is calculated from 250 randomly selected structures within the corresponding metastable state.

this state is closest to the crystallographic symmetry. In contrast, the other states exhibit a broader distribution in P1 and P2, consistent with amorphous aggregates lacking any particular geometry. For instance, states Q2 and Q3 sample a wide range of values and represent the most disordered tetrameric states. In Q0, the aggregates shift toward higher P1 and lower P2 values, indicating that the peptides are somewhat aligned but random with respect to the director vector **d**. State Q4 also exhibits some unidirectionality among the peptides, but P1 distribution is bimodal here, with a significant contribution from the cross-α arrangement. Similarly, for Q1, the conformers slightly prefer the cross-α arrangement, but are often mixed with disordered structures that sample higher P1 and lower P2 values. If we consider the shape of the aggregates (Figure 4.3b), the distinction between the states becomes less apparent. Nearly all states feature spherical aggregates, with an average compactness of 7. For the highly ordered Q5, the distribution is predominantly centered around this value, with an adjacent peak around 8. For the rest of the states (Q0 to Q4), we found finite occurrences of somewhat linear aggregates with a compactness

value around 6.

4.3.1.3 Key interactions in the six metastable states

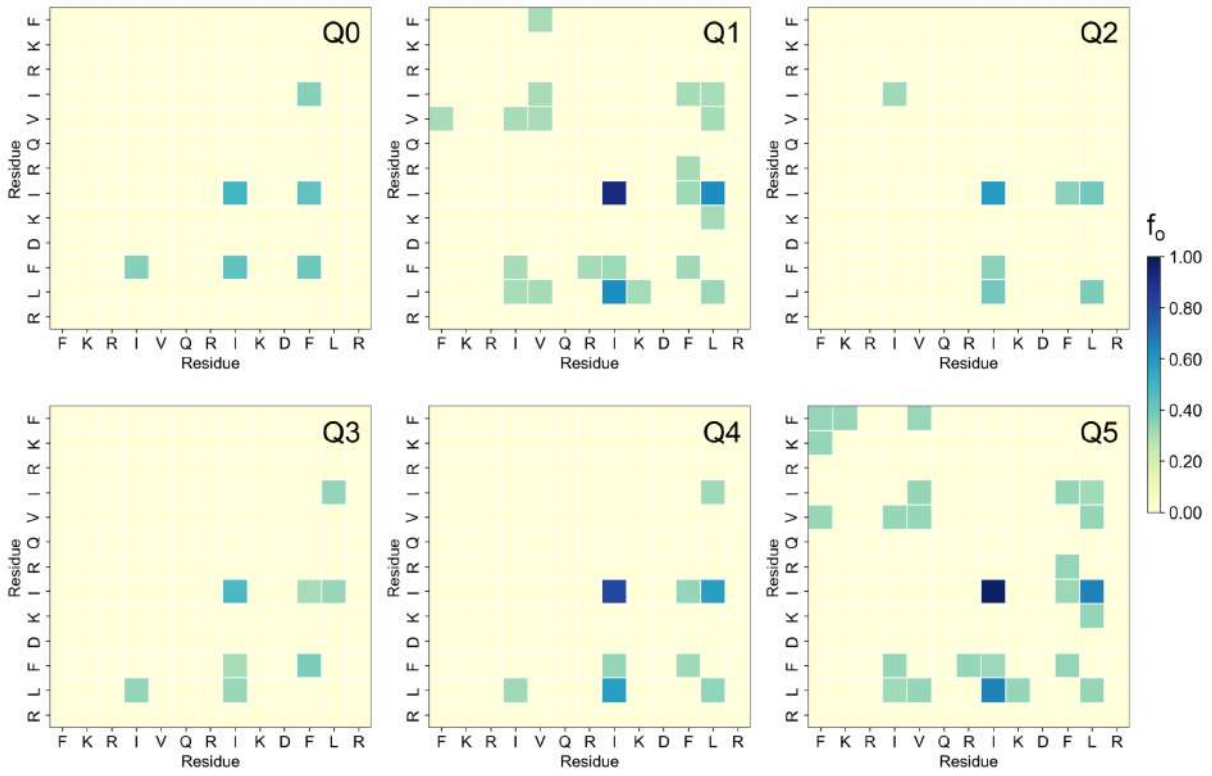

FIGURE 4.4: **Key interactions in the 6 metastable states:** Inter-peptide contact maps generated from 250 conformers randomly selected from each of the six metastable states. The color bar indicates the interaction probability (f_o).

The contact maps in Figure 4.4 illustrate the key interactions in the six metastable states, accompanied by a color bar that quantifies the interaction probability (f_o). Only the most probable contacts ($f_o \geq 0.3$) are shown for comparison. The strongest interactions occur between the I24 residues at the peptide center, consistent with our previous studies [146]. Notably, the strength of this interaction increases progressively from Q3 to Q5. In some states-particularly Q0, Q2, and Q3–the peptide interactions are weakened, hinting at loosely packed aggregates. The top-left corner of the contact maps corresponds to interactions among the N-termini of the peptides. Weak N-terminal interactions are present in only about 33 % of the metastable states. The hydrophobic residues at this end (F17, I20, and V21) interact moderately in state Q5, but these interactions weaken further in Q1.

In contrast, interactions involving the C-terminal hydrophobic residues (F27 and L28) are more prevalent. Besides interacting among themselves, these residues also form contacts with the peptide center and, to a lesser extent, with the N-terminal. For example, L28 interacts strongly with the central residues in Q1, Q4, and Q5, whereas F27 forms slightly weaker contacts. At the N-terminal, L28 and F27 primarily interact with I20 and V21, but these contacts are less frequent. Across all the states, the charged residues rarely participate due to electrostatic repulsions or polar-apolar mismatch. The contact maps thus uncover two types of interactions: (i) specific interactions that are found consistently across the states (>50%), and (ii) non-specific interactions that occur transiently. An interplay between specific and non-specific contacts allows dynamic motions during relaxation while maintaining the overall stability of the tetramer.

The underlying reason for structural relaxations is molecular interactions, especially non-bonding interactions, that can be decomposed further into electrostatic and van der Waals components (Table 4.1). In all the metastable states, the average van der Waals energy is more negative than the electrostatic energy, which suggests that hydrophobic interactions primarily govern the internal reorganization among the peptides. Both components are most favorable (i.e., lowest) in Q5, which drives the equilibrium population towards this state. In contrast, the non-bonded energy is higher (less negative) in Q2 and Q3, due to an unfavorable electrostatic component, which is either positive (Q2) or less negative (Q3). From Q3 to Q5, the electrostatic and van der Waals components become increasingly negative, reflecting a gain in stability as the tetramers convert from one state to another. Changes in the van der Waals component should be reflected in the total number of inter-peptide hydrophobic contacts. Indeed, in Q5, the peptides possess the highest number of hydrophobic contacts ($\approx$ 30) among all the states (Figure 4.3c). In the disordered state Q0, the distribution is skewed towards lower values, accounting for its minimal van der Waals stabilization. In states Q2 and Q3, a long tail in the distribution indicates more number of hydrophobic contacts, leading to improved van der Waals interactions in comparison to Q0. The distribution in states Q1 and Q4 is skewed toward higher values, which explains their greater stability than Q0, Q2, and Q3.

4.3.1.4 Interplay Between Hydrophobic and Hydrophilic Solvent Exposure Across Metastable States

Peptide aggregation is a highly cooperative process in which surrounding water molecules play a crucial role. However, MSMs are generally constructed with a focus on the biomolecule of interest and often exclude solvent information. As a result, the stabilizing influence of the solvent is frequently overlooked. Furthermore, peptide-peptide interactions alone are inadequate to explain the stability of the different metastable states. One way to circumvent this is by calculating the solvent accessibility of the aggregates in terms of the solvent accessible surface area (SASA). The SASA can be evaluated separately for the hydrophobic (apolar) and hydrophilic (polar) residues. As mentioned in Section 4.1, hydrophilic residues are positioned on the tetramer surface and are highly exposed to the solvent. In contrast, the hydrophobic residues on the other face of the peptide are masked from the solvent and constitute the hydrophobic core. We compared the SASA values (polar and apolar) relative to the crystal structure of the tetramer to assess the solvent exposure across metastable states. The MSM-derived tetramers differ significantly from the crystal structure, indicating that while some states may retain their internal ordering, they suffer from inefficient packing (Figure 4.5). This is expected, as

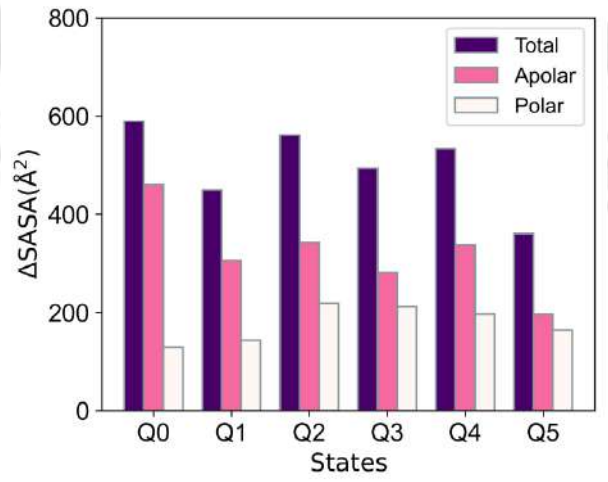

FIGURE 4.5: **Solvent accessible surface area of the metastable states:** Average solvent-accessible surface area (SASA) of polar and apolar residues relative to the crystal structure (ΔSASA). The values are averaged over 250 randomly selected conformers from each metastable state.

the crystal structure represents a tetrameric unit derived from a larger supramolecular assembly, stabilized via interactions from the neighbouring units. This is lacking in our case. Nevertheless, a quantitative comparison of SASA values offers valuable insights into the relaxation behavior among the metastable states. Overall, stability is determined by a balance between the solvent exposure of both hydrophobic and hydrophilic residues. The inherent tendency is to reduce the exposure of the hydrophobic residues while increasing the exposure of the hydrophilic ones. The SASA of hydrophobic residues deviates more than that of polar residues, further reinforcing the role of the hydrophobic core in the stability of the tetramers. To elaborate, state Q0 has the most exposed hydrophobic core and a reduced exposure of hydrophilic residues, rendering it highly unstable. In contrast, Q5 displays a buried hydrophobic core and exposed polar residues, making it the most abundant state. Although states Q2, Q3, and Q4 have higher exposure of hydrophilic residues, they also possess a relatively exposed hydrophobic core, making them less favorable than Q5. In Q1, both residue types have unfavorable solvent exposure relative to Q5, contributing to its lower stability. At the residue level (Figure 4.6b), hydrophobic

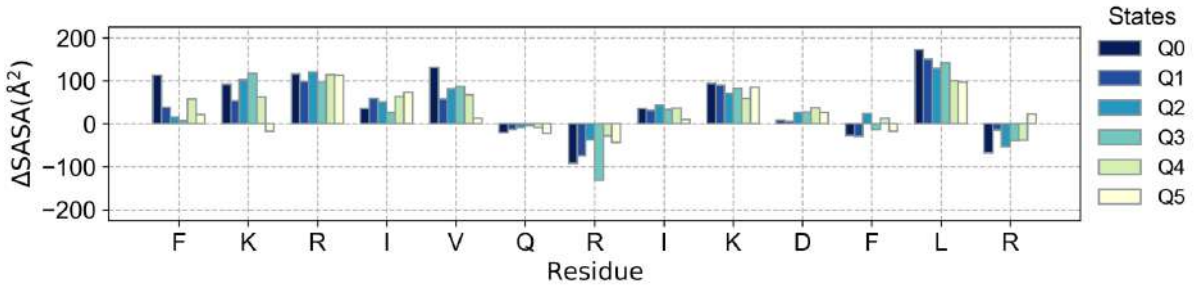

FIGURE 4.6: **Solvent accessible surface area of the residues:** Average per-residue solvent-accessible surface area (SASA) relative to that of the crystal structure (ΔSASA), computed over 250 randomly selected conformers from each metastable state.

L28 is highly exposed across all states. In contrast, the charged residues R23 and R29 are less exposed than in the crystal structure. Additionally, the N-terminal residues are more solvent-exposed compared to the C-terminal ones. The central I24 and the adjacent K25 are more exposed in the MSM-derived tetramers than in the crystal structure. Thus, the overall increase in apolar SASA can be traced back to the individual contributions from the hydrophobic residues, particularly those at the N-terminal. This finding is consistent

with our contact map analysis, which showed that C-terminal hydrophobic residues are more actively involved in hydrophobic interactions than N-terminal ones.

4.3.2 Structural relaxations in the trimer

4.3.2.1 hLL-$37_{17\text{-}29}$ trimer samples 5 metastable states

TABLE 4.2: Population, free energy, helical content and the non-covalent interaction energies (electrostatic and van der Waals) of the 5 metastable states

State	Abundance	Free Energy (kcal/mol)	Helical propensity (%)	Electrostatic (kcal/mol)	van der Waals (kcal/mol)
T0	1.94	2.00	70	40.44	-59.78
T1	7.23	1.21	72	91.33	-64.90
T2	10.22	1.01	73	49.76	-65.43
T3	25.26	0.47	75	42.18	-63.18
T4	55.33	0.00	70	31.52	-64.64

For the trimers, the 108-dimensional feature space ($\mathbb{R}^{216}$) was reduced to a 10-dimensional subspace ($\mathbb{R}^{10}$) using TICA (Figure B.3a and b, Appendix B). The conformers in this subspace were clustered into 250 centers using the k-means algorithm. The transitions among these clusters were evaluated at multiple lag times for calculating the ITs. The invariance of the ITs beyond 10 ns suggested the use of this lag time for further MSM construction (Figure B.3c, Appendix B). Next, we performed spectral analysis to identify 5 metastable states, based on the relative separation of timescales (Figure B.3d, Appendix B). The validity of this 5-state MSM was verified using the Chapman-Kolmogorov test(Figure B.4, Appendix B). The 5 metastable states were derived from the 250 clusters using the PCCA++ algorithm. Finally, the interstate-transition kinetics were computed within the framework of transition path theory. Table 4.2 summarizes the population of each state (T0-T4) along with the associated Gibbs free energy.

Figure 4.7 (top panel) shows snapshots of the five metastable states, while the transition network below illustrates the rate constants for interstate conversions. Three major pathways, accounting for 92.3 % of the net flux, drive the transformation of the system from the lowest populated state T0 to the highest populated T4. The key intermediates

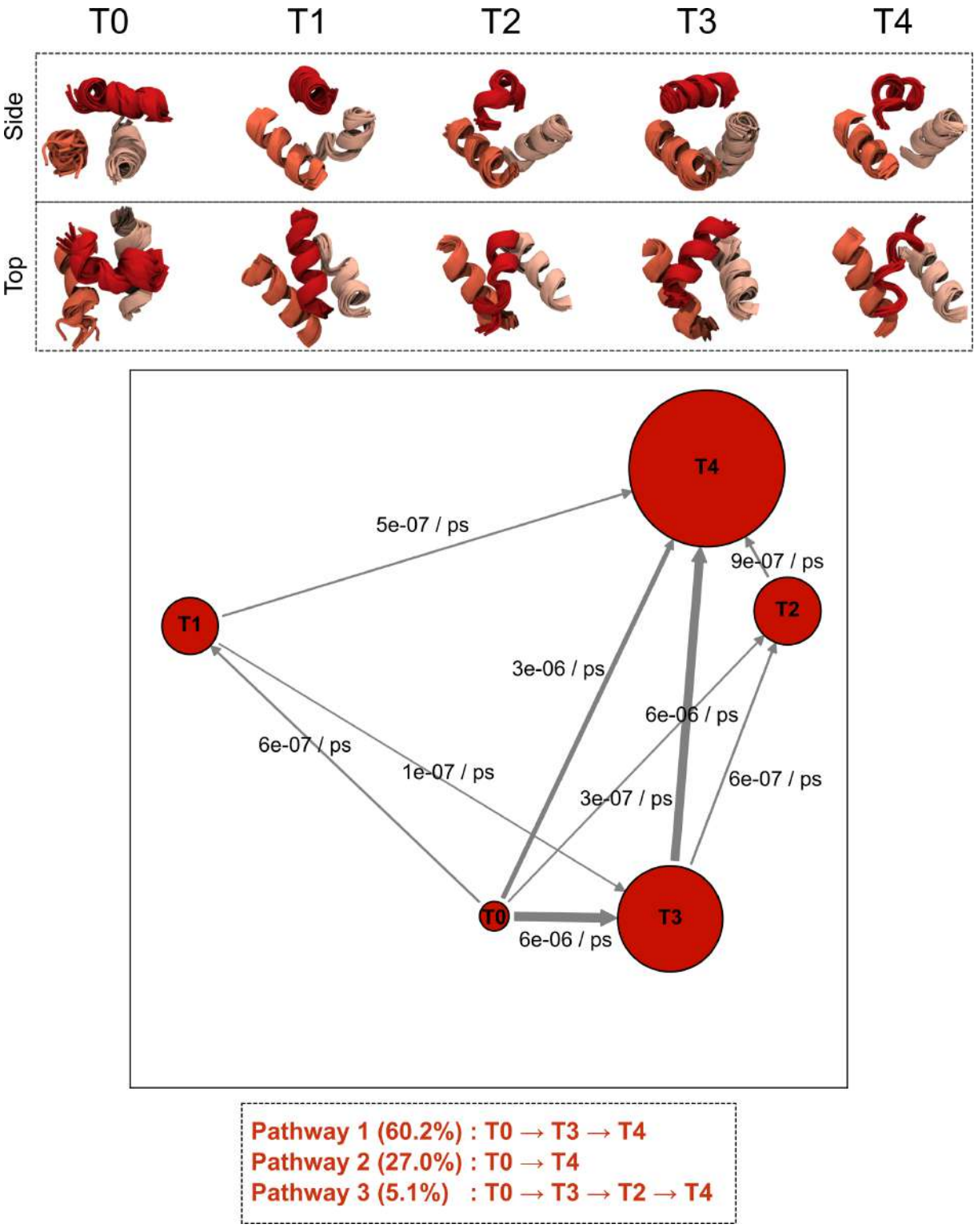

FIGURE 4.7: **Macrostates of the hLL-37$_{17\text{-}29}$ trimer and their interconversion kinetics:** Five-state MSM with representative structures obtained from 40 μs of simulation of the hLL-37$_{17\text{-}29}$ trimer. For each metastable state, both top and side views are shown, overlaid with 10 similar structures from the same state. The transition network illustrates the kinetics of interconversion between these states. The major pathways leading from state T0 to T4 are shown below.

in trimers are T2 and T3. In pathway-1, the highly ordered T3 is involved, whereas in pathway-2, the trimers convert directly from T0 to T4 in a single step. In the least prevalent pathway-3, both T2 and T3 are involved.

4.3.2.2 Structural features of the metastable states

We computed the average α-helical content for each trimeric state to investigate structural changes in the peptides. Overall, we observed a decline in the helical content compared to the tetramers, indicating a loss in structural integrity (Table 4.2). Among the five states, T3 is the most structured, followed closely by T2 and T1. In contrast, T0 and T4 possess the lowest helical content, and are the most disordered. To explore the internal

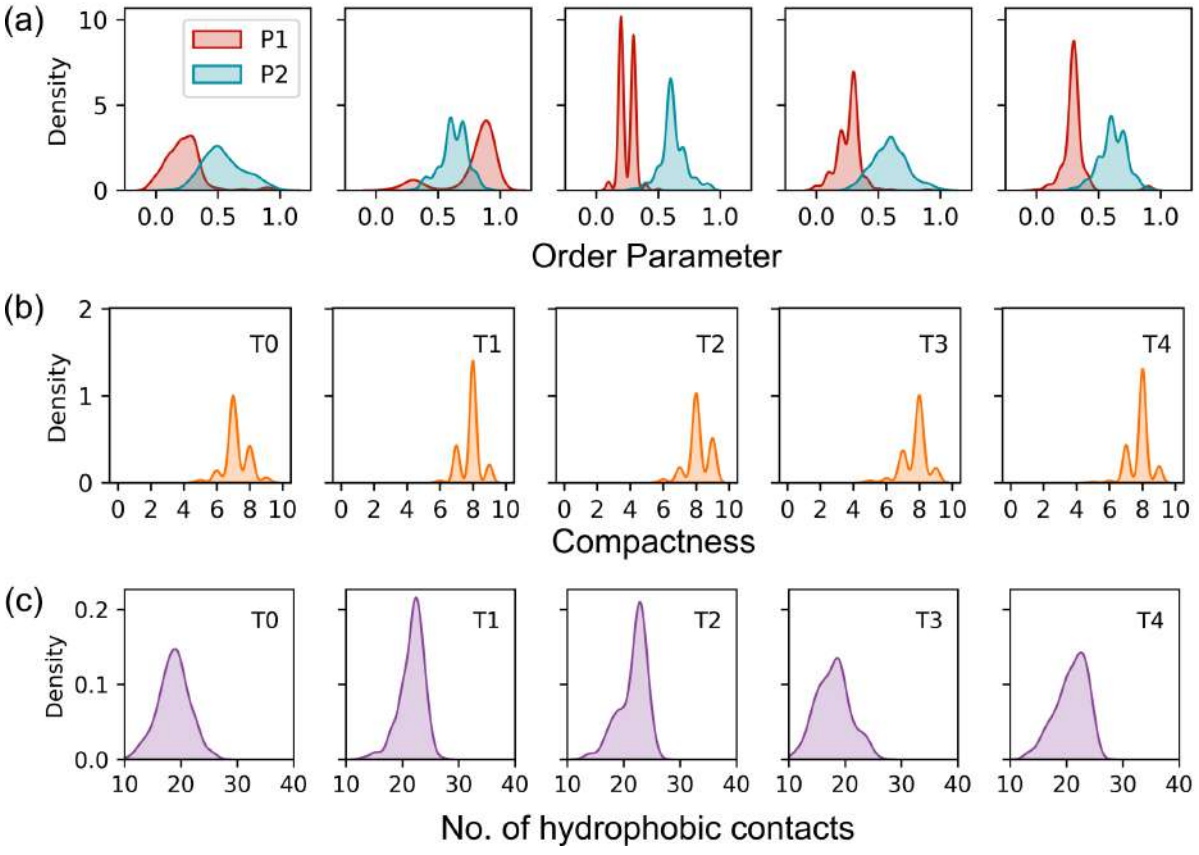

FIGURE 4.8: **Structural features of the 5 metastable states:** Distributions of (a) polar order (P1) and nematic order (P2), (b) compactness, and (c) the number of hydrophobic contacts for each metastable state of the trimer. Each distribution is calculated from 250 randomly selected structures within the corresponding metastable state.

ordering among the peptides, we examined the distribution of the order parameters (P1 and P2) in each metastable state (Figure 4.8a). In trimers, the peptides tend to be more unidirectional, which is reflected in the shift of P1 to higher values (P1>0). They are also more aligned with the director vector, reflected in a simultaneous increase in P2 (P2≥0.5). The highly unidirectional state T1 has a P1 close to 1, which is non-existent in tetramers. In T1, we also noted a small population of trimers where the peptides are randomly oriented. The remaining states display varying degrees of internal order. For example, in state T0, both P1 and P2 sample a wide range of values representing the most disordered state. In the other states, particularly T2, T3, and T4, though the peptides have a broad distribution in P2, they sample a relatively narrow range in P1. These states represent those arrangements where the peptides are somewhat aligned, but fluctuate rapidly along the director vector. When considering aggregate shape (Figure 4.8b), the trimers appear more spherical than the tetramers. Their average compactness is centered around 8 instead of 7 in the tetramers. Across all trimeric states, we also found a sporadic presence of more extended (compactness≈7) and more spherical (compactness≈9) structures. The relative abundance of these conformers varies across the states. For instance, states T1, T3, and T4 have an excess of the extended structures, whereas states T0 and T2 have an excess of the compact structures.

4.3.2.3 Key interactions in the trimer

The contact maps in Figure 4.9 illustrate the inter-residue interaction probability in the five metastable states. Like the tetramers, the most dominant interactions involve the central I24, reinforcing its role in the aggregation of hLL-$37_{17\text{-}29}$ peptides. Here, the peptides interact preferably from the C-terminal end, as evidenced by the reduced probability in the top-left corner of the maps. The hydrophobic residues (F27 and L28) at the C-terminal actively form hydrophobic contacts among themselves and with residues in the peptide center and N-terminal. Among the two, the stabilizing contacts originating from L28 are stronger, for example, L28-I20 contacts in T2, T3, and T4, and L28-I24 contacts in T0. L28 self-interactions are unique to T1 and almost as strong as the central I24 interactions. In contrast, the interactions among the N-terminal hydrophobic residues

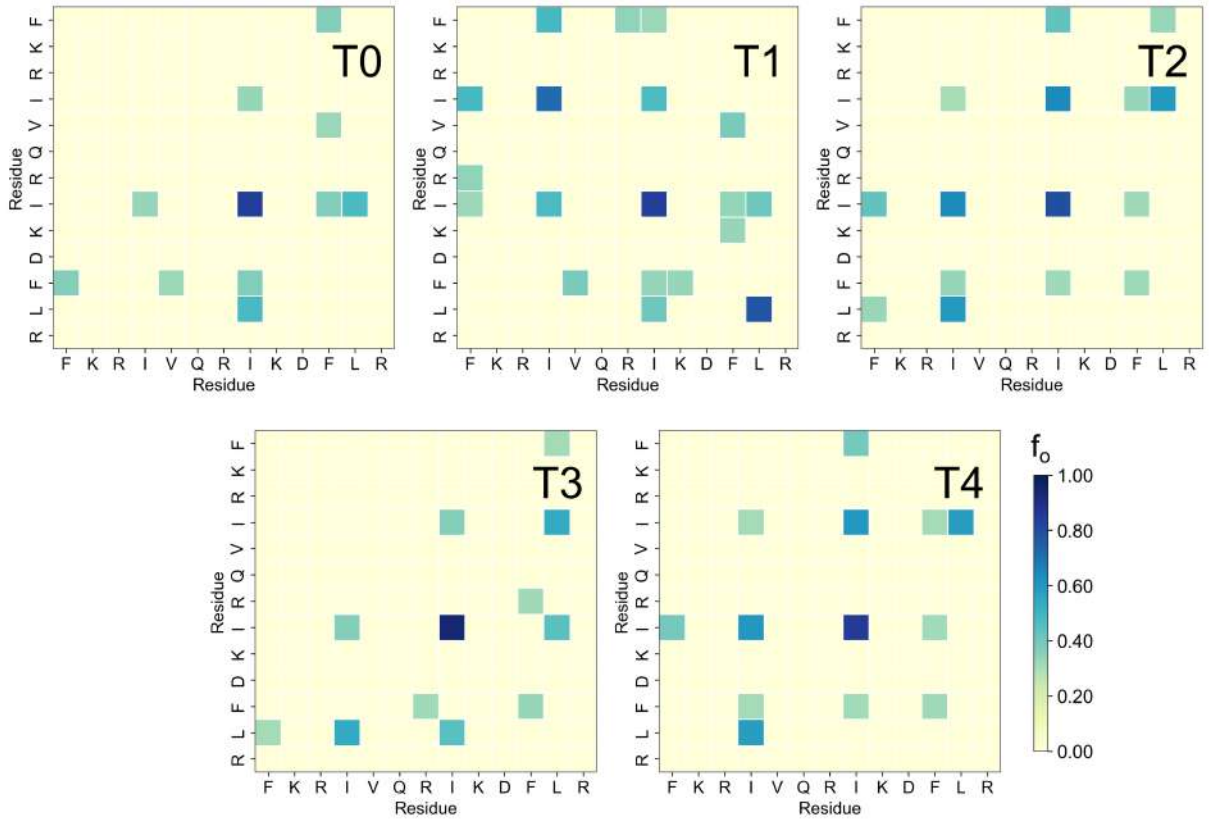

FIGURE 4.9: **Key interactions in the 5 metastable states:** Inter-peptide contact maps generated from 250 conformers randomly selected from each of the five metastable states. The color bar indicates the interaction probability (f_o).

are rare, occurring only in T1. Among them, I20 forms stronger interactions with the residues in the peptide center and the C-terminal, whereas F17 interactions are weak. The V21, which actively interacts in the tetramers, rarely forms hydrophobic contacts in the trimers. Overall, the rare interactions among the N-terminal residues in the tetramers are almost non-existent in the trimers. The trimers act as reactive intermediates during tetramer formation as they are energetically disfavoured [146]. These states are stabilized primarily through van der Waals interactions, while the electrostatic component remains positive and unfavorable for all states. Among them, state T0 has the lowest van der Waals stabilization. This interaction improves in states T1, T2, T3, and T4, with closely graded van der Waals energy (≈-64 kcal/mol). As a result, the electrostatic component determines the relative abundance of these states. This electrostatic repulsion is the highest in T1 and lowest in T4. Although T1 benefits from favorable van der Waals stabilization, its highly positive electrostatic component makes the state energetically less favorable.

In contrast, strong van der Waals interactions and minimal electrostatic destabilization make T4 the most favoured state, reflected in its greater abundance. The contact maps in Figure 4.9 and the interaction energies portray the role of hydrophobic interactions in stabilizing the trimers (Figure 4.8c). In T0, where van der Waals stabilization is weakest, the hydrophobic contacts are reduced and shift toward lower values. The remaining states have more hydrophobic contacts, corresponding to greater van der Waals stabilization. Among them, T3 and T4 show broad distributions, with T3 skewed towards lower and T4 towards higher numbers of contacts. T1 and T2, in contrast, exhibit sharp distributions in the number of hydrophobic contacts, which may account for their slight increase in van der Waals energy. In the case of trimers, the absence of a well-defined

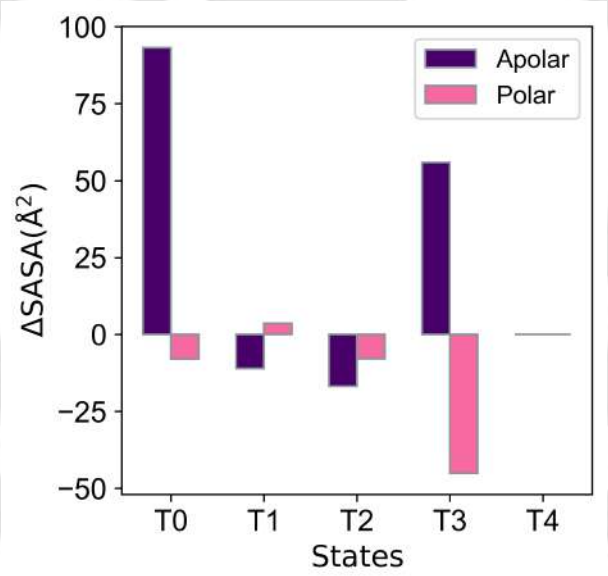

FIGURE 4.10: **Solvent accessible surface area of the trimer metastable states:** Average solvent-accessible surface area (SASA) of polar and apolar residues relative to the most abundant state T4 (ΔSASA). The values are averaged over 250 randomly selected conformers from each metastable state.

crystal structure necessitates using the most abundant state, T4, as a reference for comparing SASA values (polar and apolar). The rationale here is based on the lowest free energy of T4, which reflects a favorable arrangement of residues. Among the 5 states, T0 exhibits the most unfavorable arrangement, characterized by masked polar residues and highly exposed hydrophobic residues (Figure 4.10). Compared to T0, T3 shows reduced hydrophobic exposure; however, its polar residues are the most shielded among all the

states. In T2, while the hydrophobic residues are better exposed than in T4, the polar residues remain somewhat shielded. T1 is the only state that has favorable solvent exposure than T4, showing an optimal balance in the two residue types. In summary, states T1 and T2 exhibit favorable solvent exposure of hydrophobic and hydrophilic residues, whereas states T0 and T3 have unfavorable residue arrangements.

4.4 Conclusion

The core segment of the human LL-37 peptide, comprising residues 17–29, can self-assemble into 4-helix bundles (4HBs) with a distinct cross-α amyloid architecture. These 4HBs interact with one another to form supramolecular assemblies that resemble ribbon-like structures and hold great promise for biomedical applications. While previous studies have primarily focused on the formation of β-amyloids, understanding the mechanisms underlying α-amyloid formation is equally crucial. In this study, we employed extensive molecular dynamics simulations combined with Markov state modeling (MSM) to elucidate the relaxation pathways of hLL-$37_{17\text{-}29}$ oligomers. Specifically, we characterized trimeric intermediates and the final tetrameric bundles, providing a comprehensive view of the aggregation pathway that transforms initially disordered aggregates into ordered cross-α architectures.

For both the trimer and the tetramer, intermolecular C_α distances between hydrophobic residues were used to construct the feature space for MSM analysis. The tetramer MSM revealed six metastable states (Q0–Q5) spanning conformations from highly disordered peptide aggregates to ordered assemblies that closely resemble the cross-α architecture observed in the crystal structure. Structural relaxations across these states progressively transform disordered aggregates into highly ordered 4HBs. Most relaxation pathways involve Q3 and Q4 as key intermediates en route to the ordered Q5 state. This structural reorganization is accompanied by an increase in α-helical content and a convergence of the polar and nematic order parameters (P1$\approx$0, P2$\approx$0.5) toward values observed in the crystal structure. These relaxations are driven predominantly by van der Waals interactions that

promote the formation of a compact hydrophobic core. In addition, the peptides preferentially interact via hydrophobic residues at the C-terminal, while stabilizing interactions from the N-terminal are rare. Among the six states, Q5 achieves an optimal balance in the solvent exposure of hydrophobic and hydrophilic residues, whereas the less ordered states exhibit poor packing and increased solvent exposure of hydrophobic residues, resulting in reduced stability.

In the trimeric assemblies, the oligomers are distributed across five metastable states (T0–T4) with markedly different structural and energetic properties. Compared to the tetramers, the trimers are less ordered, exhibit lower α-helical content, and display distinct orientational preferences (higher P1 and P2 values, indicating more unidirectional alignment). Hydrophobic contacts contribute to stabilizing the trimers; however, a positive electrostatic component makes these states energetically unfavorable. Due to these unfavorable interactions, the trimers cannot exist independently and spontaneously convert into tetramers. Among the trimeric states, T4 is the most stable, characterized by favorable van der Waals packing and reduced electrostatic repulsion, whereas T0 is highly unstable due to a poorly shielded hydrophobic core.

Collectively, these results provide kinetic and structural insights into the reorganization of hLL-$37_{17\text{-}29}$ oligomers. The transition from trimer to tetramer is driven by the formation of a tightly packed hydrophobic core, which ultimately leads to tetrameric bundles with a cross-α arrangement. These findings emphasize the cooperative nature of peptide aggregation and highlight the critical role of hydrophobic residues—particularly I24 in guiding the assembly process.

Chapter 5

Membrane Interaction and Embedding of a Self-Assembled 4-Helix Bundle from the Antimicrobial hLL-$37_{17\text{-}29}$ Fragment

Overview Amyloidogenic peptides share structural and functional traits with antimicrobial peptides (AMPs), and in some cases even exhibit antibacterial activity. Both classes of peptides disrupt cell membranes, ultimately leading to cell lysis. This similarity has led to the hypothesis that AMPs may have evolved from aggregation-prone amyloidogenic templates, where incorporating cationic residues transforms an amyloidogenic fragment into an antimicrobial fragment. The human AMP LL-37, particularly its core segment (residues 17–29), retains antimicrobial activity and self-assembles into ribbon-like fibrils composed of repeating four-helix bundles (4HBs) with a distinct cross-α amyloid architecture. Since the functionality of these peptides is closely tied to membrane interactions, understanding their binding and assembly at membrane interfaces is essential. While membrane interactions of β-amyloids have been extensively characterized, those of cross-α assemblies remain largely unexplored. Here, we use atomistic molecular dynamics simulations to investigate how hLL-$37_{17–29}$ 4HBs interact with membranes. Specifically, we examine their behaviour with four model bilayers: PE:PG (3:1) and PC:PG (7:3) mimicking bacterial membranes, pure PC representing mammalian membranes, and pure PE as a control. Our simulations show that preassembled tetrameric 4HBs bind stably to anionic membranes in a face-down orientation while retaining their cross-α structure. Adsorption induces minimal structural perturbation but results in moderate shape deformation, consistent with membrane-induced compaction. Binding to the membrane surface increases membrane curvature and the ordering of the lipids near the 4HB. In addition, we have quantified the free energy associated with 4HB invasion into the bilayer interior. We also explore de novo assembly by simulating initially dispersed peptides near bacterial membranes. Our study provides a comprehensive view of cross-α amyloid interaction with membranes that can be leveraged in biomedical applications.

5.1 Introduction

Antimicrobial peptides (AMPs) such as temporins, bacteriocins, and others show a tendency to form amyloid-like deposits [180, 327–330]. Numerous studies suggest that amyloidogenic peptides share functional similarities with AMPs, and some even exhibit antibacterial properties [331]. Both classes of peptides are often cytotoxic and tend to bind to negatively charged membranes, particularly in lipid-disordered regions, leading to membrane disruption [332–335]. These observations support an intriguing theory that AMPs may have evolved from the same aggregation-prone templates found in amyloidogenic peptides. The amino acid frequency in amyloidogenic regions shows striking similarity to that in antimicrobial segments. Moreover, the intrinsic probability of a residue occurring in either region is closely related—except for positively charged residues. Incorporating cationic residues at specific positions can inhibit amyloid formation while enhancing antimicrobial activity, allowing amyloidogenic sequences to be tailored into antimicrobial segments [336]. Uperin 3.5 exemplifies this dual nature. It is amyloidogenic and capable of perturbing membranes. However, its antimicrobial activity is inversely related to its amyloidogenicity, as membrane interaction does not require aggregation. Reducing the peptide's cationic charge diminishes its membrane affinity and increases its tendency to form fibrillar amyloid deposits [337]. Similarly, the amyloid-β (Aβ) peptide found in the brain exhibits antimicrobial activity in its monomeric form but loses this function upon self-aggregation into fibrils, which are associated with neurodegenerative diseases [331, 338]. Protegrin also forms amyloid-β-like aggregates that retain antibacterial activity while exhibiting reduced cytotoxicity [339].

To better understand these overlapping properties and the functional duality of amyloidogenic peptides and AMPs, it is crucial to examine how amyloidogenic peptides interact with membranes. Amyloidogenic peptides tend to fibrillate directly on the membrane surface, disrupting membrane integrity and causing leakage [340]. Notably, leakage induced by on-pathway fibrils is greater than that caused by mature fibrils, highlighting the higher cytotoxicity of intermediate species [341]. Binding of these cytotoxic intermediates can

induce phase separation in the lipid bilayers, primarily through the uptake of raft components [342]. These early interactions reduce the lateral diffusion of lipids while increasing dynamic motions in the headgroups [343]. The interaction of β-amyloids with model membranes is governed by the nature of lipid headgroups and the presence of membrane microdomains, such as lipid rafts. Headgroups determine the extent of interaction and insertion of the Aβ protofilament: phosphatidylethanolamine (PE) lipids promote deeper insertion compared to phosphatidylcholine (PC), due to favorable electrostatic and hydrogen bonding interactions with the bilayer surface [344]. Moreover, these interactions are sensitive to the protonation states of the Aβ residues and can be tuned by altering the pH of the medium [345]. Negatively charged phosphatidylinositol (PI) lipids enhance binding to positively charged residues on tau fibrils, often clustering to aid aggregation [346]. GM1 gangliosides, concentrated in the raft domains, typically mediate interactions with Aβ amyloids and tau polymorphs, triggering structural changes in the amyloid that seed further aggregation [347, 348]. Cholesterol, another major membrane component, modulates membrane thickness and rigidity, enhancing amyloid binding during adsorption [349]. However, increased cholesterol content also increases the penetration barrier, thereby inhibiting membrane disruption [350]. Upon membrane adsorption, β-amyloids undergo structural rearrangements that promote further aggregation and contribute to membrane disruption. Aβ peptides engage distinct hydrophobic residues when binding to neuronal membranes, leading to fibril polymorphs different from those formed in solution [343]. For instance, Aβ_{1-42} tetramers elongate upon membrane binding, adopting linear rod-like conformations that enhance seeding. This elongation is more evident in the presence of cholesterol-rich lipid rafts, which induce reorganization in key hydrophobic regions. Membrane disruption in this case is associated with increased ordering of lipid tails, particularly in PC-containing bilayers [351]. Tofoleanu et al. showed that insertion of the hydrophobic C-terminal of Aβ_{9-40} protofilaments is facilitated by electrostatic interactions between charged residues near the turn region and the lipid headgroups [352]. Surface adsorption of trimers from this segment causes membrane thinning while simultaneously reinforcing inter-peptide salt bridges, thereby stabilizing the β-sheet structure [353]. As aggregate size increases, membrane invasion becomes more favorable due to a reduced

free energy barrier [350]. For example, pentamers derived from the p3 segment of Aβ (Aβ_{17-42}) exhibit strong association with negatively charged membranes, facilitated by Ca^{2+} ions [354]. These oligomers can also adopt distinct membrane-bound conformations: U-shaped in trimers and β-hairpin in dimers and monomers [355]. The aggregate morphology also plays a key role in toxicity, as Aβ42 dodecamers exhibit greater disruption of neuronal membranes compared to mature fibrils [356]. Additionally, the aggregation state influences the insertion site of peptides. In tau fragments (306–378) comprising the R3–R4 domains, monomers primarily insert via the PHF6 segment of R3, while dimers preferentially insert through the R4 domain, with weaker adsorption of PHF6 [357, 358].

LL-37 is an AMP derived from the cathelicidin family of proteins that plays a multifaceted role in the host immune system. A truncated segment of this peptide, comprising residues 17–29, retains its antimicrobial properties and assembles into ribbon-like fibrillar nanostructures. This self-assembly features a repeating four-helix bundle (4HB) with a distinct cross-α amyloid architecture. While the interactions of β-amyloids with membranes have been extensively studied, those involving α-amyloids remain poorly understood. In this chapter, we investigate the interaction of the hLL-$37_{17\text{-}29}$ 4HB with four model membranes. Two of these-PE:PG (3:1) and PC:PG (7:3)-represent bacterial membranes that differ in the nature of their zwitterionic components [359–362]. Between these two, the PE:PG membrane also serves as a model for a gram-negative bacterial membrane. In addition, we have taken a pure PC bilayer to mimic a mammalian membrane, while a pure PE bilayer serves as a control [363, 364]. Through this study, we aim to uncover the differential interactions of the 4HB with these model membranes. Specifically, we examine the nature and strength of 4HB–bilayer interactions, assess changes in both lipids and the 4HB during membrane adsorption, quantify the free energy associated with 4HB penetration into the membrane, and explore the possibility of generating these self-assembled structures in the presence of a membrane.

We have organized the remainder of the Chapter 5 as follows: In Section 5.2, we provide a detailed description of setting up the bilayer and bilayer–4HB binary systems, the protocol for molecular dynamics (MD) simulations, and the steered MD simulations used to drive the 4HB into the bilayer interior. These simulations form the basis for the subsequent

umbrella sampling used to calculate the potential of mean force (PMF) for membrane partitioning of the 4HB. In Section 5.3, we analyze the structural changes in both 4HB and the bilayer during adsorption, examine the key interactions and energetics of the process, and differentiate the partitioning energies of the 4HBs into the bilayer interior. Finally, in Section 5.4, we summarize the key findings of this study.

5.2 Materials and Methods

5.2.1 Preparation of the 4HB structure

TABLE 5.1: Details of all the systems used in Chapter 5. N_p denotes the number of peptides used in each system, and N_{lipids} denotes the total number of lipids in the bilayer. All systems have an equal distribution of lipids between the two leaflets.

Bilayer	$N_{\mathbf{lipids}}$	$N_{\mathbf{p}}$	**Orientation**	**Time (ns)**	**Box (Å^3)**
Bilayer Equilibration					
PE:PG(3:1)	200	-	-	200	79.5×74.9×80.1
PC:PG(7:3)	200	-	-	200	83.0×76.5×86.0
PE	200	-	-	200	75.9×74.5×82.6
PC	200	-	-	200	90.6×78.0×73.4
4HB+Bilayer					
PE:PG(3:1)	200	4 (4HB)	Orientation-I	1000	74.1×79.2×108.7
	200	4 (4HB)	Orientation-II	1000	-
	200	4 (4HB)	Orientation-III	1000	-
PC:PG(7:3)	200	4 (4HB)	Orientation-I	1000	82.1×79.4×99.38
	200	4 (4HB)	Orientation-II	1000	-
	200	4 (4HB)	Orientation-III	1000	-
PE	200	4 (4HB)	Orientation-I	1000	79.1×74.9×107.4
	200	4 (4HB)	Orientation-II	1000	-
	200	4 (4HB)	Orientation-III	1000	-
PC	200	4 (4HB)	Orientation-I	1000	82.9×83.0×94.5
	200	4 (4HB)	Orientation-II	1000	-
	200	4 (4HB)	Orientation-III	1000	-
hLL-37$_{17\text{-}29}$+Bilayer					
PE:PG(3:1)	200	4 (4×1)	-	4×400	74.7×79.2×107.6
PC:PG(7:3)	200	4 (4×1)	-	4×400	83.6×78.9×97.9

The 4HB coordinates were extracted from the X-ray crystal structure of hLL-37$_{17\text{-}29}$ self-assembly (PDB ID: 6S6M). To prevent spurious charged interactions at the termini, the

peptides were capped with acetyl (ACE) and N-methyl (NME) groups at the N- and C-termini, respectively [365]. The protonation states of the residues were assigned for pH 7 using `PROPKA` [217, 218]. The capping groups and hydrogen were added using the `tleap` module in AMBER20[315]. The 4HB was modelled according to the AMBER14SB force field [219]. A short energy minimization was then performed on the `tleap`-generated structure to resolve any steric clashes.

5.2.2 Preparation of model membranes

Bilayer-only models were constructed using the CHARMM-GUI web server [366, 367], based on the compositions listed in Table 5.1. Each bilayer contained 100 lipids per leaflet. For heterogeneous membranes (PE:PG and PC:PG), the lipid types were symmetrically distributed across both leaflets [368]. The bilayers were solvated on both sides (top and bottom) with 50 water molecules per lipid, resulting in a total of 10,000 water molecules per system. The negative charges on the PG lipids were neutralized by the addition of Na^+ ions. To mimic physiological salt concentration (0.15 M NaCl), excess NaCl was added to the systems. Ions were randomly placed using a Metropolis criterion to minimize overlap with lipids and water molecules. Lipid molecules were modeled using the Lipid21 force field in AMBER [369], while water and ions were represented by the TIP3P water model and the Joung and Cheatham ion parameters, respectively [220, 223].

5.2.3 Membrane equilibration

Energy minimization of the solvated bilayers was carried out in two phases over 10000 steps: the first 5000 steps employed the steepest descent algorithm for rapid initial relaxation, followed by 5000 steps of conjugate gradient minimization for further refinement [370]. The minimization was performed under constant volume conditions, with no pressure scaling or atomic restraints applied. The systems were then heated to 313.15 K in two stages to ensure a fluid-phase lipid environment. The target temperature is well above the lipid phase transition temperature (T_m) reported in earlier studies [371–375].

Initially, bilayers were rapidly heated to 100 K over 2500 steps in an NVT ensemble. This was followed by a gradual increase to the target temperature over 50000 steps in an NPT ensemble with semi-isotropic pressure coupling. The slow heating helped eliminate packing defects and promoted the formation of a compact bilayer core. During both heating phases, lipids were positionally restrained using a harmonic force constant of 10 kcal/mol Å^2. Next, the system density and box dimensions were equilibrated through 15 successive stages of 1 ns each in the NPT ensemble. In the first 10 stages, lipid restraints were progressively reduced by lowering the force constant to zero. The final five stages were run without restraints to allow full equilibration. Following this, a 200 ns production run was conducted to assess bilayer properties. The equilibrated configuration was then used to construct the 4HB–bilayer binary system in Section 5.2.4.

5.2.4 Preparation of the 4HB-bilayer systems

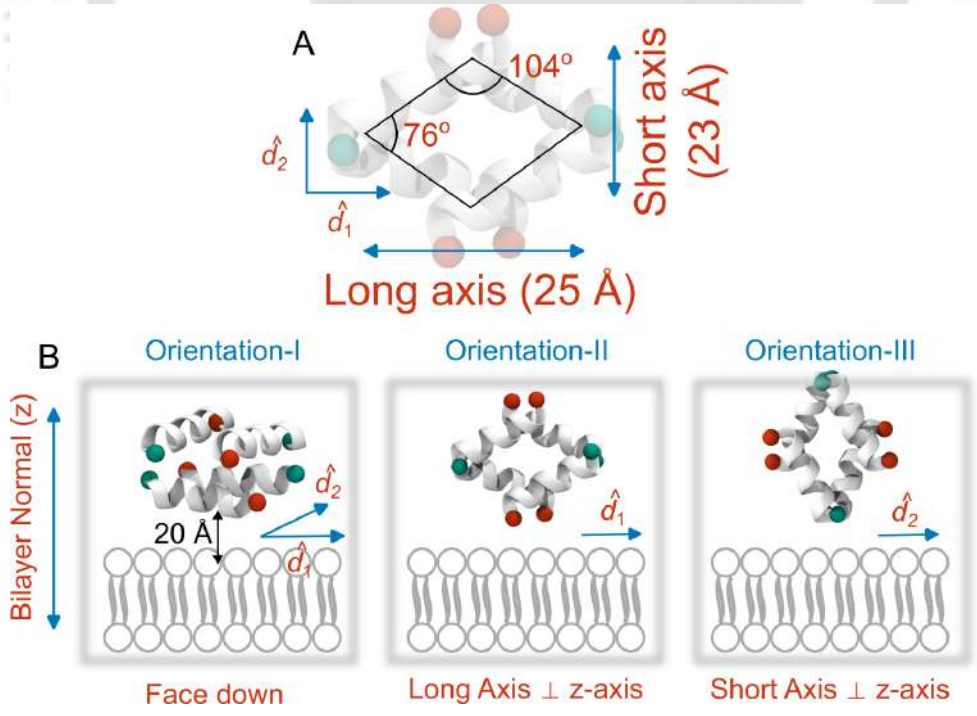

FIGURE 5.1: **4HB structure and orientation with respect to the bilayer:** A) The four-helix bundle (4HB) structure of the hLL-37$_{17–29}$ tetramer (PDB ID: 6S6M). The 4HB exhibits a distinct cross-α amyloid architecture. This protofibril has a long axis (25 Å) and a short axis (23 Å). B) Various orientations of the 4HB relative to the bilayer normal (z-axis) used to initiate the simulations.

The equilibrated bilayers were first stripped of water molecules and ions to prepare for peptide placement. The 4HB structure was then positioned above the bilayer surface at a distance of 20 Å using PACKMOL [221]. To explore different binding orientations, three distinct configurations of the 4HB relative to the bilayer normal were considered: (a) face-down, (b) long-axis, and (c) short-axis, as illustrated in Figure 5.1B. In the face-down orientation, both the long and short axes of the 4HB lie perpendicular to the bilayer normal, aligned parallel to the xy-plane. In contrast, the long-axis and short-axis orientations involved aligning either the long or short axis parallel to the bilayer normal. After positioning the 4HB, water molecules were reintroduced to maintain a minimum padding of approximately 12 Å between the peptide and the simulation box boundaries. For zwitterionic membranes, the net positive charge after addition of 4HB was neutralized by the addition of Cl^- ions. Similarly, for the anionic membranes, the net negative charge of the systems were neutralized by the addition of Na^+ions. In all the systems, excess NaCl was added to maintain a physiological salt concentration of 0.15 M. Finally, the systems underwent energy minimization for 20,000 steps using the same two-stage protocol described in Section 5.2.3.

5.2.5 MD simulation parameters

From the heating stage onward, all hydrogen atoms were constrained using the SHAKE algorithm, allowing the use of a 2 fs integration timestep [226]. A modified leapfrog integrator was used to solve the equations of motions at these discrete time intervals [151]. System temperature was maintained at 313.15 K using a Langevin thermostat with a collision frequency of 1 ps^{-1} [225]. Semi-isotropic pressure coupling was applied using a Berendsen barostat[224], with independent scaling in the xy-plane (parallel to the bilayer surface) and the z-direction, and a relaxation time of 1 ps. Short-range non-bonded interactions, namely van der Waals and electrostatics, were computed using a 10 Å spherical cutoff. For electrostatics, the Particle Mesh Ewald (PME) method [227] was employed: the real-space (short-range) component was calculated within a 10 Å cutoff, while the long-range component was evaluated in Fourier space using a grid spacing of 1 Å. Periodic

boundary conditions were applied in all three spatial dimensions to eliminate edge effects during simulations [150]. System coordinates were saved every 2,000 steps (equivalent to 4 ps) during the production runs for downstream analyses. To assess reproducibility, each system was simulated in triplicate, starting from different initial atomic coordinates (Figure 5.1). Energy minimizations were performed using the CPU-based `SANDER` module in AMBER20, while microsecond-scale production trajectories were generated using the GPU-accelerated `PMEMD` engine on NVIDIA A100 graphics units [228].

5.2.6 Steered MD-Based Insertion of 4HB into Lipid Bilayers

Insertion of 4HBs into bilayers occurs on timescales that are often inaccessible to conventional MD simulations. To overcome this, biased simulation techniques such as steered molecular dynamics (SMD) are commonly employed [376–378]. In SMD, controlled forces are applied to specific atoms to drive the 4HB into the bilayer—a method previously used to study the partitioning of β-amyloids into membranes [344, 379]. The final conformations from Section 5.2.5, where the 4HB is adsorbed on the bilayer surface, were used as starting points for the SMD simulations. Due to periodic boundary conditions, the 4HB can adsorb on either side of the bilayer during unbiased MD. To ensure consistency, the simulation box was rotated such that the 4HB was positioned above the bilayer along the positive z-direction.

The collective variable (CV) for steering was defined as the distance between the 4HB and the bilayer center, with motion constrained along the negative z-axis. The face of the 4HB in contact with the bilayer was used to define the CV: specifically, the center of mass (COM) of the C_α atoms of the peptide chains in contact with the membrane surface served as one end of the CV. The other end was fixed at the COM of the lipid headgroup phosphorus atoms at the bilayer center.

This distance was reduced at a constant rate of 0.025 Å/ns until it reached approximately 13 Å, ensuring deep embedding of the 4HB into the bilayer. Steering was performed in 2 ns windows, with a distance reduction of 0.05 Å per window to seed the subsequent simulation

stage. During pulling, the phosphorus atoms of the opposite leaflet were restrained with a force constant of 10 kcal/mol Å^2 to prevent bilayer drift.

The steering velocity was determined through several trial simulations; higher velocities led to the 4HB drifting away from the bilayer surface. For the PC system, the initial CV value was 25 Å, while for the anionic bilayers it was approximately 28 Å, both reduced to 13 Å in the final configuration. Snapshots were saved at every 1 Å decrease in the CV for initiating the umbrella sampling simulations described in Section 5.2.7.

5.2.7 Potential of mean force for 4HB membrane partition

Each window from the SMD simulations was first energy-minimized for 5,000 steps and then equilibrated for a short duration of 2 ns in NPT. This was followed by a 100 ns production run under NPT conditions. During the production phase, the CV in each window was restrained using a harmonic potential with a force constant of 7.5 kcal/mol Å^2. The sampling probability in each window was represented as $P(r)$, where r denotes the CV value for that particular window. The potential of mean force (PMF) was then computed from $P(r)$ using [380, 381]:

$$PMF = -k_{\mathrm{B}}T\ln P(r) \tag{5.1}$$

where k_{B} is the Boltzmann constant and T is the working temperature, set at 313.15 K. The potential of mean force (PMF)-or more precisely, the free energy profile-was computed using the Weighted Histogram Analysis Method (WHAM) developed by Alan Grossfield [382, 383]. The PMF was evaluated at 1 Å intervals through an iterative process, until convergence was achieved within a tolerance of 10^{-4}.

5.2.8 Analyses

The analyses were performed using the CPPTRAJ module of AMBER20, along with in-house codes developed in Python 3 and Tcl/Tk scripts executed within vmd [230, 325].

hLL-$37_{17\text{-}29}$ oligomers were identified using Stoddard's nearest-neighbor algorithm [229], which groups peptides based on a distance cutoff. Two peptides were considered part of the same cluster if their inter-atomic distances were less than 4 Å [207]. Each cluster was built iteratively by adding neighbors until no new members were found. The process was repeated till all the peptides were assigned to a cluster. The calculations were performed at each MD step to track the temporal evolution of the oligomer sizes. The root-mean square deviation of the 4HB backbone (N, C, O, C_α) from the crystal structure was calculated using the `rms` command of CPPTRAJ [234]. The polar (P1) and nematic (P2) order parameters of the tetramer were calculated based on Ref. 311. The long (principal) and short-axis of 4HB were defined based on Figure 5.1A. Thus, the long-axis connected the N-termini of the peptide pairs (1,3) and (2,4), while the short-axis connected the C-termini of the pairs (1,2) and (3,4). The tilt of 4HB with respect to the bilayer normal was measured separately along the long and short-axis from the dot product of their unit vectors ($\hat{d}1$ and $\hat{d}2$) with the z-axis. The polar (P1) and nematic (P2) order parametes were calculated using Equation 4.3 and Equation 4.4 (Chapter 4), respectively.

Membrane curvatures were calculated using the `MembraneCurvature` tool in the MDAnalysis library of Python 3 [384, 385]. First, the upper and lower leaflet surfaces were identified based on the P atoms of the lipid headgroups. Then, the curvature was calculated by dividing these surfaces into 10 × 10 grids. The mean curvature averaged over the last 200 ns of the MD trajectories was plotted on a 2-dimensional surface along with a color bar that quantifies the extent of curvature.

Lipid order parameters (S_{CD}) were calculated using the `lipidscd` command of CPPTRAJ. S_{CD} determines the orientation of the C-H bonds present in the methylene (-CH_2) and methyl (-CH_3) groups of the lipid acyl chains. S_{CD} is calculated using [369, 386, 387]:

$$S_{CD} = \frac{1}{2}\langle 3cos^2\theta - 1\rangle \tag{5.2}$$

where θ is the angle between the bilayer normal (z-axis) and the C-H bond vector, and the angular brackets represent averages over the lipid ensemble across the simulation timescale.

The running coordination number (RCN) of Na^+ ions with respect to the membrane surface was calculated using the radial distribution function, $g_{P,Na^+}(r)$, that quantifies the probability of finding a Na^+ at a distance r from the P atoms in the lipid headgroups. RCN can be calculated from $g_{P,Na^+}(r)$ based on:

$$RCN = 4\pi\rho_{Na^+} \int_0^r r^2 g_{P,Na^+}(r)\, dr \tag{5.3}$$

where ρ_{Na^+} is the number density of Na^+ in the system, r is the distance between the P atom (P31 in Lipid21) and Na^+ and dr is the volume element at r.

Salt-bridges between charged residues on the fibril surface and the lipid headgroups were calculated based on a distance cutoff of 3.5 Å. A salt bridge is formed when the positively charged N of the basic residues (Lys, Arg) interacts with the negatively charged O of the lipid phosphate. Similarly, a salt bridge is formed when the negatively charged O on acidic residues (Asp) interacts with the quarternary N of the lipid headgroups. Only unique salt-bridged pairs were considered, i.e., interactions between a pair of residues were counted only once. The non-bonded interaction energy (van der Waals and electrostatic) between the fibril and the bilayer components was calculated using the NAMD Energy Plugin (Version 1.4) in VMD [325]. A cutoff distance of 10 Å was used to calculate all the pairwise interactions.

5.3 Results

5.3.1 4HB adsorption differs across the model membranes

As described in Section 5.2.4, the 4HB was initially placed 20 Å above the upper leaflet. At the onset of the simulations, it diffuses freely and eventually binds to one of the leaflets. To understand how the 4HB attach to the membrane surface, we first explain the intrinsic structure of the hLL-$37_{17\text{-}29}$ tetramer, shown in Figure 5.1A. The tetramer consists of two layers, where the dimers in one layer criss-cross those in the adjacent layer, giving rise

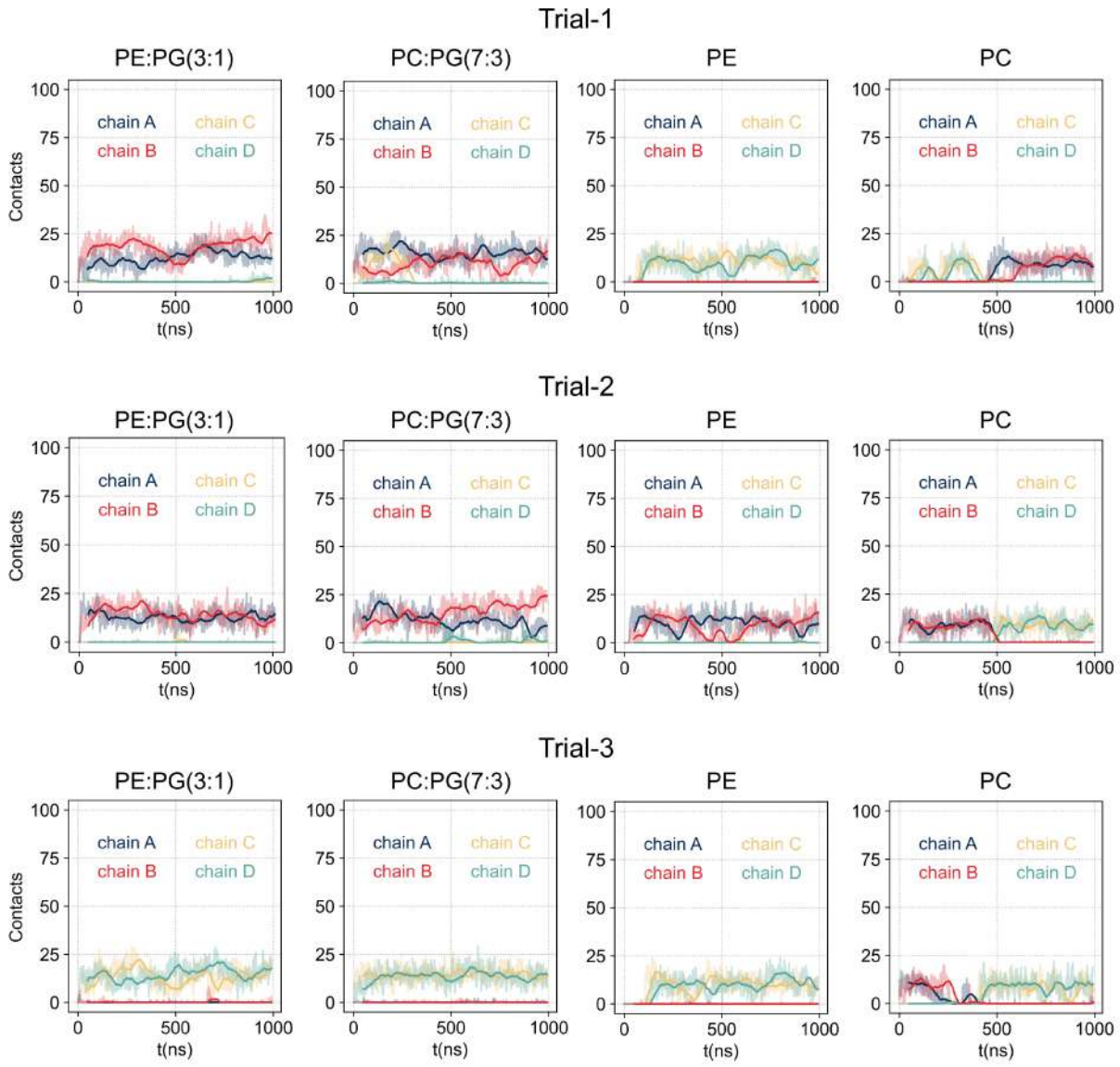

FIGURE 5.2: **Time evolution of 4HB-lipid contacts across the four bilayers:** The 4HB-lipid contacts for the three simulation trials shown as a function of simulation time, with contributions from each of the four peptide chains (A, B, C, and D) represented separately. The peptide chain labels are used solely to distinguish between the two structurally identical faces of the tetramer. A peptide-lipid contact is formed when the heavy atoms of a peptide are within 5.5 Å of the lipid headgroups.

to two identical faces: an upper face (formed by chains A and B), a lower face (formed by chains C and D), and four identical edges. The peptide nomenclature used here, is to distinguish between the two faces, which are otherwise structurally similar.

We then examined whether adsorption involves one or both faces by evaluating the number of contacts each peptide makes with the bilayer. A peptide-lipid contact is formed

when the heavy atoms of a peptide are within 5.5 Å of the lipid headgroups. Across all systems, adsorption occurs preferentially via a single face, with all observed contacts involving the peptides on that face. This face-down interaction maximizes stabilizing contacts between the peptide side chains and the lipid headgroups, making it energetically favorable. Typically, both peptides on the interacting face are involved in binding, forming approximately an equal number of contacts with the bilayer, particularly evident for the PE:PG bilayers as seen in Figure 5.2. In contrast, in the PC:PG bilayer, we observe transient rolling of the 4HB to an edge. This is marked by a decrease in interaction with one of the peptides on a particular face, accompanied by an increase in contact with a peptide from the adjacent layer. In one of the trials (Figure 5.2), the 4HB initially attached via an edge (chain B and C) before rolling onto one of the faces (chain A and B) as the simulation progresses. In another instance (Trial-2, Figure 5.2), the 4HB transiently rolls onto an edge (chain A and D) before reverting to its initial interacting face at approximately 900 ns. For the PE bilayers, contacts with one of the chains were maintained throughout the simulation, while those with the other fluctuated rapidly. This indicates weaker adsorption in the PE bilayers compared to the anionic systems. For the pure PC bilayers, the 4HB switched its interacting face midway through the simulations. This switching can occur in two scenarios: (i) the amyloid rolls on the membrane surface, or (ii) it detaches and later re-attaches by the opposite face. In the first case, interactions with one face increase as those with the other decrease. In the second case, a finite time gap exists between the loss and re-establishment of bilayer contacts on the opposite face. Both scenarios were observed in the pure PC bilayer, with a bouncing motion noted in one of the trials (Figure 5.2, Trial-1). Together, these observations indicate the weakest 4HB adsorption in the PC bilayers.

Next, we explored the extent to which the tetramers are tilted with respect to the bilayer normal during adsorption. The tilt was quantified along two axes, corresponding to the two principal dimensions of 4HB ($\hat{d}_1$ and $\hat{d}_2$), as shown in Figure 5.1A. The distribution of tilt angles reveals the preferred orientation of the 4HB on the bilayer surface (Figure 5.3). Both axes show a preference for a perpendicular orientation relative to the bilayer normal, consistent with the face-down mode of interaction. The tilt angle distribution is sharp

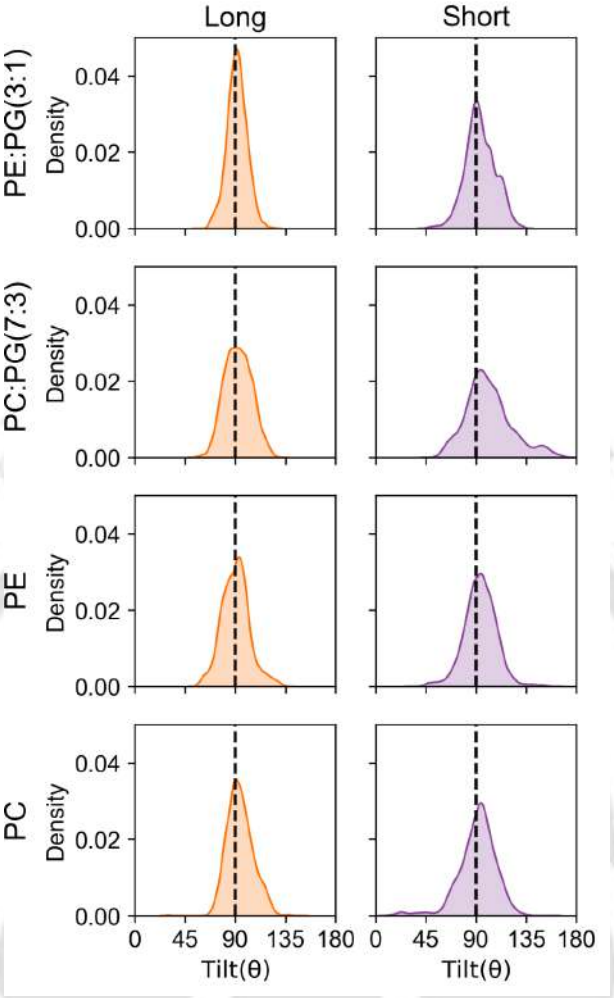

FIGURE 5.3: **Tilt of the 4HB relative to the bilayer normal:** Distribution of the tilt angles between the two principal axes (long and short) of the 4HB and the bilayer normal (z-axis), illustrating the preferred orientation of the tetramer during adsorption.

across all bilayers except for PC:PG, where it broadens, indicating increased dynamic motion of 4HB on this membrane surface. The short axis often samples higher tilt values in the anionic membranes, suggesting a stronger interaction from one of the peptides on a single face. This effect is particularly pronounced in the PC:PG bilayer. For PE:PG, we observed a more symmetric distribution across both axes, indicating equal interaction with the peptides on a particular face.

5.3.2 The difference in adsorption is explained by the electrostatic interaction energy

The differential nature of adsorption, discussed in Section 5.3.1, indicates differences in the underlying forces between the 4HB and the bilayer. To quantify these differences, we calculated the non-bonded interaction energy between the two in Table 5.2. Adsorption is primarily driven by electrostatic attraction between the surface-exposed charged residues of the 4HB and the lipid headgroups. Across all systems, the electrostatic interaction energy far exceeds the van der Waals (vdW) contribution. For example, in the anionic and pure PE membranes, electrostatic interactions are roughly 30 times stronger than vdW interactions; in the pure PC bilayer, this ratio decreases to about 20. As expected, the fibril binds approximately twice as strongly to the negatively charged bilayers (PE:PG

TABLE 5.2: Non-bonded interaction energy between the 4HB and the bilayers, decomposed into electrostatic and van der Waals contributions. The energy values are expressed in kcal/mol. Individual contributions from each lipid type are also shown. Values are averaged over multiple simulations for each 4HB–bilayer system. Numbers in parentheses indicate the standard error of the mean across simulation repeats.

System	PE/PC			PG			Total		
	Elec	vdW	Total	Elec	vdW	Total	Elec	vdW	Total
PE:PG(3:1)	-381.34 (3.50)	-15.79 (0.36)	-397.13 (3.19)	-689.75 (66.67)	-21.80 (3.00)	-711.56 (67.01)	-1071.09 (64.48)	-37.60 (2.66)	-1108.69 (64.90)
PC:PG(7:3)	-290.11 (22.96)	-20.77 (1.05)	-310.89 (24.00)	-672.62 (39.85)	-13.55 (2.04)	-686.16 (17.18)	-962.73 (17.18)	-34.32 (0.99)	-997.05 (18.05)
PE	-496.62 (21.73)	-15.42 (0.52)	-512.05 (22.09)	-	-	-	-	-	-
PC	-409.80 (17.88)	-20.19 (1.15)	-429.99 (17.36)	-	-	-	-	-	-

and PC:PG) compared to the pure zwitterionic ones. The enhanced interaction with anionic membranes is mainly due to the presence of negatively charged PG lipids, which account for 64–68% of the total interaction energy. Between the two negatively charged membranes, binding is more favorable with PE:PG than with PC:PG by approximately 111 kcal/mol. To investigate this disparity, we calculated the individual contributions from the lipid types—PG and PC/PE—in the two anionic membranes. Interestingly, the

difference in interaction energy arises largely from the zwitterionic components (PC or PE), even though PG lipids contribute more to the overall binding strength. Specifically, about 87 kcal/mol of the energy difference stems from the zwitterionic lipids. A smaller gain in stability (≈24kcal/mol) from the PG component in PE:PG is counterintuitive since these membranes have a deficit of five PG lipids per leaflet, compared to PC:PG. A closer analysis reveals that electrostatic interactions with zwitterionic lipids are the key contributors to the observed differences. Although vdW interactions with PC lipids are somewhat stronger than with PE lipids, this minute stabilization is outweighed by stronger electrostatic interactions with PE, resulting in higher overall interaction energy in PE:PG membranes. A stronger interaction with the PE component in PE:PG synergistically increases the interaction with PG lipids which explains the higher interaction here. Among the pure zwitterionic bilayers, the fibril interacts more favorably with PE than with PC. Here too, the lower vdW energy in the PE bilayer is compensated by a stronger electrostatic component, driving the net interaction in favor of PE. In summary, adsorption is dominated by electrostatic interactions. Consequently, anionic bilayers bind the 4HB more strongly than zwitterionic ones, and within each membrane category, electrostatic interactions with the zwitterionic lipids explain the preferential binding to PE-containing systems.

The differences in interaction energy are reflected in the total number of 4HB-lipid contacts formed during adsorption (Figure 5.4). Notably, 4HB forms a higher number of contacts (≈28) with anionic membranes compared to neutral membranes (<25) which explains its favorable interaction energy. The presence of the anionic PG lipids improves the overall membrane interaction of 4HB, due to the presence of positively charged residues on its surface. Among the pure zwitterionic bilayers, the number of stabilizing contacts is higher for PE (23) than for PC (18). This difference arises from the nature of the headgroup; PC lipids possess three bulky methyl groups that hinder adsorption [344].

To further distinguish between the anionic membranes, we also calculated the number of 4HB contacts with each lipid type (PC/PE and PG). Contacts with PG lipids peaks at 10 in both bilayers; however, the distribution is skewed towards higher values in PE:PG, suggesting that more number of contacts are possible in this bilayer. In contrast, the

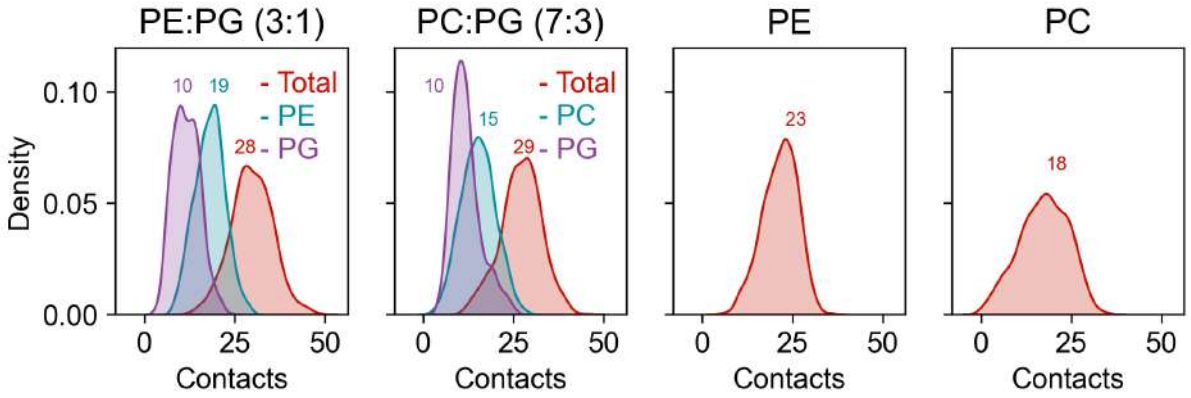

FIGURE 5.4: **Contact probability of lipids with 4HB:** Distribution of the total number of contacts formed by 4HB with the lipid bilayers. For the mixed anionic membranes, the contact probability with each lipid type is also calculated. The annotated values indicate the most probable number of contacts between 4HB and the lipids.

PC:PG system shows a sharper distribution centered around 10. For the zwitterionic components of the anionic membranes, the number of stabilizing contacts is again higher for PE in PE:PG (19) than for PC in PC:PG (15). Also, the probability of forming such contacts is greater for PE than PC. Although the absolute number of PE lipids is lower than PC across the two anionic membranes, PE still forms more contacts. This, in turn, enhances interactions with PG lipids in the PE:PG bilayer in a synergistic manner.

The electrostatic nature of adsorption suggests the formation of salt bridges between the charged residues on the 4HB surface and those on the polar headgroups of the lipid bilayer. As expected, negatively charged membranes form a higher number of salt bridges due to the presence of PG lipids, which carry explicit negative charges. For clarity, we calculated the cumulative number of salt bridges formed by each residue type (K18, R19, R23, K25, D26, and R29), considering all four peptide chains in the tetramer (Figure 5.5). Among these, the Arg residues contribute the most to salt bridge formation. Between the two Lys residues, K25 rarely participates in salt bridges, whereas the N-terminal K18 is actively involved. This suggests that K25 is likely positioned such that it cannot reach the negatively charged phosphate center of the lipid headgroups. The only negatively charged residue, D26, can distinguish between membrane types. For instance, in membranes containing PE lipids, D26 forms more salt bridges than in those containing PC lipids. This is because D26 can only interact with the positively charged quaternary nitrogen

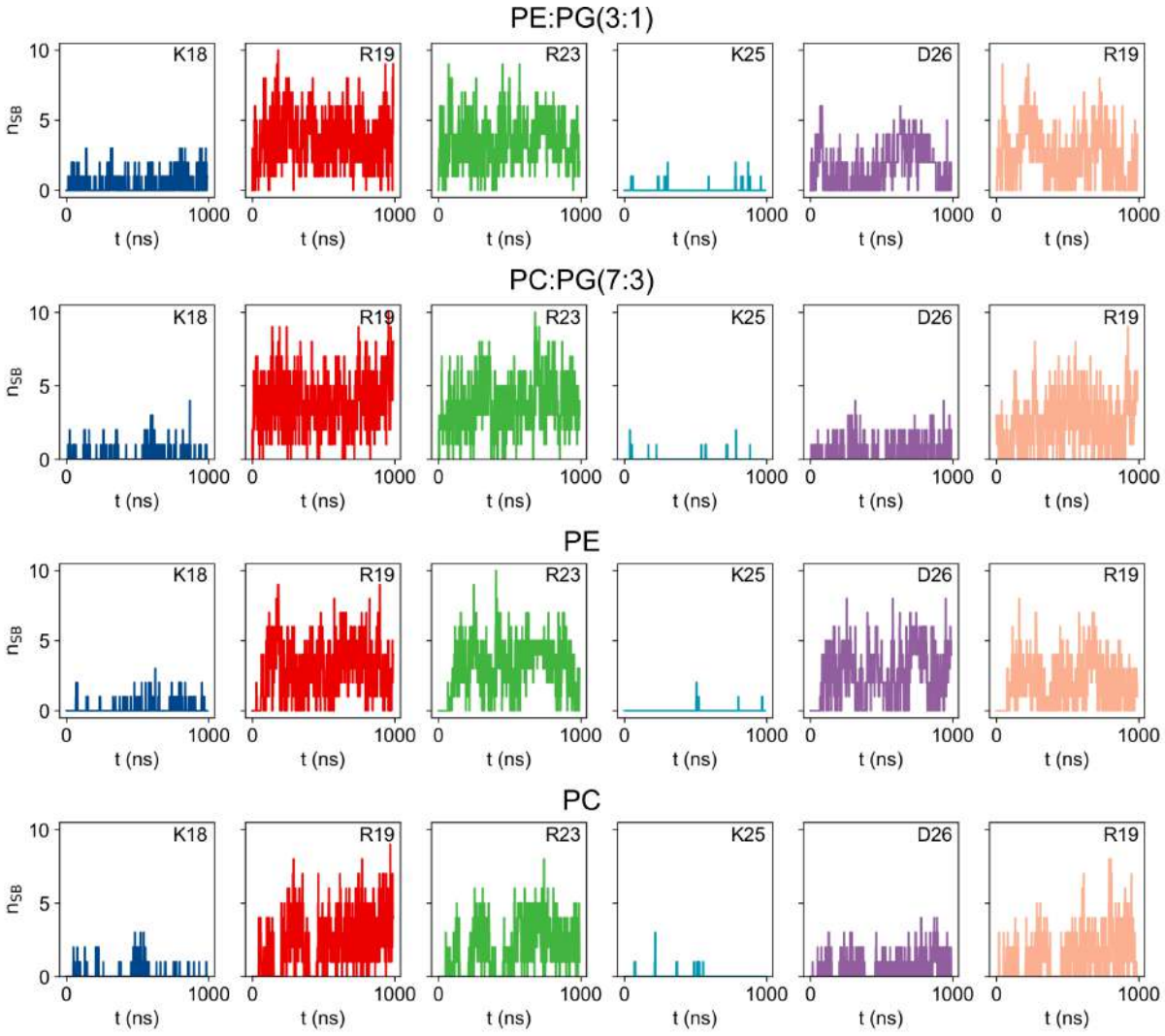

FIGURE 5.5: **Time evolution of salt bridges between 4HB and the bilayers:** Time evolution of salt bridges between the positively charged amino acids on the 4HB surface and the polar headgroups of the lipid bilayer. The total number of salt bridges includes contributions from the corresponding residues across all four peptide chains of the tetramer.

in the lipid headgroups, and the bulky tertiary-butyl groups in PC lipids hinder such interactions.

To understand how these residues adsorb onto the membrane surface, we plotted their average z-distance from the bilayer center, alongside the positions of the headgroup phosphorus (P) atoms for reference. The residue names of the two peptide chains on a single face are differentiated using the ' symbol in Figure 5.6. Across all bilayers, the 4HB preferentially attach via a single face, as indicated by the consistently lower z-distance of one

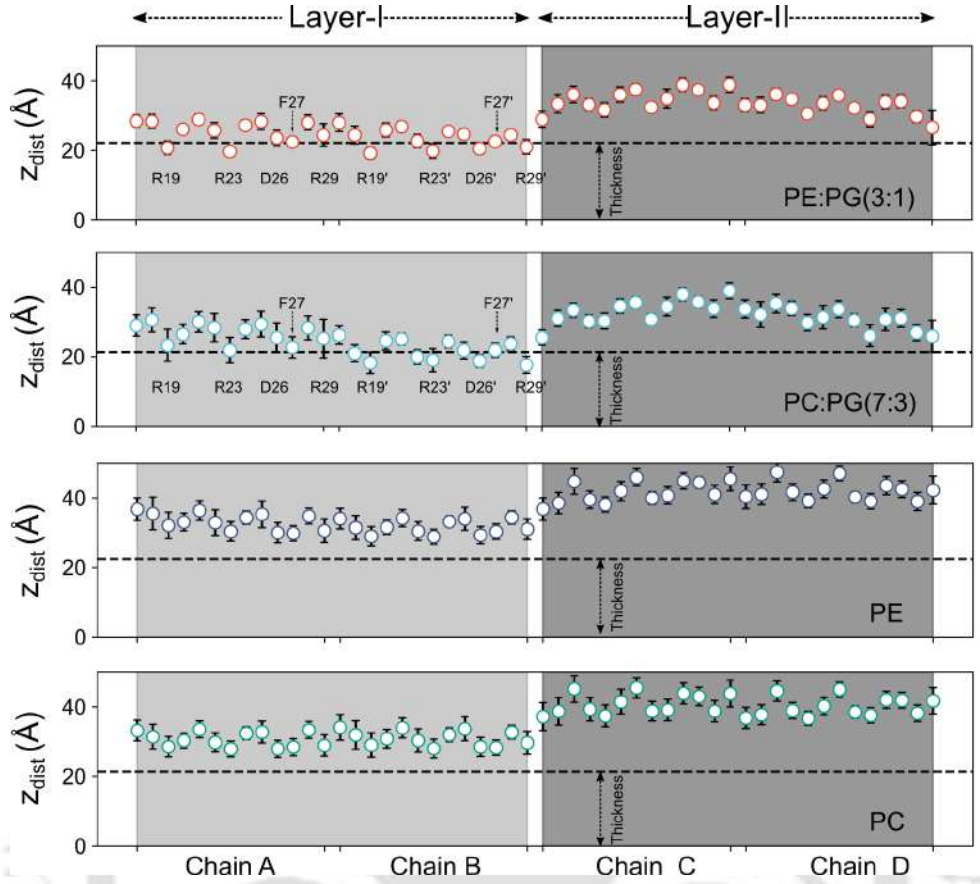

FIGURE 5.6: **Insertion depth of residues from the bilayer center:** The average z-distance of the residues from the bilayer center over the last 200 ns of the simulations. Residue labels are shown only for the anionic bilayers, where some residues extend beyond the headgroups into the interfacial region. Peptides on a single 4HB face are distinguished using the ' notation. The dotted line indicates the average position of the lipid headgroups, calculated from the P atoms.

face compared to the other. Under no circumstances do the tetramer attach via its edges. This mode of attachment is energetically favorable, as the faces possess a high positive charge density that promotes adsorption to the bilayer. The bilayers exhibit three distinct regions by depth where adsorption can occur: (i) atop the polar headgroups, (ii) in the interface between these headgroups and the tails, and (iii) in the bilayer interior consisting of densely packed tails. Attachment is primarily restricted to the polar surface of the bilayer and, in rare instances, extends to the interfacial zone, but never to the hydrophobic core. In the case of anionic membranes, positively charged residues on a single face tend to occupy the interfacial region between the polar headgroups and the hydrophobic tails. For zwitterionic membranes, these residues rarely penetrate beyond the headgroup region.

Residues that reach the interfacial zone in the anionic systems are stably held in position, as evidenced by the low variance in their z-coordinates. In the PE:PG membrane, the positively charged residues on one face of the peptide - particularly Arg - primarily intercalate into the interfacial region. Asp26 from only one of the chains is able to penetrate below the phosphate headgroups. In the PC:PG membrane, Arg residues from only one of the peptide chains intercalate into the bilayer, while those from the other chain remain in the polar region. In this case, the fibril, though attached via a single face, appears tilted toward the chain that inserts more deeply. This tilt correlates with our observation in Figure 5.3. In both anionic systems, all hydrophobic residues except F27 (and F27') remain above the plane of the P atoms due to polar–apolar mismatch. To summarize, the presence of anionic components in the bilayers facilitates stronger adsorption, whereas zwitterionic membranes allow only superficial attachment.

5.3.3 The adsorption of 4HB replaces surface bound ions

The electrostatic adsorption of freely diffusing peptides onto a two-dimensional membrane surface is associated with a loss of translational entropy [388, 389]. This entropic cost is compensated by the release of surface-bound ions [390]. Our simulations were conducted at a physiological ionic strength of 0.15 M NaCl, under which ions bind to the bilayer surface. The anionic nature of PE:PG and PC:PG membranes (due to PG lipids), promotes Na^+ binding, resulting in a higher number of adsorbed cations in these systems. In contrast, Cl^- adsorbs only to zwitterionic lipids and thus shows minimal variation across the bilayers. The absence of negative charges in pure zwitterionic bilayers slightly favors anion adsorption. To investigate the role of these ions in 4HB adsorption, we calculated their running coordination numbers (RCNs) near the phosphate headgroups (using the P atom as a reference), both in the presence and absence of the tetramer (Figure 5.7). Adsorption of the 4HB displaces some of these ions from the membrane surface. In anionic membranes, the RCN of Na^+ decreases sharply upon fibril binding, indicating cation displacement. In contrast, the RCN of Na^+ remains unchanged in zwitterionic membranes, which inherently have fewer Na^+ ions adsorbed. Similarly, for pure zwitterionic bilayers,

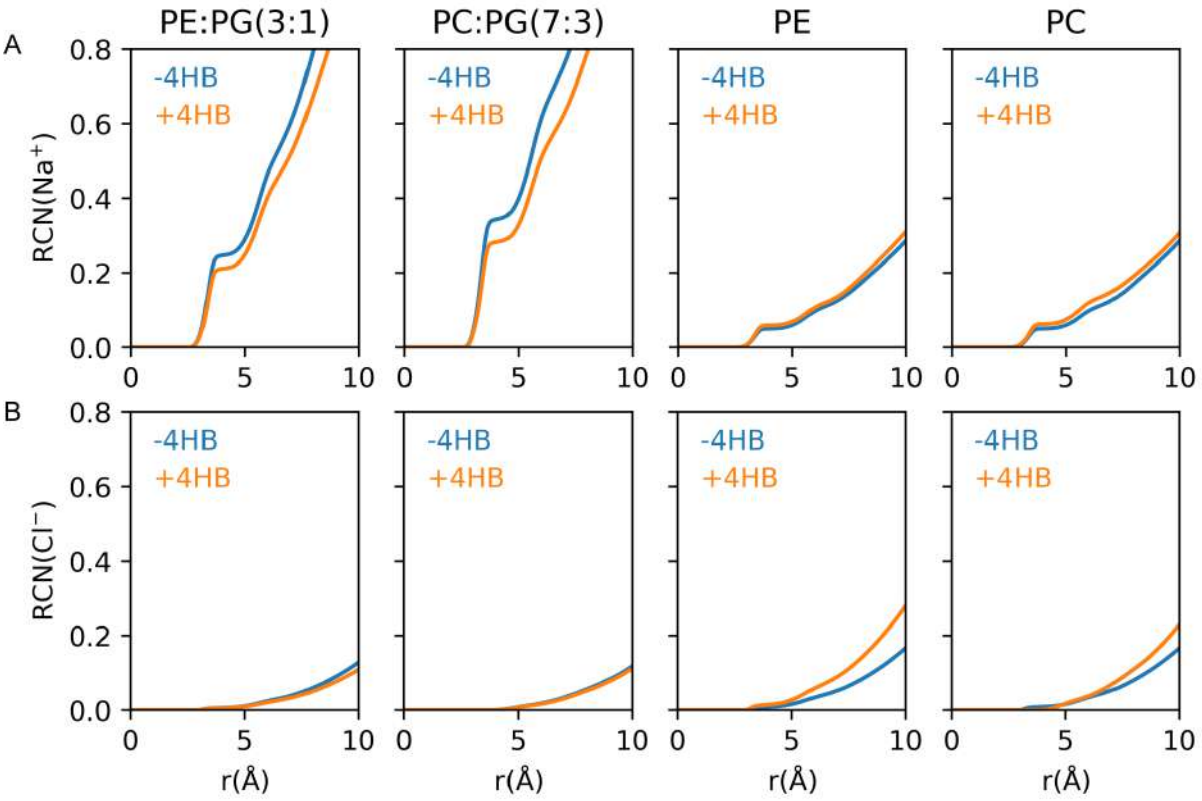

FIGURE 5.7: **Role of counterions in 4HB adsorption:** The running coordination numbers of (A) Na^+ and (B) Cl^- ions as a function of distance from the bilayer surface. The RCN is shown in the presence (+) and absence (−) of 4HB. Ion distances (r) are calculated from the phosphorus (P) atoms of the lipid headgroups.

the number of Cl^- ions decreases upon 4HB adsorption. This effect is more pronounced in PE bilayers, as PC bilayers adsorb fewer Cl^- ions due to the bulky size of the headgroups. These findings highlight the contrasting roles of Na^+ and Cl^- in modulating 4HB adsorption, depending on the nature of the bilayer. Displacement of surface-bound ions helps compensate for the entropy loss associated with 4HB adsorption, thereby making the process thermodynamically favorable.

5.3.4 Changes in the 4HB structure during membrane adsorption

The adsorption of β-amyloids to model membranes can have contrasting effects on the structure of these aggregates. In some cases, adsorption entails a loss in β-sheet content,

while in other cases it reinforces the secondary structure of the peptides [344, 353]. To check if the tetramer retains its cross-α amyloid structure during membrane adsorption, we investigated the changes in peptide structure and the internal ordering among them using: (a) the root-mean-square deviation (RMSD) of the peptide backbone (N, C, O, C_α), and (b) the polar and nematic order parameters.

The deviation in the backbone atoms from the crystal structure of the hLL-37_{17-29} tetramer over time is plotted in Figure C.1(A) (Appendix C). The constituent peptides preserve their structure upon attaching to the membrane surface, with an average RMSD of 1.5 Å. In rare cases, minor deviations from the crystal structure are observed (Traj-3 in PC, Traj-1 and 2 in PE:PG). The invariance of the peptide RMSDs is also reflected in the total helical content of 4HB (79.81±0.06% in PE:PG, 79.76±0.13% in PC:PG, 79.86±0.04% in PE, and 79.84±0.04% in PC). The total helical content in the crystal structure is close to 85%. Except for the residues at the termini, the helical propensity of the rest remains unchanged. This finding correlates with experimental observations of the full-length LL-37 peptide in the presence of membranes, where NMR measurements suggested that membranes enhance the helical structure of these peptides.

The internal ordering among the peptides is quantified by the polar and nematic order parameters. The hLL-37_{17-29} tetramer lacks a unidirectional arrangement of peptides (P1 = 0), where the individual helices are aligned at an angle (38°) to the principal axis (P2 = 0.5). A sharp distribution of P1 and P2 around values close to the crystal arrangement suggests that internal ordering is preserved (Figure C.1(B), Appendix C). The presence of satellite peaks for both P1 and P2 indicates dynamic fluctuations among the peptides in the tetramer, which is expected due to the fluid-like hydrophobic core that holds the peptides together.

To check the shape of the surface-bound 4HB, we calculated the distribution in the lengths of the long and short axes sampled during simulations (Figure 5.8). The lengths of the long and short axes in the crystal structure of 4HB are 25 Å and 23 Å, respectively. The surface-bound tetramers deviate from the crystal structure, with shortening of both axes. The mean length of the short axis shifts to 19.2 Å, and that of the long axis shifts to

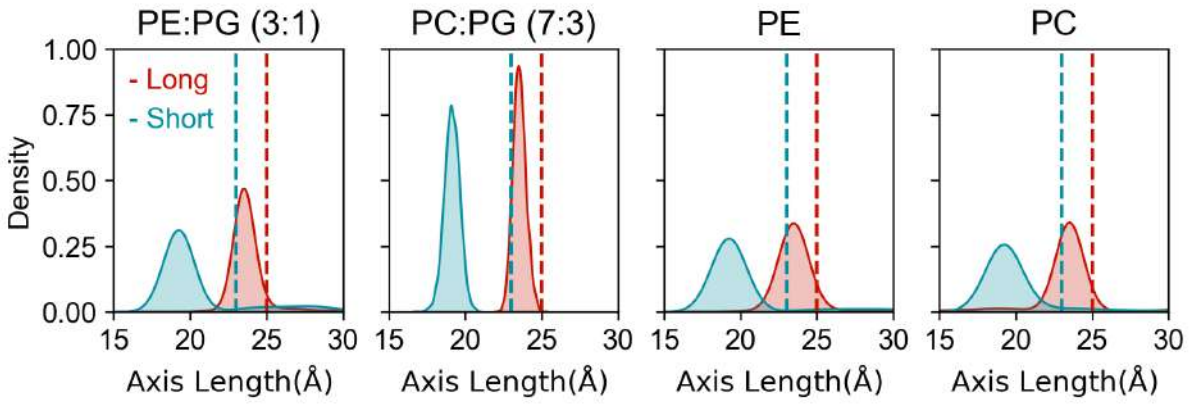

FIGURE 5.8: **Changes in the 4HB structure during bilayer adsorption:** Distributions of the long and short axis lengths of the 4HB tetramer sampled during simulations. The dotted lines indicate the corresponding axis lengths in the crystal structure (23 Å for the short axis and 25 Å for the long axis).

23.6 Å. The decrease in the length of the short axis is greater (3.8 Å) than that of the long axis (1.4 Å), indicating compression along this direction, consistent with 4HB adopting a more linear, rod-like shape. The decrease along the long axis suggests that membrane adsorption simultaneously increases the compactness of 4HB. The axes sample a sharp distribution in the presence of PC:PG, but broad distributions in the other membranes. This indicates dynamic motions within the peptides while bound to these membranes, which cease to exist in the presence of PC:PG.

5.3.5 Changes in the membrane during 4HB adsorption

Membranes interacting with AMPs often exhibit changes in curvature and lipid organization within the bilayer [74]. To investigate how pre-formed hLL-$37_{17\text{-}29}$ fibrils influence membrane properties, we compared these features in the presence and absence of 4HB. Figure 5.9 shows the curvature induced by the hLL-$37_{17\text{-}29}$ fibril across all membrane systems. In general, anionic membranes exhibit higher curvature than their zwitterionic counterparts. Among them, the PE:PG bilayer experiences the maximum curvature strain, followed by PC:PG. This increased curvature arises from the anionic PG component, which forms strong electrostatic interactions with the tetramer. In zwitterionic membranes, curvature is more pronounced in the PE bilayer than in PC, indicating

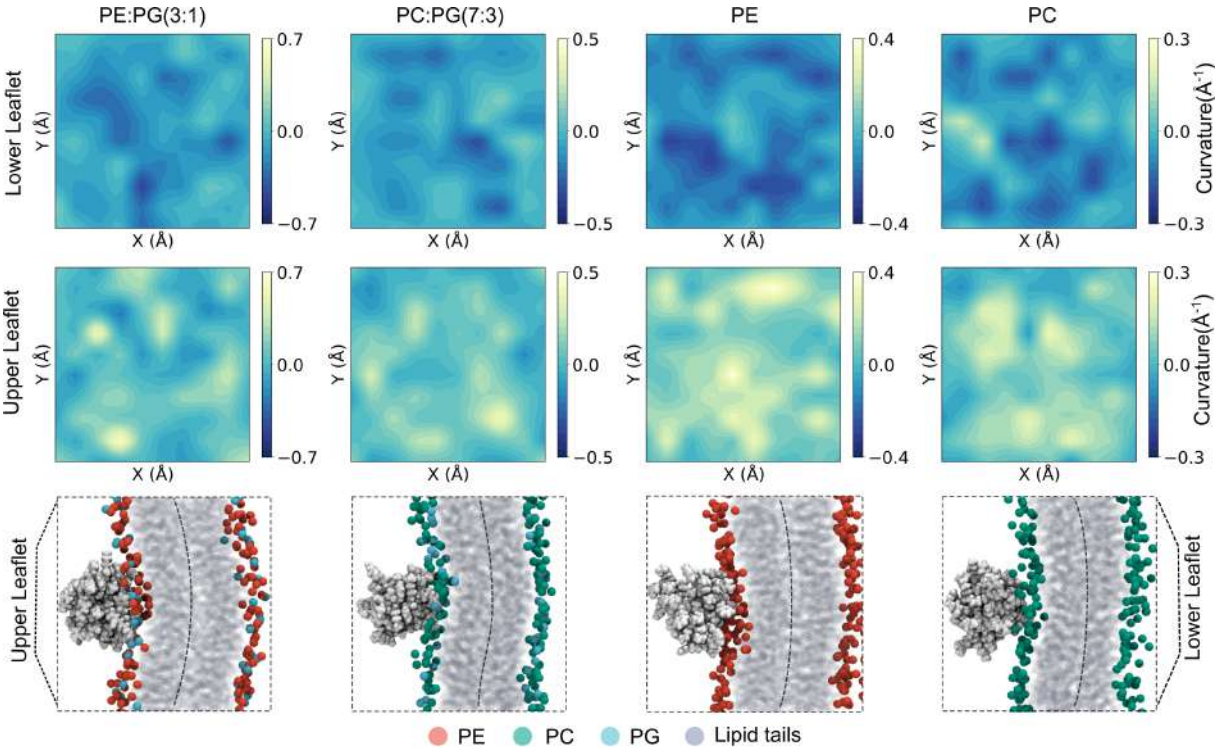

FIGURE 5.9: **Changes in the bilayer curvature during 4HB adsorption:** Mean curvature of the upper and lower leaflets of the bilayer during 4HB adsorption. In all systems, 4HB adsorbs onto the upper leaflet. Positive curvature indicates convex regions, while negative curvature indicates concave regions. The bottom panel shows snapshots of the curvature strain induced across the bilayers in the presence of 4HB.

weaker interactions in the latter due to its bulkier headgroups. Across all bilayers, the leaflet interacting with the fibril exhibits positive curvature, indicating convex regions or valleys, while the opposing leaflet displays negative curvature, indicating concave regions or peaks. The curvature appears more localized in anionic membranes, creating a rough surface, whereas it is more uniformly distributed in zwitterionic membranes.

This raised the question of whether the observed curvature is a direct consequence of tetramer interaction or an intrinsic property of the bilayers. To examine this, we also analyzed membrane curvature in the absence of the fibril. All bilayer systems exhibit some intrinsic curvature (Figure C.2, Appendix C), with anionic membranes again showing higher curvature than zwitterionic ones. However, their curvature is notably lower in the absence of the fibril. In contrast, the curvature of zwitterionic bilayers remains largely unchanged with or without the fibril. Thus, binding of the hLL-$37_{17\text{-}29}$ tetramer selectively enhances curvature in bacterial (anionic) membranes while having minimal effect

on zwitterionic membranes. As discussed in Section 5.3.3, the gain in entropy from the release of counterions drives the initial electrostatic attraction of 4HB to the membrane surface. This ion release is greatest when the stabilizing contacts between the cationic surface residues of 4HB and the anionic or polar headgroups of the bilayer are maximized. Consequently, the membrane tends to wrap around the 4HB, generating a positive mean curvature [391].

Next, we investigated the ordering of acyl chains within the bilayer using the order parameter S_{CD}. This parameter ranges from -0.5 to 1, where -0.5 indicates a parallel and 1.0 a perpendicular orientation of the acyl chains relative to the bilayer normal. We evaluated S_{CD} separately for the sn-1-palmitoyl (PA) and sn-2-oleoyl (OL) chains associated with each lipid type (PE, PC, and PG). Typically, these acyl chains show S_{CD} values between 0 and 0.25, suggesting they are tilted at an angle of approximately 45° to the bilayer normal-characteristic of a fluid membrane. Additionally, S_{CD} decreases along the acyl chain toward the bilayer interior, indicating that the -C-H vectors tend to become more parallel to the bilayer plane in this region.

With this in mind, we compared the S_{CD} values in the presence and absence of 4HB. Figure C.3 and Figure C.4 (Appendix C) shows the variation of S_{CD} with carbon number, where lower numbers correspond to carbon atoms closer to the headgroup. Across the bilayers, lipid order remains largely unaffected by the presence of 4HB, with only minor changes observed in anionic membranes. In these cases, a slight reduction in the order parameter is limited to the PG lipid acyl chains-affecting either the sn-2-oleoyl chain (as in PE:PG) or both chains (as in PC:PG). This decrease is mostly localized near the bilayer surface and diminishes in the interior. As noted in Equation 5.2, the angular brackets denote averaging over the entire lipid ensemble, which may mask structural changes occurring in lipids near the 4HB. To address this, we calculated the S_{CD} for lipid chains within 10 Å of 4HB. Figure 5.10 and Figure 5.11 compares their S_{CD} values with those in the equilibrated membrane, in the absence of 4HB. Overall, lipids in close proximity to the tetramer exhibit increased ordering in their acyl chains, especially in the sn-2-oleoyl chain. The greatest increase is observed in the unsaturated region of the oleoyl chain, around carbon atoms C9–C10. Furthermore, this increase in order is more pronounced in

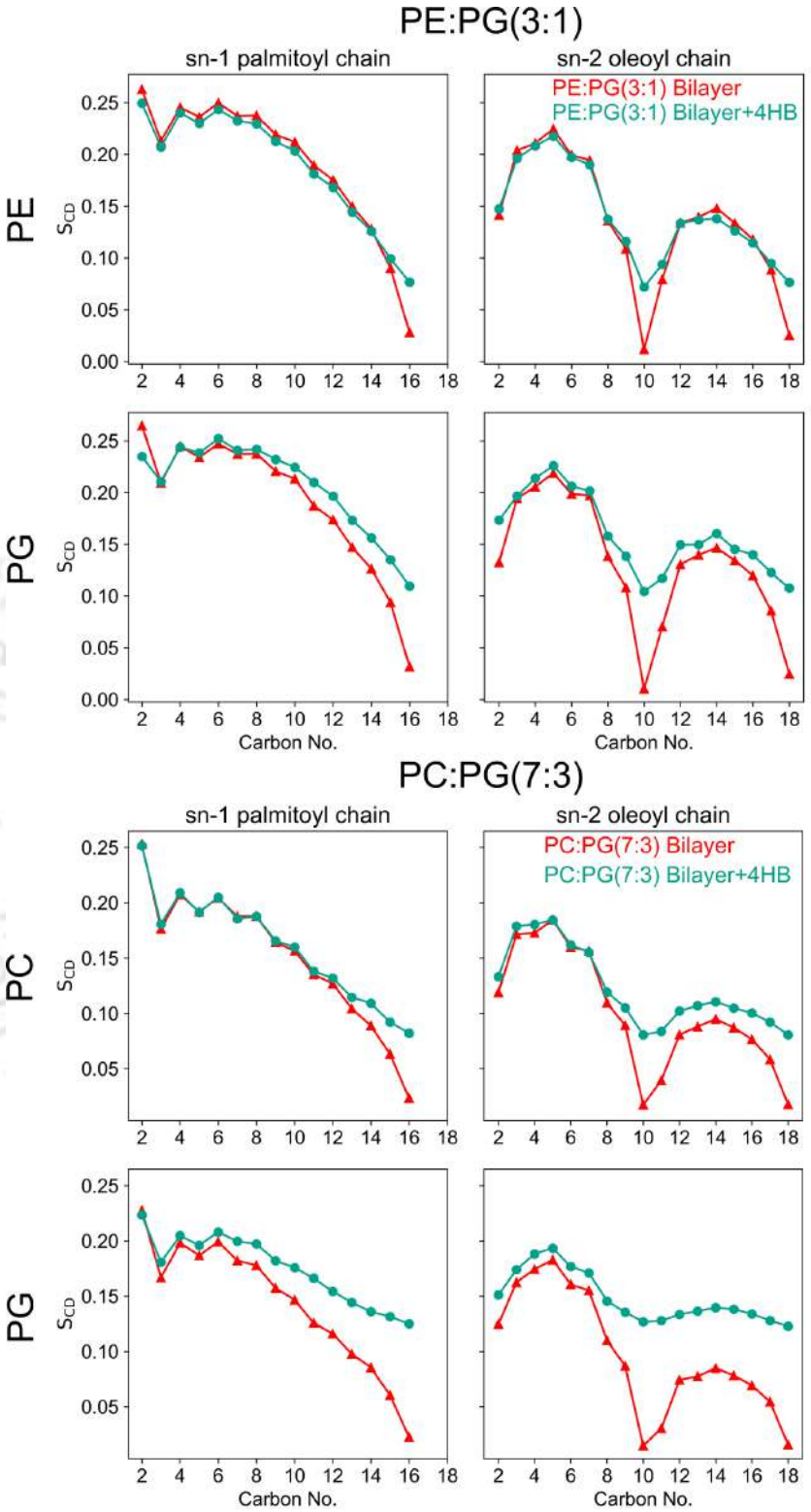

FIGURE 5.10: **Changes in lipid order during 4HB adsorption on anionic membranes:** Order parameters of the sn-1 palmitoyl chain (left) and sn-2 oleoyl chain (right) are shown for the zwitterionic components (PE/PC) and the anionic PG in the two heterogeneous bilayers, PE:PG (3:1) and PC:PG (7:3). Order parameters were calculated in the absence and presence of 4HB. Only lipids within 10 Å from 4HB are considered here.

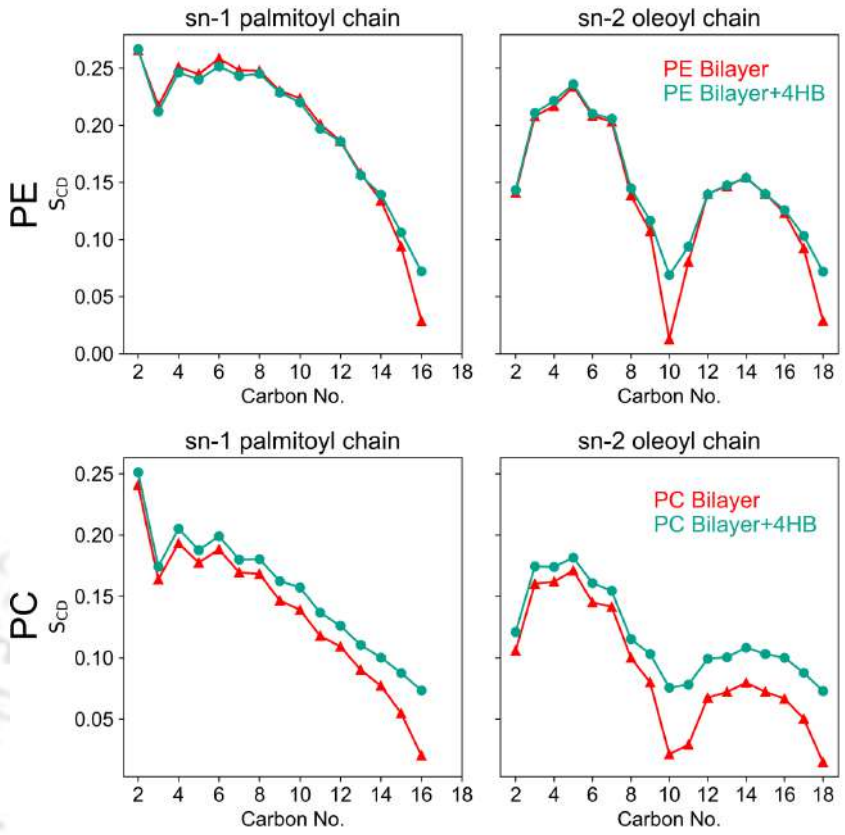

FIGURE 5.11: **Changes in lipid order during 4HB adsorption on zwitterionic membranes:** Order parameters of the sn-1 palmitoyl chain (left) and sn-2 oleoyl chain (right) are shown for the zwitterionic PE and PC bilayers. Order parameters were calculated in the absence and presence of 4HB. Only lipids within 10 Å from 4HB are considered here.

the bilayer interior than near the surface. Among the two lipid types, negatively charged PG lipids are more strongly affected than their zwitterionic counterparts in the mixed membranes (PE:PG and PC:PG) (Figure 5.10). Among the pure zwitterionic bilayers, PC chains are more ordered than PE chains (Figure 5.11). Notably, PG chains exhibit the highest degree of order among all lipid types. However, the neutral co-component also influences this ordering. Specifically, PC lipids-being more ordered than PE-enhance the order of adjacent PG lipids almost synergistically. If PG alone dictated the increase in ordering, we would expect similar changes in PE:PG membranes, which is not the case. As discussed in Figure 5.6, the 4HB sits atop the membrane surface with a few residues intercalated into the interface between lipid headgroups and tails. This mode of adsorption locally enhances lipid ordering, promoting a transition toward the gel phase by

increasing the lipid melting temperature (T_m), as previously reported for the full-length LL-37 peptide [392].

5.3.6 Free energy of membrane invasion of 4HB

The potential of mean force (PMF) for 4HB membrane invasion was examined in three of the four membrane systems. These membranes represent either bacterial (PE:PG or PC:PG) or mammalian (pure PC) compositions. The goal was to assess the therapeutic potential of 4HB aggregates. To evaluate the energy barrier to invasion, SMD simulations were initiated with 4HB adsorbed at the bilayer–water interface. All three membranes

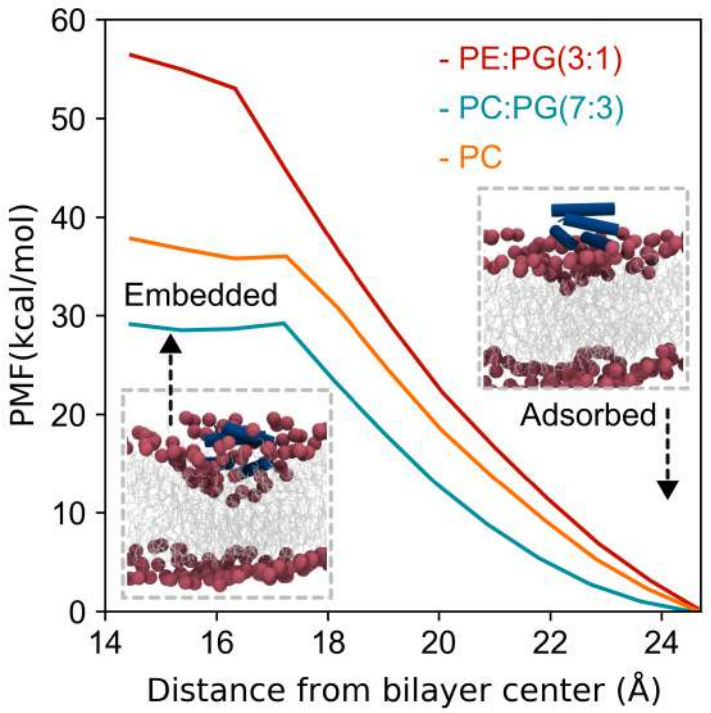

FIGURE 5.12: **Free energy of membrane invasion of 4HB:** The potential of mean force (PMF) for the transfer of 4HB into the bilayer interior from the bilayer-water interface. The PMF profiles are evaluated for the two anionic (bacterial) membranes, namely PE:PG, PC:PG and the zwitterionic (mammalian) PC membrane.

resisted penetration into the bilayer interior, but to different extent (Figure 5.12). The PMF profile rises sharply as 4HB penetrates into the bilayer core and then plateaus around 17 Å. The highest barrier was observed for the PE:PG system (≈53 kcal/mol), followed

by pure PC (≈38 kcal/mol) and then PC:PG (≈29 kcal/mol). The penetration barrier is correlated to the membrane thickness, with PE:PG being the thickest (41.21±0.52 Å) among the three. Though PC:PG (37.96±0.45 Å) and PC (37.30pm0.43 Å) bilayers have comparable thickness, the presence of the anionic PG lipids make the invasion fascile in the former. Among the two bacterial membranes, PE:PG-mimicking Gram-negative bacteria-offered the strongest resistance to 4HB entry. In a previous study, Engelberg et al. had shown that hLL-$37_{17\text{-}29}$ aggregates are active against Gram-positive bacteria [205]. Here, we observed unfavorable invasion into the Gram-negative membrane, which may indicate selective activity. In contrast, the PC:PG membrane, differing only in the headgroup of its zwitterionic component, provided the least resistance, suggesting that 4HB can translocate more easily and may therefore have therapeutic applications. For the pure PC membrane, an intermediate barrier was observed which hint at potential cytotoxic effects of 4HB.

Another possible role for 4HB aggregates is as membrane sensors. In Section 5.3.5, we showed that 4HB binds strongly to PE:PG membranes, which have higher intrinsic curvature, and that binding further increases this curvature. Consistent with this, we now observe a very high energy barrier to invasion in this system. These findings align with the model proposed by van Hilten et al. [393], which suggests that binding and sensing lie on a continuum, where strong binders tend to be poor sensors and vice versa. The exceptionally high barrier of 4HB towards PE:PG makes it a poor binder and could therefore be leveraged for sensing Gram-negative bacteria. In summary, 4HB exhibits distinct membrane invasion tendencies, leading to different functional outcomes depending on membrane composition.

5.3.7 Is it possible to self-assemble 4HBs near bacterial membranes?

From the preceding sections, we uncovered the sensing, cytotoxic, and antibacterial properties of the hLL-$37_{17\text{-}29}$ 4HB. In particular, the sensing and antibacterial effects of the 4HB raise the question of whether this self-assembly can be generated *in situ*, at the site of

infection. Previous work by Engelberg et al. [205] suggested that the peptide's antibacterial activity is linked to its aggregation tendency but did not clarify the sequence of events leading to membrane disruption. Here, we investigate whether aggregation precedes membrane binding-a possibility that could address both questions, but is difficult to capture experimentally. To this end, we monitored how 4 hLL-$37_{17\text{-}29}$ peptides, initially separated (≈20 Å), aggregate in the presence of the anionic (bacterial) membranes. Since peptide aggregation is a stochastic event, we spawned multiple trajectories starting from different initial configurations to test the consistency of the results. Figure 5.13 shows the time evolution of the oligomers, superposed with the total number of peptide-lipid contacts, quantifying the peptide-lipid interactions during aggregation. In most trajectories, the peptides oligomerize into lower-order aggregates (dimers and trimers) even before establishing contact with the lipid headgroups. However, in a few trajectories (Traj-1 in PE:PG and Traj-2 in PC:PG), the oligomer growth occurs after the peptides have adsorbed on the membrane. This indicates that aggregation generally occurs in the aqueous layer and rarely on the membrane surface. The highest tetrameric state was achieved in 3 trials (Traj-1, Traj-2 of PE:PG and Traj-1 of PC:PG bilayers), out of which two dissociated as the simulation continued. Though aggregation is favored, these incipient tetramers are generally unstable in the presence of the membrane. Among the two bilayers, PE:PG favours the trimers (and rarely tetramers), while the PC:PG favours dimers and prevents further growth. Across all systems, the number of peptide-lipid contacts increases with time as the oligomers embed on the membrane surface, except in cases where the oligomers break down. The breakdown event is reflected in the sharp decrease in peptide-lipid contacts, which increases again as the fragments embed on the membrane separately. If we recall our previous study [146], the hLL-$37_{17\text{-}29}$ peptides aggregate in the absence of a membrane via two pathways. The major pathway (70.1%) follows the sequence: [1,1,2] → [1,3] → [4], whereas the minor pathway (25.2%) follows the sequence: [1,1,2] → [2,2] → [4]. A pattern emerges where the PE:PG bilayer appears to hack into pathway-1 and stops oligomer growth beyond trimers. Conversely, the PC:PG bilayer either arrests the oligomerization at the [1,1,2] state or proceeds one step further into pathway 2, preventing further growth of the dimer pair. This is verified from the smallest oligomer size in

the systems (Figure C.5(A)), Appendix C) either a monomer (in the former case) or a dimer (in the latter). Extension of the simulations for another 200 ns failed to change the oligomer size in either of the bilayers (Figure C.5(B), Appendix C). From our observations, it is evident that the membrane environment influences the incomplete aggregation among the peptides. However, our previous studies show that the tetramers form rapidly and remain stable in solution. Since the antimicrobial activity is linked to the extent of aggregation, we may conclude that aggregation precedes membrane disruption.

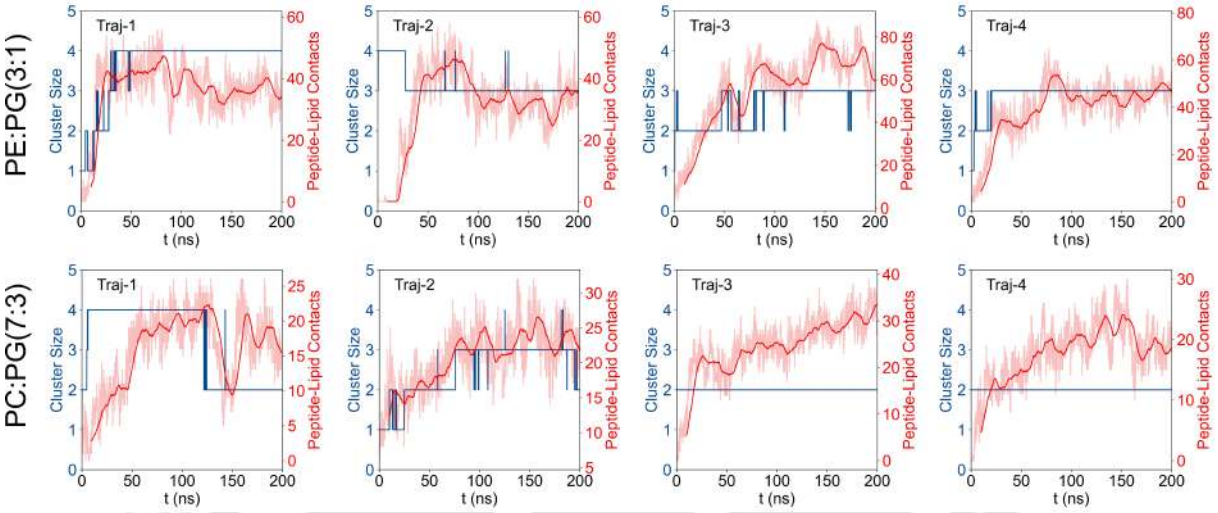

FIGURE 5.13: **Self assembly of hLL-37$_{17\text{-}29}$ in the presence of anionic (bacterial) membranes:** Time evolution of peptide clusters on the membrane surface. Clusters were identified by a nearest-neighbor approach. The number of peptide-lipid contacts have been plotted alongside to track membrane interactions during self-assembly.

5.4 Conclusion

In this chapter, we study the interaction of a pre-formed 4-helix bundle (4HB), composed of the core segment (17–29) of the human LL-37 peptide (hLL-37$_{17\text{-}29}$), with model membranes. The 4HB has a distinct cross-α amyloid architecture, representing a new type of self-assembled structure in nature. We investigate how 4HB interacts with membranes of different compositions, using four model systems: two anionic (PE:PG (3:1) and PC:PG (7:3)) and two zwitterionic (PC and PE). Our study examines the mode of

4HB–membrane interaction, the structural changes in 4HB and bilayers during these interactions, and the thermodynamic basis of binding. We also calculate the potential of mean force (PMF) for 4HB transfer from the bilayer–water interface into the bilayer core for the two anionic membranes and the zwitterionic PC bilayer. In addition, we explore whether these 4HBs can form in the presence of anionic membranes. The 4HBs adsorb onto the bilayer surface in a face-down orientation that maximizes interactions with lipid headgroups. These interactions are primarily electrostatic, with surface residues of 4HB forming salt bridges with charged headgroups. Binding is stronger with anionic membranes than with neutral ones because of the presence of PG lipids. Among the zwitterionic membranes, binding is favored to PE over PC due to the smaller headgroup of PE, which facilitates closer contact and enhances interactions with PG lipids in a synergistic manner. Adsorption occurs mainly on the membrane surface, where positively charged residues penetrate the interfacial zone between lipid headgroups and tails. Among these residues, Arg side chains intercalate more effectively than Lys. Although surface adsorption reduces translational entropy, the release of bound ions upon 4HB binding makes the process thermodynamically favorable. The displaced ions depend on bilayer composition: Na^+ ions in anionic bilayers and Cl^- ions in neutral membranes.

Adsorption alters both the 4HB and membrane structure. For 4HBs, while the secondary structure of individual peptides and their internal arrangement remain intact, the overall bundle becomes more elongated, showing unequal compression along its axes. For membranes, adsorption increases curvature, particularly in anionic bilayers. Lipids in the vicinity of 4HB also exhibit increased ordering, indicating a departure from the fluid phase. 4HBs encounter a steep energy barrier when moving from the interface into the bilayer interior. This barrier is highest in the PE:PG system, followed by PC and PC:PG. The high barrier suggests weak penetration into PE:PG membranes but possible toxicity toward PC and PC:PG bilayers. Taken together with the curvature effects, these results indicate that 4HB acts as a sensor of PE:PG membranes and as a disruptor of the other systems. Finally, we examined whether hLL-$37_{17\text{-}29}$ peptides can self-assemble into functional 4HBs in the presence of bacterial membranes. Simulations show that aggregation generally begins in the aqueous phase, and contact with the bilayer surface

inhibits further oligomer growth. Tetramers, essential for antibacterial function, were rarely formed and remained unstable near the membrane. PE:PG bilayers favored trimer formation, whereas PC:PG promoted dimers and hindered further assembly. Compared to solution-phase behavior, where tetramers readily form, the membrane environment slows or redirects aggregation pathways. These findings suggest that 4HB assembly occurs predominantly before membrane interaction, establishing a mechanistic sequence critical for the peptide's antibacterial activity.

Chapter 6

Effect of Point Mutations on the Aggregation Tendency of the Antimicrobial Fragment Peptide hLL-$37_{17\text{-}29}$

Overview

The aggregation of host defense peptides has been directly linked to their membranolytic property. An instance of such aggregation-induced cell lysis is observed in the hLL-$37_{17\text{-}29}$ peptide. Mutational studies, particularly at the Ile24 position, leads to reduced antimicrobial potency; however, direct evidence linking these mutations to altered aggregation propensities remains absent. Here, we perform all-atom molecular dynamics simulations under NPT conditions to study the aggregation behavior of the wild-type (WT) peptide and five I24 mutants with hydrophobic (I24A), charged (I24D, I24K), or polar (I24Q, I24S) substitutions. All systems exhibit rapid formation of small oligomers through hydrophobic collapse, followed by a biphasic aggregation process: an initial growth phase and a lag phase of structural reorganization. I24D and I24Q emerge as strongly aggregation-prone, I24K is aggregation-resistant, and others show intermediate behavior. Transition network analysis reveals mutation-specific aggregation pathways that deviate from the dominant WT routes. Secondary structure analysis shows that mutations destabilize the amphipathic α-helix, especially in charged variants, with helix unfolding localized near the termini. Aggregate morphology remains predominantly fibrillar across systems, though internal order and packing specificity vary. Energetically, aggregation is driven by a balance between electrostatic and van der Waals forces, with mutation-dependent preferences. Preferential interaction parameters and hydrogen-bonding analyses highlight the competition between peptide–peptide and peptide–water interactions in controlling aggregation. I24K exhibits strong solvation and minimal aggregation, whereas I24D forms hydrated yet highly aggregated clusters. These results underscore the nuanced interplay between sequence, structure, solvation, and aggregation in antimicrobial peptides, offering insights for rational design of peptide-based materials and therapeutics.

6.1 Introduction

Aggregation between antimicrobial peptides (AMPs) plays a vital role in their bioactivity and can be used to create biomaterials of medicinal importance [394]. These peptides are intrinsic components of the host immune system and provide the first line of defense against invading pathogens [296]. Due to their structural diversity and potency, AMPs have emerged as promising alternatives to conventional antibiotics, with several currently undergoing clinical trials [395, 396]. Such alternative treatments are becoming increasingly vital, as the World Health Organization (WHO) reported 1.27 million deaths related to antimicrobial resistance in 2019, making it the third leading cause of morbidity worldwide [5].

Although most studies focus on the antimicrobial effects of monomeric AMPs, their aggregates often provide significant advantages. However, the evidence on the role of aggregation in antimicrobial activity is mixed. For example, self-assembly in certain AMPs enhanced their antimicrobial property [339, 397–402], often improving their selectivity toward bacteria [403] or yeast cells [404]. Here, the mechanism of membrane disruption shares similarities with electroporation [405, 406] where the electric field induced by the aggregates perturbs the integrity of the membrane, leading to pore formation. The electric field arises from the positive charges on the peptide surface, which promote binding to the negatively charged bacterial membranes [407–410]. Moreover, the loss of translational entropy associated with binding to the membrane is lower for larger aggregates, which increases aggregation in these peptides [388, 389].

In contrast, multiple studies suggest that aggregation in AMPs inhibits their antimicrobial activity [337, 411]. The loss in antimicrobial property stems from the increased peptide-peptide interactions that increase the free energy barrier for membrane insertion [412]. In addition to binding, aggregation also reduces the ion transport capability of certain AMPs [413].

Beyond antimicrobial activity, self-assembly among AMPs can also be used to develop biomaterials for drug delivery and regenerative medicine [414, 415]. The self-assembly

is reversible, driven primarily by non-covalent interactions, leading to supramolecular structures of different morphologies [308, 416, 417]. In addition to their biocompatibility, these structures have a long shelf-life and are protected from proteolytic degradation [418]. The architecture in these structures ranges from nanoparticles [419, 420], nanofibrils [171, 295, 421], nanotubes [422], among others. The bacterial selectivity of these biomaterials depends on the extent of packing and the storage modulus [423, 424]. Notably, some AMPs can also self-assemble into hydrogels, which are influenced by the pH of the medium [425–429]. Often, the self-assembly is impeded due to the high positive charge density on these peptides, but can be improved by chemical modification of the constituent amino acids [430, 431]. Additionally, self-assembly might improve condensation and release of AMPs from the pores of mesoporous carriers with potential applications in drug delivery [432]. To take advantage of these materials, it is essential to understand the physicochemical factors that govern the self-assembly in AMPs. Self-assembly

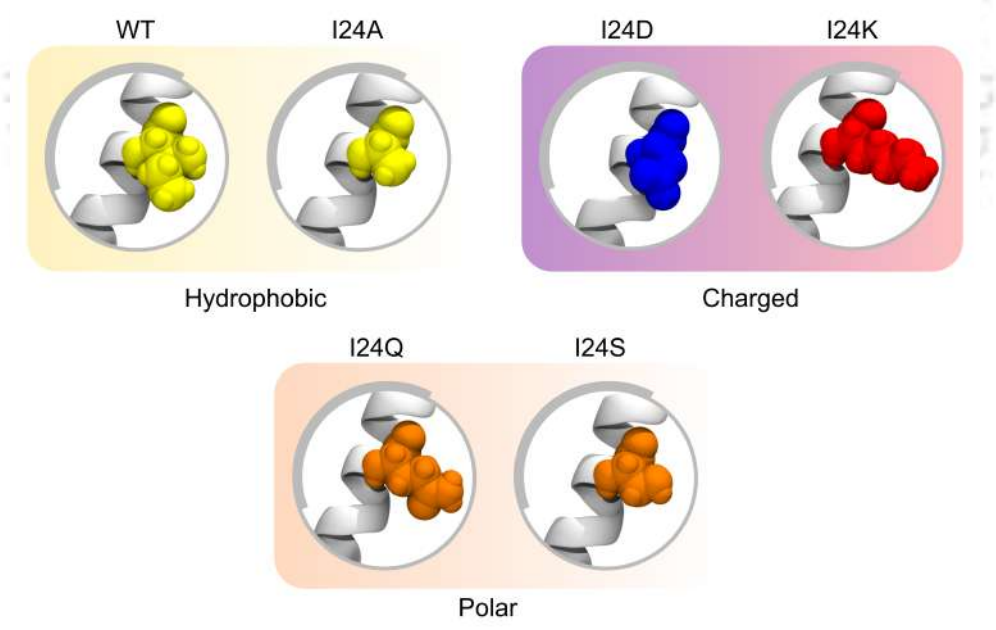

FIGURE 6.1: **Mutant peptides to study the sequence-aggregation relationship in hLL-$37_{17\text{-}29}$ peptides**: van der Waals representation of the mutated residue at position 24 of hLL-$37_{17\text{-}29}$. Mutated residues are (i) hydrophobic (yellow), (ii) cationic (red), (iii) anionic (blue), or (iv) polar which leads to differences in net charge, hydrophobicity and the Arg/Lys ratio of the peptides as elaborated in Table 6.1.

among AMPs depends on multiple factors, including peptide length, charge, concentration, secondary structure, hydrophobicity, hydrophilicity, identity of the charged residues,

TABLE 6.1: Physicochemical properties of the peptides used in Chapter 6

Peptide	Sequence	Hydrophobicity[a]	Charge[b]	R/K ratio[c]
WT	FKRIVQRIKDFLR	-0.44	+4	1.5
I24A	FKRIVQR**A**KDFLR	-0.65	+4	1.5
I24D	FKRIVQR**D**KDFLR	-1.05	+3	1.5
I24K	FKRIVQR**K**KDFLR	-1.08	+5	1
I24Q	FKRIVQR**Q**KDFLR	-1.05	+4	1.5
I24S	FKRIVQR**S**KDFLR	-0.85	+4	1.5

[a]Kyte-Dolitte hydrophobicity index
[b]`PROPKA` assigned charges
[c]Arg/Lys ratio

etc. [394, 417, 433, 434] Among these, the interplay between hydrophobic and hydrophilic forces is of particular relevance as it governs the aggregation state and the selectivity of AMPs to bacterial cells [403, 411, 435]. The peptide secondary structure also plays a key role as random coil conformations give rise to non-specific interactions forming loose aggregates [436]. Another factor is the overall charge of the peptide, where a decrease in positive charge leads to amyloid deposits with loss in antimicrobial property [337]. Besides, peptide aggregation is a cooperative process where the surrounding water molecules exert a substantial influence [437].

This Chapter explores how these factors collectively affect the aggregation of the antimicrobial fragment peptide hLL-$37_{17\text{-}29}$, derived from the full-length LL-37 peptide. Our previous study addressed how this peptide aggregates from a dispersed state using semi-empirical Markov state models and the transition path theory [146]. In addition to pathways, we have also highlighted the importance of the central Ile24 in the aggregation process. Here, we selectively mutate Ile24 to generate mutants varying in their overall charge, hydrophobicity, and hydrophilicity as illustrated in Figure 6.1. Specifically, we

substituted Ile24 with one hydrophobic (Ala), two charged (Lys and Asp), and two polar residues (Gln and Ser), each chosen for their differences in the hydrophobic length, the nature of charge, and the number of hydrogen bonding sites in their side chains (Table 6.1). These mutants were carefully selected based on a previous work, where they showed reduced antimicrobial property (MIC$\geq$100 μM) than the WT [205]. Through molecular simulations, we resolve the sequence-aggregation relationship in the hLL-$37_{17\text{-}29}$ peptides by addressing the following questions:

1. How does sequence affect the aggregation tendency (kinetics, distribution, and pathways) among the WT hLL-$37_{17\text{-}29}$ and its mutants?
2. How do mutations affect the helical structure of the peptides during aggregation?
3. How do the resulting aggregates differ in shape and size?
4. What key interactions differentiate the aggregation tendency among these peptides?
5. What is the role of water molecules in this highly cooperative aggregation process?

We have generated μs-long molecular dynamics (MD) simulations of the WT and its mutants solvated in explicit water under ambient conditions (T = 300 K, P = 1 bar) to answer our queries. From the simulated data, we first identified oligomers among peptides based on a distance cutoff using a nearest-neighbor approach adopted previously. We then deduced the population of each oligomeric state, how they develop over time, and the pathways they adopt to transform from one state to another. Next, we detected changes in the secondary structure of the peptides during aggregation and figured out their unfolding patterns. For further structural insights, we also estimated the shape and compactness of the oligomeric species for the WT and mutant systems. Following structural nuances, we identified key hydrophobic and hydrophilic interactions that drive aggregation among the peptides and calculated the energy associated with these interactions. Finally, we explored the interactions between the peptides and water molecules and the energy of these interactions in this highly cooperative aggregation process. Our study provides molecular insights into the sequence-aggregation relationship in amphipathic AMPs, which

can be utilized to design synthetic peptides or biomaterials with enhanced antimicrobial properties.

We have organized the rest of the Chapter into the following four sections: In Section 6.2, we explain how the mutant peptides and the simulation systems were created from scratch and lay out the conditions and parameters of the MD simulations. In addition, we also provide the details of the analyses used in this study. In Section 6.3, we discuss the observations we collected from our analyses and relate them to previous literature. In Section 6.4, we summarize our findings and propose a unified explanation of the structure-aggregation relationship in the hLL-$37_{17\text{-}29}$ peptide.

6.2 Computational Details

6.2.1 Preparation of the Mutant Peptides

The coordinates of the WT hLL-$37_{17\text{-}29}$ monomer were extracted from the X-ray crystal structure of the peptide self-assembly reported in the Protein Data Bank (PDB ID: 6S6M) [205]. Based on this WT template, the mutant peptides were prepared in the `tleap` module of `AMBER20` [315]. Before loading the WT into `tleap`, the X-ray designated hydrogen atoms were removed using `pdb4amber`. For the mutants, the heavy atoms of the Ile24 residue were also removed, keeping only the backbone atoms intact. The hydrogen and heavy atoms (consistent with the mutated residue) were reincorporated into the peptides based on the amino acid library maintained in `AMBER20`. The net charges on the peptides (Table 6.1) were calculated based on their protonation states at neutral pH, as predicted by `PROPKA` [217, 218]. The termini were capped with acetyl (ACE for N-terminal) and N-methyl (NME for C-terminal) groups to prevent spurious charged interactions among them [365]. The peptide parameters (charges, bonding, and non-bonding) were assigned from the `AMBERFF14SB` force field [219]. The `tleap`-generated structures were minimized `in vacuo` before using them for further system preparations.

TABLE 6.2: Details of the systems used in Chapter 6.

Peptide	N_p[a]	N_{Na^+}[b]	N_{Cl^-}[c]	**Time (ns)**
WT	8	40	72	3×1000
I24A	8	40	72	3×1000
I24D	8	40	64	3×1000
I24K	8	40	80	3×1000
I24Q	8	40	72	3×1000
I24S	8	40	72	3×1000

[a]Number of peptides
[b]Number of Na^+ ions
[c]Number of Cl^- ions

6.2.2 Preparation of the Solvated Systems

Separate systems were prepared for each peptide (WT and mutants) to study self-assembly among them. 8 copies of the peptide monomer were placed sufficiently apart (≈ 20 Å) in a cubic box using PACKMOL [221]. These dispersed systems were then solvated in `tleap` using a pre-equilibrated water box at 298 K with a padding of 12 Å to prevent peptides from interacting with their images. Roughly 15000 water molecules (≈ 1875 per peptide) were added per system. The water molecules were modelled using the rigid TIP3P force field [220]. An adequate number of Na^+ and Cl^- ions were added to ensure electroneutrality and mimic a physiological ionic strength of 0.15 M NaCl [222]. The ion parameters, compatible with TIP3P water, were obtained from the works of Joung and Cheatham [223]. Multiple copies of each system were prepared to check data reproducibility. The composition of the systems used in this study is tabulated in Table 6.2.

6.2.3 Simulations of Peptide Assembly

Systems were relaxed in two steps – steepest descent followed by conjugated gradient method – of 5000 cycles each [365, 438]. The CPU-based `SANDER` implementation of AMBER20 was used to minimize steric clashes between the peptides and the surroundings till the energy converged to a minimum ($\approx 10^{-5}$ kcal/mol). The minimized systems were then heated in increments of 50 K over 6 stages (25 ps each) and equilibrated at 300 K (for 1 ns) under NVT conditions [439]. To fix the box volume and eliminate void spaces, the systems were further equilibrated (4 ns) under NPT conditions. The final concentration of the peptides post-equilibration (box length≈78 Å) was around 0.03 (M). During equilibration, the peptides were held in place with harmonic positional restraints having a force constant of 10 kcal/(mol Å^2). Following this, the systems were simulated unrestrained under NPT conditions for 1 μs each. The μs-long trajectories were attained using the `PMEMD` module of AMBER20 running on NVIDIA A100 graphics units [228]. During production, the state of the system at time $t + \Delta t$ was determined from the coordinates at time t fed into a discrete-timestep leapfrog integrator [151]. The integration was performed every 2 fs (Δt) after restraining high-frequency motions of the covalently bonded H using the SHAKE algorithm [226]. The isothermal conditions were enforced using a Langevin thermostat with a collision frequency of 1 ps^{-1} [225]. A constant pressure of 1 bar was maintained using the Berendsen barostat with a coupling constant of 2 ps [224]. The short-range non-bonded interactions (vdW and electrostatic) were calculated using a spherical cutoff of 10 Å. The electrostatic component, in particular, was determined using the Particle Mesh Ewald (PME) summation method: the short-range component was calculated in the real space (with a spherical cutoff), and the long-range component was evaluated in the Fourier space with grids placed every 1 Å [227]. Periodicity of the cubic box was preserved along the three coordinate axes to remove surface effects during simulation [150]. The system coordinates were logged every 2000 steps (4 ps) during production for further analyses. Each system was simulated thrice, starting from different initial coordinates and velocities, to test the reproducibility of the results.

6.2.4 Analyses

Clusters among peptides were identified based on a distance cutoff of 4 Å using the nearest-neighbour algorithm discussed in Chapter 3 [146, 229]. The percentage abundance of the oligomers was calculated based on:

$$P(n) = \frac{\langle N(n,t) \rangle}{\sum_{n} \langle N(n,t) \rangle} \times 100 \tag{6.1}$$

where $N(n,t)$ denotes the number of oligomers of size n at time t and the angular brackets denote time and ensemble averages. The oligomeric states computed in each frame discretize the continuous MD trajectories into temporal transitions between the 8 oligomeric states. These transitions were captured in an 8×8 matrix, where the rows and columns enumerate the aggregate size of the peptides. The element (i, j) in this transition matrix represents the total number of transitions from state i to state j, pooled over multiple simulation repeats of each system (Figure D.1, Appendix D). This matrix was used to construct the coarse-grained transition networks using the NetworkX library in Python 3 [440, 441]. Only the upper diagonal elements (oligomer growth events) were used to construct transition networks. The node sizes and the edge weights were normalized relative to the highest populated state and the highest frequency transitions, respectively. The secondary structure of the peptides was determined using the Dictionary of Secondary Structure Prediction (DSSP) algorithm proposed by Kabsch et al [324].

The compactness of each oligomer was quantified based on Equation 4.2. The polar (P1) order parameter of the aggregates were evaluated according to Equation 4.3 in Chapter 4.3. Contacts between the residues of a peptide pair were based on a similar 4 Å cutoff distance. All possible peptide pairs within each oligomer were checked for contacts, with each successful contact assigned a value of 1 and the absence of contact assigned 0. The contact information was recorded in a matrix where the rows and columns represent the residues in the peptides. The final contact maps were normalized by the total number of pairwise interactions and represented as heatmaps using the Seaborn library of Python

3 [441]. Hydrogen bonds were identified based on geometric criteria established in previous studies [442–444]. These bonds were broadly categorized according to the interacting partners: peptide–peptide (PP) and peptide–water (PW). The peptide–peptide hydrogen bonds were further divided into intra-peptide and inter-peptide. The dehydration behavior of the peptides was measured in terms of r_d, defined as[445]:

$$r_d = \frac{n_{HB}^{PP}(\text{intra})}{n_{HB}^{PP}(\text{intra}) + n_{HB}^{PP}(\text{inter}) + n_{HB}^{PW}} \tag{6.2}$$

To explore the aggregation landscape, the number of hydrophobic contacts ($n_{\text{HC}}^{\text{PP}}$) and inter-peptide hydrogen bonds ($n_{\text{HB}}^{\text{PP}}$) were jointly projected onto a free energy surface (FES). The free energy (ΔG_i) for each state i was calculated following[378, 446]:

$$\Delta G_i = -k_{\text{B}} T \ln\left(\frac{P_i}{P_{max}}\right) \tag{6.3}$$

where P_i/P_{max} is the probability distribution ratio of state i relative to the maximum populated state, and k_{B} and T represent the Boltzmann constant and temperature, respectively. The The non-bonded interaction energies (van der Waals and electrostatic) were calculated using NAMD Energy Plugin (Version 1.4) in VMD [325]. The total non-bonded energy was also classified as hydrophobic or hydrophilic depending on the residue types used for calculation - hydrophobic for residues Phe, Ile, Val, Leu, and hydrophilic for Lys, Arg, Gln, and Asp [445]. The aggregation propensity of the peptides relative to their interaction with water can be quantified using the preferential interaction parameter, τ_{PW}^{PP}, expressed as [447–449]:

$$\tau_{PW}^{PP} = \rho_P(G_{PP} - G_{PW}) \tag{6.4}$$

where G_{PP} and G_{PW} are the Kirkwood-Buff (KB) integrals derived from the radial distribution functions of a peptide around a reference peptide ($g_{PP}(r)$) and water around a reference peptide ($g_{PW}(r)$), respectively. The radial distances were calculated based on their center-of-mass coordinates.

6.3 Results and discussion

6.3.1 Mutations alter the kinetics and aggregation pathways in hLL-37$_{17\text{-}29}$ variants

We conducted NPT simulations (T=300 K, P=1 atm) of the WT and its mutants in explicit water to assess how point mutations affect their aggregation tendency. For consistency in our discussions, we have conserved the original residue numbering of the WT peptide as it appears in the core segment of the full-length human LL-37 peptide. Accordingly, the N-terminal Phe begins at 17, and the C-terminal Arg ends at 29. The mutants differ at residue 24, which is an Ile in the WT (Table 6.1).

Our results and discussions are organized into 4 main parts. The first part describes the kinetics of oligomer formation and the pathways via which these oligomers are formed. The second part focuses on the structural characteristics of the oligomers and the peptides constituting them. The third part examines the nature and strength of the peptide-peptide interactions. Finally, the fourth part explores the role of water in the aggregation process. During the simulations, the peptides aggregate into oligomers of various sizes, broadly categorized into three groups: (a) lower order oligomers - monomers, dimers, and trimers; (b) intermediate oligomers - tetramers and pentamers; and (c) higher order oligomers - hexamers and above.

To investigate the aggregation kinetics of the WT and mutant peptides, we tracked the time evolution of the largest aggregate size in each system [441]. The maximum cluster sizes shown in Figure 6.2A represent averages over multiple replicas for each simulated system. Overall, point mutations resulted in distinct aggregation kinetics among the hLL-37$_{17\text{-}29}$ mutants. In most systems, intermediate oligomers formed almost spontaneously - either at the end of equilibration or within the first 50 ns of the production run. The I24K mutant was a notable exception, where intermediate oligomers remained unstable and frequently dissociated into smaller aggregates, failing to form higher-order structures.

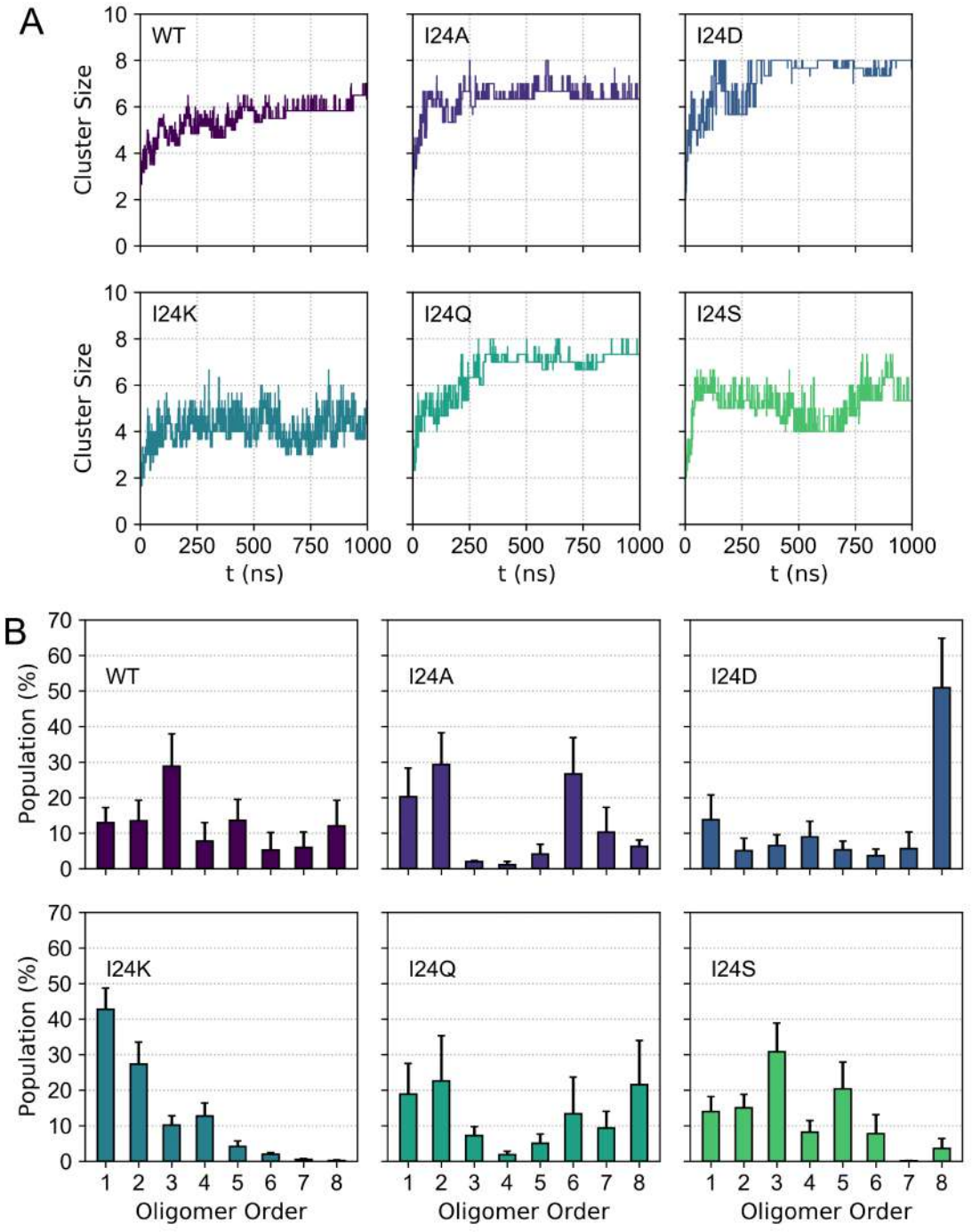

FIGURE 6.2: **Kinetics of oligomerization and oligomer populations:**(A)Temporal evolution of the average cluster size of the WT and the mutant systems, starting from a completely dispersed state, having eight peptides placed sufficiently apart (≈20 Å) in a cubic simulation box solvated with TIP3P water. (B) The percentage population of the different oligomeric states of the WT and the mutant systems. The cluster size and oligomer populations are averaged over the 'n' simulation repeats of each peptide system. The error bars represent the standard error of the mean population, taken across the 'n' replicas of each system.

The rapid initial aggregation observed in the other systems can be attributed to hydrophobic collapse, which minimizes the solvent exposure of the hydrophobic residues [450–452]. Following this collapse, the aggregation kinetics can be divided into two distinct phases: (i) a growth phase and (ii) a lag phase [453]. During the growth phase, small and intermediate oligomers mature into higher-order aggregates, concluding once a stable aggregate size is reached. Dissociation events during this phase are excluded, as they typically represent short-lived, diffusion-controlled encounter complexes. In the subsequent lag phase, the higher-order oligomers undergo repeated association and dissociation with smaller oligomers, driven by structural reorganization within the peptides, until a stable assembly is achieved.

In the WT, the growth phase extended up to 625 ns. During this period, the systems fluctuated around a pentamer before eventually growing into a hexamer. Several higher-order encounter complexes were observed but dissociated shortly after formation. The resulting hexamer served as a seed for the next lag phase, during which the aggregate size fluctuated between 6 and 7 before maturing into an octamer in the later stages (≈950 ns) of the simulation. For I24A, I24D, and I24Q mutants, the growth phase was relatively short, spanning up to 250 ns, during which stable hexamers formed. These systems subsequently fluctuated between size 6 and 7 aggregates in the lag phase, with occasional transitions to the octamer. Among them, the I24D mutant displayed fewer association-dissociation events, and its octamers were relatively long-lived. In contrast, oligomer growth in I24S was arrested at intermediate stages. Initially formed pentamers dissociated into tetramers midway through the simulation (500-700 ns) before they reassembled. Toward the end of the simulation, pentamers in I24S occasionally grew into larger aggregates (6-7), but these encounter complexes were extremely unstable and disintegrated almost immediately.

The temporal changes in the average cluster size suggest that multiple oligomeric states are sampled as the peptides aggregate from a fully dispersed state. To determine which states are preferred, we calculated their populations in the WT and the mutants [454]. The populations, averaged over multiple simulation repeats for each peptide system, are presented with the standard error of the mean in Figure 6.2B. In the WT, lower-order

oligomers - particularly trimers - are the most abundant. Among intermediate and higher-order states, pentamers and octamers are the most preferred within their respective ranges. Overall, the WT shows a balanced sampling of low to intermediate aggregates. The I24S mutant shows a similar preference for trimers and pentamers, closely resembling the WT. However, this mutant's octamer population is significantly reduced, demonstrating a weaker tendency to develop into higher aggregates. In contrast, the I24A mutant shows a marked decrease in intermediate states and a strong preference for hexamers. Other higher oligomers are less abundant, with the heptamer slightly more preferred than the octamer. The increase in the monomer and dimer population - almost comparable to the hexamer - suggests a decrease in the aggregation tendency beyond the hexamer in I24A. A similar trend is observed in I24Q, which exhibits fewer intermediate states than lower and higher-order oligomers. However, unlike I24A, I24Q strongly favors octamer formation, making it the second mutant (after I24D) to favor this state. For I24D, the octamer is unequivocally the most preferred state, indicating a strong aggregation tendency in this mutant. Otherwise, these peptides remain as monomers or are equally distributed among the other oligomeric sizes. The I24K mutant shows a distinct shift towards monomer and dimer populations, suggesting a drastic reduction in its aggregation tendency. The populations of the other states decrease progressively with increasing size. Based on these population trends, I24D and I24Q emerge as highly aggregation-prone mutants, while I24K shows strong resistance to aggregation. The other variants exhibit moderate (WT and I24A) to weak aggregation tendencies (I24S), often stopping at intermediate oligomeric states.

Based on Figure 6.2B, we hypothesize that mutations alter the populations and, consequently, the identity of the oligomeric species responsible for forming higher-order aggregates. To test this hypothesis, we constructed transition networks depicting routes via which peptides aggregate to higher oligomeric forms (Figure 6.3). The networks are drawn between states that denote the size, i.e., the number of peptides in the oligomer, without incorporating any finer molecular descriptors (for example, the oligomer shape, the nature of interaction in them, etc.). The node size indicates a state's population, and the edge thickness connecting a pair of nodes reflects the transition frequency between them.

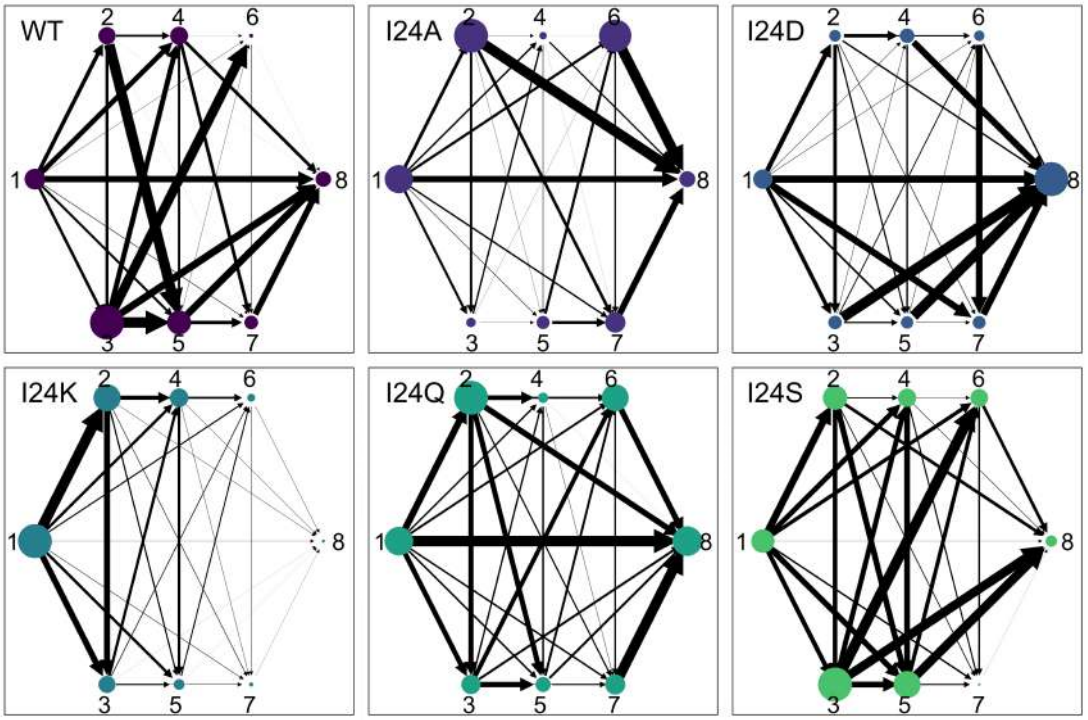

FIGURE 6.3: **Transition pathways in the WT and mutant peptides:** Coarse-grained transition networks represent the conversion between the different oligomeric states of the WT and the mutant systems. Only step-up transitions, i.e., transitions from lower to higher oligomeric states, have been represented. Self-transitions have been filtered out since they fail to contribute to oligomer growth. The node size is proportional to the state population, and the edge thickness is proportional to the transition frequency between states. The nodes and the edges have been normalized relative to the most populated state and the most frequent transition, respectively.

The nodes and the edges are normalized such that the largest node represents the highest populated oligomer, and the thickest edge represents the most frequent transition. In the WT, the most prominent pathway involves a trimer combining with a pentamer to form an octamer. Another prevalent route is the fusion of a heptamer with a monomer to yield an octamer. Both pentamers and heptamers originate predominantly from the highly abundant trimers when they coalesce with a dimer or a tetramer. The less populated hexamers also originate from the trimers but do not grow into the octamer. We also observed a low, yet finite, probability of two tetramers combining to produce an octamer - a mode of assembly previously reported for hypothetical amphipathic peptides using coarse-grained MD simulations [455]. The aggregation pathways in the mutants deviate markedly from those in the WT. For instance, the highly abundant hexamer in I24A accepts a dimer

to produce an octamer, an almost non-existent pathway in the WT. In I24D, all the intermediate states contribute to octamer formation. While the 3+5 combination is most favored, the other two pathways, i.e., 4+4 and 1+7, are profound and almost equiprobable. Here, the heptamers originate from the hexamers instead of the trimers, as seen in WT. For I24K, where the aggregation tendency is significantly reduced, we found that the conversion to higher-order oligomers decreases progressively with increasing oligomer size. Growth is arrested at the tetramer state, which is evident from the low populations of the higher states. In I24Q, the sparsely populated intermediate states participate less in octamer formation. Instead, the higher oligomers associate with smaller ones to produce the octamer. In I24S, we observe an increased encounter between trimers and pentamers, as seen in WT. However, the 2+6 pathway, absent in the WT, also contributes to octamer formation in this mutant. The other pathways, i.e., 1+7 and 4+4, are almost non-existent in I24S. In summary, mutations impact the kinetics of aggregation, the populations of the oligomeric states, and the transition pathways between them.

6.3.2 Disruptive Effects of Increased Charge Density on Helical Structure

The hLL-$37_{17\text{-}29}$ fragment adopts a helical structure – almost exclusively in the presence of a membrane - with distinct hydrophobic and hydrophilic faces that complement each other [147, 456]. While this helical structure is not a prerequisite for its antibacterial property, it is critical in membrane binding and biomaterials fabrication [303, 457, 458]. To investigate whether the helical structure is preserved during aggregation, we analyzed changes in the secondary structure of the peptides using the DSSP algorithm [324]. Figure 6.4A illustrates the difference in the helical contents of the mutants compared to the WT (70.58%) - the helix percentage decreases in all the mutants, suggesting structural loss during aggregation. The extent of this disruption depends on the nature of the mutated residue. For instance, charged substitutions led to the most significant perturbations, with I24K showing greater structural loss than I24D. Among the mutants with polar substitutions, I24Q displayed less structural deviation than I24S. Despite its high aggregation

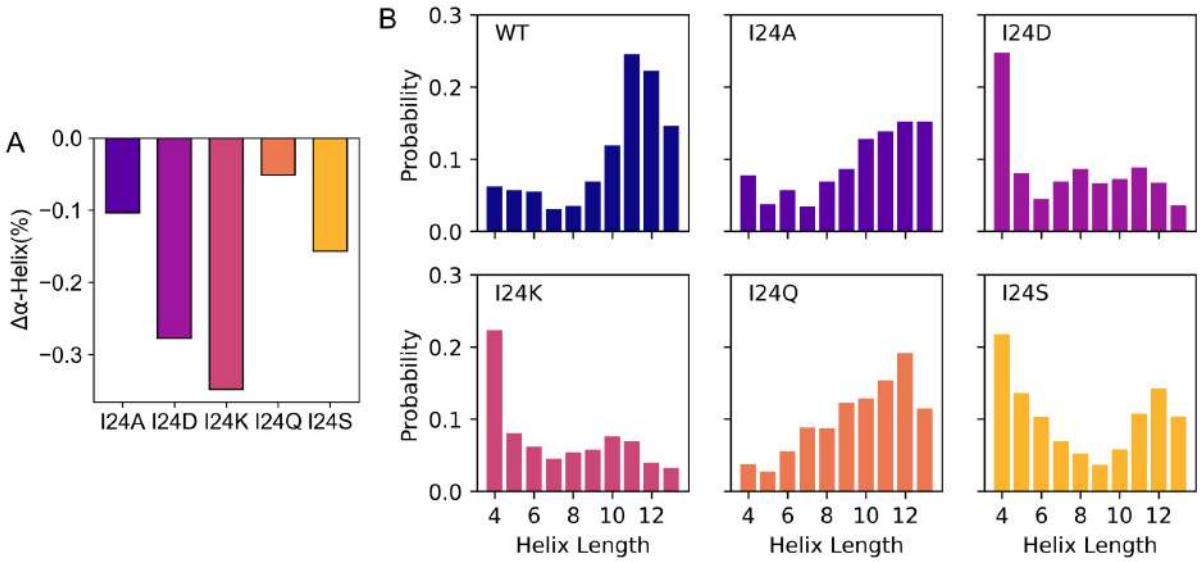

FIGURE 6.4: **Changes in secondary structure:** (A) Difference in total α-helix ($\Delta\alpha$-Helix) content of the mutant peptides relative to the WT. (B) Distribution of helix lengths in the WT and mutant peptides. The shortest helix comprises four residues, while the longest can accommodate up to 13 residues, corresponding to the peptide length minus the capping groups.

tendency, I24Q preserved its helical structure similar to the WT. The partial unfolding in the mutants indicates the presence of shorter helices in the aggregates. To assess the preferred helix length in WT and mutant peptides, we calculated the sequence length of residues involved in α-helix formation and plotted their distribution in Figure 6.4B. The shortest helix consists of 4 residues (where the i^{th} C=O is hydrogen bonded to $(i+4)^{th}$ N-H), while the longest in our case is 13, which is the length of hLL-$37_{17\text{-}29}$ minus the capping groups. Consistent with our previous observation, WT peptides were the least structurally perturbed and formed the most extended helices. In contrast, systems like I24K and I24D, which showed reduced α-helix content, exhibited a skew toward shorter helices. In I24S, although shorter helices were preferred, we occasionally observed a preference for longer ones, while intermediate helices were rarely present. Peptides with I24Q and I24A mutations favored longer helices, with this tendency being more pronounced in I24Q.

Figures 6.4A and 6.4B hint at helix unfolding during aggregation but fail to convey any information regarding the site of unfolding. To address this, we calculated the probability

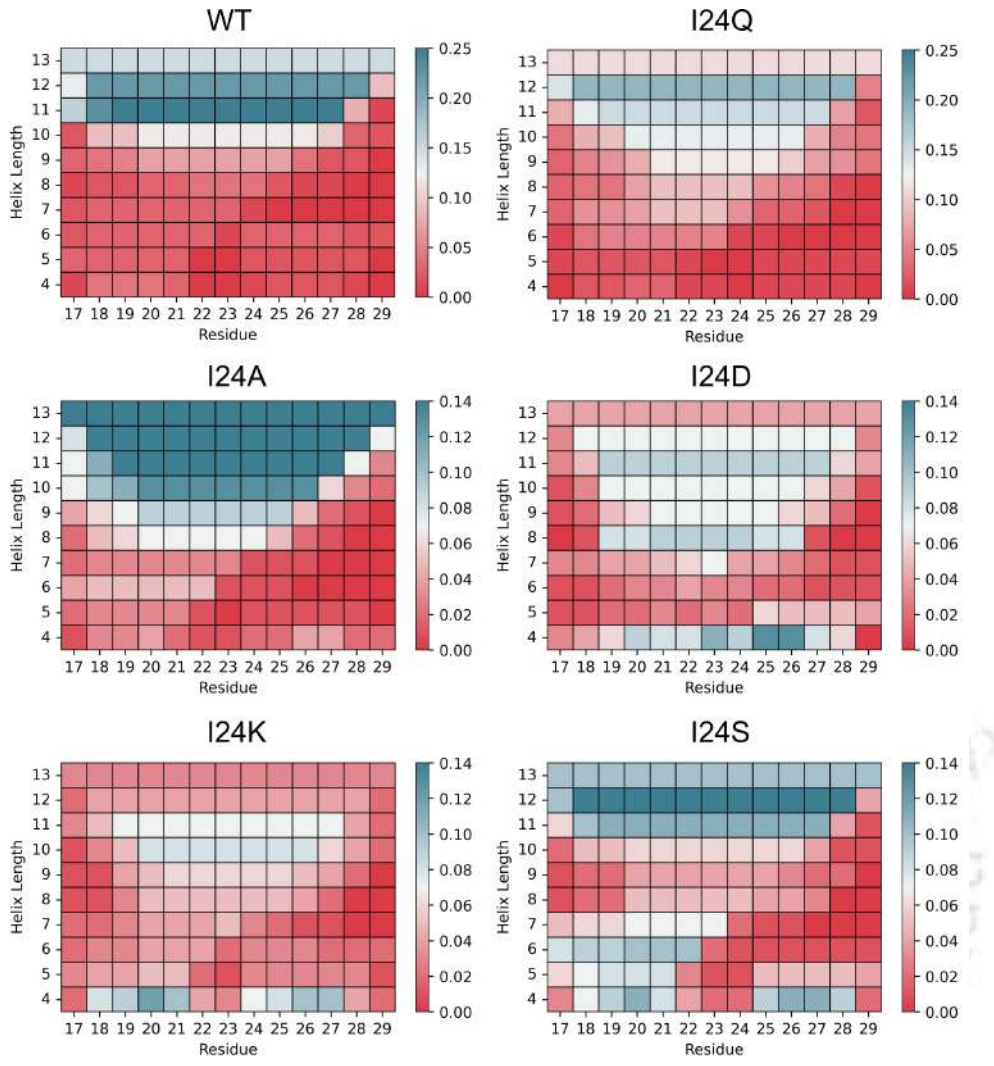

FIGURE 6.5: Residue-wise probability of participating in an α-helix of length l ($4 \leq l \leq 13$) for the WT and mutant systems.

of a residue residing in a length 'l' helix. Across all systems, the loss in secondary structure occurred primarily at the termini, with unfolding more probable at the C-terminal (Figure 6.5). For I24D, short helices preferentially formed near the C-terminal, specifically around residues 25 and 26, adjacent to the negatively charged D24. For I24K and I24S, unfolding initiated near central residues (23 and 24) with short helices formed at both termini. Overall, the increased charge density in I24K and I24D led to the maximum loss of helical structure. Such an inverse relation between the two was earlier reported for α-helical co-polypeptides of Leu and Lys [459]. In I24K, the presence of charged K24, flanked by R23 and K25, destabilized the structure through electrostatic repulsion, leading to maximal secondary structure loss.

6.3.3 Larger aggregates adopt compact structures with randomly oriented peptides

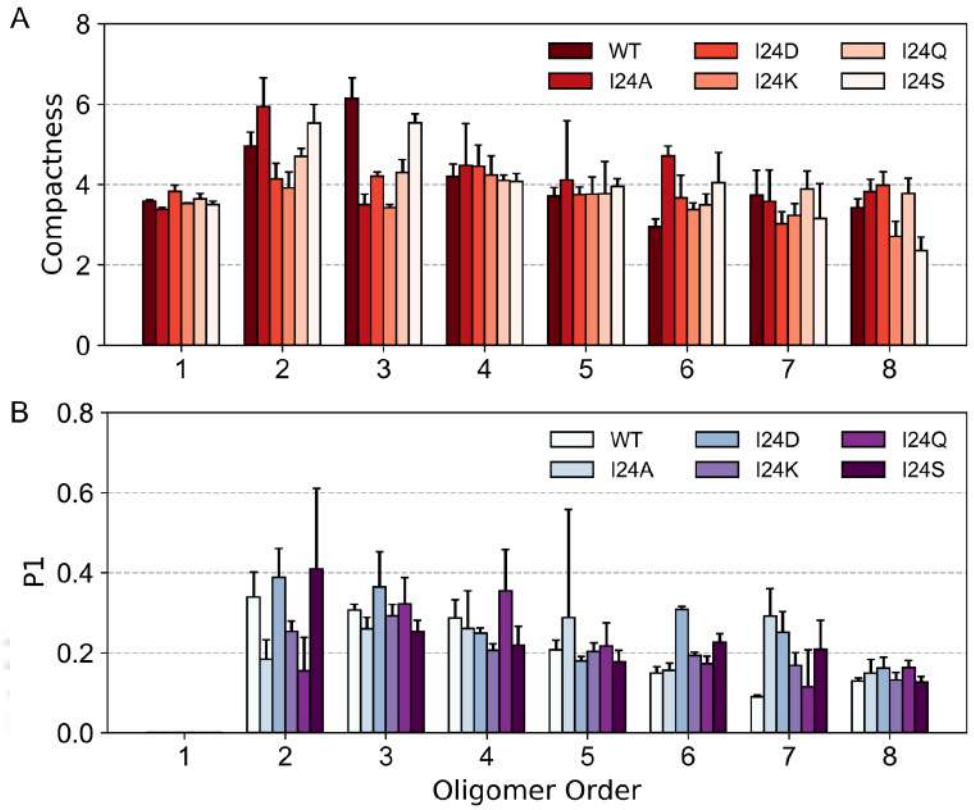

FIGURE 6.6: **Stuctural features of the oligomers:** (A) Compactness as a function of oligomer size for the WT and mutant systems. Compactness ranges from 0 (linear, rod-like aggregates) to 1 (spherical aggregates). (B) Polar order parameter (P_1) of the peptides as a function of oligomer size for the WT and mutant systems. P_1 ranges from 0, representing randomly oriented peptides, to 1, indicating a highly unidirectional arrangement. P_1 was calculated only for dimers and higher-order aggregates.

Having clarified the structural aspects of the individual peptides, we next explored the aggregate morphology - specifically the shape and the internal ordering among peptides – using two metrics: (i) the compactness factor [207] and (ii) the polar order parameter (P_1) [311]. The compactness factor, ranging from 1 (linear, rod-like aggregates) to 10 (spherical aggregates), revealed that the aggregates were predominantly linear with an average compactness around 4, typical of fibrillar architecture(Figure 6.6A). The lower and higher-order oligomers vary widely in compactness, but the intermediate oligomers remained relatively consistent. In the case of dimers and trimers, the WT and I24S formed

spherical aggregates, while the remaining mutants formed linear ones. Notably, the most common dimer in I24A was also highly spherical. Among the higher-order oligomers (6 and above), a direct relationship emerged between oligomer shape and population: more compact oligomers were also more abundant, while extended structures were rare, likely due to inefficient hydrophobic packing. To delve deeper into the internal ordering among the peptides, we calculated the polar order parameter (P_1) for the WT and mutant aggregates. P_1 captures the directional alignment among the peptides, especially relevant for α-helical peptides due to their intrinsic directionality. By definition, P_1 varies from 0 (random orientations) to 1 (highly aligned). An average P_1 value below 0.4 indicates anisotropy in the peptide arrangement (Figure 6.6B). As oligomer size increases, peptide orientations become increasingly random, with the highest anisotropy in octameric assemblies across all systems. In the case of dimers, antiparallel arrangements were favored in I24A, I24Q, and I24K. Among higher-order oligomers, only the I24Q tetramers and I24D hexamers showed strong orientational preferences. The WT heptamers were the least ordered among all peptide systems.

6.3.4 Mutations alter the interaction sites within the mutants

To identify key interactions driving aggregation, we calculated the contact probability (P) between residues by considering every pair of peptides within an oligomer [441]. In Figure 6.7, we present the average interaction probability, accompanied by color bars that quantify the extent of interaction. For I24S and WT, we observed stronger inter-residue interactions ($0.0 \leq P \leq 0.4$) compared to the other mutants ($0.0 \leq P \leq 0.2$). Also, the highest interaction is seen only for a particular pair of residues (I24-I24 in WT and F27-F27 in I24S), which hints at the specificity of these contacts. Except for the WT, all other mutants display a shift in interactions towards the C-terminal end. This indicates that mutating I24 disrupts the hydrophobic center of the peptide and inhibits the formation of a hydrophobic core, physically forcing other hydrophobic residues to compensate (primarily F27 and L28 at the C-terminal). Although the peptides could have approached via the N-terminal, charged residues at this end (K18 and R19) prevent

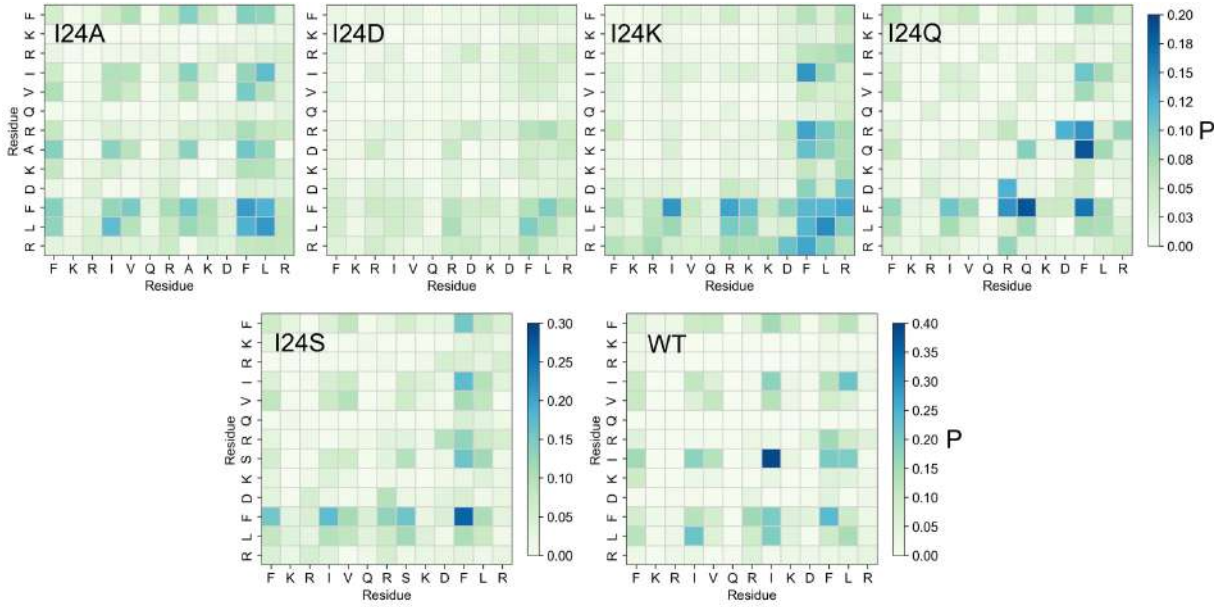

FIGURE 6.7: **Interactions in the WT and mutants:** Inter-residue contact maps of the WT and the mutants. The color bar quantifies the interaction probability (P) between two residues in an oligomer of size 'n' ($n \geq 1$). The contact maps are normalized over all possible interactions in a peptide pair.

such interactions. Instead, F27 and L28 at the C-terminal interact with each other and with other hydrophobic residues in the mutants. Additionally, F27 interacts with the hydrophobic chain of R23 in I24K and I24Q, and exclusively with Q24 in I24Q.

In contrast to the strong aggregation tendency observed for I24D peptides in Section 6.3.1, the contact maps reveal a very low probability of interaction among residues. This can be attributed to a loss of interaction specificity and the larger size of the aggregates, where only a few peptides are in actual contact while the rest are clustered based on the nearest-neighbor algorithm.

6.3.5 The mode of interaction shifts from van der Waals to electrostatic in the mutants

To explain the differences in the aggregation tendency of the WT and mutant systems, we next calculated the non-covalent interaction energy among the peptides [460, 461]. In Table 6.3, we represent the average interaction energy per peptide along with the standard

TABLE 6.3: Total non-bonded interaction energy among the WT and mutant peptides. The average values are reported along with the standard error of the mean taken over multiple simulation repeats

Peptide	Interaction Energy (kcal/mol)
WT	-19.25±2.66
I24A	-21.63±0.82
I24D	-103.24±5.12
I24K	-20.35±0.80
I24Q	-57.82±1.44
I24S	-47.18±0.97

error of the mean. The peptides interact favorably in all the systems, as indicated by a negative total interaction energy. In particular, the interaction is highest in the strongly aggregated I24D mutant. The I24Q mutant, with an uncharged but polar Q residue, shows the next best interaction, followed closely by I24S. The interaction energy is moderate and almost comparable for the WT, I24A, and I24K mutants, which cannot explain the disparity in their aggregation tendencies.

The total interaction energy, decomposed into electrostatic and van der Waals components, reveals the interplay between these two forces in deciding the extent of aggregation (Figure 6.8). Both components contribute to favorable peptide-peptide interactions in I24D, I24K, I24Q, and I24S. In I24D, the electrostatic component exceeds the van der Waals contribution (roughly three times), revealing the electrostatic origin of its strong aggregation tendency. For mutants involving polar residues, i.e., I24Q and I24S, these two forces contribute almost equally to the stability of the aggregates. In I24K, however, the van der Waals contribution dominates over the electrostatic component. Given that hLL-$37_{17\text{-}29}$ already carries a net positive charge of +4 units, introducing another positively charged residue in I24K further increases electrostatic repulsion among the peptides, thereby decreasing the overall electrostatic energy. Consequently, the weak aggregation

tendency observed in I24K arises almost entirely from van der Waals interactions. In contrast, introducing a negatively charged residue in I24D promotes favorable interactions among the peptides, as reflected by its highly negative electrostatic component.

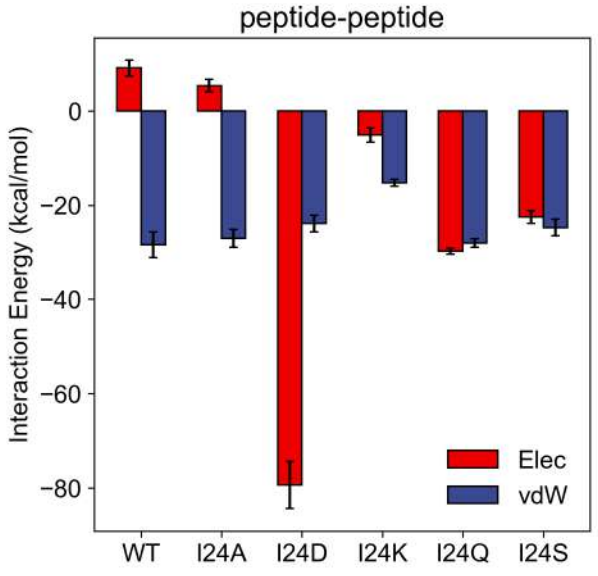

FIGURE 6.8: **Non-bonded interaction energy among the peptides:** The total non-bonded interaction energy decomposed into electrostatic (red) and van der Waals (blue) contributions. The individual energy terms are averaged over the 'n' simulation repeats of each peptide system. The error bars represent the standard error of the mean, taken across the 'n' replicas of each system.

A complete reversal is observed in WT and I24A, where the peptides have unfavorable electrostatic interactions. But this positive increase is compensated by a highly favorable van der Waals interaction, which makes the overall energy negative. Thus, the mode of interaction can be classified as purely hydrophobic (as in WT and I24A), weakly hydrophobic (as in I24K), or electrostatic (as in I24D), with this distinction less evident in I24Q or I24S.

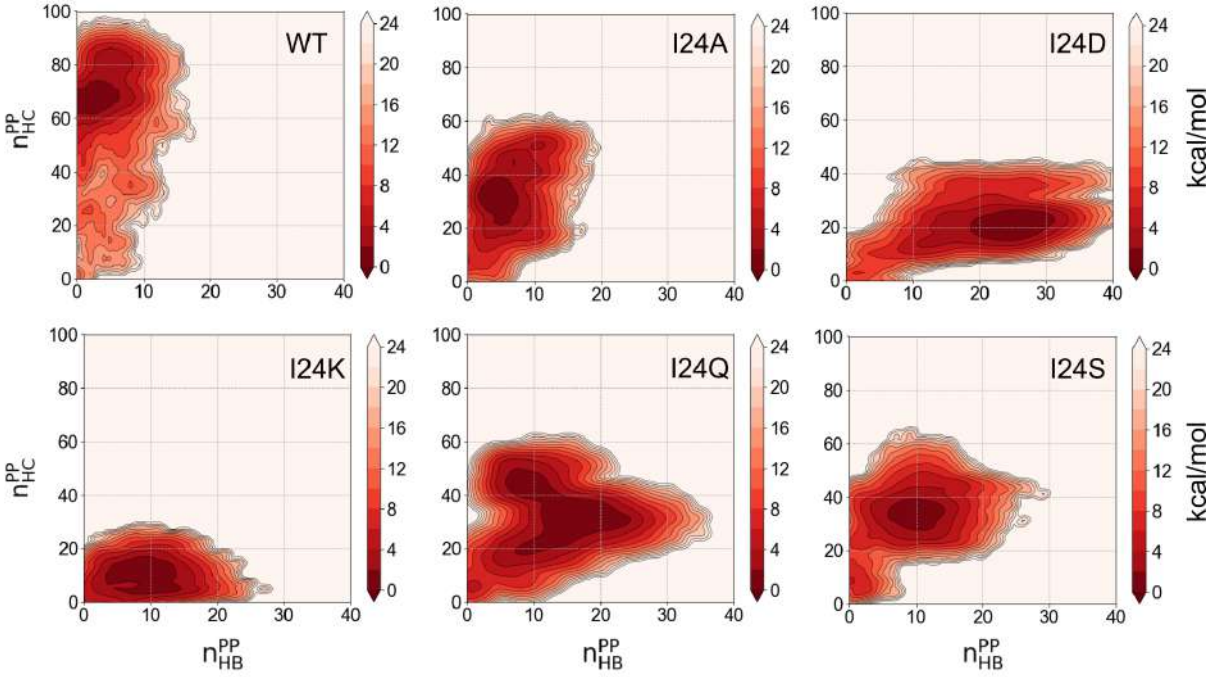

FIGURE 6.9: **Nature of interactions among the peptides:** Joint distribution of the inter-peptide hydrogen bonds (n_{HB}^{PP}) and hydrophobic contacts (n_{HC}^{PP}) and the contact area projected on a 2D free energy surface (FES). The colorbar represents the free energy calculated using Equation 6.3.

6.3.6 Hydrophobic interactions and hydrogen bonding exhibit an inverse relationship within the aggregates

For all the systems, we found favorable van der Waals interactions (though reduced in I24K), which suggests that hydrophobic interactions play a significant role during aggregation. We also observed favorable electrostatic interactions for mutations involving charged and polar residues, which hint at the possibility of hydrogen bonding. To discuss how these two influence the aggregation tendency, we next quantified the number of inter-peptide hydrogen bonds (n_{HB}^{PP}) and hydrophobic contacts (n_{HC}^{PP}) for each peptide system. For comparison, we calculated the joint probability distribution of these two quantities and projected them on a 2D free energy surface in Figure 6.9. Densely populated regions in the free energy surface are associated with low energies and signify the preferred state of the systems. In WT, aggregation is primarily driven by hydrophobic interactions, with a very low probability of hydrogen bonding between peptides. Replacement of the

I24 residue reduces the number of hydrophobic contacts in the mutants, making hydrogen bonding a key factor in determining their aggregation behavior. Both hydrophobic contacts and hydrogen bonds are the lowest in I24K, which is reflected in its weak aggregation tendency. In I24D, an increase in hydrogen bonding compensates for the loss of hydrophobic interactions, thereby promoting aggregation. For I24A, the mutation reduces hydrophobic contacts but does not enhance hydrogen bonding between the peptides. In I24S, the incorporation of a Ser residue leads to an increase in hydrogen bonds. For I24Q, we found two distinct regions: one where hydrophobic contacts are more than hydrogen bonds, and the other where hydrogen bonds exceed hydrophobic interactions. Grossly, we observe a reciprocal relationship in these two interactions where an increase in one leads to a decrease in the other. This is explained by the amphipathic nature of the peptides, where hydrophobic and hydrophilic residues occupy opposite faces of the helix [146]. In summary, systems where hydrogen bonding dominates tend to exhibit faster aggregation (I24D and I24Q), whereas systems dominated by hydrophobic interactions also aggregate, but with slower kinetics (WT, I24A, and I24S).

6.3.7 Charged and polar mutations enhance inter-Peptide hydrogen bonding via sidechain interactions

Next, we categorized hydrogen bonds into two types: (i) main-chain and (ii) sidechain hydrogen bonds, and computed their distributions for all peptides. Overall, sidechain hydrogen bonds are more prevalent than backbone hydrogen bonds, as the sidechains are more exposed (Figure 6.10). Additionally, the backbone amide and carbonyl oxygen atoms participate in intramolecular hydrogen bonds, contributing to the peptides' helical structure. In mutants where this helical structure is disrupted, such as I24K and I24D, we observed increased hydrogen bonding among the peptide backbones. For I24A, cross-interactions between sidechains and backbone atoms occur (not shown in Figure 6.10), likely due to the smaller size of the Ala residue compared to the other mutants.

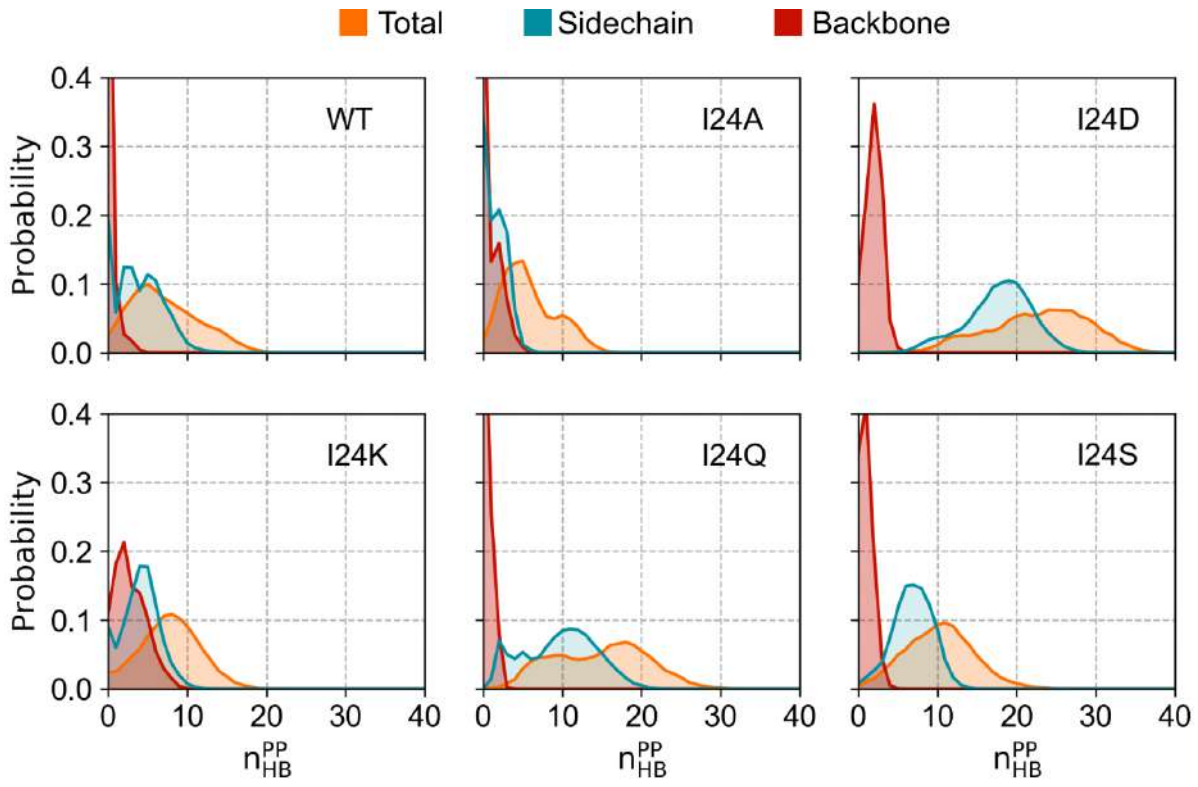

FIGURE 6.10: Distribution of peptide–peptide hydrogen bonds (n_{HB}^{PP}) in the WT and mutant systems, categorized into total, sidechain–sidechain, and backbone–backbone hydrogen bonds.

To identify the residues involved in inter-peptide hydrogen bonding, we next determined the number of hydrogen bonds contributed by each residue. We also distinguished between the types of hydrogen bonds - sidechain or backbone. In WT, with the exception of the Arg residues (R19 and R23), most hydrogen bonds originate from the C-terminal end (Figure 6.11). The Arg residues participate in both sidechain and backbone-sidechain hydrogen bonds, whereas the other residues primarily form sidechain hydrogen bonds. A similar pattern is observed in I24A, except at F17, whose backbone atoms can form hydrogen bonds with side chains of other residues. Additionally, the number of hydrogen bonds per residue is reduced in I24A compared to WT. In I24D, almost all residues except V21 participate in hydrogen bonding. The mutated D24 residue contributes the most, followed by R29 and D26. The presence of an additional negatively charged residue significantly enhances hydrogen bonding in this mutant, with sidechain hydrogen bonds dominating. In I24K, nearly all residues are capable of forming hydrogen bonds, although the overall number is lower than in I24D. This reduction can be attributed to the net

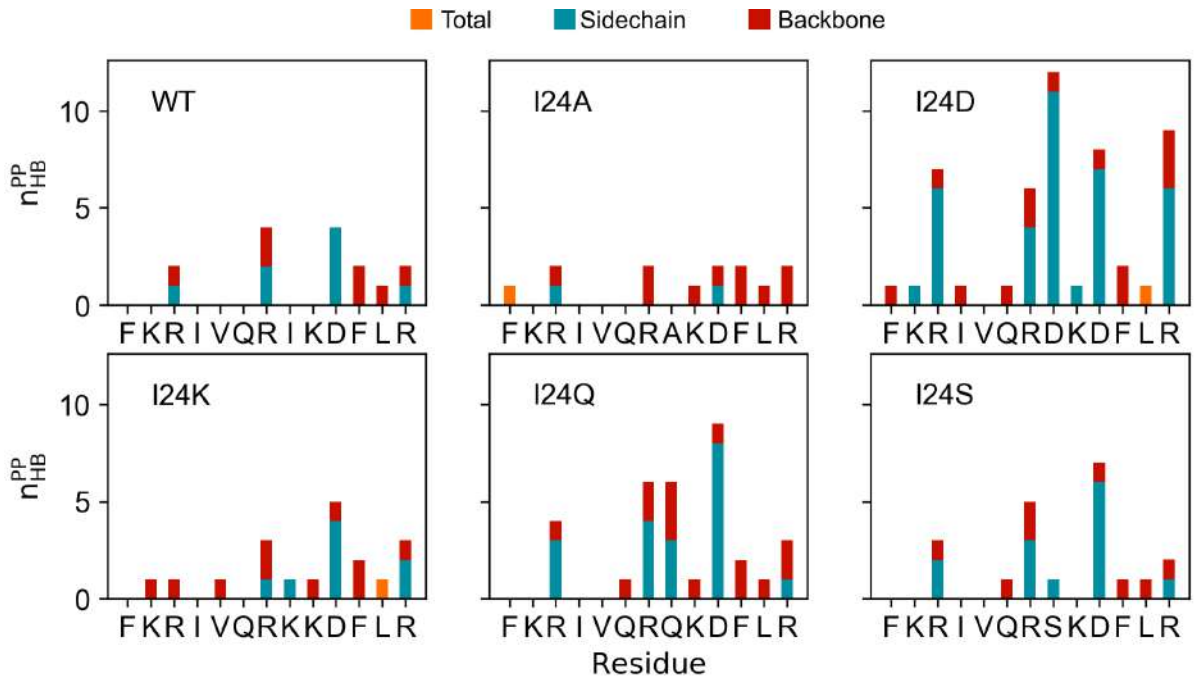

FIGURE 6.11: **Residue-wise inter-peptide hydrogen bonds:** Average number of hydrogen bonds formed per residue per peptide, categorized into total, side-chain, and backbone hydrogen bonds. Values are averaged over multiple simulation repeats for each system.

increase in positive charge, which impedes the peptides from coming within hydrogen bonding distance. Interestingly, the two adjacent Lys residues display contrasting behaviors: K24 primarily forms sidechain interactions, while K25 forms backbone hydrogen bonds exclusively. The I24Q mutant exhibits the second highest number of hydrogen bonds, with sidechain interactions playing the dominant role. In I24S, the introduction of a Ser residue with a hydroxyl (-OH) group increases the number of hydrogen bonds relative to WT, particularly at the C-terminal residues.

In summary, mutating I24 to polar or charged residues generally increases overall hydrogen bonding across the peptide chain, engaging nearly every residue. The only exception is I24K, where electrostatic repulsion outweighs stabilization from hydrogen bonds.

6.3.8 Peptide–peptide interactions operate over long distances in the aggregation-prone mutants

Since peptide aggregation is a cooperative process guided by multiple competing interactions (peptide-peptide (PP), peptide-water (PW), and water-water (WW)), we next explored the role of water in the aggregation of WT and mutants [437]. First, we compared the opposing roles of PP (promote aggregation) and PW (inhibit aggregation) interactions using the preferential interaction parameter, τ_{PW}^{PP}, which quantifies the preference for PP over PW interactions [447–449]. A positive value of τ_{PW}^{PP} indicates that PP interactions exceed PW interactions, favoring aggregation [462]. Overall, τ_{PW}^{PP} is positive for all systems, suggesting that aggregation is feasible (Figure 6.12A). On closer inspection, we found that the absolute value of τ_{PW}^{PP} varies across systems, leading to different aggregation tendencies. For example, in I24D and I24Q, τ_{PW}^{PP} increases monotonically beyond 10 Å, indicating that PP interactions operate over long distances and strongly aid aggregation. This is reflected in the peptides collapsing into a single octamer during simulation. In contrast, for WT, I24A, and I24S, τ_{PW}^{PP} reaches a maximum and then decreases at longer distances. In these systems, PP interactions are effective only up to ≈20 Å, beyond which PW interactions become dominant. This limits the growth of oligomers, resulting in an abundance of intermediate-sized aggregates in these variants. For I24K, τ_{PW}^{PP} shows a low positive value, consistent with its weak aggregation tendency.

6.3.9 I24 mutations modulate peptide solvation energy

To gain further insights into PW interactions, we calculated the non-covalent interaction energy between peptides and water, decomposed into electrostatic and van der Waals components. The average PW interaction energy per peptide is shown in Figure 6.12B, with error bars representing deviations from the mean. We observed favorable PW interactions across all systems, with values approximately ten times higher than the corresponding PP interactions. This higher PW interaction arises from the high surface-to-volume ratio of

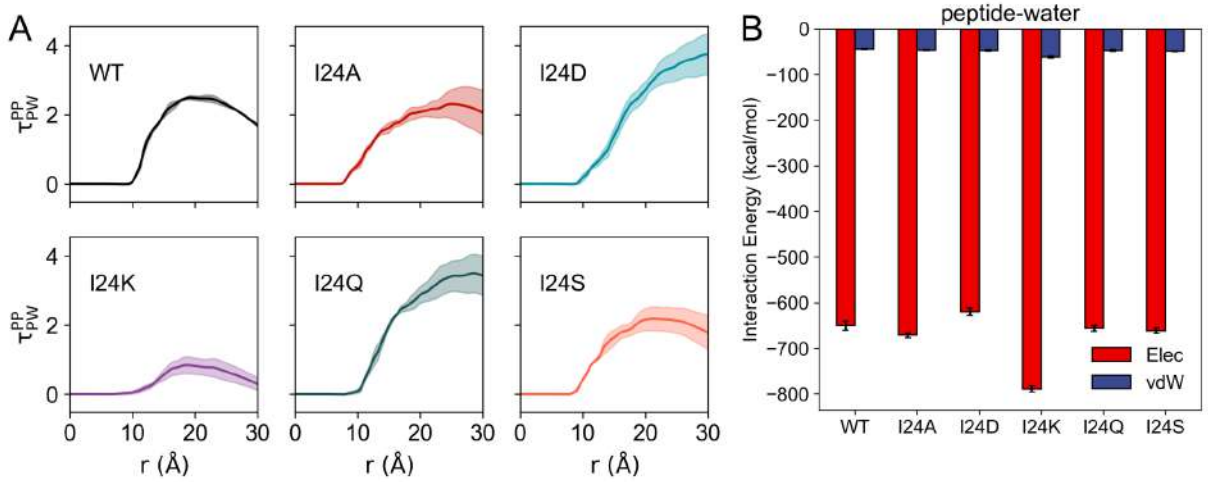

FIGURE 6.12: **Mutational effect on the solvation energetics of the peptides:** (A) Preferential interaction parameter (τ_{PP}^{PW}) comparing peptide–peptide interactions to peptide–water interactions. Values are averaged over n simulation repeats for each peptide system, with the shaded region representing the standard error of the mean across replicas. (B) Total non-bonded interaction energy between peptides and water (PW), decomposed into electrostatic (red) and van der Waals (blue) contributions.

the aggregates, where a large portion of the peptide surfaces remains exposed to the solvent, allowing numerous stabilizing contacts with water molecules. These interactions are predominantly electrostatic, driven by hydrogen bonding between water molecules and donor/acceptor sites on the peptides.

Among the mutants, the weakly aggregating I24K exhibits the highest PW electrostatic interaction, while the strongly aggregating I24D shows the lowest. Additionally, I24K displays the largest van der Waals interaction with water (–61.73 ± 2.11 kcal/mol), compared to approximately –46 kcal/mol for the other systems. This observation aligns with our earlier findings from τ_{PP}^{PW}, where I24K prefers to be solvated, but I24D prefers to interact with other peptides. Differences in the PW interaction energy are less evident for WT, I24A, I24Q, and I24S mutants.

The amphipathic nature of these peptides results in a balanced distribution of hydrophobic and hydrophilic residues, each contributing differently to water interactions. To explore these contributions, we calculated the total PW interaction energy separately for hydrophobic (Phe, Ile, Val, Leu, Ala) and hydrophilic (Lys, Arg, Gln, Ser) residues (Table 6.4). In mutants involving charged residues, namely I24D and I24K, hydrophobic

TABLE 6.4: The average hydrophilic and hydrophobic non-bonded interaction energy in the WT and the mutants, along with the standard error of the mean.

Peptide	**hydrophobic (kcal/mol)**	**hydrophilic (kcal/mol)**
WT	-58.33±3.37	-642.14±1.66
I24A	-58.39±1.70	-639.54±2.63
I24D	-80.36±4.28	-571.40±9.95
I24K	-75.02±5.01	-759.63±7.25
I24Q	-55.30±3.51	-635.36±7.04
I24S	-59.31±2.45	-626.15±7.15

residues exhibit higher interaction with water compared to the other systems, with I24D having the highest among the two. This suggests that charged substitutions at I24 increase the solvent exposure of hydrophobic residues. When considering hydrophilic residues, I24D shows the lowest PW interaction among all peptides, while I24K shows the highest. This reinforces our observation in Figure 6.12A, indicating that I24K peptides are more solvated than I24D. The absolute values of interaction energy suggest that the extent of hydrophilic residue–water interaction primarily dictates the total PW interaction energy. For the other systems, differences between hydrophilic and hydrophobic PW contributions are less pronounced, with PP interactions playing a more dominant role in driving aggregation.

6.3.10 Hydration-aggregation trade-offs in the mutants

The electrostatic interactions shown in Figure 6.12B suggest strong hydrogen bonding between the peptides and surrounding water molecules. To assess the role of these hydrogen bonds during aggregation, we calculated their time evolution for the WT and mutant

systems (Figure 6.13A). Except for I24K, all systems show an initial decline in PW hydrogen bonds as peptides transition from a dispersed to an aggregated state. This decrease reflects the displacement of water molecules from the solvation shell as PP interactions begin to form. Notably, the extent of this decrease is more pronounced for I24D, I24Q, and I24S compared to WT and I24A. This indicates that mutations introducing charged residues or polar residues perturb the individual peptide solvation shells more than hydrophobic substitutions. In contrast, for I24K, we observed an increase in PW hydrogen bonds over time, as PP interactions are disfavored in this mutant. Furthermore, at any given time point, the two charged mutants (I24D and I24K) exhibit a higher number of PW hydrogen bonds compared to the other systems, revealing the higher water solubility of their aggregates.

The time evolution of the PW hydrogen bonds gives an idea about the temporal forces that dictate aggregation. However, to understand the state of aggregates at equilibrium, we need to consider the average number of PW hydrogen bonds. Considering the average over the last 200 ns, I24K shows the highest number of PW hydrogen bonds, followed by I24D (Figure 6.13B). In I24A, the extent of aggregation increases, and consequently, the number of PW hydrogen bonds decreases relative to the WT. In the case of I24Q and I24S, the number of PW hydrogen bonds improves compared to the WT, but fails to compete with the I24D and I24K variants. Though the number of hydrogen bonding sites is higher in I24Q, the average number of PW hydrogen bonds is almost comparable to I24S. Peptide–water (PW) hydrogen bonds primarily form between surface-exposed water molecules and those trapped within peptide clusters. The dehydration ratio (r_d) in Equation 6.2 quantifies the number of water molecules displaced from peptides during aggregation. In general, r_d is inversely related to the number of PW hydrogen bonds (Figure 6.13B). For I24K, r_d is the lowest, consistent with its weak aggregation tendency and the presence of well-solvated peptide aggregates. In the case of I24D, a similar reduction in r_d might be expected due to its second-highest PW hydrogen bonds. However, this mutant also exhibits strong PP interactions, as indicated by its high aggregation tendency. The coexistence of strong PW and PP interactions prevents a decline in r_d, resulting in well-hydrated, viscous, fluid-like clusters in I24D. In contrast, I24Q forms

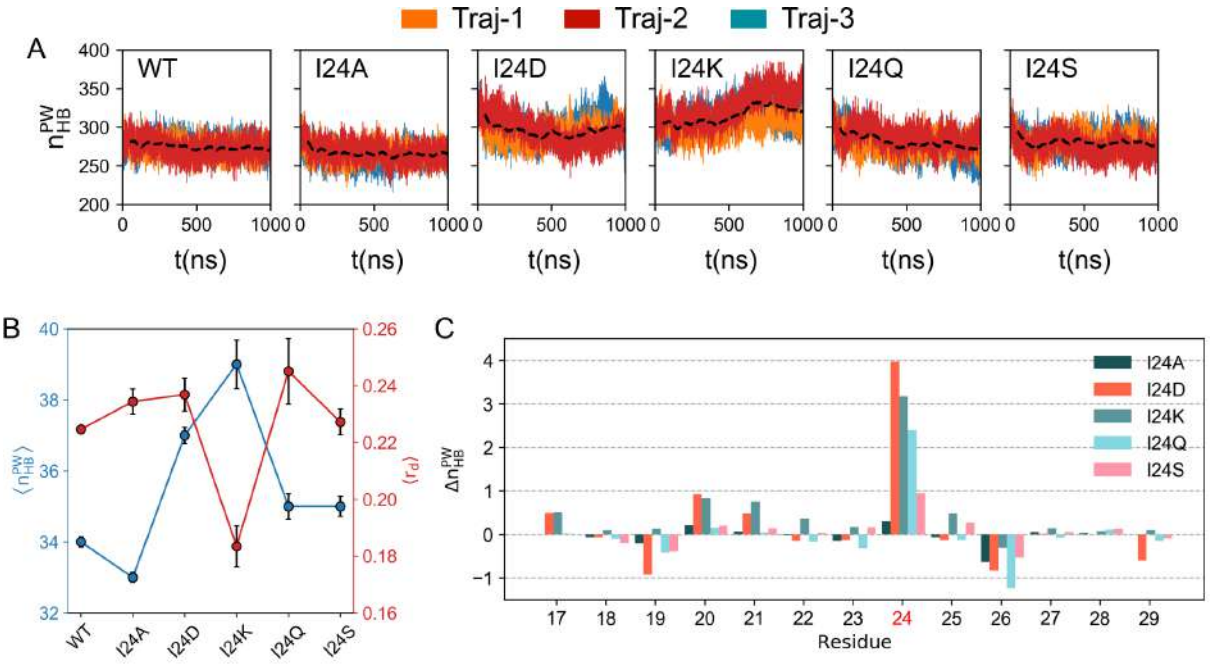

FIGURE 6.13: **Mutational effects on peptide-water hydrogen bonds:** (A) Time evolution of peptide–water hydrogen bonds for the WT and mutant systems, shown for all three simulation repeats. The dotted lines represent the rolling average taken over 100 consecutive MD steps. (B) Average number of peptide–water hydrogen bonds (n_{HB}^{PW}) and the corresponding dehydration ratio (r_d) for the WT and mutants. Error bars represent the standard error of the mean. (C) Per-residue difference in peptide–water hydrogen bonds relative to the WT.

relatively dry aggregates, where PP interactions dominate over PW interactions, leading to higher r_d values. I24A, which aggregates more readily than WT, forms the fewest PW hydrogen bonds and is therefore more dehydrated than WT. In I24S, the dehydration ratio is comparable to WT, but the number of PW hydrogen bonds is higher. This increase is balanced by stronger PP interactions, possibly due to the presence of the polar Ser residue, which prevents the decrease in r_d relative to the WT.

6.3.11 Mutations lead to differential solvation across peptide segments

Next, we calculated the per-residue contribution to the peptide–water (PW) hydrogen bonds in the mutants relative to the WT (Figure 6.13C). The mutated residue at position

24 shows the highest positive deviation in PW hydrogen bonds, indicating enhanced solvation of the peptide core compared to the WT. This increase is more pronounced in charged mutations than in polar ones, with Asp showing greater solvation than Lys among the charged residues. Among the polar substitutions, Gln forms more PW hydrogen bonds than Ser, likely due to its greater number of hydrogen-bonding sites. The hydrophobic Ala shows the smallest positive deviation, but its small methyl sidechain allows water to access the backbone—unlike the bulkier Ile sidechain in the WT, which hinders such interactions. Improved solvation at the peptide center enhances the overall solvation of hydrophobic residues at the N-terminal, particularly I20, V21, and, to a lesser extent, F17 (only in charged mutants). This is accompanied by a reduction in PW hydrogen bonds at D26, near the C-terminal. Additionally, R19 at the N-terminal forms fewer PW hydrogen bonds in most mutants, except in I24K, where this trend is reversed. This differential solvation at the two termini correlates with the interaction pattern observed in Section 6.3.4, where peptides preferentially interact via the C-terminal end, leaving the N-terminal more exposed to water.

In summary, mutations at I24 lead to differential solvation across the peptide: increased water accessibility at the central and N-terminal hydrophobic regions, and reduced solvation at the C-terminal. These shifts influence both the aggregation propensity and the water content of the resulting clusters.

6.4 Conclusions

In this Chapter, we investigated the sequence–aggregation relationship of the hLL-$37_{17–29}$ peptide, given its reported link to antimicrobial activity. We performed MD simulations of the wild-type (WT) and its mutants under NPT conditions (300 K, 1 atm) in explicit water. The mutants differ at position 24, where Ile is replaced by hydrophobic (I24A), charged (I24D, I24K), or polar (I24Q, I24S) residues. All systems rapidly formed small and intermediate oligomers through an initial hydrophobic collapse, reducing solvent exposure of nonpolar residues. From these early encounters, aggregation followed two kinetic

phases: (i) a growth phase where small clusters merge into larger aggregates, and (ii) a lag phase characterized by repeated association–dissociation events as peptides reorganize into stable assemblies. In WT, the growth phase was relatively slow compared to I24A, I24D, and I24Q. In contrast, I24K failed to grow beyond tetramers, while I24S stalled around pentamers. These trends classify I24D and I24Q as strongly aggregation-prone, I24K as aggregation-resistant, and the remaining variants—WT and I24A (moderate) and I24S (weak)-as partial aggregators. Transition network analysis shows that aggregation pathways vary across mutants. While WT primarily aggregates via 3+5 and 1+7 routes, mutants follow different or less favored pathways. I24D aggregates through multiple equally probable routes, whereas I24K exhibits a steady decline in transitions with increasing oligomer size, reflecting arrested growth. The amphipathic α-helical structure of hLL-$37_{17–29}$, though not essential for antimicrobial function, is crucial for membrane binding and self-assembly. Using DSSP, we found that all mutants showed reduced helical content relative to WT (70.6%), with charged substitutions causing greater disruption (I24K $\geq$ I24D) than polar ones (I24Q $\geq$ I24S). Remarkably, I24Q retained WT-like helicity despite its strong aggregation tendency, while I24K and I24D shifted toward shorter helices. Unfolding occurred primarily at the termini—at the C-terminal in I24D and near residues 23–24 in I24K and I24S—driven by local charge effects. In I24K, the dense cluster of positive charges (K24 flanked by R23 and K25) induced maximum structural loss. Morphologically, all systems formed mostly linear, fibril-like aggregates. Larger oligomers (size $\geq$ 6) displayed a correlation between compactness and abundance, suggesting that tight hydrophobic packing stabilizes higher-order states. Internally, peptides showed low orientational order, though anisotropy increased with size. In the WT, specific inter-residue interactions centered on the peptide core (I24-I24) were prominent, while in mutants, these shifted toward the C-terminal, especially F27–F27 and L28–L28. Charged residues at the N-terminal, such as K18 and R19, discouraged approach from that end. Interestingly, I24D, despite its strong aggregation, exhibited low contact specificity, indicating loosely packed clusters. Energetically, all peptides aggregated via favorable non-covalent interactions, though the dominant force differed across variants. I24D aggregation was electrostatically driven, while I24Q and I24S showed balanced electrostatic

and van der Waals interactions. I24K, due to its excess positive charge, experienced electrostatic repulsion and relied primarily on van der Waals interactions, resulting in weak aggregation. WT and I24A experienced unfavorable electrostatics, fully compensated by hydrophobic interactions, making them classic hydrophobic aggregators. For I24D and I24Q, long-range peptide–peptide (PP) interactions dominated over peptide–water (PW) interactions, leading to single-octamer collapse. In contrast, WT, I24A, and I24S showed limited PP interaction ranges (20 Å), resulting in more abundant intermediate oligomers. I24K preferred solvation, with strong electrostatic and van der Waals PW interactions counteracting aggregation. Across all systems, PW interaction energies outweighed PP energies due to the high surface-to-volume ratio of aggregates. I24K had the strongest PW interactions, while I24D had the weakest, reinforcing their opposing aggregation behaviors. Charged mutations, particularly I24D, increased water exposure of hydrophobic residues. Hydrophilic residues, however, contributed more significantly to overall PW energy, with I24K showing the highest and I24D the lowest values. During aggregation, PW hydrogen bonds declined in all systems except I24K, where they increased due to failed PP contacts. Equilibrium water content followed the trend: I24K (most hydrated) $\leq$ WT/I24S $\leq$ I24Q/I24A (most dehydrated). I24D struck a balance, forming viscous, water-rich clusters. Changes in hydration were centered at the mutation site, enhancing solvation of N-terminal hydrophobic residues (I20, V21) while reducing solvation near the C-terminal (e.g., D26), thus influencing aggregation behavior and water content in the resulting assemblies.

Chapter 7

Summary

Resistance to antibiotics has become a major concern in modern society and calls for urgent attention. In response, there is growing interest in alternatives to conventional antibiotics, with antimicrobial peptides (AMPs) receiving particular focus. AMPs are short, cationic peptides that form an essential component of the innate immune system, providing the first line of defense against invading pathogens.

In this thesis, we investigate the aggregation pathways of the hLL-$37_{17–29}$ peptide, a proteolytic fragment of LL-37 that retains antimicrobial activity and shows potential as an alternative to traditional antibiotics. This fragment peptide has the tendency to aggregate into fibrils with a distinct cross-α amyloid architecture. Since the antimicrobial activity of this peptide is closely linked to its self-assembly behavior, our study first characterizes how dispersed peptides associate to form early oligomers. We then examine how these oligomers undergo structural reorganization to form ordered assemblies with the characteristic cross-α amyloid architecture. Building on this, we investigate how specific point mutations modulate the aggregation propensity of the peptide, and finally, we analyze the interactions of the smallest stable oligomer (tetramer) with model membranes. A schematic summary of these studies and their main findings is shown in Fig. 7.1. We have structured this thesis into seven chapters. In Chapter 1, we provide a brief introduction to antimicrobial resistance and how AMPs can be leveraged to fight against it. We also introduce the peptide of interest, hLL-$37_{17\text{-}29}$, which is at the center of this entire study.

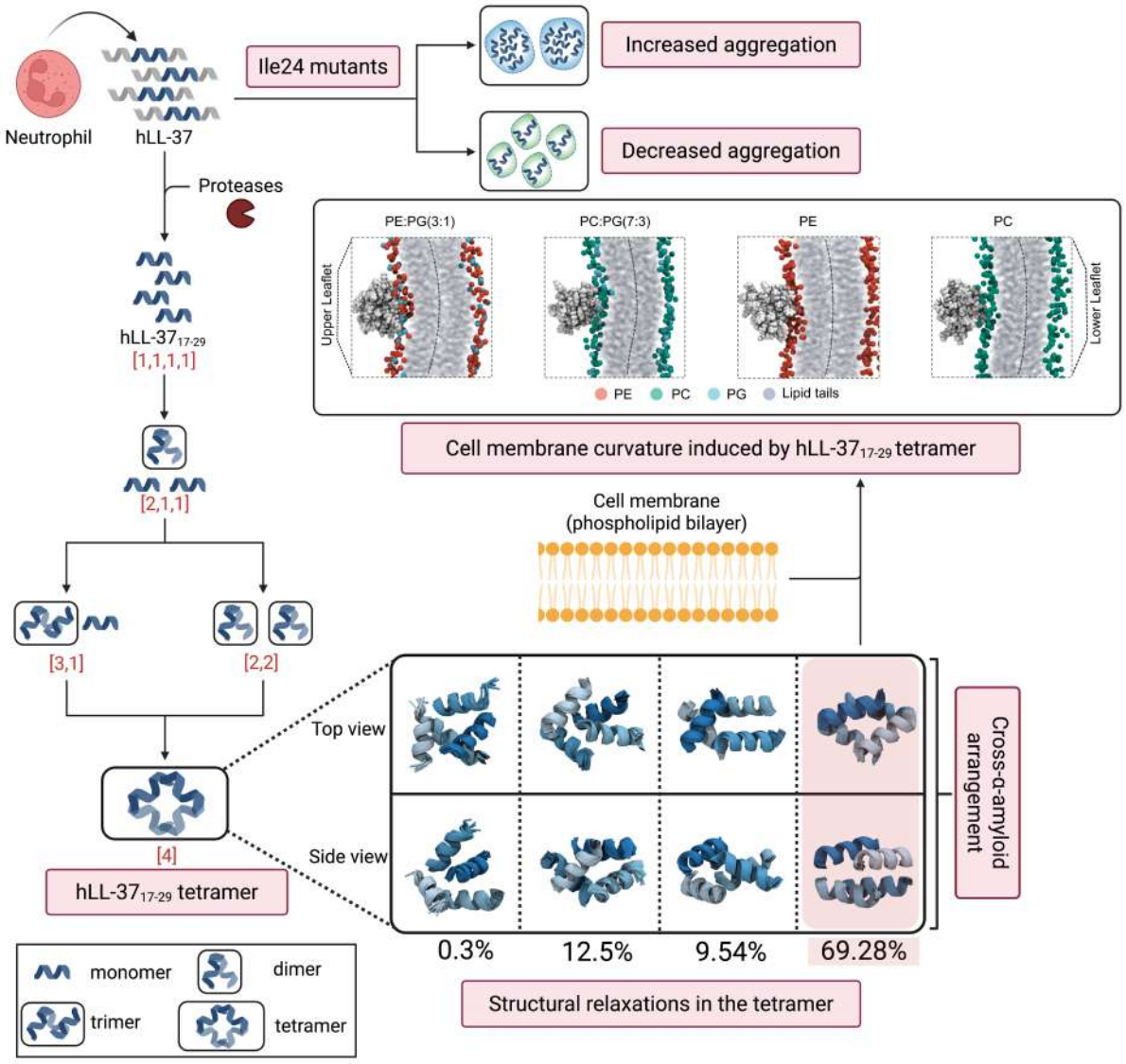

FIGURE 7.1: **Overview of the thesis:** A schematic summary of the studies presented in this work, highlighting aggregation pathways and and membrane interactions of hLL-$37_{17–29}$ peptides.

In Chapter 2, we provide a theoretical background for the computational and statistical tools used in this thesis, namely molecular dynamics (MD) simulations and Markov state modelling (MSM).

Chapter 3 investigates the aggregation mechanism of hLL-$37_{17\text{-}29}$ using atomistic MD simulations combined with semi-empirical Markov State Models. Simulations of systems with 4 and 8 peptides reveal that aggregation begins from a dispersed state via association of smaller oligomers into intermediate structures that eventually mature into higher-order

aggregates. Tetramers form readily and remain stable in 4-peptide systems, whereas 8-peptide systems segregate predominantly into trimers and pentamers, with occasionally coalesce into octamers. Transition-path analysis highlights multiple aggregation routes, with trimers acting as key intermediates. The peptides retain their α-helical structure during aggregation, stabilized by intramolecular salt bridges, while hydrophobic interactions, especially involving I20, I24, and Phe residues (F17, F27) drive assembly. Alanine scanning confirms the critical role of I24 in aggregation, consistent with experimental evidence of reduced activity in I24 mutants.

Chapter 4 uses molecular dynamics and Markov state modeling to uncover how hLL-$37_{17–29}$ self-assembles into 4-helix bundles (4HBs) with cross-α amyloid architecture. The simulations reveal that aggregation proceeds through disordered trimeric intermediates, which are unstable and spontaneously reorganize into tetramers with a compact hydrophobic core. Six metastable tetramer states (Q0–Q5) describe a pathway from disordered aggregates to ordered cross-α architectures, with Q3 and Q4 serving as key intermediates en route to the highly ordered Q5. The Q5 state exhibits optimal packing, high α-helical content, and low solvent exposure of hydrophobic residues. In contrast, trimers populate five less ordered states (T0–T4), with unfavorable electrostatic interactions and poor packing which reduces their stability. Overall, these findings demonstrate that van der Waals interactions among I24 guides the cooperative transition from trimers to tetramers, producing the stable, 4HB assemblies observed experimentally.

Chapter 5 examines how a pre-formed 4-helix bundle (4HB) derived from hLL-$37_{17\text{-}29}$ interacts with model membranes of different compositions. Simulations reveal that the 4HB preferentially adsorbs onto membrane surfaces in a face-down orientation driven by electrostatic interactions, with stronger binding observed for anionic membranes. Among zwitterionic bilayers, the 4HB shows a preference for PE over PC. Upon adsorption, cationic Arg residues penetrate the interfacial region of anionic membranes. The loss of translational entropy due to binding is offset by the release of ions from the membrane surface. Binding of the 4HB induces changes in both the peptide and the membrane: the 4HB undergoes elongation in shape, while the membrane exhibits increased local curvature in anionic systems. Lipids within 10 Å of the bound 4HB also display a marked increase

in their order parameter which disrupts the fluid nature of the bilayers. Potential of mean force calculations reveal that insertion of the 4HB into the membrane is associated with a significant energy barrier, particularly in PE:PG bilayers. This suggests that the 4HB primarily acts as a sensor for PE:PG membranes, while it has a higher likelihood of disrupting PC and PC:PG bilayers. Finally, simulations of peptide self-assembly near membranes indicate that 4HB formation occurs mainly in solution, as the membrane surface inhibits further oligomerization and stabilizes only smaller aggregates. Together, these findings clarify the sequence of events and mechanisms by which hLL-$37_{17\text{-}29}$ aggregates interact with and modulate different membrane types.

Chapter 6 investigates how amino acid substitutions at position I24 influence the aggregation of hLL-$37_{17–29}$ using MD simulations. Across all variants, peptides undergo a rapid hydrophobic collapse to form intermediate oligomers, followed by a growth phase and a subsequent lag phase. During the growth phase, smaller oligomers coalesce with intermediates to form larger aggregates, whereas the lag phase is characterized by repeated association–dissociation events as the oligomers reorganize structurally. The kinetics, specifically the duration of these phases, vary significantly among the mutants. I24D and I24Q exhibit a strong tendency to aggregate, while I24K resists aggregation due to electrostatic repulsion. The wild type (WT), I24S, and I24A display intermediate behavior. Mutations generally reduce the helical content relative to the WT, with charged substitutions causing the most prominent structural loss. The resulting aggregates are predominantly linear and fibril-like, with larger assemblies stabilized through hydrophobic packing. Analysis of inter-residue interactions reveals that mutations shift the key contacts from the peptide core towards the C-terminal region. The balance of electrostatic and van der Waals interactions dictates the fate of the aggregates: I24D forms loosely packed, electrostatically stabilized clusters; I24Q and I24S display a balance between electrostatic and van der Waals forces; I24K remains hydrated with weak packing; and WT and I24A aggregates are primarily stabilized by hydrophobic interactions. Overall, the residue at position 24 exerts a strong influence on aggregation pathways, structural organization, and hydration, offering insights into sequence–aggregation relationships relevant to antimicrobial function.

To conclude, this thesis offers structural and functional insights into the aggregation of the hLL-$37_{17–29}$ peptide that could be leveraged for the design of novel therapeutics and biomaterials.

References

[1] About Antimicrobial Resistance. https:////www.cdc.gov/antimicrobial-resistance/about/index.html, Accessed: 30-01-2025.

[2] Tenover, F. C. Mechanisms of Antimicrobial Resistance in Bacteria. *Am. J. Med.* **2006**, *119*, S3–S10.

[3] Khameneh, B.; Diab, R.; Ghazvini, K.; Bazzaz, B. S. F. Breakthroughs in Bacterial Resistance Mechanisms and the Potential Ways to Combat Them. *Microb. Pathog.* **2016**, *95*, 32–42.

[4] Zhou, G.; Shi, Q.-S.; Huang, X.-M.; Xie, X.-B. The Three Bacterial Lines of Defense against Antimicrobial Agents. *Int. J. Mol. Sci.* **2015**, *16*, 21711–21733.

[5] Murray, C. J. L.; Ikuta, K. S.; Sharara, F.; Swetschinski, L.; Aguilar, G. R.; Gray, A.; Han, C.; Bisignano, C.; Rao, P.; Wool, E. et al. Global Burden of Bacterial Antimicrobial Resistance in 2019: A Systematic Analysis. *Lancet* **2022**, *399*, 629–655.

[6] Naddaf, M. 40 Million Deaths by 2050: Toll of Drug-Resistant Infections to Rise by 70%. *Nature* **2024**, *633*, 747–748.

[7] Founou, R. C.; Founou, L. L.; Essack, S. Y. Clinical and Economic Impact of Antibiotic Resistance in Developing Countries: A Systematic Review and Meta-Analysis. *PloS One* **2017**, *12*, e0189621.

[8] Levy, S. B.; Marshall, B. Antibacterial Resistance Worldwide: Causes, Challenges and Responses. *Nat. Med.* **2004**, *10*, S122–S129.

[9] Read, A. F.; Woods, R. J. Antibiotic Resistance Management. *Evol., Med., Public Health* **2014**, *2014*, 147.

[10] Iskandar, K.; Murugaiyan, J.; Hammoudi Halat, D.; Hage, S. E.; Chibabhai, V.; Adukkadukkam, S.; Roques, C.; Molinier, L.; Salameh, P.; Van Dongen, M. Antibiotic Discovery and Resistance: The Chase and the Race. *Antibiotics* **2022**, *11*, 182.

[11] Hutchings, M. I.; Truman, A. W.; Wilkinson, B. Antibiotics: Past, Present and Future. *Curr. Opin. Microbiol.* **2019**, *51*, 72–80.

[12] Naghavi, M.; Vollset, S. E.; Ikuta, K. S.; Swetschinski, L. R.; Gray, A. P.; Wool, E. E.; Aguilar, G. R.; Mestrovic, T.; Smith, G.; Han, C. et al. Global Burden of Bacterial Antimicrobial Resistance 1990–2021: A Systematic Analysis with Forecasts to 2050. *Lancet* **2024**, *404*, 1199–1226.

[13] Uddin, T. M.; Chakraborty, A. J.; Khusro, A.; Zidan, B. R. M.; Mitra, S.; Emran, T. B.; Dhama, K.; Ripon, M. K. H.; Gajdács, M.; Sahibzada, M. U. K. et al. Antibiotic Resistance in Microbes: History, Mechanisms, Therapeutic Strategies and Future Prospects. *J. Infect. Public Health* **2021**, *14*, 1750–1766.

[14] Parmar, A.; Lakshminarayanan, R.; Iyer, A.; Mayandi, V.; Leng Goh, E. T.; Lloyd, D. G.; Chalasani, M. L. S.; Verma, N. K.; Prior, S. H.; Beuerman, R. W. et al. Design and Syntheses of Highly Potent Teixobactin Analogues Against Staphylococcus aureus, Methicillin-Resistant Staphylococcus aureus (MRSA), and Vancomycin-Resistant Enterococci (VRE) In Vitro and In Vivo. *J. Med. Chem.* **2018**, *61*, 2009–2017.

[15] Zaman, S. B.; Hussain, M. A.; Nye, R.; Mehta, V.; Mamun, K. T.; Hossain, N. A Review on Antibiotic Resistance: Alarm Bells are Ringing. *Cureus* **2017**, *9*.

[16] Parmanik, A.; Das, S.; Kar, B.; Bose, A.; Dwivedi, G. R.; Pandey, M. M. Current Treatment Strategies Against Multidrug-Resistant Bacteria: A Review. *Curr. Microbiol.* **2022**, *79*, 388.

[17] Davies, J.; Davies, D. Origins and Evolution of Antibiotic Resistance. *Microbiol. Mol. Biol. Rev.* **2010**, *74*, 417–433.

[18] Koch, N.; Islam, N. F.; Sonowal, S.; Prasad, R.; Sarma, H. Environmental Antibiotics and Resistance Genes as Emerging Contaminants: Methods of Detection and Bioremediation. *Curr. Res. Microbial Sci.* **2021**, *2*, 100027.

[19] Martinez, J. L. General Principles of Antibiotic Resistance in Bacteria. *Drug Discovery Today:Technol.* **2014**, *11*, 33–39.

[20] Cox, G.; Wright, G. D. Intrinsic Antibiotic Resistance: Mechanisms, Origins, Challenges and Solutions. *Int. J. Med. Microbiol.* **2013**, *303*, 287–292.

[21] Holmes, A. H.; Moore, L. S.; Sundsfjord, A.; Steinbakk, M.; Regmi, S.; Karkey, A.; Guerin, P. J.; Piddock, L. J. Understanding the Mechanisms and Drivers of Antimicrobial Resistance. *Lancet* **2016**, *387*, 176–187.

[22] Munita, J. M.; Arias, C. A. Mechanisms of Antibiotic Resistance. *Virulence Mech. Bact. Pathog.* **2016**, 481–511.

[23] Fernández, L.; Hancock, R. E. Adaptive and Mutational Resistance: Role of Porins and Efflux Pumps in Drug Resistance. *Clin. Microbiol. Rev.* **2012**, *25*, 661–681.

[24] Rizi, K. S.; Ghazvini, K.; Noghondar, M. K. Adaptive Antibiotic Resistance: Overview and Perspectives. *J. Infect. Dis. Ther* **2018**, *6*, 2332–0877.

[25] Ghai, I.; Ghai, S. Understanding Antibiotic Resistance via Outer Membrane Permeability. *Infect. Drug Resist.* **2018**, 523–530.

[26] Dutt, Y.; Dhiman, R.; Singh, T.; Vibhuti, A.; Gupta, A.; Pandey, R. P.; Raj, V. S.; Chang, C.-M.; Priyadarshini, A. The Association Between Biofilm Formation and Antimicrobial Resistance with Possible Ingenious Bio-Remedial Approaches. *Antibiotics* **2022**, *11*, 930.

[27] Van Acker, H.; Van Dijck, P.; Coenye, T. Molecular Mechanisms of Antimicrobial Tolerance and Resistance in Bacterial and Fungal Biofilms. *Trends Microbiol.* **2014**, *22*, 326–333.

[28] Ashley, R. E.; Dittmore, A.; McPherson, S. A.; Turnbough Jr, C. L.; Neuman, K. C.; Osheroff, N. Activities of Gyrase and Topoisomerase IV on Positively Supercoiled DNA. *Nucleic Acids Res.* **2017**, *45*, 9611–9624.

[29] Saha, M.; Sarkar, A. Review on Multiple Facets of Drug Resistance: A Rising Challenge in the 21st Century. *J. Xenobiot.* **2021**, *11*, 197–214.

[30] Foster, T. J. Antibiotic Resistance in Staphylococcus aureus. Current Status and Future Prospects. *FEMS Microbiol. Rev.* **2017**, *41*, 430–449.

[31] Wendlandt, S.; Shen, J.; Kadlec, K.; Wang, Y.; Li, B.; Zhang, W.-J.; Feßler, A. T.; Wu, C.; Schwarz, S. Multidrug Resistance Genes in Staphylococci from Animals that Confer Resistance to Critically and Highly Important Antimicrobial Agents in Human Medicine. *Trends Microbiol.* **2015**, *23*, 44–54.

[32] Choi, U.; Lee, C.-R. Distinct Roles of Outer Membrane Porins in Antibiotic Resistance and Membrane Integrity in Escherichia coli. *Front. Microbiol.* **2019**, *10*, 953.

[33] Nikaido, H.; Pagès, J.-M. Broad-Specificity Efflux Pumps and their Role in Multidrug Resistance of Gram-Negative Bacteria. *FEMS Microbiol. Rev.* **2012**, *36*, 340–363.

[34] Poole, K. Efflux-Mediated Antimicrobial Resistance. *J. Antimicrob. Chemother.* **2005**, *56*, 20–51.

[35] Chaw, P.; Höpner, J.; Mikolajczyk, R. The Knowledge, Attitude and Practice of Health Practitioners Towards Antibiotic Prescribing and Resistance in Developing Countries—A Systematic Review. *J. Clin. Pharm. Ther.* **2018**, *43*, 606–613.

[36] Chokshi, A.; Sifri, Z.; Cennimo, D.; Horng, H. Global Contributors to Antibiotic Resistance. *J. Global Infect. Dis.* **2019**, *11*, 36–42.

[37] Klein, E. Y.; Van Boeckel, T. P.; Martinez, E. M.; Pant, S.; Gandra, S.; Levin, S. A.; Goossens, H.; Laxminarayan, R. Global Increase and Geographic Convergence in

Antibiotic Consumption between 2000 and 2015. *Proc. Natl. Acad. Sci.* **2018**, *115*, E3463–E3470.

[38] Van Boeckel, T. P.; Brower, C.; Gilbert, M.; Grenfell, B. T.; Levin, S. A.; Robinson, T. P.; Teillant, A.; Laxminarayan, R. Global Trends in Antimicrobial Use in Food Animals. *Proc. Natl. Acad. Sci.* **2015**, *112*, 5649–5654.

[39] Michael, C. A.; Dominey-Howes, D.; Labbate, M. The Antimicrobial Resistance Crisis: Causes, Consequences, and Management. *Front. Public Health* **2014**, *2*, 145.

[40] Pulia, M.; Kern, M.; Schwei, R. J.; Shah, M. N.; Sampene, E.; Crnich, C. J. Comparing Appropriateness of Antibiotics for Nursing Home Residents by Setting of Prescription Initiation: A Cross-Sectional Analysis. *Antimicrob. Resist. Infect. Control* **2018**, *7*, 1–8.

[41] Woolhouse, M.; Waugh, C.; Perry, M. R.; Nair, H. Global Disease Burden Due to Antibiotic Resistance–State of the Evidence. *J. Global Health* **2016**, *6*, 010306.

[42] DiMasi, J. A.; Grabowski, H. G.; Hansen, R. W. Innovation in the Pharmaceutical Industry: New Estimates of R&D Costs. *J. Health Econ.* **2016**, *47*, 20–33.

[43] Chang, Q.; Wang, W.; Regev-Yochay, G.; Lipsitch, M.; Hanage, W. P. Antibiotics in Agriculture and the Risk to Human Health: How Worried Should we be? *Evol. Appl.* **2015**, *8*, 240–247.

[44] Castro-Sánchez, E.; Moore, L. S.; Husson, F.; Holmes, A. H. What are the Factors Driving Antimicrobial Resistance? Perspectives from a Public Event in London, England. *BMC Infec. Dis.* **2016**, *16*, 1–5.

[45] Frost, I.; Van Boeckel, T. P.; Pires, J.; Craig, J.; Laxminarayan, R. Global Geographic Trends in Antimicrobial Resistance: The Role of International Travel. *J. Travel Med.* **2019**, *26*, taz036.

[46] McCubbin, K. D.; Anholt, R. M.; de Jong, E.; Ida, J. A.; Nóbrega, D. B.; Kastelic, J. P.; Conly, J. M.; Götte, M.; McAllister, T. A.; Orsel, K. et al. Knowledge

Gaps in the Understanding of Antimicrobial Resistance in Canada. *Front. Public Health* **2021**, *9*, 726484.

[47] Arcilla, M. S.; van Hattem, J. M.; Haverkate, M. R.; Bootsma, M. C.; van Genderen, P. J.; Goorhuis, A.; Grobusch, M. P.; Oude Lashof, A. M.; Molhoek, N.; Schultsz, C. et al. Import and Spread of Extended-Spectrum β-Lactamase-Producing Enterobacteriaceae by International Travellers (COMBAT Study): A Prospective, Multicentre Cohort Study. *Lancet Infect. Dis.* **2017**, *17*, 78–85.

[48] Lewnard, J. A.; Charani, E.; Gleason, A.; Hsu, L. Y.; Khan, W. A.; Karkey, A.; Chandler, C. I.; Mashe, T.; Khan, E. A.; Bulabula, A. N. et al. Burden of Bacterial Antimicrobial Resistance in Low-Income and Middle-Income Countries Avertible by Existing Interventions: An Evidence Review and Modelling Analysis. *Lancet* **2024**, *403*, 2439–2454.

[49] Micoli, F.; Bagnoli, F.; Rappuoli, R.; Serruto, D. The Role of Vaccines in Combatting Antimicrobial Resistance. *Nat. Rev. Microbiol.* **2021**, *19*, 287–302.

[50] Klugman, K. P.; Black, S. Impact of Existing Vaccines in Reducing Antibiotic Resistance: Primary and Secondary Effects. *Proc. Natl. Acad. Sci.* **2018**, *115*, 12896–12901.

[51] Mendelson, M.; Lewnard, J. A.; Sharland, M.; Cook, A.; Pouwels, K. B.; Alimi, Y.; Mpundu, M.; Wesangula, E.; Weese, J. S.; Røttingen, J.-A. et al. Ensuring Progress on Sustainable Access to Effective Antibiotics at the 2024 UN General Assembly: A Target-Based Approach. *Lancet* **2024**, *403*, 2551–2564.

[52] Laxminarayan, R.; Impalli, I.; Rangarajan, R.; Cohn, J.; Ramjeet, K.; Trainor, B. W.; Strathdee, S.; Sumpradit, N.; Berman, D.; Wertheim, H. et al. Expanding Antibiotic, Vaccine, and Diagnostics Development and Access to Tackle Antimicrobial Resistance. *Lancet* **2024**, *403*, 2534–2550.

[53] Li, J.; Zhou, P.; Wang, J.; Li, H.; Xu, H.; Meng, Y.; Ye, F.; Tan, Y.; Gong, Y.; Yin, X. Worldwide Dispensing of Non-Prescription Antibiotics in Community Pharmacies and Associated Factors: A Mixed-Methods Systematic Review. *Lancet Infect. Dis.* **2023**, *23*, e361–e370.

[54] Lin, L.; Sun, R.; Yao, T.; Zhou, X.; Harbarth, S. Factors Influencing Inappropriate Use of Antibiotics in Outpatient and Community Settings in China: A Mixed-Methods Systematic Review. *BMJ Glob. Health* **2020**, *5*, e003599.

[55] Coll, F.; Goulouris, T.; Blane, B.; Yeats, C. A.; Raven, K. E.; Ludden, C.; Khokhar, F. A.; Wilson, H. J.; Roberts, L. W.; Harrison, E. M. et al. Antibiotic Resistance Determination Using Enterococcus Faecium Whole-Genome Sequences: A Diagnostic Accuracy Study Using Genotypic and Phenotypic Data. *Lancet Microbe* **2024**, *5*, e151–e163.

[56] Baker, K. S.; Jauneikaite, E.; Nunn, J. G.; Midega, J. T.; Atun, R.; Holt, K. E.; Walia, K.; Howden, B. P.; Tate, H.; Okeke, I. N. et al. Evidence Review and Recommendations for the Implementation of Genomics for Antimicrobial Resistance Surveillance: Reports From an International Expert Group. *Lancet Microbe* **2023**, *4*, e1035–e1039.

[57] Wang, H.; Jia, C.; Li, H.; Yin, R.; Chen, J.; Li, Y.; Yue, M. Paving the Way for Precise Diagnostics of Antimicrobial Resistant Bacteria. *Front. Mol. Biosci.* **2022**, *9*, 976705.

[58] Argimón, S.; Masim, M. A.; Gayeta, J. M.; Lagrada, M. L.; Macaranas, P. K.; Cohen, V.; Limas, M. T.; Espiritu, H. O.; Palarca, J. C.; Chilam, J. et al. Integrating Whole-Genome Sequencing Within the National Antimicrobial Resistance Surveillance Program in the Philippines. *Nat. Commun.* **2020**, *11*, 2719.

[59] Organization, W. H. *Global Antimicrobial Resistance and Use Surveillance System (GLASS) Report 2022*; World Health Organization: World Health Organization, 2022.

[60] Ho, C. S.; Wong, C. T.; Aung, T. T.; Lakshminarayanan, R.; Mehta, J. S.; Rauz, S.; McNally, A.; Kintses, B.; Peacock, S. J.; de la Fuente-Nunez, C. et al. Antimicrobial Resistance: A Concise Update. *Lancet Microbe* **2025**, *6*.

[61] François, B.; Jafri, H. S.; Chastre, J.; Sánchez-García, M.; Eggimann, P.; Dequin, P.-F.; Huberlant, V.; Soria, L. V.; Boulain, T.; Bretonnière, C. et al. Efficacy and Safety of Suvratoxumab for Prevention of Staphylococcus Aureus Ventilator-Associated Pneumonia (SAATELLITE): A Multicentre, Randomised, Double-Blind, Placebo-Controlled, Parallel-Group, Phase 2 Pilot Trial. *Lancet Infect. Dis.* **2021**, *21*, 1313–1323.

[62] Gerding, D. N.; Kelly, C. P.; Rahav, G.; Lee, C.; Dubberke, E. R.; Kumar, P. N.; Yacyshyn, B.; Kao, D.; Eves, K.; Ellison, M. C. et al. Bezlotoxumab for Prevention of Recurrent Clostridium Difficile Infection in Patients at Increased Risk for Recurrence. *Clin. Infect. Dis.* **2018**, *67*, 649–656.

[63] Zurawski, D. V.; McLendon, M. K. Monoclonal Antibodies as an Antibacterial Approach Against Bacterial Pathogens. *Antibiotics* **2020**, *9*, 155.

[64] Cavaco, M.; Castanho, M. A.; Neves, V. The Use of Antibody–Antibiotic Conjugates to Fight Bacterial Infections. *Front. Microbiol.* **2022**, *13*, 835677.

[65] Lehar, S. M.; Pillow, T.; Xu, M.; Staben, L.; Kajihara, K. K.; Vandlen, R.; DePalatis, L.; Raab, H.; Hazenbos, W. L.; Morisaki, H. J. et al. Novel Antibody–Antibiotic Conjugate Eliminates Intracellular S. Aureus. *Nature* **2015**, *527*, 323–328.

[66] Hsu, P. D.; Lander, E. S.; Zhang, F. Development and Applications of CRISPR-Cas9 for Genome Engineering. *Cell* **2014**, *157*, 1262–1278.

[67] Bikard, D.; Euler, C. W.; Jiang, W.; Nussenzweig, P. M.; Goldberg, G. W.; Duportet, X.; Fischetti, V. A.; Marraffini, L. A. Exploiting CRISPR-Cas Nucleases to Produce Sequence-Specific Antimicrobials. *Nat. Biotechnol.* **2014**, *32*, 1146–1150.

[68] Salmond, G. P.; Fineran, P. C. A Century of the Phage: Past, Present and Future. *Nat. Rev. Microbiol.* **2015**, *13*, 777–786.

[69] El Haddad, L.; Harb, C. P.; Gebara, M. A.; Stibich, M. A.; Chemaly, R. F. A Systematic and Critical Review of Bacteriophage Therapy Against Multidrug-Resistant ESKAPE Organisms in Humans. *Clin. Infect. Dis.* **2019**, *69*, 167–178.

[70] Green, S. I.; Clark, J. R.; Santos, H. H.; Weesner, K. E.; Salazar, K. C.; Aslam, S.; Campbell, J. W.; Doernberg, S. B.; Blodget, E.; Morris, M. I. et al. A Retrospective, Observational Study of 12 Cases of Expanded-Access Customized Phage Therapy: Production, Characteristics, and Clinical Outcomes. *Clin. Infect. Dis.* **2023**, *77*, 1079–1091.

[71] Pirnay, J.-P.; Djebara, S.; Steurs, G.; Griselain, J.; Cochez, C.; De Soir, S.; Glonti, T.; Spiessens, A.; Vanden Berghe, E.; Green, S. et al. Personalized Bacteriophage Therapy Outcomes for 100 Consecutive Cases: A Multicentre, Multinational, Retrospective Observational Study. *Nat. Microbiol.* **2024**, *9*, 1434–1453.

[72] Borin, J. M.; Avrani, S.; Barrick, J. E.; Petrie, K. L.; Meyer, J. R. Coevolutionary Phage Training Leads to Greater Bacterial Suppression and Delays the Evolution of Phage Resistance. *Proc. Natl. Acad. Sci. U.S.A.* **2021**, *118*, e2104592118.

[73] Magana, M.; Pushpanathan, M.; Santos, A. L.; Leanse, L.; Fernandez, M.; Ioannidis, A.; Giulianotti, M. A.; Apidianakis, Y.; Bradfute, S.; Ferguson, A. L. et al. The Value of Antimicrobial Peptides in the Age of Resistance. *Lancet Infect. Dis.* **2020**, *20*, e216–e230.

[74] Mookherjee, N.; Anderson, M. A.; Haagsman, H. P.; Davidson, D. J. Antimicrobial Host Defence Peptides: Functions and Clinical Potential. *Nat. Rev. Drug Discov.* **2020**, *19*, 311–332.

[75] Cherkasov, A.; Hilpert, K.; Jenssen, H.; Fjell, C. D.; Waldbrook, M.; Mullaly, S. C.; Volkmer, R.; Hancock, R. E. Use of Artificial Intelligence in the Design of Small Peptide Antibiotics Effective Against a Broad Spectrum of Highly Antibiotic-Resistant Superbugs. *ACS Chem. Biol.* **2009**, *4*, 65–74.

[76] Porto, W. F.; Irazazabal, L.; Alves, E. S.; Ribeiro, S. M.; Matos, C. O.; Pires, Á. S.; Fensterseifer, I. C.; Miranda, V. J.; Haney, E. F.; Humblot, V. et al. In Silico Optimization of a Guava Antimicrobial Peptide Enables Combinatorial Exploration for Peptide Design. *Nat. Commun.* **2018**, *9*, 1490.

[77] Cesaro, A.; Lin, S.; Pardi, N.; de la Fuente-Nunez, C. Advanced Delivery Systems for Peptide Antibiotics. *Adv. Drug Deliv. Rev.* **2023**, *196*, 114733.

[78] Ting, D. S. J.; Li, J.; Verma, C. S.; Goh, E. T.; Nubile, M.; Mastropasqua, L.; Said, D. G.; Beuerman, R. W.; Lakshminarayanan, R.; Mohammed, I. et al. Evaluation of Host Defense Peptide (CaD23)-Antibiotic Interaction and Mechanism of Action: Insights from Experimental and Molecular Dynamics Simulations Studies. *Front. Pharmacol.* **2021**, *12*, 731499.

[79] Ting, D. S. J.; Goh, E. T. L.; Mayandi, V.; Busoy, J. M.; Aung, T. T.; Periayah, M. H.; Nubile, M.; Mastropasqua, L.; Said, D. G.; Htoon, H. M. et al. Hybrid Derivative of Cathelicidin and Human Beta Defensin-2 Against Gram-Positive Bacteria: A Novel Approach for the Treatment of Bacterial Keratitis. *Sci. Rep.* **2021**, *11*, 18304.

[80] Lázár, V.; Martins, A.; Spohn, R.; Daruka, L.; Grézal, G.; Fekete, G.; Számel, M.; Jangir, P. K.; Kintses, B.; Csörgő, B. et al. Antibiotic-Resistant Bacteria Show Widespread Collateral Sensitivity to Antimicrobial Peptides. *Nat. Microbiol.* **2018**, *3*, 718–731.

[81] Pletzer, D.; Mansour, S. C.; Hancock, R. E. Synergy Between Conventional Antibiotics and Anti-Biofilm Peptides in a Murine, Sub-Cutaneous Abscess Model Caused by Recalcitrant ESKAPE Pathogens. *PLoS Pathog.* **2018**, *14*, e1007084.

[82] De La Fuente-Núñez, C.; Cardoso, M. H.; de Souza Cândido, E.; Franco, O. L.; Hancock, R. E. Synthetic Antibiofilm Peptides. *Biochim. Biophys. Acta, Biomembr.* **2016**, *1858*, 1061–1069.

[83] Ji, S.; An, F.; Zhang, T.; Lou, M.; Guo, J.; Liu, K.; Zhu, Y.-G.; Wu, J.; Wu, R. Antimicrobial Peptides: An Alternative to Traditional Antibiotics. *Eur. J. Med. Chem.* **2023**, *265*, 116072.

[84] He, K.; Ludtke, S. J.; Worcester, D. L.; Huang, H. W. Neutron Scattering in the Plane of Membranes: Structure of Alamethicin Pores. *Biophys. J.* **1996**, *70*, 2659–2666.

[85] Ehrenstein, G.; Lecar, H. Electrically Gated Ionic Channels in Lipid Bilayers. *Q. Rev. Biophys.* **1977**, *10*, 1–34.

[86] Yang, L.; Harroun, T. A.; Weiss, T. M.; Ding, L.; Huang, H. W. Barrel-Stave Model or Toroidal Model? A Case Study on Melittin Pores. *Biophys. J.* **2001**, *81*, 1475–1485.

[87] Hallock, K. J.; Lee, D.-K.; Ramamoorthy, A. MSI-78, an Analogue of the Magainin Antimicrobial Peptides, Disrupts Lipid Bilayer Structure via Positive Curvature Strain. *Biophys. J.* **2003**, *84*, 3052–3060.

[88] Matsuzaki, K.; Murase, O.; Fujii, N.; Miyajima, K. An Antimicrobial Peptide, Magainin 2, Induced Rapid Flip-Flop of Phospholipids Coupled with Pore Formation and Peptide Translocation. *Biochemistry* **1996**, *35*, 11361–11368.

[89] Yamaguchi, S.; Hong, T.; Waring, A.; Lehrer, R. I.; Hong, M. Solid-State NMR Investigations of Peptide–Lipid Interaction and Orientation of a β-Sheet Antimicrobial Peptide, Protegrin. *Biochemistry* **2002**, *41*, 9852–9862.

[90] Ladokhin, A. S.; White, S. H. 'Detergent-Like' Permeabilization of Anionic Lipid Vesicles by Melittin. *Biochim. Biophys. Acta, Biomembr.* **2001**, *1514*, 253–260.

[91] Shai, Y. Mechanism of the Binding, Insertion and Destabilization of Phospholipid Bilayer Membranes by α-Helical Antimicrobial and Cell Non-Selective Membrane-Lytic Peptides. *Biochim. Biophys. Acta, Biomembr.* **1999**, *1462*, 55–70.

[92] Pouny, Y.; Rapaport, D.; Mor, A.; Nicolas, P.; Shai, Y. Interaction of Antimicrobial Dermaseptin and Its Fluorescently Labeled Analogs with Phospholipid Membranes. *Biochemistry* **1992**, *31*, 12416–12423.

[93] Le, M. N.-T.; Kawada-Matsuo, M.; Komatsuzawa, H. Efficiency of Antimicrobial Peptides Against Multidrug-Resistant Staphylococcal Pathogens. *Front. Microbiol.* **2022**, *13*, 930629.

[94] Cochrane, S. A.; Findlay, B.; Bakhtiary, A.; Acedo, J. Z.; Rodriguez-Lopez, E. M.; Mercier, P.; Vederas, J. C. Antimicrobial Lipopeptide Tridecaptin A1 Selectively Binds to Gram-Negative Lipid II. *Proc. Natl. Acad. Sci. U.S.A.* **2016**, *113*, 11561–11566.

[95] Panina, I.; Taldaev, A.; Efremov, R.; Chugunov, A. Molecular Dynamics Insight Into the Lipid II Recognition by Type A Lantibiotics: Nisin, Epidermin, and Gallidermin. *Micromachines* **2021**, *12*, 1169.

[96] Zhao, X.; Yin, Z.; Breukink, E.; Moll, G. N.; Kuipers, O. P. An Engineered Double Lipid II Binding Motifs-Containing Lantibiotic Displays Potent and Selective Antimicrobial Activity Against Enterococcus Faecium. *Antimicrob. Agents Chemother.* **2020**, *64*, 10–1128.

[97] Konstantinova, S.; Grishin, A.; Lyashchuk, A.; Vasina, I.; Karyagina, A.; Lunin, V. Influence of NaCl and pH on Lysostaphin Catalytic Activity, Cell Binding, and Bacteriolytic Activity. *Appl. Microbiol. Biotechnol.* **2022**, *106*, 6519–6534.

[98] Lorenzon, E. N.; Piccoli, J. P.; Santos-Filho, N. A.; Cilli, E. M. Dimerization of Antimicrobial Peptides: A Promising Strategy to Enhance Antimicrobial Peptide Activity. *Protein Pept. Lett.* **2019**, *26*, 98–107.

[99] Xia, Y.; Cebrián, R.; Xu, C.; Jong, A. d.; Wu, W.; Kuipers, O. P. Elucidating the Mechanism by Which Synthetic Helper Peptides Sensitize Pseudomonas Aeruginosa to Multiple Antibiotics. *PLoS Pathog.* **2021**, *17*, e1009909.

[100] Hamzah, N.; Singhal, N.; Padhye, L.; Swift, S. Effect of Surfactants on Aspergillus Brasiliensis ATCC 16404 Physicochemical Properties. *J. Environ. Chem. Eng.* **2018**, *6*, 3392–3398.

[101] Yasir, M.; Dutta, D.; Willcox, M. D. P. Mode of Action of the Antimicrobial Peptide Mel4 Is Independent of Staphylococcus Aureus Cell Membrane Permeability. *PLoS One* **2019**, *14*, e0215703.

[102] Parker, J. P.; Devocelle, M.; Morgan, M. P.; Marmion, C. J. Derivatisation of Buforin IIb, a Cationic Henicosapeptide, to Afford Its Complexation to Platinum (II) Resulting in a Novel Platinum (II)–Buforin IIb Conjugate With Anti-Cancer Activity. *Dalton Trans.* **2016**, *45*, 13038–13041.

[103] He, S.-w.; Wang, G.-h.; Yue, B.; Zhou, S.; Zhang, M. TO17: A Teleost Antimicrobial Peptide That Induces Degradation of Bacterial Nucleic Acids and Inhibits Bacterial Infection in Red Drum, Sciaenops Ocellatus. *Fish Shellfish Immunol.* **2018**, *72*, 639–645.

[104] Di Somma, A.; Canè, C.; Moretta, A.; Duilio, A. Interaction of Temporin-L Analogues With the E. Coli FtsZ Protein. *Antibiotics* **2021**, *10*, 704.

[105] Tymoszewska, A.; Aleksandrzak-Piekarczyk, T. The Lactococcal DgkB (YecE) and DxsA Genes for Lipid Metabolism Are Involved in the Resistance to Cell Envelope-Acting Antimicrobials. *Int. J. Mol. Sci.* **2021**, *22*, 1014.

[106] Singleton, A. H.; Bergum, O. E. T.; Søgaard, C. K.; Røst, L. M.; Olsen, C. E.; Blindheim, F. H.; Ræder, S. B.; Bjørnstad, F. A.; Sundby, E.; Hoff, B. H. et al. Activation of Multiple Stress Responses in Staphylococcus Aureus Substantially Lowers the Minimal Inhibitory Concentration When Combining Two Novel Antibiotic Drug Candidates. *Front. Microbiol.* **2023**, *14*, 1260120.

[107] Kim, S.; Hwang, J. S.; Lee, D. G. Lactoferricin B Like Peptide Triggers Mitochondrial Disruption-Mediated Apoptosis by Inhibiting Respiration Under Nitric Oxide Accumulation in Candida Albicans. *IUBMB Life* **2020**, *72*, 1515–1527.

[108] Pavithrra, G.; Rajasekaran, R. Gramicidin Peptide to Combat Antibiotic Resistance: A Review. *Int. J. Pept. Res. Ther.* **2020**, *26*, 191–199.

[109] Jiang, S.; Zha, Y.; Zhao, T.; Jin, X.; Zhu, R.; Wei, S.; Wang, R.; Song, Y.; Li, L.; Lyu, J. et al. Antimicrobial Peptide Temporin Derivatives Inhibit Biofilm Formation and Virulence Factor Expression of Streptococcus Mutans. *Front. Microbiol.* **2023**, *14*, 1267389.

[110] Mishra, B.; Wang, G. Individual and Combined Effects of Engineered Peptides and Antibiotics on Pseudomonas Aeruginosa Biofilms. *Pharmaceuticals* **2017**, *10*, 58.

[111] De la Fuente-Núñez, C.; Reffuveille, F.; Haney, E. F.; Straus, S. K.; Hancock, R. E. W. Broad-Spectrum Anti-Biofilm Peptide That Targets a Cellular Stress Response. *PLoS Pathog.* **2014**, *10*, e1004152.

[112] Sun, Z.; Xi, J.; Yang, C.; Cong, W. Quorum Sensing Regulation Methods and Their Effects on Biofilm in Biological Waste Treatment Systems: A Review. *Front. Environ. Sci. Eng.* **2022**, *16*, 1–13.

[113] Memariani, H.; Memariani, M. Antibiofilm Properties of Cathelicidin LL-37: An In-Depth Review. *World J. Microbiol. Biotechnol.* **2023**, *39*, 99.

[114] Roy, R.; Tiwari, M.; Donelli, G.; Tiwari, V. Strategies for Combating Bacterial Biofilms: A Focus on Anti-Biofilm Agents and Their Mechanisms of Action. *Virulence* **2018**, *9*, 522–554.

[115] Gordya, N.; Yakovlev, A.; Kruglikova, A.; Tulin, D.; Potolitsina, E.; Suborova, T.; Bordo, D.; Rosano, C.; Chernysh, S. Natural Antimicrobial Peptide Complexes in the Fighting of Antibiotic Resistant Biofilms: Calliphora Vicina Medicinal Maggots. *PLoS One* **2017**, *12*, e0173559.

[116] Libardo, M. D. J.; Bahar, A. A.; Ma, B.; Fu, R.; McCormick, L. E.; Zhao, J.; McCallum, S. A.; Nussinov, R.; Ren, D.; Angeles-Boza, A. M. et al. Nuclease Activity Gives an Edge to Host-Defense Peptide Piscidin 3 Over Piscidin 1, Rendering It More Effective Against Persisters and Biofilms. *FEBS J.* **2017**, *284*, 3662–3683.

[117] Li, H.; Niu, J.; Wang, X.; Niu, M.; Liao, C. The Contribution of Antimicrobial Peptides to Immune Cell Function: A Review of Recent Advances. *Pharmaceutics* **2023**, *15*, 2278.

[118] Urmi, U. L.; Vijay, A. K.; Kuppusamy, R.; Islam, S.; Willcox, M. D. P. A Review of the Antiviral Activity of Cationic Antimicrobial Peptides. *Peptides* **2023**, *166*, 171024.

[119] Bogdanov, I. V.; Streltsova, M. A.; Kovalenko, E. I.; Sapozhnikov, A. M.; Panteleev, P. V.; Ovchinnikova, T. V. Epithelial-Immune Cell Crosstalk Determines the Activation of Immune Cells In Vitro by the Human Cathelicidin LL-37 at Low Physiological Concentrations. *Biomolecules* **2023**, *13*, 1316.

[120] Kościuczuk, E. M.; Lisowski, P.; Jarczak, J.; Strzałkowska, N.; Jóźwik, A.; Horbańczuk, J.; Krzyżewski, J.; Zwierzchowski, L.; Bagnicka, E. Cathelicidins: Family of Antimicrobial Peptides. A Review. *Mol. Biol. Rep.* **2012**, *39*, 10957–10970.

[121] Zanetti, M. Cathelicidins, Multifunctional Peptides of the Innate Immunity. *J. Leukoc. Biol.* **2004**, *75*, 39–48.

[122] Johansson, J.; Gudmundsson, G. H.; Rottenberg, M. E.; Berndt, K. D.; Agerberth, B. Conformation-Dependent Antibacterial Activity of the Naturally Occurring Human Peptide LL-37. *J. Biol. Chem.* **1998**, *273*, 3718–3724.

[123] Bhattacharjya, S.; Zhang, Z.; Ramamoorthy, A. LL-37: Structures, Antimicrobial Activity, and Influence on Amyloid-Related Diseases. *Biomolecules* **2024**, *14*, 320.

[124] Lenarčič, B.; Ritonja, A.; Dolenc, I.; Stoka, V.; Berbič, S.; Pungerčar, J.; Štrukelj, B.; Turk, V. Pig Leukocyte Cysteine Proteinase Inhibitor (PLCPI), a New Member of the Stefin Family. *FEBS Lett.* **1993**, *336*, 289–292.

[125] Ritonja, A.; Kopitar, M.; Jerala, R.; Turk, V. Primary Structure of a New Cysteine Proteinase Inhibitor from Pig Leucocytes. *FEBS Lett.* **1989**, *255*, 211–214.

[126] Storici, P.; Tossi, A.; Lenarčič, B.; Romeo, D. Purification and Structural Characterization of Bovine Cathelicidins, Precursors of Antimicrobial Peptides. *Eur. J. Biochem.* **1996**, *238*, 769–776.

[127] Scocchi, M.; Wang, S.; Zanetti, M. Structural Organization of the Bovine Cathelicidin Gene Family and Identification of a Novel Member. *FEBS Lett.* **1997**, *417*, 311–315.

[128] Porcelli, F.; Verardi, R.; Shi, L.; Henzler-Wildman, K. A.; Ramamoorthy, A.; Veglia, G. NMR Structure of the Cathelicidin-Derived Human Antimicrobial Peptide LL-37 in Dodecylphosphocholine Micelles. *Biochemistry* **2008**, *47*, 5565–5572.

[129] Ding, B.; Soblosky, L.; Nguyen, K.; Geng, J.; Yu, X.; Ramamoorthy, A.; Chen, Z. Physiologically-Relevant Modes of Membrane Interactions by the Human Antimicrobial Peptide, LL-37, Revealed by SFG Experiments. *Sci. Rep.* **2013**, *3*, 1854.

[130] Wang, G. Structures of Human Host Defense Cathelicidin LL-37 and Its Smallest Antimicrobial Peptide KR-12 in Lipid Micelles. *J. Biol. Chem.* **2008**, *283*, 32637–32643.

[131] Henzler Wildman, K. A.; Lee, D.-K.; Ramamoorthy, A. Mechanism of Lipid Bilayer Disruption by the Human Antimicrobial Peptide, LL-37. *Biochemistry* **2003**, *42*, 6545–6558.

[132] Mücke, P.-A.; Maaß, S.; Kohler, T. P.; Hammerschmidt, S.; Becher, D. Proteomic Adaptation of *Streptococcus pneumoniae* to the Human Antimicrobial Peptide LL-37. *Microorganisms* **2020**, *8*, 413.

[133] Sun, C.; Zhu, M.; Yang, Z.; Pan, X.; Zhang, Y.; Wang, Q.; Xiao, W. LL-37 Secreted by Epithelium Promotes Fibroblast Collagen Production: A Potential Mechanism of Small Airway Remodeling in Chronic Obstructive Pulmonary Disease. *Lab. Invest.* **2014**, *94*, 991–1002.

[134] Tripathi, S.; Wang, G.; White, M.; Rynkiewicz, M.; Seaton, B.; Hartshorn, K. Identifying the Critical Domain of LL-37 Involved in Mediating Neutrophil Activation

in the Presence of Influenza Virus: Functional and Structural Analysis. *PLoS One* **2015**, *10*, e0133454.

[135] Dhiman, A.; Talukdar, S.; Chaubey, G. K.; Dilawari, R.; Modanwal, R.; Chaudhary, S.; Patidar, A.; Boradia, V. M.; Kumbhar, P.; Raje, C. I. et al. Regulation of Macrophage Cell Surface GAPDH Alters LL-37 Internalization and Downstream Effects in the Cell. *J. Innate Immun.* **2023**, *15*, 581–598.

[136] Heilborn, J. D.; Nilsson, M. F.; Jimenez, C. I. C.; Sandstedt, B.; Borregaard, N.; Tham, E.; Sørensen, O. E.; Weber, G.; Ståhle, M. Antimicrobial Protein hCAP18/LL-37 Is Highly Expressed in Breast Cancer and Is a Putative Growth Factor for Epithelial Cells. *Int. J. Cancer* **2005**, *114*, 713–719.

[137] Chen, X.; Zou, X.; Qi, G.; Tang, Y.; Guo, Y.; Si, J.; Liang, L. Roles and Mechanisms of Human Cathelicidin LL-37 in Cancer. *Cell. Physiol. Biochem.* **2018**, *47*, 1060–1073.

[138] Piktel, E.; Niemirowicz, K.; Wnorowska, U.; Watek, M.; Wollny, T.; Głuszek, K.; Góźdź, S.; Levental, I.; Bucki, R. The Role of Cathelicidin LL-37 in Cancer Development. *Arch. Immunol. Ther. Exp.* **2016**, *64*, 33–46.

[139] Wu, W. K. K.; Wang, G.; Coffelt, S. B.; Betancourt, A. M.; Lee, C. W.; Fan, D.; Wu, K.; Yu, J.; Sung, J. J. Y.; Cho, C. H. Emerging Roles of the Host Defense Peptide LL-37 in Human Cancer and Its Potential Therapeutic Applications. *Int. J. Cancer* **2010**, *127*, 1741–1747.

[140] Verjans, E.-T.; Zels, S.; Luyten, W.; Landuyt, B.; Schoofs, L. Molecular Mechanisms of LL-37-Induced Receptor Activation: An Overview. *Peptides* **2016**, *85*, 16–26.

[141] Yang, B.; Good, D.; Mosaiab, T.; Liu, W.; Ni, G.; Kaur, J.; Liu, X.; Jessop, C.; Yang, L.; Fadhil, R. et al. Significance of LL-37 on Immunomodulation and Disease Outcome. *Biomed. Res. Int.* **2020**, *2020*, 8349712.

[142] Doss, M.; White, M. R.; Tecle, T.; Hartshorn, K. L. Human Defensins and LL-37 in Mucosal Immunity. *J. Leukoc. Biol.* **2010**, *87*, 79–92.

[143] Wang, G.; Narayana, J. L.; Mishra, B.; Zhang, Y.; Wang, F.; Wang, C.; Zarena, D.; Lushnikova, T.; Wang, X. Design of Antimicrobial Peptides: Progress Made with Human Cathelicidin LL-37. *Antimicrob. Pept.* **2019**, 215–240.

[144] Bucki, R.; Leszczyńska, K.; Namiot, A.; Sokołowski, W. Cathelicidin LL-37: A Multitask Antimicrobial Peptide. *Arch. Immunol. Ther. Exp.* **2010**, *58*, 15–25.

[145] Jiang, X.; Yang, C.; Qiu, J.; Ma, D.; Xu, C.; Hu, S.; Han, W.; Yuan, B.; Lu, Y. Nanomolar LL-37 Induces Permeability of a Biomimetic Mitochondrial Membrane. *Nanoscale* **2022**, *14*, 17654–17660.

[146] Mitra, A.; Paul, S. Pathways of hLL-$37_{17–29}$ Aggregation Give Insight into the Mechanism of α-Amyloid Formation. *J. Phys. Chem. B* **2023**, *127*, 8162–8175.

[147] Li, X.; Li, Y.; Han, H.; Miller, D. W.; Wang, G. Solution Structures of Human LL-37 Fragments and NMR-Based Identification of a Minimal Membrane-Targeting Antimicrobial and Anticancer Region. *J. Am. Chem. Soc.* **2006**, *128*, 5776–5785.

[148] Gunasekera, S.; Muhammad, T.; Strömstedt, A. A.; Rosengren, K. J.; Göransson, U. Backbone Cyclization and Dimerization of LL-37-Derived Peptides Enhance Antimicrobial Activity and Proteolytic Stability. *Front. Microbiol.* **2020**, *11*, 168.

[149] Yun, H.; Min, H. J.; Lee, C. W. NMR Structure and Bactericidal Activity of KR-12 Analog Derived from Human LL-37 as a Potential Cosmetic Preservative. *J. Anal. Sci. Technol.* **2020**, *11*, 1–9.

[150] Allen, M. P.; Tildesley, D. J. *Computer Simulation of Liquids*, 2nd ed.; Oxford University Press, 2017.

[151] Tuckerman, M. E. *Statistical Mechanics: Theory and Molecular Simulation*, 1st ed.; Oxford University Press, 2010.

[152] Hollingsworth, S. A.; Dror, R. O. Molecular Dynamics Simulation for All. *Neuron* **2018**, *99*, 1129–1143.

[153] Molgedey, L.; Schuster, H. G. Separation of a Mixture of Independent Signals Using Time Delayed Correlations. *Phys. Rev. Lett.* **1994**, *72*, 3634.

[154] Naritomi, Y.; Fuchigami, S. Slow Dynamics of a Protein Backbone in Molecular Dynamics Simulation Revealed by Time-Structure Based Independent Component Analysis. *J. Chem. Phys.* **2013**, *139*.

[155] Metzner, P.; Schütte, C.; Vanden-Eijnden, E. Transition Path Theory for Markov Jump Processes. *Multiscale Model. Simul.* **2009**, *7*, 1192–1219.

[156] Tarjan, R. Depth-First Search and Linear Graph Algorithms. *SIAM J. Comput.* **1972**, *1*, 146–160.

[157] Scherer, M. K.; Trendelkamp-Schroer, B.; Paul, F.; Pérez-Hernández, G.; Hoffmann, M.; Plattner, N.; Wehmeyer, C.; Prinz, J.-H.; Noé, F. PyEMMA 2: A Software Package for Estimation, Validation, and Analysis of Markov Models. *J. Chem. Theo. Comput.* **2015**, *11*, 5525–5542.

[158] Rambaran, R. N.; Serpell, L. C. Amyloid Fibrils. *Prion* **2008**, *2*, 112–117.

[159] Roy, R.; Paul, S. Illustrating the Effect of Small Molecules Derived from Natural Resources on Amyloid Peptides. *J. Phys. Chem. B* **2023**, *127*, 600–615.

[160] Tayeb-Fligelman, E.; Tabachnikov, O.; Moshe, A.; Goldshmidt-Tran, O.; Sawaya, M. R.; Coquelle, N.; Colletier, J.-P.; Landau, M. The Cytotoxic *Staphylococcus aureus* PSMα3 Reveals a Cross-α Amyloid-Like Fibril. *Science* **2017**, *355*, 831–833.

[161] Tayeb-Fligelman, E.; Salinas, N.; Tabachnikov, O.; Landau, M. *Staphylococcus aureus* PSMα3 Cross-α Fibril Polymorphism and Determinants of Cytotoxicity. *Structure* **2020**, *28*, 301–313.

[162] Nelson, R.; Sawaya, M. R.; Balbirnie, M.; Madsen, A. Ø.; Riekel, C.; Grothe, R.; Eisenberg, D. Structure of the Cross-β Spine of Amyloid-Like Fibrils. *Nature* **2005**, *435*, 773–778.

[163] Sawaya, M. R.; Sambashivan, S.; Nelson, R.; Ivanova, M. I.; Sievers, S. A.; Apostol, M. I.; Thompson, M. J.; Balbirnie, M.; Wiltzius, J. J. W.; McFarlane, H. T.

et al. Atomic Structures of Amyloid Cross-β Spines Reveal Varied Steric Zippers. *Nature* **2007**, *447*, 453–457.

[164] Paravastu, A. K.; Leapman, R. D.; Yau, W.-M.; Tycko, R. Molecular Structural Basis for Polymorphism in Alzheimer's β-Amyloid Fibrils. *Proc. Natl. Acad. Sci.* **2008**, *105*, 18349–18354.

[165] Colletier, J.-P.; Laganowsky, A.; Landau, M.; Zhao, M.; Soriaga, A. B.; Goldschmidt, L.; Flot, D.; Cascio, D.; Sawaya, M. R.; Eisenberg, D. Molecular Basis for Amyloid-β Polymorphism. *Proc. Natl. Acad. Sci.* **2011**, *108*, 16938–16943.

[166] Eisenberg, D.; Jucker, M. The Amyloid State of Proteins in Human Diseases. *Cell* **2012**, *148*, 1188–1203.

[167] Knowles, T. P.; Vendruscolo, M.; Dobson, C. M. The Amyloid State and Its Association with Protein Misfolding Diseases. *Nat. Rev. Mol. Cell Biol.* **2014**, *15*, 384–396.

[168] Sunde, M.; Serpell, L. C.; Bartlam, M.; Fraser, P. E.; Pepys, M. B.; Blake, C. C. Common Core Structure of Amyloid Fibrils by Synchrotron X-ray Diffraction. *J. Mol. Biol.* **1997**, *273*, 729–739.

[169] Bera, S.; Mondal, S.; Xue, B.; Shimon, L. J.; Cao, Y.; Gazit, E. Rigid Helical-Like Assemblies from a Self-Aggregating Tripeptide. *Nat. Mater.* **2019**, *18*, 503–509.

[170] Wei, G.; Su, Z.; Reynolds, N. P.; Arosio, P.; Hamley, I. W.; Gazit, E.; Mezzenga, R. Self-Assembling Peptide and Protein Amyloids: From Structure to Tailored Function in Nanotechnology. *Chemical Society Reviews* **2017**, *46*, 4661–4708.

[171] Schnaider, L.; Brahmachari, S.; Schmidt, N. W.; Mensa, B.; Shaham-Niv, S.; Bychenko, D.; Adler-Abramovich, L.; Shimon, L. J.; Kolusheva, S.; DeGrado, W. F. et al. Self-Assembling Dipeptide Antibacterial Nanostructures with Membrane Disrupting Activity. *Nat. Commun.* **2017**, *8*, 1365.

[172] Mondal, S.; Adler-Abramovich, L.; Lampel, A.; Bram, Y.; Lipstman, S.; Gazit, E. Formation of Functional Super-Helical Assemblies by Constrained Single Heptad Repeat. *Nature Commun.* **2015**, *6*, 8615.

[173] Rufo, C. M.; Moroz, Y. S.; Moroz, O. V.; Stöhr, J.; Smith, T. A.; Hu, X.; DeGrado, W. F.; Korendovych, I. V. Short Peptides Self-Assemble to Produce Catalytic Amyloids. *Nat. Chem.* **2014**, *6*, 303–309.

[174] Makhlynets, O. V.; Gosavi, P. M.; Korendovych, I. V. Short Self-Assembling Peptides Are Able to Bind to Copper and Activate Oxygen. *Angew. Chem. Int. Ed.* **2016**, *55*, 9017–9020.

[175] Tao, K.; Makam, P.; Aizen, R.; Gazit, E. Self-Assembling Peptide Semiconductors. *Science* **2017**, *358*, 1–7.

[176] Yan, X.; Zhu, P.; Li, J. Self-Assembly and Application of Diphenylalanine-Based Nanostructures. *Chem. Soc. Rev.* **2010**, *39*, 1877–1890.

[177] Kim, S.; Kim, J. H.; Lee, J. S.; Park, C. B. Beta-Sheet-Forming, Self-Assembled Peptide Nanomaterials Towards Optical, Energy, and Healthcare Applications. *Small* **2015**, *11*, 3623–3640.

[178] Reches, M.; Gazit, E. Casting Metal Nanowires Within Discrete Self-Assembled Peptide Nanotubes. *Science* **2003**, *300*, 625–627.

[179] Jang, H.; Arce, F. T.; Mustata, M.; Ramachandran, S.; Capone, R.; Nussinov, R.; Lal, R. Antimicrobial Protegrin-1 Forms Amyloid-Like Fibrils with Rapid Kinetics Suggesting a Functional Link. *Biophys. J.* **2011**, *100*, 1775–1783.

[180] Zhao, H.; Sood, R.; Jutila, A.; Bose, S.; Fimland, G.; Nissen-Meyer, J.; Kinnunen, P. K. Interaction of the Antimicrobial Peptide Pheromone Plantaricin A with Model Membranes: Implications for a Novel Mechanism of Action. *Biochim. Biophys. Acta, Biomembr.* **2006**, *1758*, 1461–1474.

[181] Auvynet, C.; El Amri, C.; Lacombe, C.; Bruston, F.; Bourdais, J.; Nicolas, P.; Rosenstein, Y. Structural Requirements for Antimicrobial Versus Chemoattractant Activities for Dermaseptin S9. *FEBS J.* **2008**, *275*, 4134–4151.

[182] Salinas, N.; Tayeb-Fligelman, E.; Sammito, M. D.; Bloch, D.; Jelinek, R.; Noy, D.; Usón, I.; Landau, M. The Amphibian Antimicrobial Peptide Uperin 3.5 is a Cross-α/Cross-β Chameleon Functional Amyloid. *Proc. Natl. Acad. Sci.* **2021**, *118*, 1–8.

[183] Xhindoli, D.; Pacor, S.; Benincasa, M.; Scocchi, M.; Gennaro, R.; Tossi, A. The Human Cathelicidin LL-37-A Pore-Forming Antibacterial Peptide and Host-Cell Modulator. *Biochim. Biophys. Acta, Biomembr.* **2016**, *1858*, 546–566.

[184] Lai, Y.; Gallo, R. L. AMPed Up Immunity: How Antimicrobial Peptides Have Multiple Roles in Immune Defense. *Trends Immunol.* **2009**, *30*, 131–141.

[185] Dürr, U. H.; Sudheendra, U.; Ramamoorthy, A. LL-37, The Only Human Member of the Cathelicidin Family of Antimicrobial Peptides. *Biochim. Biophys. Acta, Biomembr.* **2006**, *1758*, 1408–1425.

[186] Vandamme, D.; Landuyt, B.; Luyten, W.; Schoofs, L. A Comprehensive Summary of LL-37, The Factotum Human Cathelicidin Peptide. *Cell. Immunol.* **2012**, *280*, 22–35.

[187] Wang, G.; Mishra, B.; Epand, R. F.; Epand, R. M. High-Quality 3D Structures Shine Light on Antibacterial, Anti-Biofilm and Antiviral Activities of Human Cathelicidin LL-37 and Its Fragments. *Biochim. Biophys. Acta, Biomembr.* **2014**, *1838*, 2160–2172.

[188] Yang, D.; Chen, Q.; Schmidt, A. P.; Anderson, G. M.; Wang, J. M.; Wooters, J.; Oppenheim, J. J.; Chertov, O. LL-37, the Neutrophil Granule–and Epithelial Cell–Derived Cathelicidin, Utilizes Formyl Peptide Receptor–Like 1 (FPRL1) as a Receptor to Chemoattract Human Peripheral Blood Neutrophils, Monocytes, and T Cells. *J. Exp. Med.* **2000**, *192*, 1069–1074.

[189] Kahlenberg, J. M.; Kaplan, M. J. Little Peptide, Big Effects: The Role of LL-37 in Inflammation and Autoimmune Disease. *J. Immunol.* **2013**, *191*, 4895–4901.

[190] Scott, M. G.; Davidson, D. J.; Gold, M. R.; Bowdish, D.; Hancock, R. E. The Human Antimicrobial Peptide LL-37 is a Multifunctional Modulator of Innate Immune Responses. *J. Immunol.* **2002**, *169*, 3883–3891.

[191] Hölzl, M. A.; Hofer, J.; Steinberger, P.; Pfistershammer, K.; Zlabinger, G. J. Host Antimicrobial Proteins as Endogenous Immunomodulators. *Immunol. Lett.* **2008**, *119*, 4–11.

[192] Yin, J.; Fu-Shin, X. Y. LL-37 via EGFR Transactivation to Promote High Glucose–Attenuated Epithelial Wound Healing In Organ-Cultured Corneas. *Invest. Ophthalmol. Visual Sci.* **2010**, *51*, 1891–1897.

[193] Carretero, M.; Escámez, M. J.; García, M.; Duarte, B.; Holguín, A.; Retamosa, L.; Jorcano, J. L.; Del Río, M.; Larcher, F. In vitro and In Vivo Wound Healing-Promoting Activities of Human Cathelicidin LL-37. *J. Invest. Dermatol.* **2008**, *128*, 223–236.

[194] Steinstraesser, L.; Lam, M. C.; Jacobsen, F.; Porporato, P. E.; Chereddy, K. K.; Becerikli, M.; Stricker, I.; Hancock, R. E. W.; Lehnhardt, M.; Sonveaux, P. et al. Skin Electroporation of a Plasmid Encoding hCAP-18/LL-37 Host Defense Peptide Promotes Wound Healing. *Mol.Ther.* **2014**, *22*, 734–742.

[195] Grönberg, A.; Mahlapuu, M.; Ståhle, M.; Whately-Smith, C.; Rollman, O. Treatment with LL-37 is Safe and Effective in Enhancing Healing of Hard-to-Heal Venous Leg Ulcers: A Randomized, Placebo-Controlled Clinical Trial. *Wound Repair Regen.* **2014**, *22*, 613–621.

[196] Pütsep, K.; Carlsson, G.; Boman, H. G.; Andersson, M. Deficiency of Antibacterial Peptides in Patients with Morbus Kostmann: An Observation Study. *Lancet* **2002**, *360*, 1144–1149.

[197] Ong, P. Y.; Ohtake, T.; Brandt, C.; Strickland, I.; Boguniewicz, M.; Ganz, T.; Gallo, R. L.; Leung, D. Y. Endogenous antimicrobial peptides and skin infections in atopic dermatitis. *N.Engl. J. Med.* **2002**, *347*, 1151–1160.

[198] Sood, R.; Domanov, Y.; Pietiäinen, M.; Kontinen, V. P.; Kinnunen, P. K. Binding of LL-37 to Model Biomembranes: Insight Into Target vs Host Cell Recognition. *Biochim. Biophys. Acta, Biomembr.* **2008**, *1778*, 983–996.

[199] Shahmiri, M.; Enciso, M.; Adda, C. G.; Smith, B. J.; Perugini, M. A.; Mechler, A. Membrane Core-Specific Antimicrobial Action of Cathelicidin LL-37 Peptide Switches Between Pore and Nanofibre Formation. *Sci. Rep.* **2016**, *6*, 1–11.

[200] Lee, E. Y.; Zhang, C.; Di Domizio, J.; Jin, F.; Connell, W.; Hung, M.; Malkoff, N.; Veksler, V.; Gilliet, M.; Ren, P. et al. Helical Antimicrobial Peptides Assemble Into Protofibril Scaffolds that Present Ordered dsDNA to TLR9. *Nat. Commun.* **2019**, *10*, 1–10.

[201] Wang, G.; Epand, R. F.; Mishra, B.; Lushnikova, T.; Thomas, V. C.; Bayles, K. W.; Epand, R. M. Decoding the Functional Roles of Cationic Side Chains of the Major Antimicrobial Region of Human Cathelicidin LL-37. *Antimicrob. Agents Chemother.* **2012**, *56*, 845–856.

[202] Nagant, C.; Pitts, B.; Nazmi, K.; Vandenbranden, M.; Bolscher, J.; Stewart, P. S.; Dehaye, J.-P. Identification of Peptides Derived from the Human Antimicrobial Peptide LL-37 Active Against Biofilms Formed by *Pseudomonas aeruginosa* Using a Library of Truncated Fragments. *Antimicrob. Agents Chemother.* **2012**, *56*, 5698–5708.

[203] Wang, G.; Watson, K. M.; Buckheit Jr, R. W. Anti-Human Immunodeficiency Virus Type 1 Activities of Antimicrobial Peptides Derived from Human and Bovine Cathelicidins. *Antimicrob. Agents Chemother.* **2008**, *52*, 3438–3440.

[204] Schmidtchen, A.; Frick, I.-M.; Andersson, E.; Tapper, H.; Björck, L. Proteinases of Common Pathogenic Bacteria Degrade and Inactivate the Antibacterial Peptide LL-37. *Mol. Microbiol.* **2002**, *46*, 157–168.

[205] Engelberg, Y.; Landau, M. The Human LL-37 (17-29) Antimicrobial Peptide Reveals a Functional Supramolecular Structure. *Nat. Commun.* **2020**, *11*, 3894.

[206] Sengupta, U.; Carballo-Pacheco, M.; Strodel, B. Automated Markov State Models for Molecular Dynamics Simulations of Aggregation and Self-Assembly. *J. Chem. Phys.* **2019**, *150*, 115101.

[207] Illig, A.-M.; Strodel, B. Performance of Markov State Models and Transition Networks on Characterizing Amyloid Aggregation Pathways from MD Data. *J. Chem. Theo. Comput.* **2020**, *16*, 7825–7839.

[208] Bowman, G. R.; Beauchamp, K. A.; Boxer, G.; Pande, V. S. Progress and Challenges in the Automated Construction of Markov State Models for Full Protein Systems. *J. Chem. Phys.* **2009**, *131*, 124101.

[209] Bowman, G. R.; Huang, X.; Pande, V. S. Using Generalized Ensemble Simulations and Markov State Models to Identify Conformational States. *Methods* **2009**, *49*, 197–201.

[210] Bowman, G. R.; Huang, X.; Pande, V. S. Network Models for Molecular Kinetics and Their Initial Applications to Human Health. *Cell research* **2010**, *20*, 622–630.

[211] Huang, X.; Bowman, G. R.; Bacallado, S.; Pande, V. S. Rapid Equilibrium Sampling Initiated from Nonequilibrium Data. *Proc. Natl. Acad. Sci.* **2009**, *106*, 19765–19769.

[212] Yang, Y. I.; Gao, Y. Q. Computer Simulation Studies of Aβ_{37-42} Aggregation Thermodynamics and Kinetics in Water and Salt Solution. *J. Phys. Chem. B* **2015**, *119*, 662–670.

[213] Noé, F.; Schütte, C.; Vanden-Eijnden, E.; Reich, L.; Weikl, T. R. Constructing the Equilibrium Ensemble of Folding Pathways from Short Off-Equilibrium Simulations. *Proc. Natl. Acad. Sci.* **2009**, *106*, 19011–19016.

[214] Vanden-Eijnden, E.; E, W. Transition-Path Theory and Path-Finding Algorithms for the Study of Rare Events. *Ann. Rev. Phys. Chem.* **2010**, *61*, 391–420.

[215] E, W.; Vanden-Eijnden, E. Towards a Theory of Transition Paths. *J. Stat. Phys.* **2006**, *123*, 503–523.

[216] Case, D. A.; Ben-Shalom, I. Y.; Brozell, S. R.; Cerutti, D. S.; Cheatham III, T. E.; Cruzeiro, V. W. D.; Darden, T. A.; Duke, R. E.; Ghoreishi, D.; Gilson, M. K. et al. Amber 18. 2018; University of California: San Francisco, CA.

[217] Søndergaard, C. R.; Olsson, M. H. M.; Rostkowski, M.; Jensen, J. H. Improved Treatment of Ligands and Coupling Effects in Empirical Calculation and Rationalization of pK_a values. *J. Chem. Theo. Comput.* **2011**, *7*, 2284–2295.

[218] Olsson, M. H. M.; Søndergaard, C. R.; Rostkowski, M.; Jensen, J. H. PROPKA3: Consistent Treatment of Internal and Surface Residues in Empirical pK_a predictions. *J. Chem. Theory Comput.* **2011**, *7*, 525–537.

[219] Maier, J. A.; Martinez, C.; Kasavajhala, K.; Wickstrom, L.; Hauser, K. E.; Simmerling, C. ff14SB: Improving the Accuracy of Protein Side Chain and Backbone Parameters from ff99SB. *J. Chem. Theo. Comput.* **2015**, *11*, 3696–3713.

[220] Jorgensen, W. L.; Chandrasekhar, J.; Madura, J. D.; Impey, R. W.; Klein, M. L. Comparison of Simple Potential Functions for Simulating Liquid Water. *J. Chem. Phys.* **1983**, *79*, 926–935.

[221] Martínez, L.; Andrade, R.; Birgin, E. G.; Martínez, J. M. PACKMOL: A Package for Building Initial Configurations for Molecular Dynamics Simulations. *J. Comput. Chem.* **2009**, *30*, 2157–2164.

[222] Schmit, J. D.; Kariyawasam, N. L.; Needham, V.; Smith, P. E. SLTCAP: A Simple Method for Calculating the Number of Ions Needed for MD Simulation. *J. Chem. Theo. Comput,* **2018**, *14*, 1823–1827.

[223] Joung, I. S.; Cheatham III, T. E. Determination of Alkali and Halide Monovalent Ion Parameters for Use in Explicitly Solvated Biomolecular Simulations. *J. Phys. Chem.* **2008**, *112*, 9020–9041.

[224] Berendsen, H. J. C.; Postma, J. P. M.; van Gunsteren, W. F.; DiNola, A.; Haak, J. R. Molecular Dynamics with Coupling to an External Bath. *J. Chem. Phys.* **1984**, *81*, 3684–3690.

[225] Pastor, R. W.; Brooks, B. R.; Szabo, A. An Analysis of the Accuracy of Langevin and Molecular Dynamics Algorithms. *Mol. Phys.* **1988**, *65*, 1409–1419.

[226] Ryckaert, J.-P.; Ciccotti, G.; Berendsen, H. J. C. Numerical Integration of the Cartesian Equations of Motion of a System with Constraints: Molecular Dynamics of n-Alkanes. *J. Comput. Phys.* **1977**, *23*, 327–341.

[227] Essmann, U.; Perera, L.; Berkowitz, M. L.; Darden, T.; Lee, H.; Pedersen, L. G. A Smooth Particle Mesh Ewald Method. *J. Chem. Phys.* **1995**, *103*, 8577–8593.

[228] Salomon-Ferrer, R.; Gotz, A. W.; Poole, D.; Le Grand, S.; Walker, R. C. Routine Microsecond Molecular Dynamics Simulations with AMBER on GPUs. 2. Explicit Solvent Particle Mesh Ewald. *J. Chem. Theory Comput.* **2013**, *9*, 3878–3888.

[229] Stoddard, S. D. Identifying Clusters in Computer Experiments on Systems of Particles. *J. Comput. Phys.* **1978**, *27*, 291–293.

[230] Roe, D. R.; Cheatham III, T. E. PTRAJ and CPPTRAJ: Software for Processing and Analysis of Molecular Dynamics Trajectory Data. *J. Chem. Theory Comput.* **2013**, *9*, 3084–3095.

[231] Roy, R.; Paul, S. Disparate Effect of Hybrid Peptidomimetics Containing Isomers of Aminobenzoic Acid on hIAPP Aggregation. *J. Phys. Chem. B* **2022**, *126*, 10427–10444.

[232] Hou, T.; Wang, J.; Li, Y.; Wang, W. Assessing the Performance of the MM/PBSA and MM/GBSA Methods. 1. The Accuracy of Binding Free Energy Calculations Based on Molecular Dynamics Simulations. *J. Chem. Inf. Model.* **2011**, *51*, 69–82.

[233] Miller III, B. R.; McGee Jr, T. D.; Swails, J. M.; Homeyer, N.; Gohlke, H.; Roitberg, A. E. MMPBSA.py: An Efficient Program for End-State Free Energy Calculations. *J. Chem. Theo. Comput.* **2012**, *8*, 3314–3321.

[234] Roy, R.; Paul, S. hIAPP-Amyloid-Core Derived d-Peptide Prevents hIAPP Aggregation and Destabilizes Its Protofibrils. *J. Phys. Chem. B* **2022**, *126*, 822–839.

[235] Carballo-Pacheco, M.; Strodel, B. Advances in the Simulation of Protein Aggregation at the Atomistic Scale. *J. Phys. Chem. B* **2016**, *120*, 2991–2999.

[236] Hu, X.; Crick, S. L.; Bu, G.; Frieden, C.; Pappu, R. V.; Lee, J.-M. Amyloid Seeds Formed by Cellular Uptake, Concentration, and Aggregation of the Amyloid-β Peptide. *Proc. Natl. Acad. Sci.* **2009**, *106*, 20324–20329.

[237] Singh, G.; Brovchenko, I.; Oleinikova, A.; Winter, R. Peptide Aggregation in Finite Systems. *Biophys. J.* **2008**, *95*, 3208–3221.

[238] Sun, X.; Lai, L. Protein Fibrils Formed by Rationally Designed α-Helical Peptides. *Langmuir* **2020**, *36*, 6126–6131.

[239] Liu, C.; Henning-Knechtel, A.; Österlund, N.; Wu, J.; Wang, G.; Gräslund, R. A. O.; Kirmizialtin, S.; Luo, J. Oligomer Dynamics of LL-37 Truncated Fragments Probed by α-Hemolysin Pore and Molecular Simulations. *Small* **2023**, Research Article. DOI:10.1002/smll.202206232 (accessed 2023–03–27).

[240] Chatani, E.; Yamamoto, N. Recent Progress on Understanding the Mechanisms of Amyloid Nucleation. *Biophys. Rev.* **2018**, *10*, 527–534.

[241] Törnquist, M.; Michaels, T. C. T.; Sanagavarapu, K.; Yang, X.; Meisl, G.; Cohen, S. I. A.; Knowles, T. P. J.; Linse, S. Secondary Nucleation in Amyloid Formation. *Chem. Commun.* **2018**, *54*, 8667–8684.

[242] Lehn, J.-M. Perspectives in supramolecular chemistry—from molecular recognition towards molecular information processing and self-organization. *Angew. Chem., Int. Ed. Engl.* **1990**, *29*, 1304–1319.

[243] Li, T.; Lu, X.-M.; Zhang, M.-R.; Hu, K.; Li, Z. Peptide-Based Nanomaterials: Self-Assembly, Properties and Applications. *Bioact. Mater.* **2022**, *11*, 268–282.

[244] Aida, T.; Meijer, E.; Stupp, S. Functional supramolecular polymers. *Science* **2012**, *335*, 813–817.

[245] Philp, D.; Stoddart, J. F. Self-Assembly in Natural and Unnatural Systems. *Angew. Chem., Int. Ed. Engl.* **1996**, *35*, 1154–1196.

[246] Ashton, P. R.; Ballardini, R.; Balzani, V.; Bělohradský, M.; Gandolfi, M. T.; Philp, D.; Prodi, L.; Raymo, F. M.; Reddington, M. V.; Spencer, N. et al. Self-Assembly, Spectroscopic, and Electrochemical Properties of [n]Rotaxanes1. *J. Am. Chem. Soc.* **1996**, *118*, 4931–4951.

[247] Wang, Y.; Hu, A. Carbon Quantum Dots: Synthesis, Properties and Applications. *J. Mater. Chem. C* **2014**, *2*, 6921–6939.

[248] Whitesides, G. M.; Grzybowski, B. Self-Assembly at All Scales. *Science* **2002**, *295*, 2418–2421.

[249] Zeng, F.; Huang, W.-Q.; Xiao, J.-H.; Li, Y.-Y.; Peng, W.; Hu, W.; Li, K.; Huang, G.-F. Isotype Heterojunction g-C_3N_4/g-C_3N_4 Nanosheets as 2D Support to Highly Dispersed 0D Metal Oxide Nanoparticles: Generalized Self-Assembly and Its High Photocatalytic Activity. *J. Phys. D: Appl. Phys.* **2018**, *52*, 025501.

[250] Cordier, P.; Tournilhac, F.; Soulié-Ziakovic, C.; Leibler, L. Self-Healing and Thermoreversible Rubber from Supramolecular Assembly. *Nature* **2008**, *451*, 977–980.

[251] Burnworth, M.; Tang, L.; Kumpfer, J. R.; Duncan, A. J.; Beyer, F. L.; Fiore, G. L.; Rowan, S. J.; Weder, C. Optically Healable Supramolecular Polymers. *Nature* **2011**, *472*, 334–337.

[252] De Greef, T. F. A.; Smulders, M. M. J.; Wolffs, M.; Schenning, A. P. H. J.; Sijbesma, R. P.; Meijer, E. W. Supramolecular Polymerization. *Chem. Rev.* **2009**, *109*, 5687–5754.

[253] Pumera, M. Graphene-Based Nanomaterials for Energy Storage. *Energy Environ. Sci.* **2011**, *4*, 668–674.

[254] Kamat, P. V. Graphene-Based Nanoassemblies for Energy Conversion. *J. Phys. Chem. Lett.* **2011**, *2*, 242–251.

[255] Westervelt, R. Graphene Nanoelectronics. *Science* **2008**, *320*, 324–325.

[256] Kushner, D. Self-Assembly of Biological Structures. *Bacteriol. Rev.* **1969**, *33*, 302–345.

[257] Chen, C.; Liu, K.; Li, J.; Yan, X. Functional Architectures Based on Self-Assembly of Bio-Inspired Dipeptides: Structure Modulation and its Photoelectronic Applications. *Adv. Colloid Interface Sci.* **2015**, *225*, 177–193.

[258] Fleming, S.; Ulijn, R. V. Design of Nanostructures Based on Aromatic Peptide Amphiphiles. *Chem. Soc. Rev.* **2014**, *43*, 8150–8177.

[259] Bortolini, C.; C. Jones, N.; V. Hoffmann, S.; Besenbacher, F.; Dong, M. The Influence of the Localised Charge of C- and N-Termini on Peptide Self-Assembly. *Soft Matter* **2016**, *12*, 373–377.

[260] Cui, H.; Cheetham, A. G.; Pashuck, E. T.; Stupp, S. I. Amino Acid Sequence in Constitutionally Isomeric Tetrapeptide Amphiphiles Dictates Architecture of One-Dimensional Nanostructures. *J. Am. Chem. Soc.* **2014**, *136*, 12461–12468.

[261] Lee, N. R.; Bowerman, C. J.; Nilsson, B. L. Effects of Varied Sequence Pattern on the Self-Assembly of Amphipathic Peptides. *Biomacromolecules* **2013**, *14*, 3267–3277.

[262] Lee, N. R.; Bowerman, C. J.; Nilsson, B. L. Sequence Length Determinants for Self-Assembly of Amphipathic β-Sheet Peptides. *Pept. Sci.* **2013**, *100*, 738–750.

[263] Tiné, M. R.; Alderighi, M.; Duce, C.; Ghezzi, L.; Solaro, R. Effect of Temperature on Self-Assembly of an Ionic Tetrapeptide. *J.Therm. Anal. Calorim.* **2011**, *103*, 75–80.

[264] Luo, Z.; Zhao, X.; Zhang, S. Structural Dynamic of a Self-Assembling Peptide d-EAK16 Made of Only D-Amino Acids. *PLoS One* **2008**, *3*, e2364.

[265] Cui, J.; Liu, A.; Guan, Y.; Zheng, J.; Shen, Z.; Wan, X. Tuning the Helicity of Self-Assembled Structure of a Sugar-Based Organogelator by the Proper Choice of Cooling Rate. *Langmuir* **2010**, *26*, 3615–3622.

[266] Huang, R.; Qi, W.; Su, R.; Zhao, J.; He, Z. Solvent and Surface Controlled Self-Assembly of Diphenylalanine Peptide: From Microtubes to Nanofibers. *Soft Matter* **2011**, *7*, 6418–6421.

[267] Zhao, Y.; Wang, J.; Deng, L.; Zhou, P.; Wang, S.; Wang, Y.; Xu, H.; Lu, J. R. Tuning the Self-Assembly of Short Peptides via Sequence Variations. *Langmuir* **2013**, *29*, 13457–13464.

[268] Zhao, Y.; Deng, L.; Wang, J.; Xu, H.; Lu, J. R. Solvent Controlled Structural Transition of KI4K Self-Assemblies: From nanotubes to Nanofibrils. *Langmuir* **2015**, *31*, 12975–12983.

[269] Goldberger, J. E.; Berns, E. J.; Bitton, R.; Newcomb, C. J.; Stupp, S. I. Electrostatic Control of Bioactivity. *Angew. Chem.* **2011**, *123*, 6416–6419.

[270] Ghosh, A.; Haverick, M.; Stump, K.; Yang, X.; Tweedle, M. F.; Goldberger, J. E. Fine-Tuning the pH Trigger of Self-Assembly. *J. Am. Chem. Soc.* **2012**, *134*, 3647–3650.

[271] Zhao, Y.; Yokoi, H.; Tanaka, M.; Kinoshita, T.; Tan, T. Self-Assembled pH-Responsive Hydrogels Composed of the RATEA16 Peptide. *Biomacromolecules* **2008**, *9*, 1511–1518.

[272] Cui, H.; Muraoka, T.; Cheetham, A. G.; Stupp, S. I. Self-Assembly of Giant Peptide Nanobelts. *Nano Lett.* **2009**, *9*, 945–951.

[273] Xiong, W.; Hu, K.; Li, Z.; Jiang, Y.; Li, Z.; Li, Z.; Wang, X. A Wearable System Based on Core-Shell Structured Peptide-Co9S8 Supercapacitor and Triboelectric Nanogenerator. *Nano Energy* **2019**, *66*, 104149.

[274] Hu, K.; Jiang, Y.; Xiong, W.; Li, H.; Zhang, P.-Y.; Yin, F.; Zhang, Q.; Geng, H.; Jiang, F.; Li, Z. et al. Tuning Peptide Self-Assembly by an In-Tether Chiral Center. *Sci. Adv.* **2018**, *4*, 1–8.

[275] Hu, K.; Zheng, C.; An, M.; Ma, X.; Wang, L. A Peptide-Based Supercapacitor and its Performance Improvement via TiO_2 Coating. *J. Mater. Chem. A* **2018**, *6*, 8047–8052.

[276] Liu, P.; Yan, J.; Guang, Z.; Huang, Y.; Li, X.; Huang, W. Recent Advancements of Polyaniline-Based Nanocomposites for Supercapacitors. *J. Power Sources* **2019**, *424*, 108–130.

[277] Liu, Q.; Wang, J.; Boyd, B. J. Peptide-Based Biosensors. *Talanta* **2015**, *136*, 114–127.

[278] Pavan, S.; Berti, F. Short Peptides as Biosensor Transducers. *Anal. Bioanal. Chem.* **2012**, *402*, 3055–3070.

[279] Bellat, V.; Ting, R.; Southard, T. L.; Vahdat, L.; Molina, H.; Fernandez, J.; Aras, O.; Stokol, T.; Law, B. Functional Peptide Nanofibers with Unique Tumor Targeting and Enzyme-Induced Local Retention Properties. *Adv. Funct. Mater.* **2018**, *28*, 1803969.

[280] Cheng, K.; Ding, Y.; Zhao, Y.; Ye, S.; Zhao, X.; Zhang, Y.; Ji, T.; Wu, H.; Wang, B.; Anderson, G. J. et al. Sequentially Responsive Therapeutic Peptide Assembling Nanoparticles for Dual-Targeted Cancer Immunotherapy. *Nano Lett.* **2018**, *18*, 3250–3258.

[281] Crombez, L.; Aldrian-Herrada, G.; Konate, K.; Nguyen, Q. N.; McMaster, G. K.; Brasseur, R.; Heitz, F.; Divita, G. A New Potent Secondary Amphipathic Cell–penetrating Peptide for siRNA Delivery Into Mammalian Cells. *Mol. Ther.* **2009**, *17*, 95–103.

[282] An, H.-W.; Li, L.-L.; Wang, Y.; Wang, Z.; Hou, D.; Lin, Y.-X.; Qiao, S.-L.; Wang, M.-D.; Yang, C.; Cong, Y. et al. A Tumour-Selective Cascade Activatable Self-Detained System for Drug Delivery and Cancer Imaging. *Nat. Commun.* **2019**, *10*, 4861.

[283] Wang, H.; Yang, C.; Wang, L.; Kong, D.; Zhang, Y.; Yang, Z. Self-Assembled Nanospheres as a Novel Delivery System for Taxol: A Molecular Hydrogel with Nanosphere Morphology. *Chem. Commun.* **2011**, *47*, 4439–4441.

[284] Felício, M. R.; Silva, O. N.; Gonçalves, S.; Santos, N. C.; Franco, O. L. Peptides with Dual Antimicrobial and Anticancer Activities. *Front. Chem.* **2017**, *5*, 1–9.

[285] Gaspar, D.; Veiga, A. S.; Castanho, M. A. R. B. From Antimicrobial to Anticancer Peptides. A review. *Front. Microbiol.* **2013**, *4*, 1–16.

[286] Ding, Y.; Ji, T.; Zhao, Y.; Zhang, Y.; Zhao, X.; Zhao, R.; Lang, J.; Zhao, X.; Shi, J.; Sukumar, S. et al. Improvement of Stability and Efficacy of C16Y Therapeutic Peptide via Molecular Self-Assembly into Tumor-Responsive Nanoformulation. *Mol. Cancer Ther.* **2015**, *14*, 2390–2400.

[287] Mumcuoglu, D.; Sardan Ekiz, M.; Gunay, G.; Tekinay, T.; Tekinay, A. B.; Guler, M. O. Cellular Internalization of Therapeutic Oligonucleotides by Peptide Amphiphile Nanofibers and Nanospheres. *ACS Appl. Mater. Interfaces* **2016**, *8*, 11280–11287.

[288] Li, Y.; Zheng, X.; Cao, Z.; Xu, W.; Zhang, J.; Gong, M. Self-Assembled Peptide (CADY-1) Improved the Clinical Application of Doxorubicin. *Int. J. Pharm.* **2012**, *434*, 209–214.

[289] Li, M.; Liu, P.; Gao, G.; Deng, J.; Pan, Z.; Wu, X.; Xie, G.; Yue, C.; Cho, C. H.; Ma, Y. et al. Smac Therapeutic Peptide Nanoparticles Inducing Apoptosis of Cancer Cells for Combination Chemotherapy with Doxorubicin. *ACS Appl. Mater. Interfaces* **2015**, *7*, 8005–8012.

[290] Hernandez, A.; Hartgerink, J. D.; Young, S. Self-Assembling Peptides as Immunomodulatory Biomaterials. *Front. Bioeng. Biotechnol.* **2023**, *11*, 1–12.

[291] Jiang, L.; Xu, D.; Sellati, T. J.; Dong, H. Self-Assembly of Cationic Multidomain Peptide Hydrogels: Supramolecular Nanostructure and Rheological Properties Dictate Antimicrobial Activity. *Nanoscale* **2015**, *7*, 19160–19169.

[292] Gupta, K.; Jang, H.; Harlen, K.; Puri, A.; Nussinov, R.; Schneider, J. P.; Blumenthal, R. Mechanism of Membrane Permeation Induced by Synthetic β-Hairpin Peptides. *Biophys. J.* **2013**, *105*, 2093–2103.

[293] Kretsinger, J. K.; Haines, L. A.; Ozbas, B.; Pochan, D. J.; Schneider, J. P. Cytocompatibility of Self-Assembled β-Hairpin Peptide Hydrogel Surfaces. *Biomaterials* **2005**, *26*, 5177–5186.

[294] Haines, L. A.; Rajagopal, K.; Ozbas, B.; Salick, D. A.; Pochan, D. J.; Schneider, J. P. Light-Activated Hydrogel Formation via the Triggered Folding and Self-Assembly of a Designed Peptide. *J. Am. Chem. Soc.* **2005**, *127*, 17025–17029.

[295] Veiga, A. S.; Sinthuvanich, C.; Gaspar, D.; Franquelim, H. G.; Castanho, M. A. R. B.; Schneider, J. P. Arginine-rich self-assembling peptides as potent antibacterial gels. *Biomaterials* **2012**, *33*, 8907–8916.

[296] Lazzaro, B. P.; Zasloff, M.; Rolff, J. Antimicrobial peptides: Application informed by evolution. *Science* **2020**, *368*, eaau5480.

[297] Jenssen, H.; Hamill, P.; Hancock, R. E. W. Peptide Antimicrobial Agents. *Clin. Microbiol. Rev.* **2006**, *19*, 491–511.

[298] Giuliani, A.; Pirri, G.; Nicoletto, S. Antimicrobial Peptides: An Overview of a Promising Class of Therapeutics. *Open Life Sci.* **2007**, *2*, 1–33.

[299] Seo, M.-D.; Won, H.-S.; Kim, J.-H.; Mishig-Ochir, T.; Lee, B.-J. Antimicrobial Peptides for Therapeutic Applications: A Review. *Molecules* **2012**, *17*, 12276–12286.

[300] Zasloff, M. Antimicrobial Peptides of Multicellular Organisms. *Nature* **2002**, *415*, 389–395.

[301] Cederlund, A.; Gudmundsson, G. H.; Agerberth, B. Antimicrobial Peptides Important in Innate Immunity. *FEBS J.* **2011**, *278*, 3942–3951.

[302] Timofeeva, L.; Kleshcheva, N. Antimicrobial Polymers: Mechanism of Action, Factors of Activity, and Applications. *Appl. Microbiol. Biotechnol.* **2011**, *89*, 475–492.

[303] Bahar, A. A.; Ren, D. Antimicrobial Peptides. *Pharmaceuticals* **2013**, *6*, 1543–1575.

[304] Cudic, M.; Otvos Jr, L. Intracellular Targets of Antibacterial Peptides. *Curr. Drug Targets* **2002**, *3*, 101–106.

[305] Brogden, K. A. Antimicrobial Peptides: Pore Formers or Metabolic Inhibitors in Bacteria? *Nat. Rev. Microbiol.* **2005**, *3*, 238–250.

[306] McCloskey, A. P.; Gilmore, B. F.; Laverty, G. Evolution of Antimicrobial Peptides to Self-Assembled Peptides for Biomaterial Applications. *Pathogens* **2014**, *3*, 791–821.

[307] Tian, X.; Sun, F.; Zhou, X.; Luo, S.; Chen, L. Role of Peptide Self-Assembly in Antimicrobial Peptides. *J Pept. Sci.* **2015**, *21*, 530–539.

[308] Sun, L.; Zheng, C.; Webster, T. J. Self-assembled peptide nanomaterials for biomedical applications: Promises and pitfalls. *Int. J. Nanomed.* **2017**, 73–86.

[309] Li, X.; Li, Y.; Han, H.; Miller, D. W.; Wang, G. Solution Structures of Human LL-37 Fragments and NMR-Based Identification of a Minimal Membrane-Targeting Antimicrobial and Anticancer Region. *J. Am. Chem. Soc.* **2006**, *128*, 5776–5785.

[310] Engelberg, Y.; Landau, M. The Human LL-37 (17-29) Antimicrobial Peptide Reveals a Functional Supramolecular Structure. *Nat. Commun.* **2020**, *11*, 3894.

[311] Osborne, K. L.; Bachmann, M.; Strodel, B. Thermodynamic Analysis of Structural Transitions During GNNQQNY Aggregation. *Proteins* **2013**, *81*, 1141–1155.

[312] Cecchini, M.; Rao, F.; Seeber, M.; Caflisch, A. Replica Exchange Molecular Dynamics Simulations of Amyloid Peptide Aggregation. *J. Chem. Phys.* **2004**, *121*, 10748–10756.

[313] Paul, A.; Samantray, S.; Anteghini, M.; Khaled, M.; Strodel, B. Thermodynamics and Kinetics of the Amyloid-β Peptide Revealed by Markov State Models Based on MD Data in Agreement with Experiment. *Chem. Sci.* **2021**, *12*, 6652–6669.

[314] Weng, J.; Yang, M.; Wang, W.; Xu, X.; Tian, Z. Revealing Thermodynamics and Kinetics of Lipid Self-Assembly by Markov State Model Analysis. *J. Am. Chem. Soc.* **2020**, *142*, 21344–21352.

[315] Case, D. A.; Ben-Shalom, I. Y.; Brozell, S. R.; Cerutti, D. S.; Cheatham III, T. E.; Cruzeiro, V. W. D.; Darden, T. A.; Duke, R. E.; Ghoreishi, D.; Gilson, M. K. et al. Amber 20. 2020; University of California: San Francisco, CA.

[316] Senne, M.; Trendelkamp-Schroer, B.; Mey, A. S.; Schütte, C.; Noé, F. EMMA: A Software Package for Markov Model Building and Analysis. *J. Chem. Theo. Comput.* **2012**, *8*, 2223–2238.

[317] Scherer, M. K.; Trendelkamp-Schroer, B.; Paul, F.; Pérez-Hernández, G.; Hoffmann, M.; Plattner, N.; Wehmeyer, C.; Prinz, J.-H.; Noé, F. PyEMMA 2: A Software Package for Estimation, Validation, and Analysis of Markov Models. *J. Chem. Theo. Comput.* **2015**, *11*, 5525–5542.

[318] Sengupta, U.; Carballo-Pacheco, M.; Strodel, B. Automated Markov State Models for Molecular Dynamics Simulations of Aggregation and Self-Assembly. *J. Chem. Phys.* **2019**, *150*.

[319] Prinz, J.-H.; Wu, H.; Sarich, M.; Keller, B.; Senne, M.; Held, M.; Chodera, J. D.; Schütte, C.; Noé, F. Markov Models of Molecular Kinetics: Generation and Validation. *J. Chem. Phys.* **2011**, *134*.

[320] Swope, W. C.; Pitera, J. W.; Suits, F. Describing Protein Folding Kinetics by Molecular Dynamics Simulations. 1. Theory. *J. Phys. Chem. B* **2004**, *108*, 6571–6581.

[321] Deuflhard, P.; Weber, M. Robust Perron Cluster Analysis in Conformation Dynamics. *Linear Algebra Appl.* **2005**, *398*, 161–184.

[322] Röblitz, S.; Weber, M. Fuzzy Spectral Clustering by PCCA+: Application to Markov State Models and Data Classification. *Adv. Data Anal. Classif.* **2013**, *7*, 147–179.

[323] Prinz, J.-H.; Wu, H.; Sarich, M.; Keller, B.; Senne, M.; Held, M.; Chodera, J. D.; Schütte, C.; Noé, F. Markov Models of Molecular Kinetics: Generation and Validation. *J. Chem. Phys.* **2011**, *134*.

[324] Kabsch, W.; Sander, C. Dictionary of Protein Secondary Structure: Pattern Recognition of Hydrogen-Bonded and Geometrical Features. *Biopolymers* **1983**, *22*, 2577–2637.

[325] Humphrey, W.; Dalke, A.; Schulten, K. VMD: visual molecular dynamics. *J. Mol. Graphics* **1996**, *14*, 33–38.

[326] Shrake, A.; Rupley, J. A. Environment And Exposure To Solvent Of Protein Atoms. Lysozyme And Insulin. *J. Mol. Biol.* **1973**, *79*, 351–371.

[327] Mahalka, A. K.; Kinnunen, P. K. J. Binding of Amphipathic α-Helical Antimicrobial Peptides to Lipid Membranes: Lessons from Temporins B and L. *Biochim. Biophys. Acta, Biomembr.* **2009**, *1788*, 1600–1609.

[328] Trexler, A. J.; Nilsson, M. R. The Formation of Amyloid Fibrils from Proteins in the Lysozyme Family. *Curr. Protein Pept. Sci.* **2007**, *8*, 537–557.

[329] Nilsson, M. R.; Dobson, C. M. In Vitro Characterization of Lactoferrin Aggregation and Amyloid Formation. *Biochemistry* **2003**, *42*, 375–382.

[330] Torrent, M.; Odorizzi, F.; Nogués, M. V.; Boix, E. Eosinophil Cationic Protein Aggregation: Identification of an N-Terminus Amyloid Prone Region. *Biomacromolecules* **2010**, *11*, 1983–1990.

[331] Soscia, S. J.; Kirby, J. E.; Washicosky, K. J.; Tucker, S. M.; Ingelsson, M.; Hyman, B.; Burton, M. A.; Goldstein, L. E.; Duong, S.; Tanzi, R. E. et al. The Alzheimer's Disease-Associated Amyloid β-Protein Is an Antimicrobial Peptide. *PLoS One* **2010**, *5*, e9505.

[332] Hertel, C.; Terzi, E.; Hauser, N.; Jakob-Røtne, R.; Seelig, J.; Kemp, J. A. Inhibition of the Electrostatic Interaction Between β-Amyloid Peptide and Membranes

Prevents β-Amyloid-Induced Toxicity. *Proc. Natl. Acad. Sci. U.S.A.* **1997**, *94*, 9412–9416.

[333] Zhao, H.; Tuominen, E. K. J.; Kinnunen, P. K. J. Formation of Amyloid Fibers Triggered by Phosphatidylserine-Containing Membranes. *Biochemistry* **2004**, *43*, 10302–10307.

[334] Stöckl, M.; Fischer, P.; Wanker, E.; Herrmann, A. α-Synuclein Selectively Binds to Anionic Phospholipids Embedded in Liquid-Disordered Domains. *J. Mol. Biol.* **2008**, *375*, 1394–1404.

[335] Ambroggio, E. E.; Kim, D. H.; Separovic, F.; Barrow, C. J.; Barnham, K. J.; Bagatolli, L. A.; Fidelio, G. D. Surface Behavior and Lipid Interaction of Alzheimer β-Amyloid Peptide 1–42: A Membrane-Disrupting Peptide. *Biophys. J.* **2005**, *88*, 2706–2713.

[336] Torrent, M.; Valle, J.; Noguès, M. V.; Boix, E.; Andreu, D. The Generation of Antimicrobial Peptide Activity: A Trade-Off Between Charge and Aggregation? *Angew. Chem., Int. Ed.* **2011**, *50*, 10686.

[337] Martin, L. L.; Kubeil, C.; Piantavigna, S.; Tikkoo, T.; Gray, N. P.; John, T.; Calabrese, A. N.; Liu, Y.; Hong, Y.; Hossain, M. A. et al. Amyloid Aggregation and Membrane Activity of the Antimicrobial Peptide Uperin 3.5. *Pept. Sci.* **2018**, *110*, e24052.

[338] Kumar, D. K. V.; Choi, S. H.; Washicosky, K. J.; Eimer, W. A.; Tucker, S.; Ghofrani, J.; Lefkowitz, A.; McColl, G.; Goldstein, L. E.; Tanzi, R. E. et al. Amyloid-β Peptide Protects Against Microbial Infection in Mouse and Worm Models of Alzheimer's Disease. *Sci. Transl. Med.* **2016**, *8*, 340ra72.

[339] Gour, S.; Kumar, V.; Singh, A.; Gadhave, K.; Goyal, P.; Pandey, J.; Giri, R.; Yadav, J. K. Mammalian antimicrobial peptide protegrin-4 self assembles and forms amyloid-like aggregates: Assessment of its functional relevance. *J. Pept. Sci.* **2019**, *25*, e3151.

[340] Matthes, D.; de Groot, B. L. Molecular Dynamics Simulations Reveal the Importance of Amyloid-β Oligomer β-Sheet Edge Conformations in Membrane Permeabilization. *J. Biol. Chem.* **2023**, *299*, 103034.

[341] Friedman, R.; Pellarin, R.; Caflisch, A. Amyloid Aggregation on Lipid Bilayers and Its Impact on Membrane Permeability. *J. Mol. Biol.* **2009**, *387*, 407–415.

[342] Sasahara, K.; Morigaki, K.; Shinya, K. Effects of Membrane Interaction and Aggregation of Amyloid-β Peptide on Lipid Mobility and Membrane Domain Structure. *Phys. Chem. Chem. Phys.* **2013**, *15*, 8929–8939.

[343] Kenyaga, J.; Cheng, Q.; Qiang, W. Early-Stage β-Amyloid–Membrane Interactions Modulate Lipid Dynamics and Influence Structural Interfaces and Fibrillation. *J. Biol. Chem.* **2022**, *298*, 102491.

[344] Tofoleanu, F.; Brooks, B. R.; Buchete, N.-V. Modulation of Alzheimer's Aβ Protofilament–Membrane Interactions by Lipid Headgroups. *ACS Chem. Neurosci.* **2015**, *6*, 446–455.

[345] Qian, Z.; Zou, Y.; Zhang, Q.; Chen, P.; Ma, B.; Wei, G.; Nussinov, R. Atomistic-Level Study of the Interactions Between hIAPP Protofibrils and Membranes: Influence of pH and Lipid Composition. *Biochim. Biophys. Acta Biomembr.* **2018**, *1860*, 1818–1825.

[346] Chowdhury, U. D.; Paul, A.; Bhargava, B. L. Phosphatidylinositol (PI) Lipids Modulate the Binding of Tau Fibrils on Lipid Bilayers. bioRxiv, preprint, 2023.

[347] Hoshino, T.; Mahmood, M. I.; Mori, K.; Matsuzaki, K. Binding and Aggregation Mechanism of Amyloid-β Peptides onto the GM1 Ganglioside-Containing Lipid Membrane. *J. Phys. Chem. B* **2013**, *117*, 8085–8094.

[348] Chowdhury, U.; Paul, A.; Bhargava, B. Interaction of the Tau Fibrils with the Neuronal Membrane. *Biophys. Chem.* **2023**, *298*, 107024.

[349] Liu, Y.; Zhang, D.; Zhang, Y.; Tang, Y.; Xu, L.; He, H.; Wu, J.; Zheng, J. Molecular Dynamics Simulations of Cholesterol Effects on the Interaction of hIAPP with Lipid Bilayer. *J. Phys. Chem. B* **2020**, *124*, 7830–7841.

[350] Xiang, N.; Lyu, Y.; Zhu, X.; Narsimhan, G. Investigation of the Interaction of Amyloid-β Peptide (11–42) Oligomers with a 1-Palmitoyl-2-Oleoyl-sn-Glycero-3-Phosphocholine (POPC) Membrane Using Molecular Dynamics Simulation. *Phys. Chem. Chem. Phys.* **2018**, *20*, 6817–6829.

[351] Brown, A.; Bevan, D. Molecular Dynamics Simulations of Amyloid-β Peptide (1–42): Tetramer Formation and Membrane Interactions. *Biophys. J.* **2016**, *111*, 937–949.

[352] Tofoleanu, F.; Buchete, N.-V. Molecular Interactions of Alzheimer's Aβ Protofilaments with Lipid Membranes. *J. Mol. Biol.* **2012**, *421*, 572–586.

[353] Dong, X.; Sun, Y.; Wei, G.; Nussinov, R.; Ma, B. Binding of Protofibrillar Aβ Trimers to Lipid Bilayer Surface Enhances Aβ Structural Stability and Causes Membrane Thinning. *Phys. Chem. Chem. Phys.* **2017**, *19*, 27556–27569.

[354] Yu, X.; Wang, Q.; Pan, Q.; Zhou, F.; Zheng, J. Molecular Interactions of Alzheimer Amyloid-β Oligomers with Neutral and Negatively Charged Lipid Bilayers. *Phys. Chem. Chem. Phys.* **2013**, *15*, 8878–8889.

[355] Jang, H.; Connelly, L.; Teran Arce, F.; Ramachandran, S.; Kagan, B. L.; Lal, R.; Nussinov, R. Mechanisms for the Insertion of Toxic, Fibril-Like β-Amyloid Oligomers into the Membrane. *J. Chem. Theory Comput.* **2013**, *9*, 822–833.

[356] Nguyen, H. L.; Linh, H. Q.; Krupa, P.; La Penna, G.; Li, M. S. Amyloid β Dodecamer Disrupts the Neuronal Membrane More Strongly Than the Mature Fibril: Understanding the Role of Oligomers in Neurotoxicity. *J. Phys. Chem. B* **2022**, *126*, 3659–3672.

[357] Nguyen, P. H.; Derreumaux, P. Molecular Dynamics Simulations of the Tau R3–R4 Domain Monomer in the Bulk Solution and at the Surface of a Lipid Bilayer Model. *J. Phys. Chem. B* **2022**, *126*, 3431–3438.

[358] Nguyen, P. H.; Derreumaux, P. Molecular Dynamics Simulations of the Tau Amyloid Fibril Core Dimer at the Surface of a Lipid Bilayer Model: I. In Alzheimer's Disease. *J. Phys. Chem. B* **2022**, *126*, 4849–4856.

[359] Lee, J.; Jung, S. W.; Cho, A. E. Molecular Insights into the Adsorption Mechanism of Human β-Defensin-3 on Bacterial Membranes. *Langmuir* **2016**, *32*, 1782–1790.

[360] Amos, S.-B. T. A.; Vermeer, L. S.; Ferguson, P. M.; Kozlowska, J.; Davy, M.; Bui, T. T.; Drake, A. F.; Lorenz, C. D.; Mason, A. J. Antimicrobial Peptide Potency Is Facilitated by Greater Conformational Flexibility When Binding to Gram-Negative Bacterial Inner Membranes. *Sci. Rep.* **2016**, *6*, 37639.

[361] Ramamoorthy, A.; Thennarasu, S.; Tan, A.; Gottipati, K.; Sreekumar, S.; Heyl, D. L.; An, F. Y. P.; Shelburne, C. E. Deletion of All Cysteines in Tachyplesin I Abolishes Hemolytic Activity and Retains Antimicrobial Activity and Lipopolysaccharide Selective Binding. *Biochemistry* **2006**, *45*, 6529–6540.

[362] Cheng, J. T. J.; Hale, J. D.; Elliott, M.; Hancock, R. E. W.; Straus, S. K. The Importance of Bacterial Membrane Composition in the Structure and Function of Aurein 2.2 and Selected Variants. *Biochim. Biophys. Acta, Biomembr.* **2011**, *1808*, 622–633.

[363] Loose, M.; Schwille, P. Biomimetic Membrane Systems to Study Cellular Organization. *J. Struct. Biol.* **2009**, *168*, 143–151.

[364] Mukherjee, S.; Kar, R. K.; Nanga, R. P. R.; Mroue, K. H.; Ramamoorthy, A.; Bhunia, A. Accelerated Molecular Dynamics Simulation Analysis of MSI-594 in a Lipid Bilayer. *Phys. Chem. Chem. Phys.* **2017**, *19*, 19289–19299.

[365] Devi, M.; Paul, S. Comprehending the Efficacy of Whitlock's Caffeine-Pincered Molecular Tweezer on β-Amyloid Aggregation. *ACS Chem. Neurosci.* **2024**, *15*, 3202–3219.

[366] Jo, S.; Lim, J. B.; Klauda, J. B.; Im, W. CHARMM-GUI Membrane Builder for Mixed Bilayers and Its Application to Yeast Membranes. *Biophys. J.* **2009**, *97*, 50–58.

[367] Wu, E. L.; Cheng, X.; Jo, S.; Rui, H.; Song, K. C.; Dávila-Contreras, E. M.; Qi, Y.; Lee, J.; Monje-Galvan, V.; Venable, R. M. et al. CHARMM-GUI Membrane Builder Toward Realistic Biological Membrane Simulations. *J. Comput. Chem.* **2014**, *35*, 1997–2004.

[368] Mukherjee, S.; Kar, R. K.; Nanga, R. P. R.; Mroue, K. H.; Ramamoorthy, A.; Bhunia, A. Accelerated Molecular Dynamics Simulation Analysis of MSI-594 in a Lipid Bilayer. *Phys. Chem. Chem. Phys.* **2017**, *19*, 19289–19299.

[369] Dickson, C. J.; Walker, R. C.; Gould, I. R. Lipid21: Complex Lipid Membrane Simulations with AMBER. *J. Chem. Theory Comput.* **2022**, *18*, 1726–1736.

[370] Moral, R.; Paul, S. Exploring Cyclic Peptide Nanotube Stability Across Diverse Lipid Bilayers and Unveiling Water Transport Dynamics. *Langmuir* **2023**, *40*, 882–895.

[371] Pal, T.; Paul, R.; Paul, S. Phenylpropanoids on the Inhibition of β-Amyloid Aggregation and the Movement of These Molecules through the POPC Lipid Bilayer. *Langmuir* **2022**, *38*, 7775–7790.

[372] Paul, R.; Bera, S.; Devi, M.; Paul, S. Inhibition of Aβ16–22 Peptide Aggregation by Small Molecules and Their Permeation through POPC Lipid Bilayer: Insight from Molecular Dynamics Simulation Study. *J. Chem. Inf. Model.* **2022**, *62*, 5193–5207.

[373] Paul, R.; Paul, S. Translocation of Endo-Functionalized Molecular Tubes across Different Lipid Bilayers: Atomistic Molecular Dynamics Simulation Study. *Langmuir* **2021**, *37*, 10376–10387.

[374] Silvius, J. R.; others *Lipid-Protein Interactions*; John Wiley & Sons, New York, 1982; Vol. 2; pp 239–281.

[375] Lyu, Y.; Xiang, N.; Mondal, J.; Zhu, X.; Narsimhan, G. Characterization of Interactions between Curcumin and Different Types of Lipid Bilayers by Molecular Dynamics Simulation. *J. Phys. Chem. B* **2018**, *122*, 2341–2354.

[376] Grubmüller, H.; Heymann, B.; Tavan, P. Ligand Binding: Molecular Mechanics Calculation of the Streptavidin–Biotin Rupture Force. *Science* **1996**, *271*, 997–999.

[377] Izrailev, S.; Stepaniants, S.; Balsera, M.; Oono, Y.; Schulten, K. Molecular Dynamics Study of Unbinding of the Avidin–Biotin Complex. *Biophys. J.* **1997**, *72*, 1568–1581.

[378] Mitra, A.; Pandijothi, V.; Paul, S. Computational Insight into the Peptide-Based Inhibition of α-Cobratoxin. *Phys. Chem. Chem. Phys.* **2024**, *26*, 28274–28287.

[379] Raman, E. P.; Takeda, T.; Barsegov, V.; Klimov, D. K. Mechanical Unbinding of Aβ Peptides from Amyloid Fibrils. *J. Mol. Biol.* **2007**, *373*, 785–800.

[380] Mitra, A.; Chattaraj, K. G.; Paul, S. Elucidating the Hydrotropic Mechanism of the Antagonistic Salt PPh_4Cl. *J. Phys. Chem. B* **2023**, *127*, 996–1012.

[381] Devi, M.; Mandal, P.; Panda, A. N.; Paul, S. Shape Selective Copper-Based Metallo-Tweezer: Bridging Molecular Recognition and Solubility Enhancement of Natural Therapeutics. *J. Phys. Chem. B* **2025**, Just Accepted, DOI: 10.1021/acs.jpcb.xxxxxxx.

[382] Grossfield, A. WHAM: The Weighted Histogram Analysis Method. University of Rochester, 2012; http://membrane.urmc.rochester.edu/content/wham.

[383] Kumar, S.; Rosenberg, J. M.; Bouzida, D.; Swendsen, R. H.; Kollman, P. A. The Weighted Histogram Analysis Method for Free-Energy Calculations on Biomolecules. I. The Method. *J. Comput. Chem.* **1992**, *13*, 1011–1021.

[384] Gowers, R. J.; Linke, M.; Barnoud, J.; Reddy, T. J. E.; Melo, M. N.; Seyler, S. L.; Domanski, J.; Dotson, D. L.; Buchoux, S.; Kenney, I. M. et al. *MDAnalysis: A Python Package for the Rapid Analysis of Molecular Dynamics Simulations*; 2019.

[385] Michaud-Agrawal, N.; Denning, E. J.; Woolf, T. B.; Beckstein, O. MDAnalysis: A Toolkit for the Analysis of Molecular Dynamics Simulations. *J. Comput. Chem.* **2011**, *32*, 2319–2327.

[386] Piggot, T. J.; Allison, J. R.; Sessions, R. B.; Essex, J. W. On the Calculation of Acyl Chain Order Parameters from Lipid Simulations. *J. Chem. Theo. Comput.* **2017**, *13*, 5683–5696.

[387] Dickson, C. J.; Madej, B. D.; Skjevik, Å. A.; Betz, R. M.; Teigen, K.; Gould, I. R.; Walker, R. C. Lipid14: The Amber Lipid Force Field. *J. Chem. Theo. Comput.* **2014**, *10*, 865–879.

[388] Ringstad, L.; Schmidtchen, A.; Malmsten, M. Effect of peptide length on the interaction between consensus peptides and DOPC/DOPA bilayers. *Langmuir* **2006**, *22*, 5042–5050.

[389] Bysell, H.; Schmidtchen, A.; Malmsten, M. Binding and release of consensus peptides by poly(acrylic acid) microgels. *Biomacromolecules* **2009**, *10*, 2162–2168.

[390] Wong, G. C. L.; Pollack, L. Electrostatics of Strongly Charged Biological Polymers: Ion-Mediated Interactions and Self-Organization in Nucleic Acids and Proteins. *Annu. Rev. Phys. Chem.* **2010**, *61*, 171–189.

[391] Schmidt, N. W.; Wong, G. C. L. Antimicrobial Peptides and Induced Membrane Curvature: Geometry, Coordination Chemistry, and Molecular Engineering. *Curr. Opin. Solid State Mater. Sci.* **2013**, *17*, 151–163.

[392] Henzler-Wildman, K. A.; Martinez, G. V.; Brown, M. F.; Ramamoorthy, A. Perturbation of the Hydrophobic Core of Lipid Bilayers by the Human Antimicrobial Peptide LL-37. *Biochemistry* **2004**, *43*, 8459–8469.

[393] van Hilten, N.; Methorst, J.; Verwei, N.; Risselada, H. J. Physics-based Generative Model of Curvature Sensing Peptides; Distinguishing Sensors from Binders. *Science Adv.* **2023**, *9*, eade8839.

[394] Häffner, S. M.; Malmsten, M. Influence of self-assembly on the performance of antimicrobial peptides. *Curr. Opin. Colloid Interface Sci.* **2018**, *38*, 56–79.

[395] Czaplewski, L.; Bax, R.; Clokie, M.; Dawson, M.; Fairhead, H.; Fischetti, V. A.; Foster, S.; Gilmore, B. F.; Hancock, R. E. W.; Harper, D. et al. Alternatives to antibiotics–A pipeline portfolio review. *Lancet Infect. Dis.* **2016**, *16*, 239–251.

[396] Koo, H. B.; Seo, J. Antimicrobial peptides under clinical investigation. *Pept. Sci.* **2019**, *111*, e24122.

[397] Leontiadou, H.; Mark, A. E.; Marrink, S. J. Antimicrobial peptides in action. *J. Am. Chem. Soc.* **2006**, *128*, 12156–12161.

[398] Li, W.; Sani, M.-A.; Jamasbi, E.; Otvos Jr, L.; Hossain, M. A.; Wade, J. D.; Separovic, F. Membrane interactions of proline-rich antimicrobial peptide, Chex1-Arg20, multimers. *Biochim. Biophys. Acta, Biomembr.* **2016**, *1858*, 1236–1243.

[399] Li, N. N.; Li, J. Z.; Liu, P.; Pranantyo, D.; Luo, L.; Chen, J. C.; Kang, E.-T.; Hu, X. F.; Li, C. M.; Xu, L. Q. An Antimicrobial Peptide with an Aggregation-Induced Emission (AIE) Luminogen for Studying Bacterial Membrane Interactions and Antibacterial Actions. *Chem. Commun.* **2017**, *53*, 3315–3318.

[400] Chen, J.; Gao, M.; Wang, L.; Li, S.; He, J.; Qin, A.; Ren, L.; Wang, Y.; Tang, B. Z. Aggregation-Induced Emission Probe for Study of the Bactericidal Mechanism of Antimicrobial Peptides. *ACS Appl. Mater. Interfaces* **2018**, *10*, 11436–11442.

[401] Kummer, N.; Wu, T.; De France, K. J.; Zuber, F.; Ren, Q.; Fischer, P.; Campioni, S.; Nyström, G. Self-assembly pathways and antimicrobial properties of lysozyme in different aggregation states. *Biomacromolecules* **2021**, *22*, 4327–4336.

[402] Lin, B.; Hung, A.; Singleton, W.; Darmawan, K. K.; Moses, R.; Yao, B.; Wu, H.; Barlow, A.; Sani, M.-A.; Sloan, A. J. et al. The Effect of Tailing Lipidation on the Bioactivity of Antimicrobial Peptides and Their Aggregation Tendency: Special Issue: Emerging Investigators. *Aggregate* **2023**, *4*, e329.

[403] Vaezi, Z.; Bortolotti, A.; Luca, V.; Perilli, G.; Mangoni, M. L.; Khosravi-Far, R.; Bobone, S.; Stella, L. Aggregation Determines the Selectivity of Membrane-Active

Anticancer and Antimicrobial Peptides: The Case of killerFLIP. *Biochim. Biophys. Acta, Biomembr.* **2020**, *1862*, 183107.

[404] Lorenzón, E. N.; Sanches, P. R. S.; Nogueira, L. G.; Bauab, T. M.; Cilli, E. M. Dimerization of aurein 1.2: Effects in structure, antimicrobial activity and aggregation of *Candida albicans* cells. *Amino Acids* **2013**, *44*, 1521–1528.

[405] Weaver, J. C. Electroporation theory: Concepts and mechanisms. *Plant Cell Electroporation Electrofusion Protoc.* **1995**, 3–28.

[406] Tsong, T. Y. Electroporation of cell membranes. *Biophys. J.* **1991**, *60*, 297–306.

[407] Sun, S.; Zhao, G.; Huang, Y.; Cai, M.; Shan, Y.; Wang, H.; Chen, Y. Specificity and mechanism of action of α-helical membrane-active peptides interacting with model and biological membranes by single-molecule force spectroscopy. *Sci. Rep.* **2016**, *6*, 29145.

[408] Barreto-Santamaría, A.; Curtidor, H.; Arévalo-Pinzón, G.; Herrera, C.; Suárez, D.; Pérez, W. H.; Patarroyo, M. E. A new synthetic peptide having two target of antibacterial action in *E. coli* ML35. *Front. Microbiol.* **2016**, *7*, 2006.

[409] Lv, Y.; Wang, J.; Gao, H.; Wang, Z.; Dong, N.; Ma, Q.; Shan, A. Antimicrobial properties and membrane-active mechanism of a potential α-helical antimicrobial derived from cathelicidin PMAP-36. *PLoS One* **2014**, *9*, e86364.

[410] Dangel, A.; Ackermann, N.; Abdel-Hadi, O.; Maier, R.; Önder, K.; Francois, P.; Müller, C. W.; Pané-Farré, J.; Engelmann, S.; Schrenzel, J. et al. A de novo-designed antimicrobial peptide with activity against multiresistant *Staphylococcus aureus* acting on RsbW kinase. *FASEB J.* **2013**, *27*, 4476–4488.

[411] Zai, Y.; Xi, X.; Ye, Z.; Ma, C.; Zhou, M.; Chen, X.; Siu, S. W. I.; Chen, T.; Wang, L.; Kwok, H. F. Aggregation and Its Influence on the Bioactivities of a Novel Antimicrobial Peptide, Temporin-PF, and Its Analogues. *Int. J. Mol. Sci.* **2021**, *22*, 4509.

[412] Zou, R.; Zhu, X.; Tu, Y.; Wu, J.; Landry, M. P. Activity of antimicrobial peptide aggregates decreases with increased cell membrane embedding free energy cost. *Biochemistry* **2018**, *57*, 2606–2610.

[413] Daschbach, M. M.; Negin, S.; You, L.; Walsh, M.; Gokel, G. W. Aggregation and supramolecular membrane interactions that influence anion transport in tryptophan-containing synthetic peptides. *Chem. – Eur. J.* **2012**, *18*, 7608–7623.

[414] Roy, A.; Franco, O. L.; Mandal, S. M. Biomedical exploitation of self-assembled peptide based nanostructures. *Curr. Prot. Pept. Sci.* **2013**, *14*, 580–587.

[415] Lombardi, L.; Falanga, A.; Del Genio, V.; Galdiero, S. A new hope: Self-assembling peptides with antimicrobial activity. *Pharmaceutics* **2019**, *11*, 166.

[416] Chang, R.; Yuan, C.; Zhou, P.; Xing, R.; Yan, X. Peptide self-assembly: From ordered to disordered. *Acc. Chem. Res.* **2024**, *57*, 289–301.

[417] Cui, H.; Webber, M. J.; Stupp, S. I. Self-assembly of peptide amphiphiles: From molecules to nanostructures to biomaterials. *Pept. Sci.* **2010**, *94*, 1–18.

[418] Elsawy, M. A. *Peptide bionanomaterials: From design to application*; Springer Nature, 2023.

[419] Kaba, S. A.; Brando, C.; Guo, Q.; Mittelholzer, C.; Raman, S.; Tropel, D.; Aebi, U.; Burkhard, P.; Lanar, D. E. A nonadjuvanted polypeptide nanoparticle vaccine confers long-lasting protection against rodent malaria. *J. Immunol.* **2009**, *183*, 7268–7277.

[420] Burkhard, P.; Lanar, D. E. Malaria vaccine based on self-assembling protein nanoparticles. *Expert Rev. Vaccines* **2015**, *14*, 1525–1527.

[421] Chen, W.; Yang, S.; Li, S.; Lang, J. C.; Mao, C.; Kroll, P.; Tang, L.; Dong, H. Self-assembled peptide nanofibers display natural antimicrobial peptides to selectively kill bacteria without compromising cytocompatibility. *ACS Appl. Mater. Interfaces* **2019**, *11*, 28681–28689.

[422] Porter, S. L.; Coulter, S. M.; Pentlavalli, S.; Thompson, T. P.; Laverty, G. Self-assembling diphenylalanine peptide nanotubes selectively eradicate bacterial biofilm infection. *Acta Biomater.* **2018**, *77*, 96–105.

[423] Jiang, L.; Xu, D.; Sellati, T. J.; Dong, H. Self-assembly of cationic multidomain peptide hydrogels: Supramolecular nanostructure and rheological properties dictate antimicrobial activity. *Nanoscale* **2015**, *7*, 19160–19169.

[424] Xu, D.; Ran, Q.; Xiang, Y.; Jiang, L.; Smith, B. M.; Bou-Abdallah, F.; Lund, R.; Li, Z.; Dong, H. Toward hemocompatible self-assembling antimicrobial nanofibers: Understanding the synergistic effect of supramolecular structure and PEGylation on hemocompatibility. *RSC Adv.* **2016**, *6*, 15911–15919.

[425] Salick, D. A.; Kretsinger, J. K.; Pochan, D. J.; Schneider, J. P. Inherent antibacterial activity of a peptide-based β-hairpin hydrogel. *J. Am. Chem. Soc.* **2007**, *129*, 14793–14799.

[426] Salick, D. A.; Pochan, D. J.; Schneider, J. P. Design of an injectable β-hairpin peptide hydrogel that kills methicillin-resistant *Staphylococcus aureus*. *Adv. Mater.* **2009**, *21*, 4120–4123.

[427] Azoulay, Z.; Aibinder, P.; Gancz, A.; Moran-Gilad, J.; Navon-Venezia, S.; Rapaport, H. Assembly of cationic and amphiphilic β-sheet FKF tripeptide confers antibacterial activity. *Acta Biomater.* **2021**, *125*, 231–241.

[428] Guo, Z.; Wang, Y.; Tan, T.; Ji, Y.; Hu, J.; Zhang, Y. Antimicrobial D-peptide hydrogels. *ACS Biomater. Sci. Eng.* **2021**, *7*, 1703–1712.

[429] Cao, F.; Mei, L.; Zhu, G.; Song, M.; Zhang, X. An injectable molecular hydrogel assembled by antimicrobial peptide PAF26 for antimicrobial application. *RSC Adv.* **2019**, *9*, 30803–30808.

[430] Lombardi, L.; Shi, Y.; Falanga, A.; Galdiero, E.; de Alteriis, E.; Franci, G.; Chourpa, I.; Azevedo, H. S.; Galdiero, S. Enhancing the potency of antimicrobial peptides through molecular engineering and self-assembly. *Biomacromolecules* **2019**, *20*, 1362–1374.

[431] Lombardi, L.; Li, J.; Williams, D. R. Peptide-based biomaterials for combatting infections and improving drug delivery. *Pharmaceutics* **2024**, *16*, 1468.

[432] Braun, K.; Pochert, A.; Gerber, M.; Raber, H. F.; Lindén, M. Influence of mesopore size and peptide aggregation on the adsorption and release of a model antimicrobial peptide onto/from mesoporous silica nanoparticles *in vitro*. *Mol. Syst. Des. Eng.* **2017**, *2*, 393–400.

[433] Hamley, I. W. Self-assembly of amphiphilic peptides. *Soft Matter* **2011**, *7*, 4122–4138.

[434] Dehsorkhi, A.; Castelletto, V.; Hamley, I. W. Self-assembling amphiphilic peptides. *J. Pept. Sci.* **2014**, *20*, 453–467.

[435] Gong, H.; Liao, M.; Hu, X.; Fa, K.; Phanphak, S.; Ciumac, D.; Hollowell, P.; Shen, K.; Clifton, L. A.; Campana, M. et al. Aggregated amphiphilic antimicrobial peptides embedded in bacterial membranes. *ACS Appl. Mater. Interfaces* **2020**, *12*, 44420–44432.

[436] Torrent, M.; Andreu, D.; Nogués, V. M.; Boix, E. Connecting Peptide Physicochemical and Antimicrobial Properties by a Rational Prediction Model. *PLoS One* **2011**, *6*, e16968.

[437] Thirumalai, D.; Reddy, G.; Straub, J. E. Role of water in protein aggregation and amyloid polymorphism. *Acc. Chem. Res.* **2012**, *45*, 83–92.

[438] Moral, R.; Paul, S. Understanding the Role of Solvent Polarity and Amino Acid Composition of Cyclic Peptides in Nanotube Stability. *J. Phys. Chem. B* **2025**, *129*, 3590–3603.

[439] Jhawar, M.; Paul, S. Unveiling the Inhibitory Effect of Magnolol in the Aggregation of Human Calcitonin (hCT): A Comprehensive In-Silico Study. *ChemPhysChem* **2025**, e202400679.

[440] Barz, B.; Wales, D. J.; Strodel, B. A Kinetic Approach to the Sequence–Aggregation Relationship in Disease-Related Protein Assembly. *J. Phys. Chem. B* **2014**, *118*, 1003–1011.

[441] Carballo-Pacheco, M.; Ismail, A. E.; Strodel, B. On the Applicability of Force Fields to Study the Aggregation of Amyloidogenic Peptides Using Molecular Dynamics Simulations. *J. Chem. Theory Comput.* **2018**, *14*, 6063–6075.

[442] Thakuria, S.; Paul, S. Discrepant Effects of Hydrated and Neat Reline on the Conformational Stability of a Knotted Protein. *J. Phys. Chem. B* **2025**, *129*, 4629–4640.

[443] Paul, S.; Patey, G. N. Structure and Interaction in Aqueous Urea–Trimethylamine-N-Oxide Solutions. *J. Am. Chem. Soc.* **2007**, *129*, 4476–4482.

[444] Paul, R.; Mitra, A.; Paul, S. Phase Separation Property of a Hydrophobic Deep Eutectic Solvent–Water Binary Mixture: A Molecular Dynamics Simulation Study. *J. Chem. Phys.* **2021**, *154*.

[445] Li, N. K.; Xie, Y.; Yingling, Y. G. Insights into Structure and Aggregation Behavior of Elastin-Like Polypeptide Coacervates: All-Atom Molecular Dynamics Simulations. *J. Phys. Chem. B* **2021**, *125*, 8627–8635.

[446] Roy, R.; Paul, S. Theoretical Investigation of the Inhibitory Mechanism of Norepinephrine on hIAPP Amyloid Aggregation and the Destabilization of Protofibrils. *J. Phys. Chem. B* **2020**, *124*, 10913–10929.

[447] Ganguly, P.; Boserman, P.; van der Vegt, N. F. A.; Shea, J.-E. Trimethylamine N-Oxide Counteracts Urea Denaturation by Inhibiting Protein–Urea Preferential Interaction. *J. Am. Chem. Soc.* **2018**, *140*, 483–492.

[448] Ganguly, P.; van der Vegt, N. F. A. Convergence of Sampling Kirkwood–Buff Integrals of Aqueous Solutions with Molecular Dynamics Simulations. *J. Chem. Theory Comput.* **2013**, *9*, 1347–1355.

[449] Ganguly, P.; Shea, J.-E. Distinct and Nonadditive Effects of Urea and Guanidinium Chloride on Peptide Solvation. *J. Phys. Chem. Lett.* **2019**, *10*, 7406–7413.

[450] Kim, W.; Hecht, M. H. Generic Hydrophobic Residues Are Sufficient to Promote Aggregation of the Alzheimer's Aβ42 Peptide. *Proc. Natl. Acad. Sci. U.S.A.* **2006**, *103*, 15824–15829.

[451] Meijer, J. T.; Roeters, M.; Viola, V.; Löwik, D. W. P. M.; Vriend, G.; van Hest, J. C. M. Stabilization of Peptide Fibrils by Hydrophobic Interaction. *Langmuir* **2007**, *23*, 2058–2063.

[452] Auer, S.; Dobson, C. M.; Vendruscolo, M.; Maritan, A. Self-Templated Nucleation in Peptide and Protein Aggregation. *Phys. Rev. Lett.* **2008**, *101*, 258101.

[453] Das, B. K.; Singh, O.; Chakraborty, D. Exploring the Barriers in the Aggregation of a Hexadecameric Human Prion Peptide Through the Markov State Model. *ACS Chem. Neurosci.* **2023**, *14*, 3622–3645.

[454] Barz, B.; Liao, Q.; Strodel, B. Pathways of Amyloid-β Aggregation Depend on Oligomer Shape. *J. Am. Chem. Soc.* **2018**, *140*, 319–327.

[455] Smith, A. V.; Hall, C. K. Protein Refolding versus Aggregation: Computer Simulations on an Intermediate-Resolution Protein Model. *J. Mol. Biol.* **2001**, *312*, 187–202.

[456] Bonucci, A.; Caldaroni, E.; Balducci, E.; Pogni, R. A Spectroscopic Study of the Aggregation State of the Human Antimicrobial Peptide LL-37 in Bacterial Versus Host Cell Model Membranes. *Biochemistry* **2015**, *54*, 6760–6768.

[457] Bin Hafeez, A.; Jiang, X.; Bergen, P. J.; Zhu, Y. Antimicrobial Peptides: An Update on Classifications and Databases. *Int. J. Mol. Sci.* **2021**, *22*, 11691.

[458] Seefeldt, A. C.; Nguyen, F.; Antunes, S.; Pérébaskine, N.; Graf, M.; Arenz, S.; Inampudi, K. K.; Douat, C.; Guichard, G.; Wilson, D. N. et al. The Proline-Rich Antimicrobial Peptide Onc112 Inhibits Translation by Blocking and Destabilizing the Initiation Complex. *Nat. Struct. Mol. Biol.* **2015**, *22*, 470–475.

[459] Singh, N. K.; Agarwal, M.; Radhakrishna, M. Understanding the Helical Stability of Charged Peptides. *Proteins* **2023**, *91*, 268–276.

[460] Paul, S.; Paul, S. Controlling the Self-Assembly of Human Calcitonin: A Theoretical Approach Using Molecular Dynamics Simulations. *Phys. Chem. Chem. Phys.* **2021**, *23*, 14496–14510.

[461] Paul, S.; Paul, S. How Does Aqueous Choline-O-Sulfate Solution Nullify the Action of Urea in Protein Denaturation? *J. Chem. Inf. Model.* **2018**, *58*, 1858–1869.

[462] Roy, R.; Paul, S. Potential of ATP Toward Prevention of hIAPP Oligomerization and Destabilization of hIAPP Protofibrils: An In Silico Perspective. *J. Phys. Chem. B* **2021**, *125*, 3510–3526.

Appendix A

Supporting materials for Chapter 3

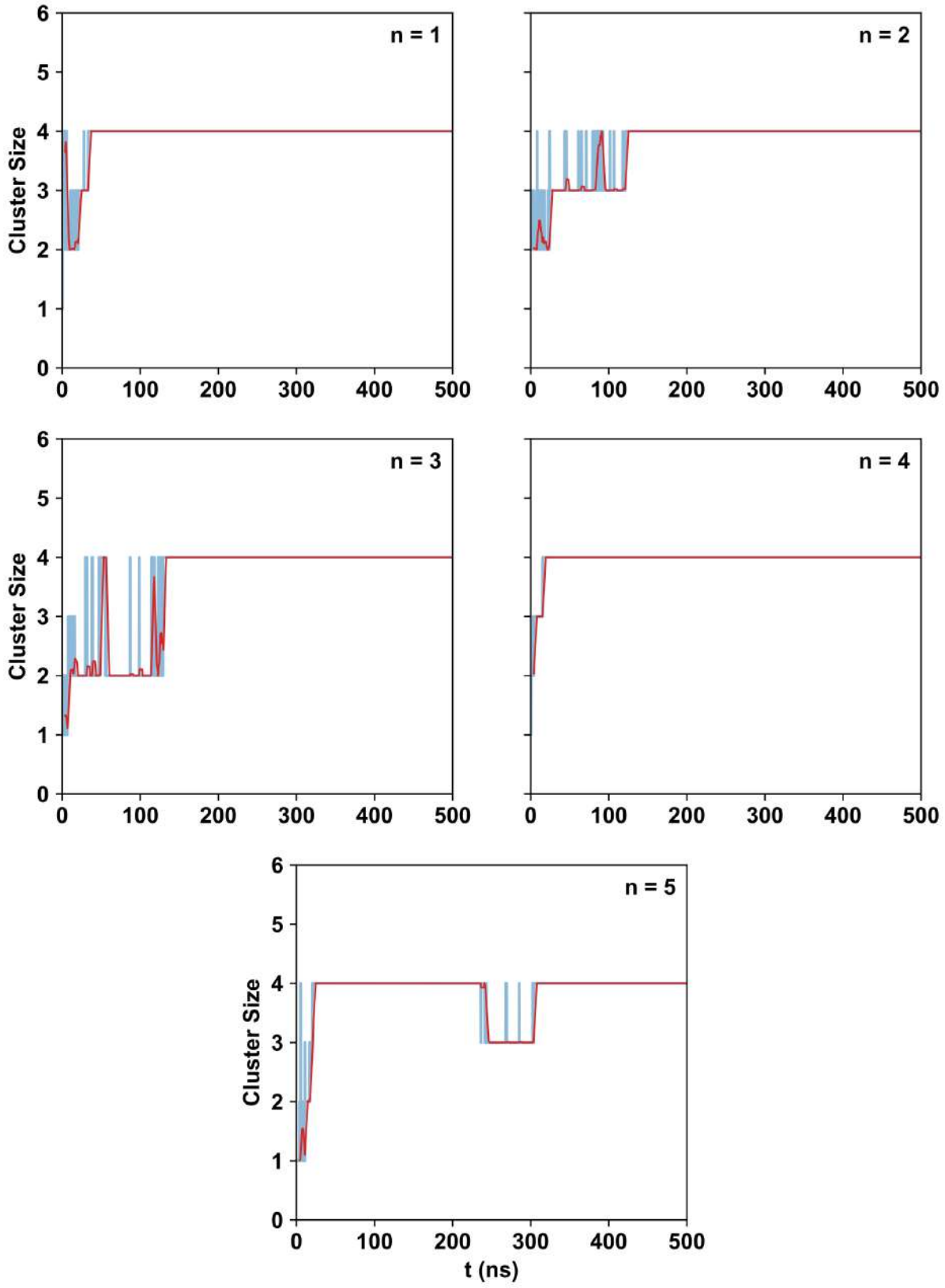

FIGURE A.1: Time evolution of the maximum cluster size for hll-4 systems. The rolling averages of the time series data are taken over 500 windows. System replicas are labelled as n.

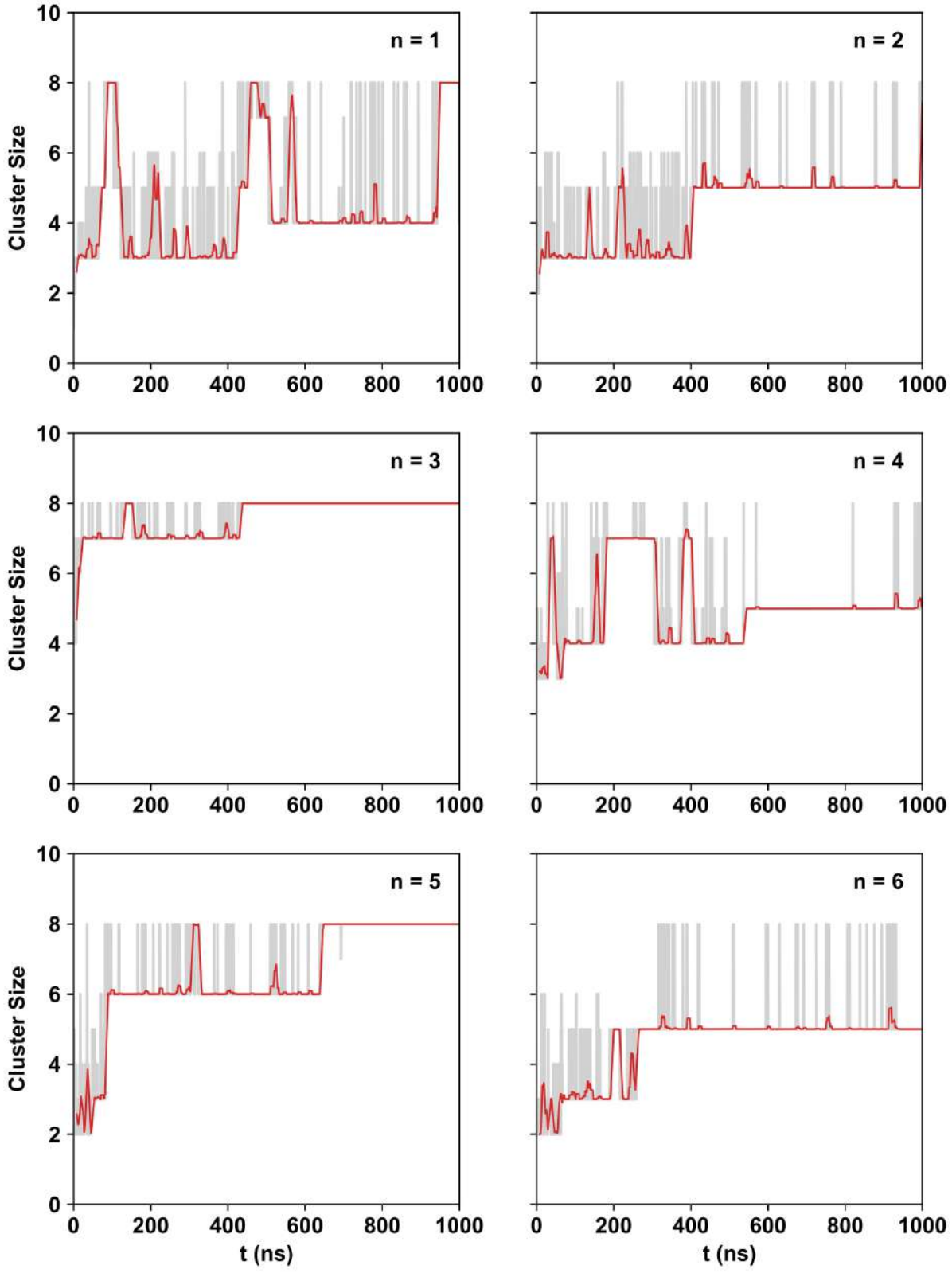

FIGURE A.2: Time evolution of the maximum cluster size for hll-8 systems. The rolling averages of the time series data are taken over 500 windows. System replicas are labelled as n.

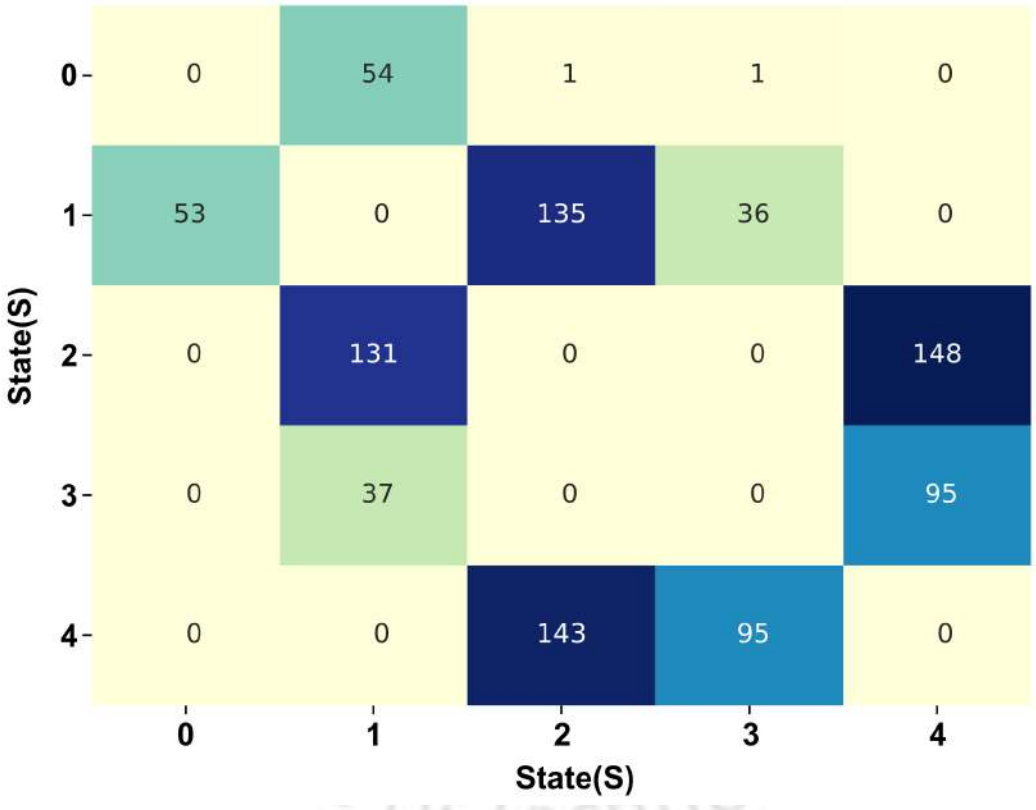

FIGURE A.3: Heatmap representation of the transition matrix for hll-4 systems.

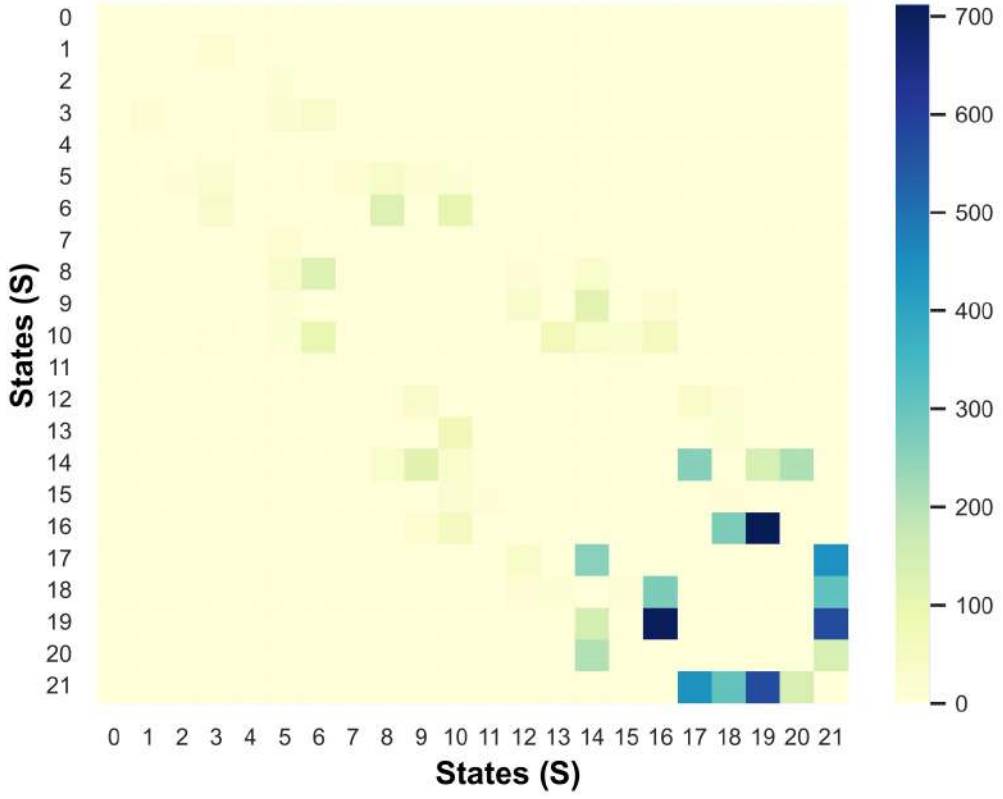

FIGURE A.4: Heatmap representation of the transition matrix for hll-8 systems.

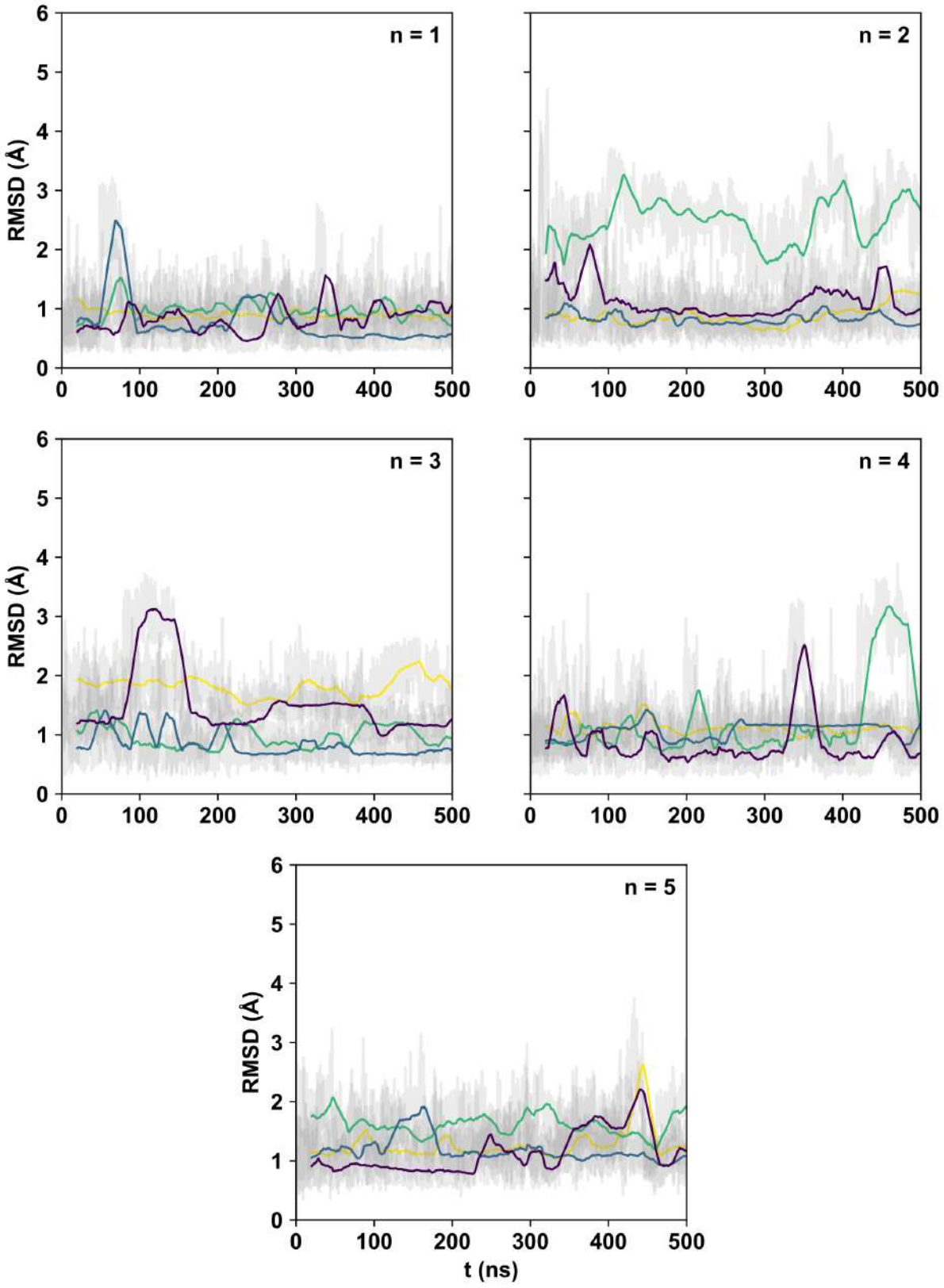

FIGURE A.5: Root mean square deviation (RMSD) of the peptide backbone atoms as a function of time for hll-4 systems. The peptides are represented by different colours. The rolling average of the RMSD data is taken over 500 windows.

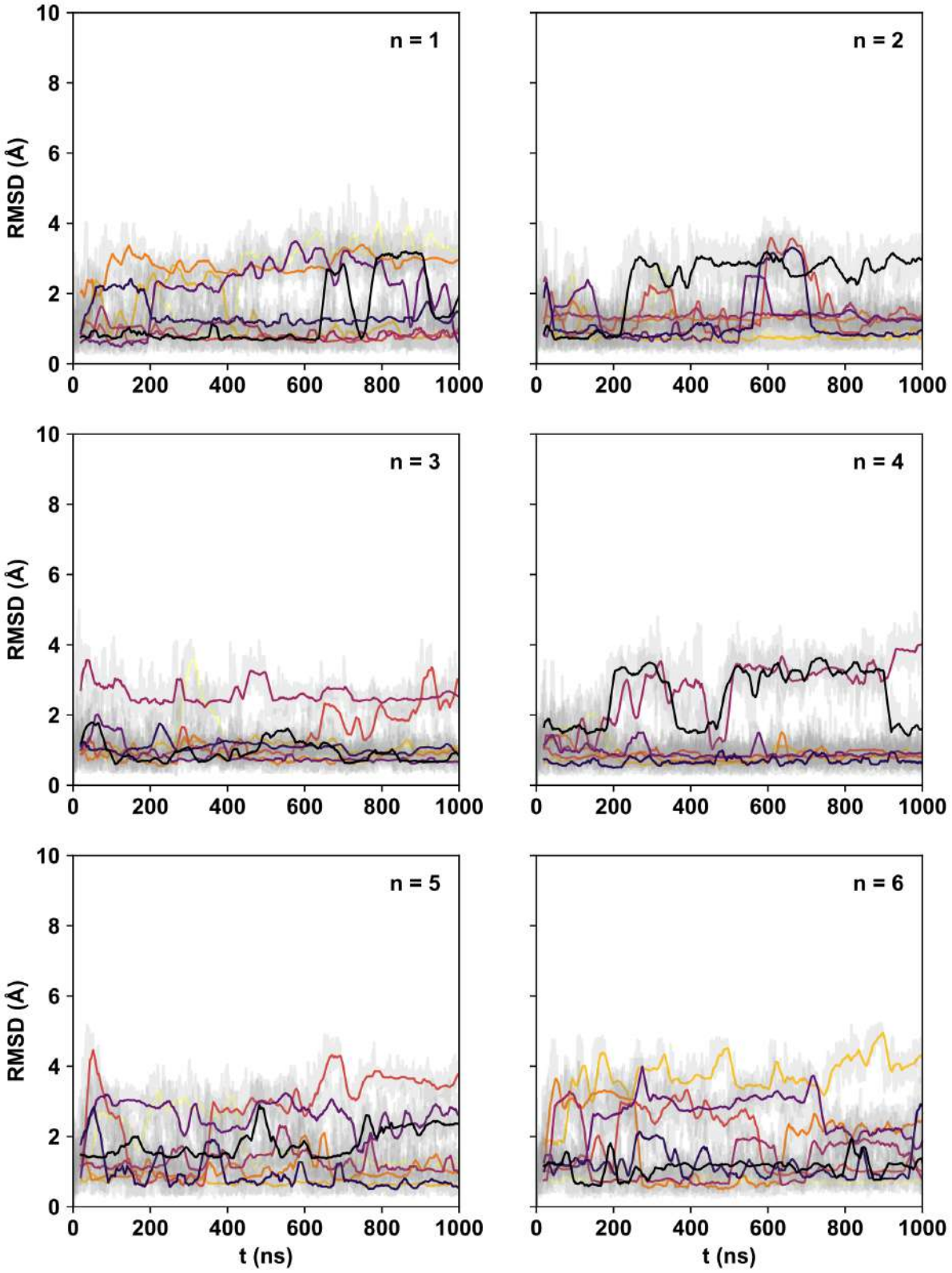

FIGURE A.6: Root mean square deviation (RMSD) of the peptide backbone atoms as a function of time for hll-8 systems. The peptides are represented by different colours. The rolling average of the RMSD data is taken over 500 windows.

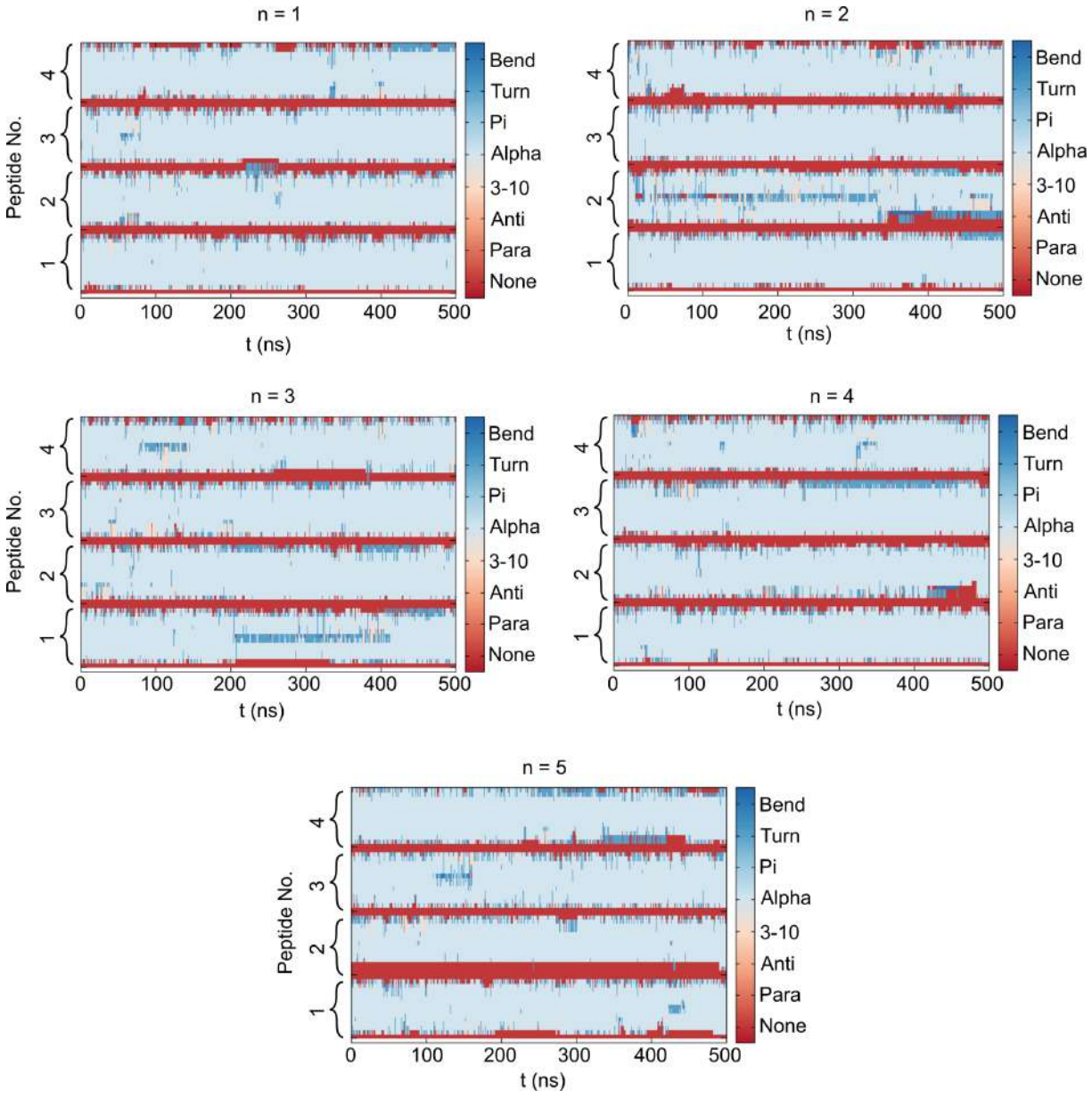

FIGURE A.7: Time evolution of the secondary structure of the peptides for hll-4 systems.

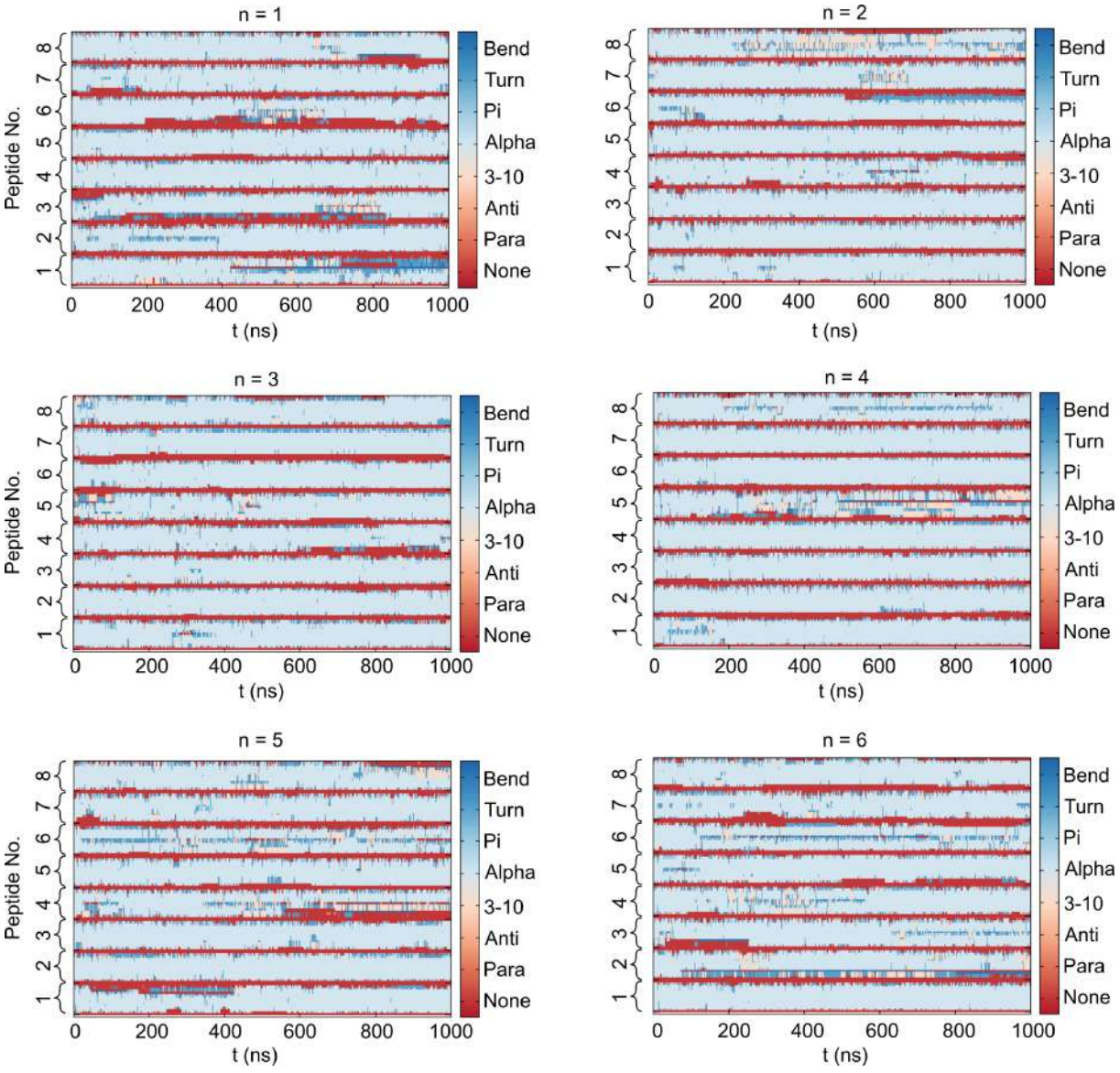

FIGURE A.8: Time evolution of the secondary structure of the peptides for hll-8 systems.

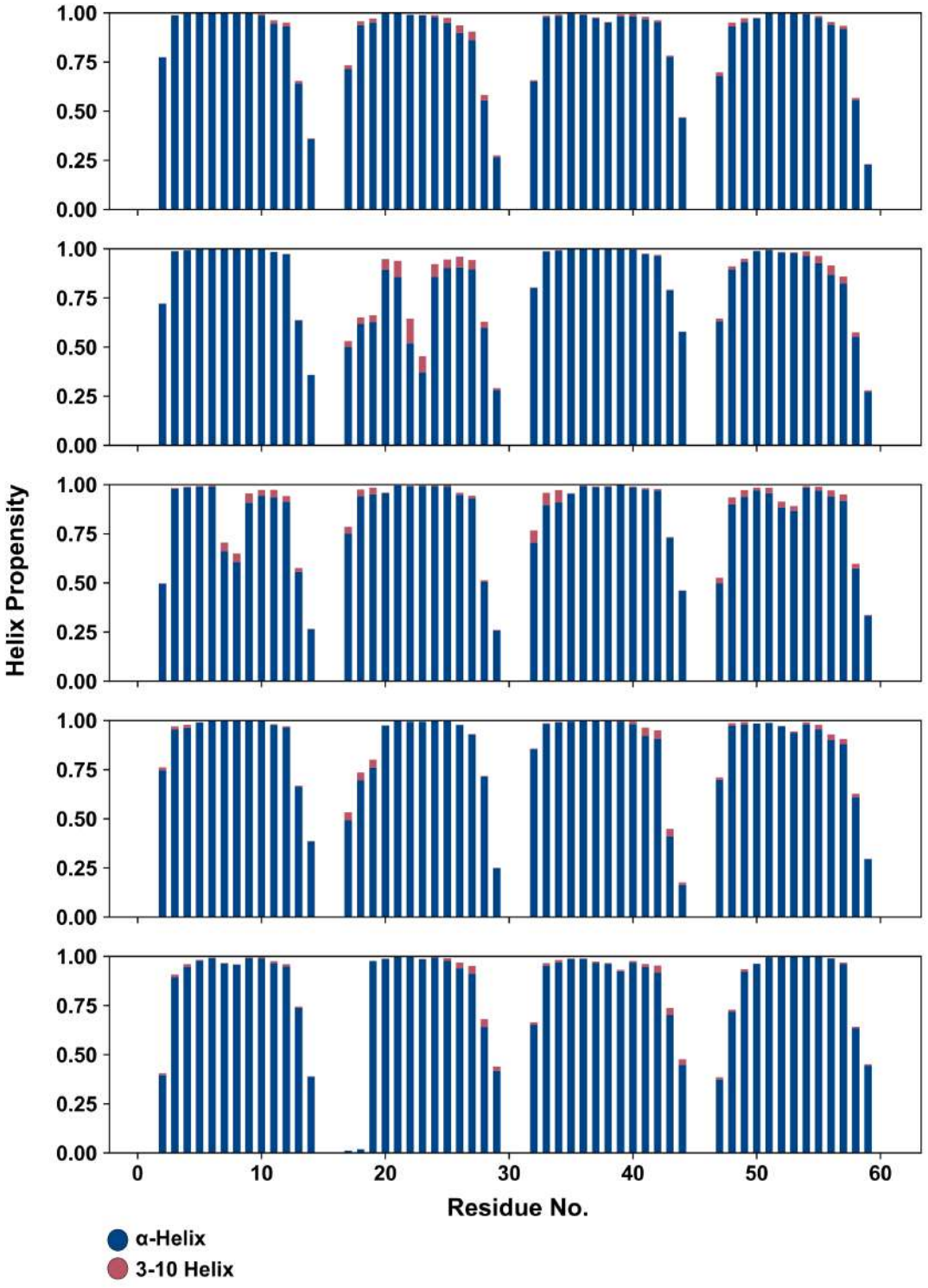

FIGURE A.9: Residue wise secondary structure propensity for hll-4 systems.

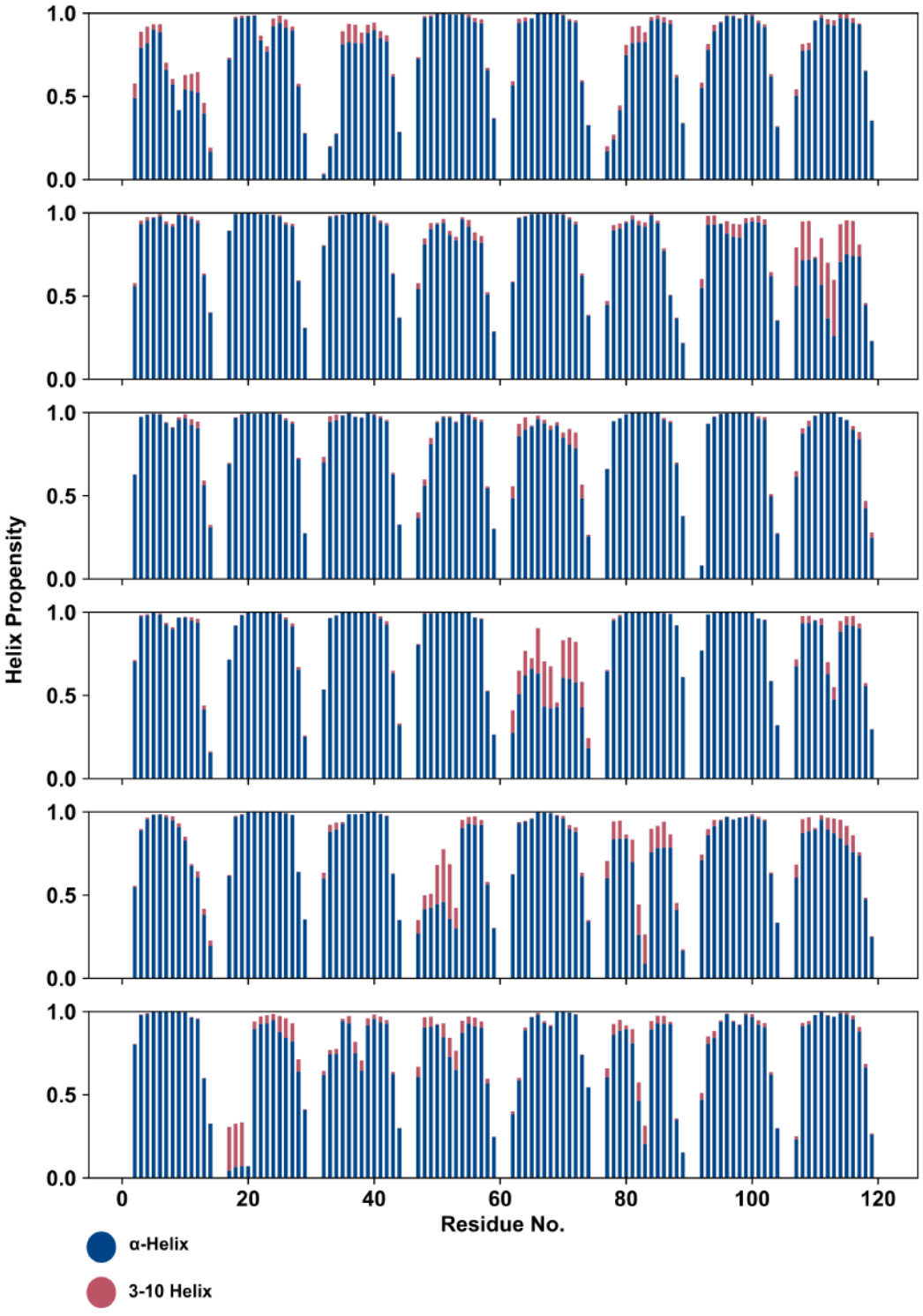

FIGURE A.10: Residue wise secondary structure propensity for hll-8 systems.

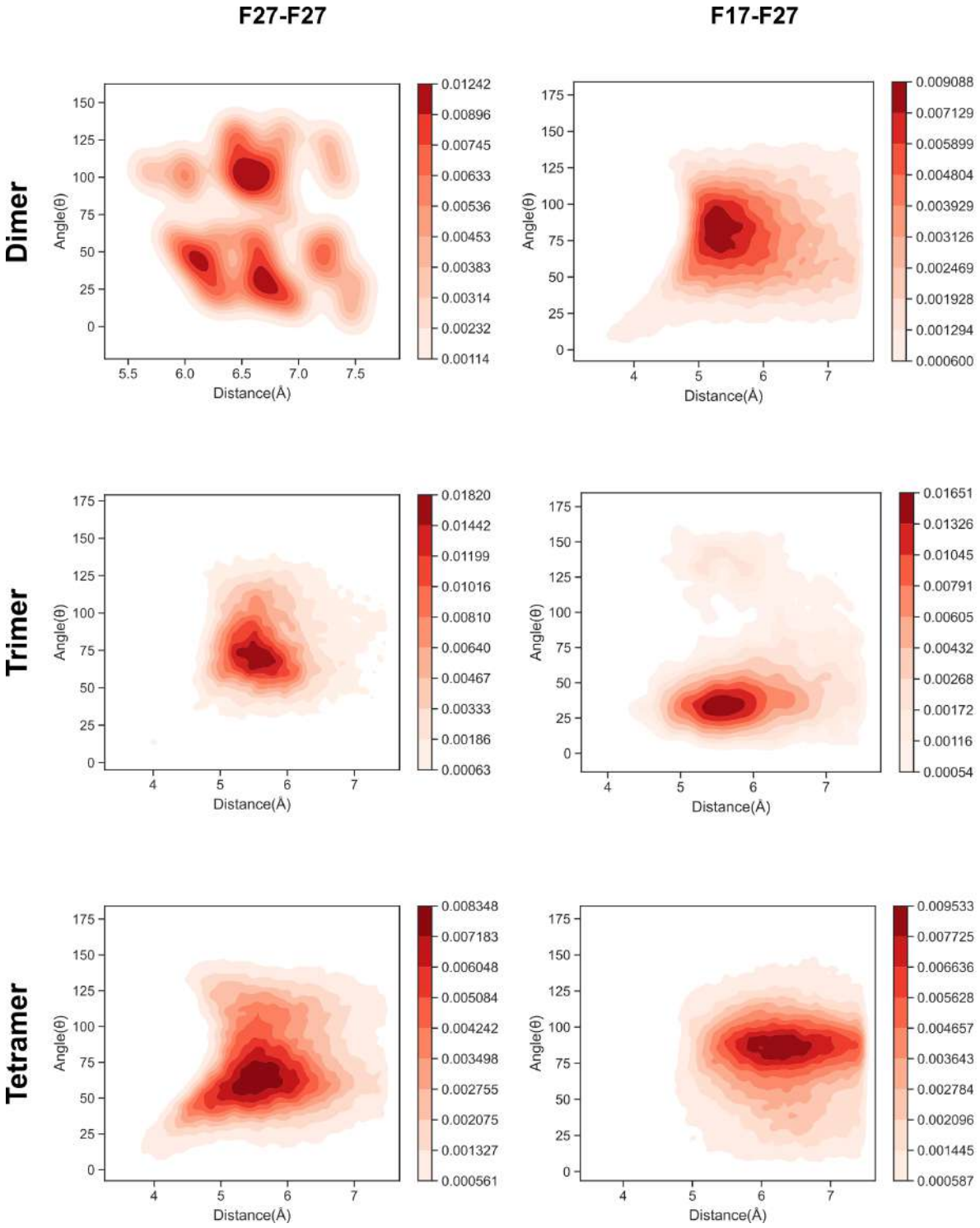

FIGURE A.11: π-stacking interaction in the Phe residues of dimers, trimers and tetramers.

Appendix B

Supporting materials for Chapter 4

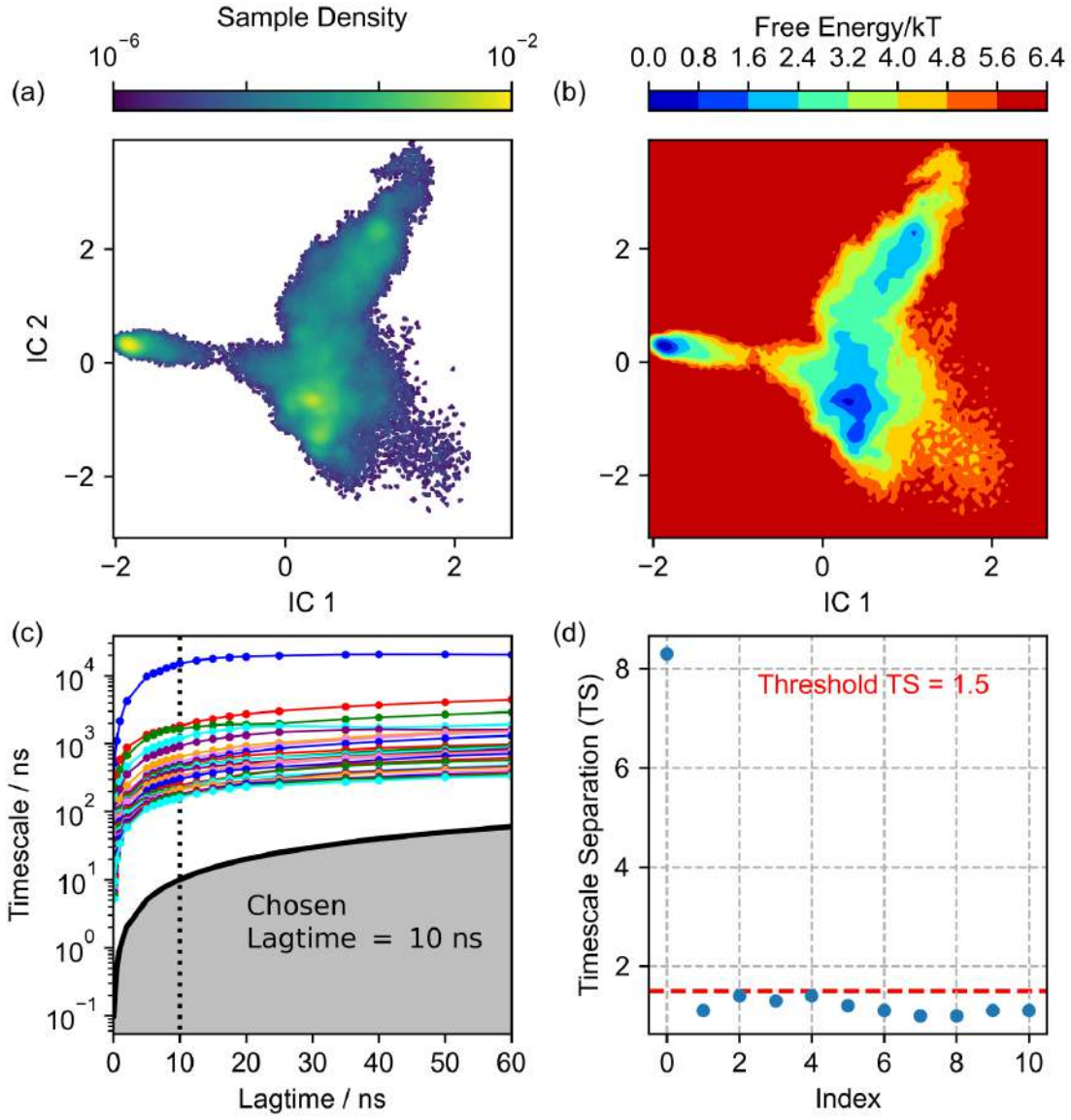

FIGURE B.1: **Characteristics and validation of the tetramer MSM:** (a) Sample density of tetramer conformations obtained from 50 μs of cumulative molecular dynamics (MD) simulations performed under NPT conditions. The densities are projected onto the top two TICA components (lag time = 1 ns) using inter-residue distances between hydrophobic residues as the feature vector. (b) The corresponding free energy surface in the TICA space. (c) Implied timescales of the tetramer relaxation processes computed from MSMs at different lag times. The shaded region denotes non-resolvable processes. (d) Relative separation of implied timescales for the MSM constructed at a 10 ns lag time. The number of macrostates is determined based on the relative timescale separations greater than 1.5.

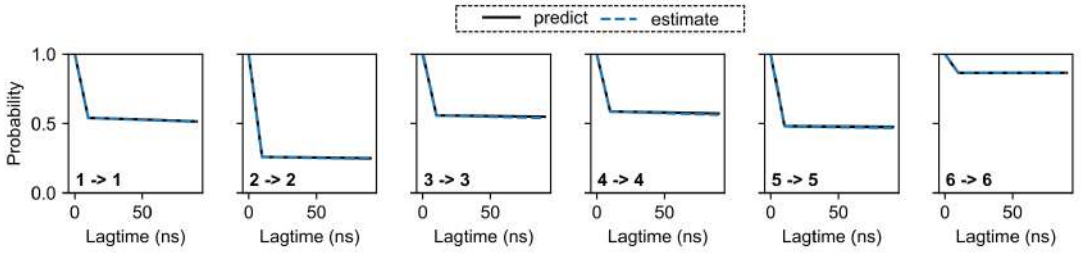

FIGURE B.2: **Chapman Kolomogorov (CK) test for the hLL-37$_{17\text{-}29}$ tetramers:** The CK-test validates the 6 macrostate MSM at a lag time of 10 ns. The estimated (blue dotted) values are in close agreement with the predicted values (black solid).

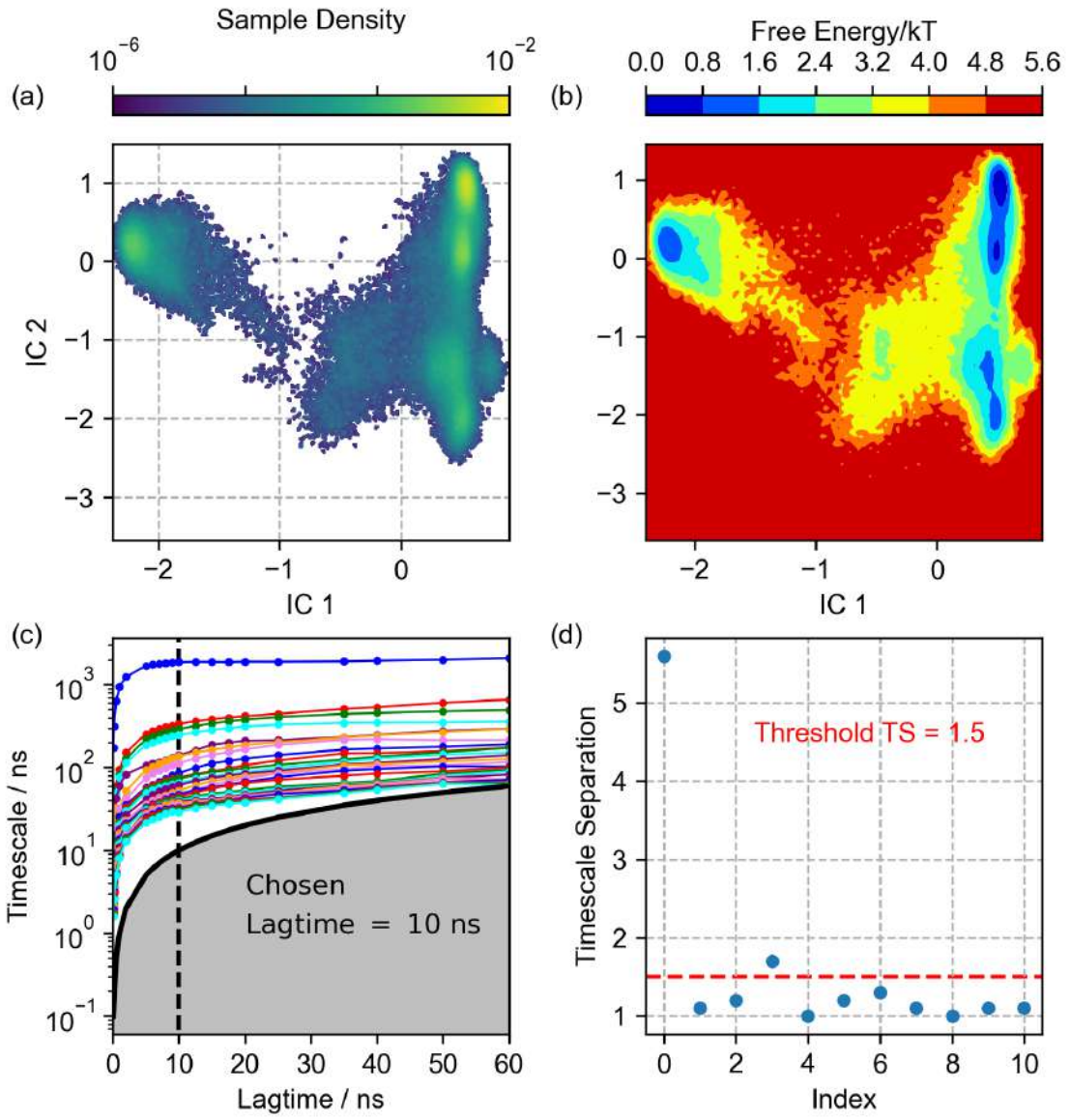

FIGURE B.3: **Characteristics and validation of the trimer MSM:** (a) Sample density of trimer conformations obtained from 40 μs of cumulative molecular dynamics (MD) simulations performed under NPT conditions. The densities are projected onto the top two TICA components (lag time = 1 ns) using inter-residue distances between hydrophobic residues as the feature vector. (b) The corresponding free energy surface in the TICA space. (c) Implied timescales of trimer relaxation processes computed from MSMs at different lag times. The shaded region denotes non-resolvable processes. (d) Relative separation of implied timescales for the MSM constructed at a 10 ns lag time. The number of macrostates is determined based on relative timescale separations greater than 1.5.

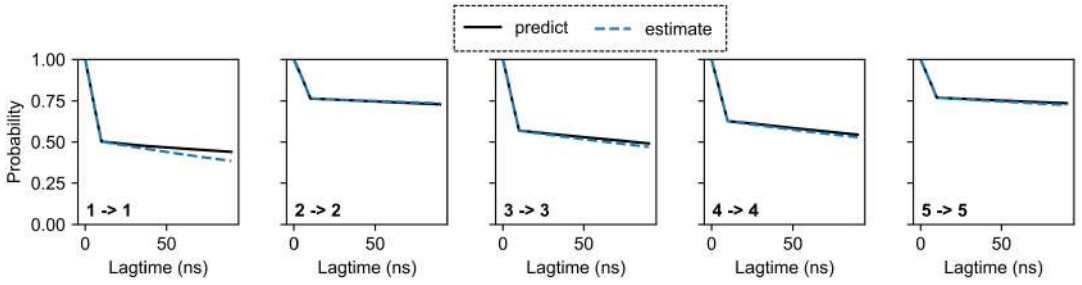

FIGURE B.4: **Chapman Kolomogorov (CK) test for the hLL-37$_{17\text{-}29}$ trimers:** The CK-test validates the 5 macrostate MSM at a lag time of 10 ns. The estimated (blue dotted) values are in close agreement with the predicted values (black solid).

Appendix C

Supporting materials for Chapter 5

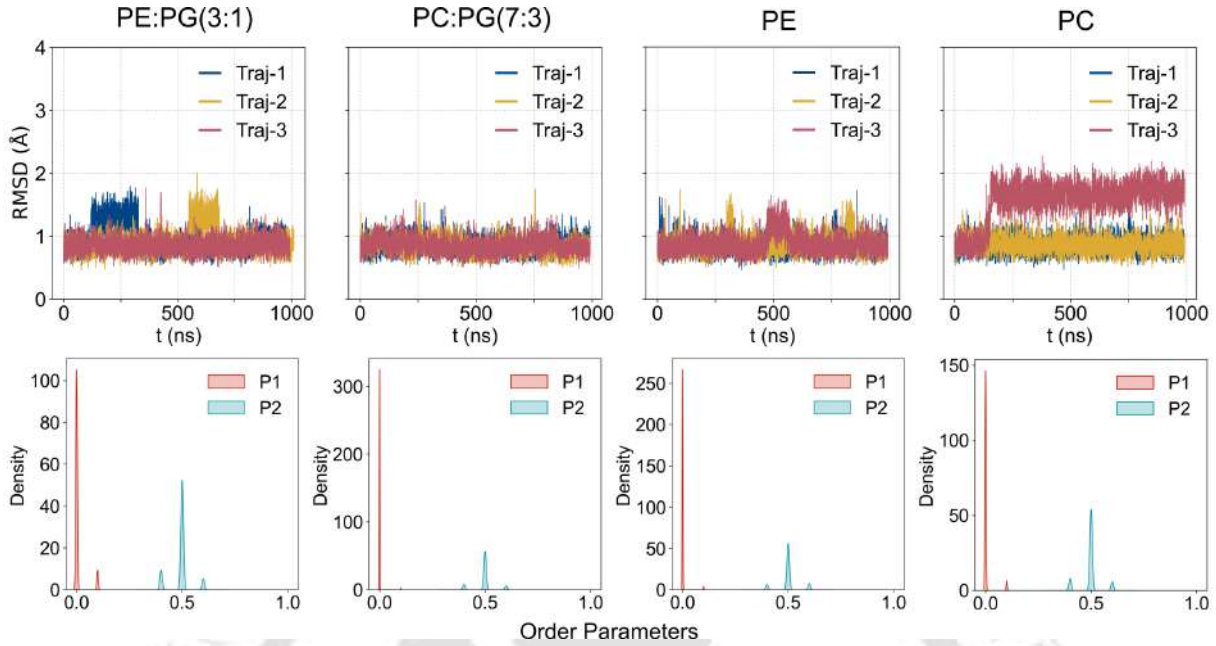

FIGURE C.1: **Structural changes in 4HB during bilayer adsorption:** A) Root mean square deviation (RMSD) in the peptide backbone atoms from the crystal structure of 4HB as a function of time. B) Distribution in the polar and nematic order parameters of 4HB in the membrane-bound state.

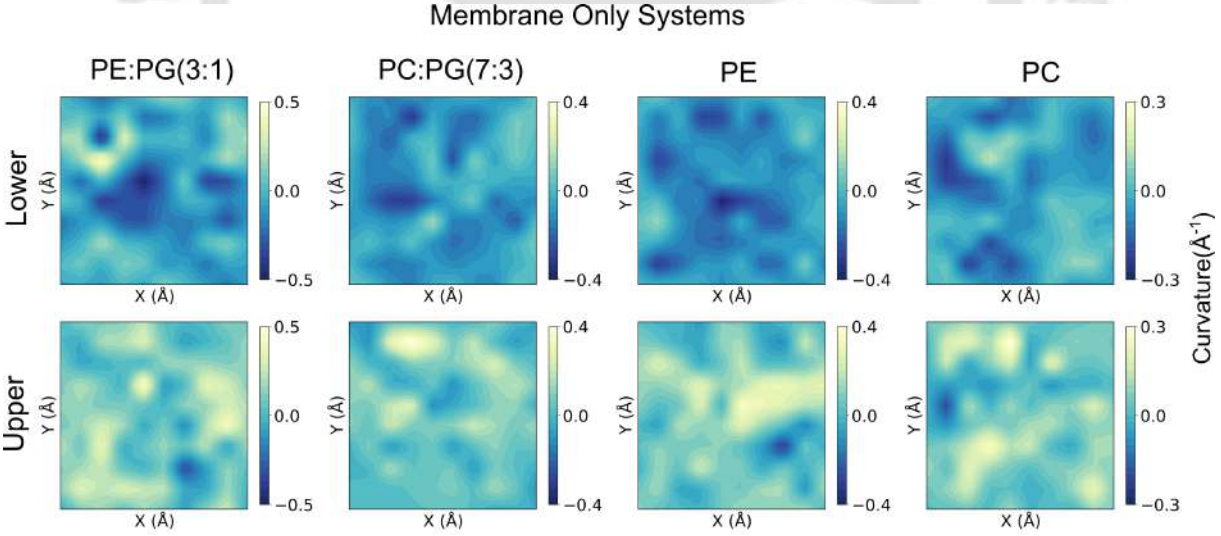

FIGURE C.2: **Curvature of the bilayers in the absence of 4HB:** Mean curvature of the upper and lower leaflets of the pure bilayer. Positive curvature indicates convex regions, while negative curvature indicates concave regions.

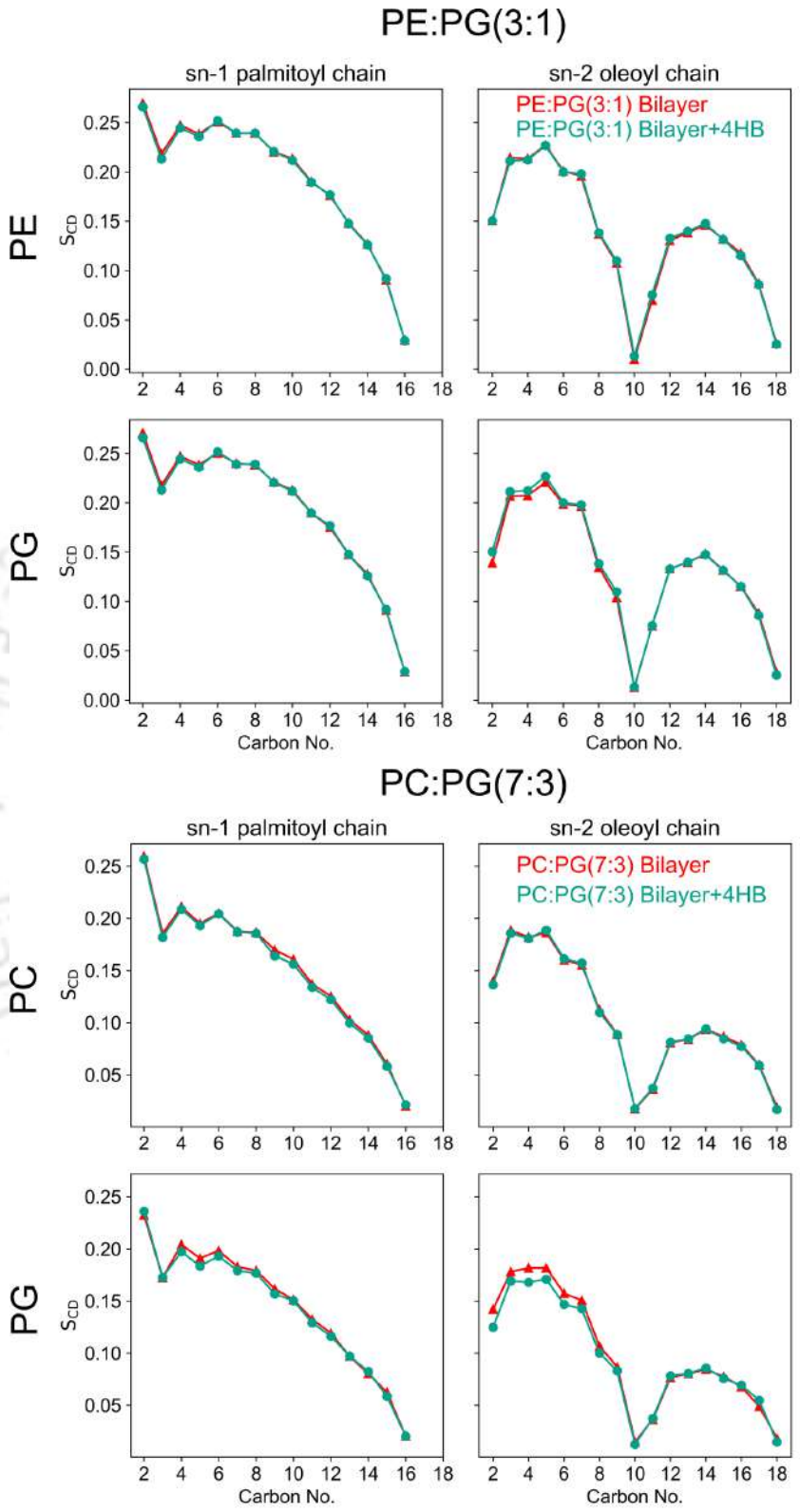

FIGURE C.3: **Changes in lipid order during 4HB adsorption on anionic membranes:** Order parameters of the sn-1 palmitoyl chain (left) and sn-2 oleoyl chain (right) are shown for the zwitterionic components (PE/PC) and the anionic PG in the two heterogeneous bilayers, PE:PG (3:1) and PC:PG (7:3). Order parameters were calculated in the absence and presence of 4HB.

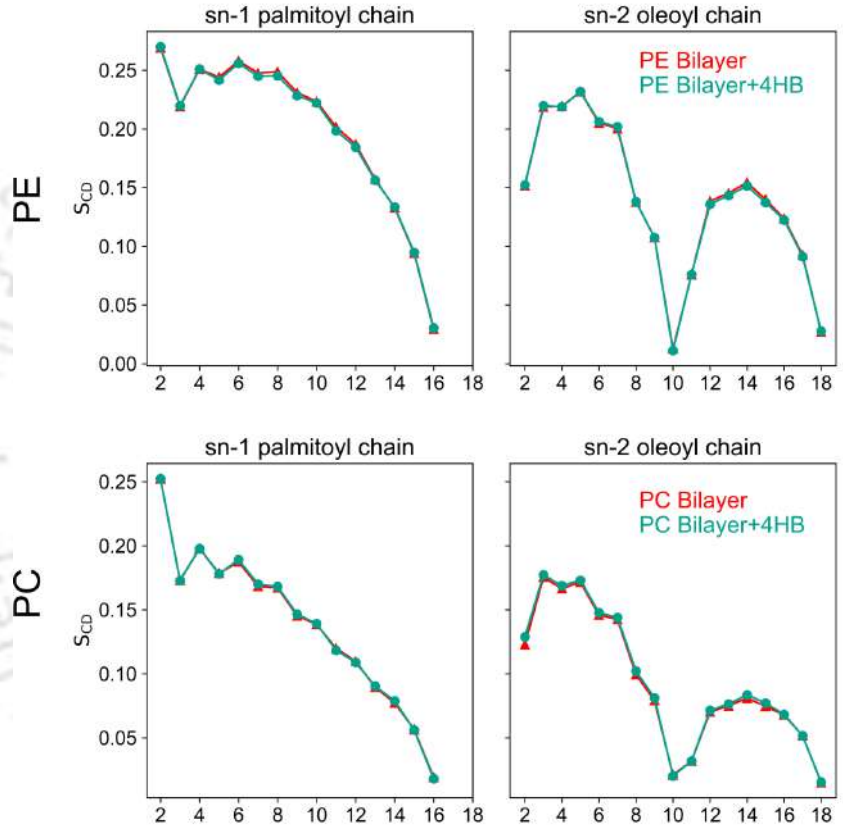

FIGURE C.4: **Changes in lipid order during 4HB adsorption on zwitterionic membranes:** Order parameters of the sn-1 palmitoyl chain (left) and sn-2 oleoyl chain (right) are shown for the zwitterionic PE and PC bilayers. Order parameters were calculated in the absence and presence of 4HB.

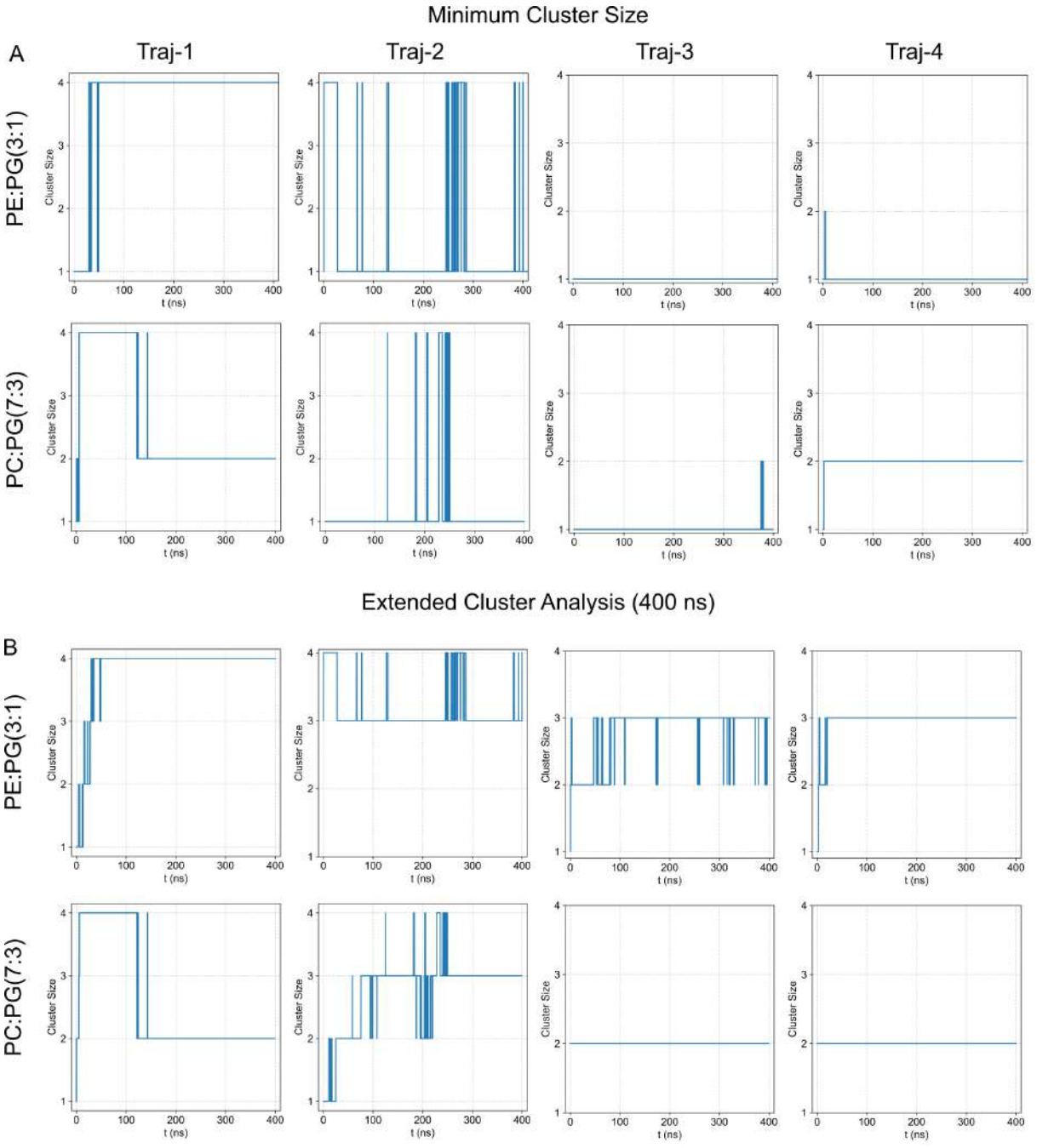

FIGURE C.5: **Self assembly of hLL-37$_{17\text{-}29}$ in the presence of anionic (bacterial) membranes:** (A) Minimum cluster size as a function of simulation time (B) Evolution of peptide clusters extended upto 400 ns.

Appendix D

Supporting materials for Chapter 6

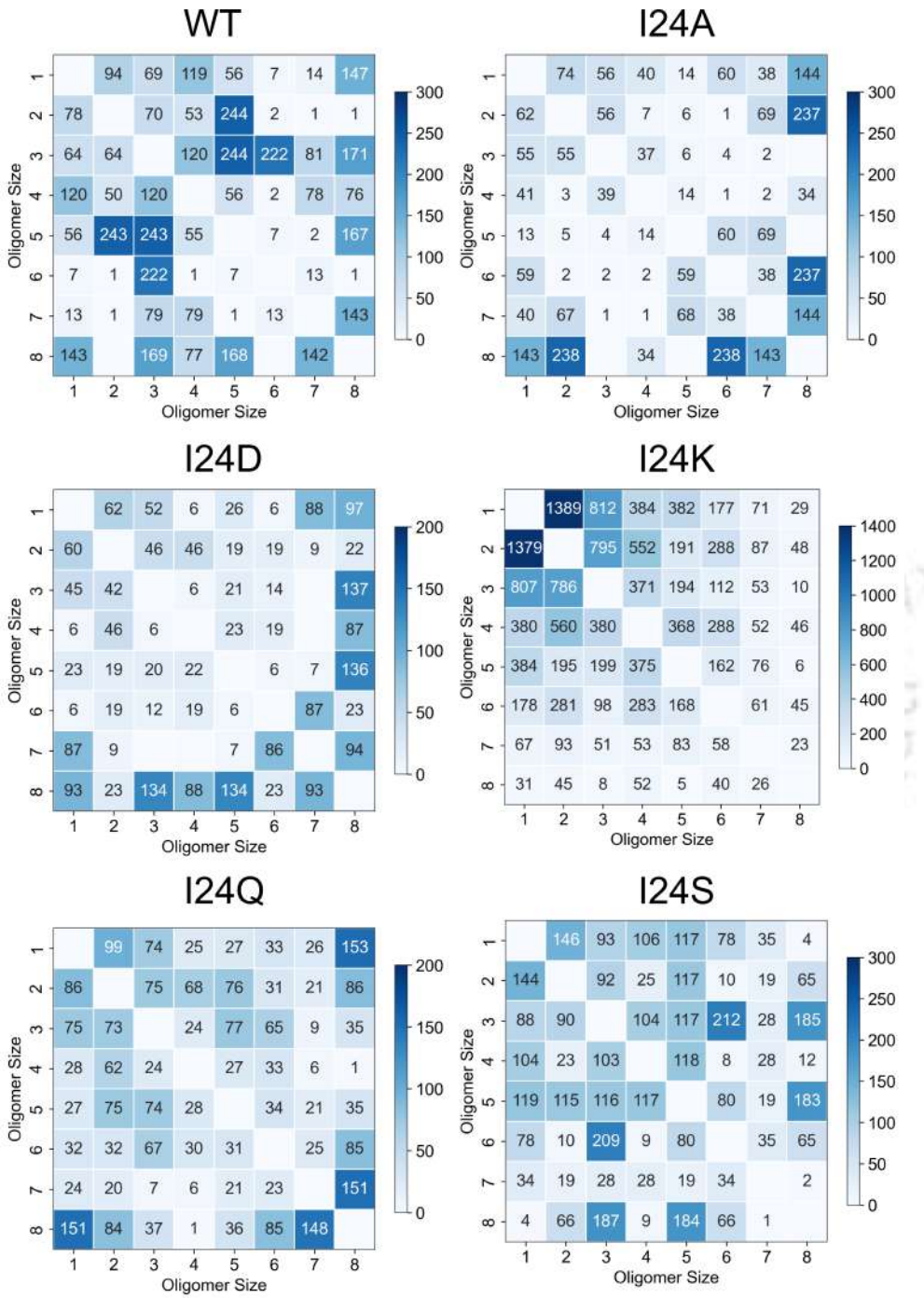

FIGURE D.1: Heatmap representation of the transition matrices of the WT and mutant systems. The rows and columns enumerate the oligomer size. The color bar quantifies the frequency of transitions between two states.

List of Publications

Articles Published

1. **Aritra Mitra** and Sandip Paul. Membrane Interaction and Embedding of a Self-Assembled 4-Helix Bundle from the Antimicrobial hLL-$37_{17\text{-}29}$ Fragment. *Langmuir*, (Accepted, In Press, 2025).

2. **Aritra Mitra** and Sandip Paul. Effect of Point Mutations on the Aggregation Tendency of the Antimicrobial Fragment Peptide hLL-$37_{17\text{-}29}$. *J. Phys. Chem. B*, **129**, 11474 (2025).

3. **Aritra Mitra**, Viswas Pandijothi, and Sandip Paul. Computational insight into the peptide-based inhibition of cobratoxin. *Phys. Chem. Chem. Phys.*, **26**, 28274 (2024).

4. **Aritra Mitra** and Sandip Paul. Pathways of hLL-$37_{17\text{-}29}$ aggregation give insight into the mechanism of amyloid formation. *J. Phys. Chem. B*, **127**, 8162 (2023).

5. Madhusmita Devi, Rimjhim Moral, Sanjib Thakuria, Mitra, **Aritra Mitra**, and Sandip Paul. Hydrophobic Deep Eutectic Solvents as Greener Substitutes for Conventional Extraction Media: Examples and Techniques. *ACS Omega*, **8**, 9702 (2023).

6. **Aritra Mitra**†, Krishna Gopal Chattaraj†, and Sandip Paul. Elucidating the Hydrotropic Mechanism of the Antagonistic Salt PPh_4Cl. *J. Phys. Chem. B*, **127**, 996 (2023). († indicates equal contribution)

7. Rabindranath Paul, **Aritra Mitra**, and Sandip Paul. A Computational Approach on the Stereoselective Binding of Peptides from Aqueous Medium with Endo-Functionalized Molecular Tubes. *Phys. Chem. Chem. Phys.*, **23**, 22703 (2021).

8. Rabindranath Paul[†], **Aritra Mitra**[†], Sandip Paul. Phase separation property of a hydrophobic deep eutectic solvent–water binary mixture: A molecular dynamics simulation study. *J. Chem. Phys.*, **154**, 244504 (2021). ([†] indicates equal contribution)

Articles Communicated

1. **Aritra Mitra** and Sandip Paul. Markov State Models Reveal How hLL-$37_{17\text{-}29}$ Tetramers Relax from a Disordered State to a Cross-α Amyloid Geometry. (2025)

Conferences and Workshops

1. Presented poster at the Structure and Dynamics of Chemical and Biomolecular Systems (SDCBS23) conducted by IIT Kanpur (2023).

2. Presented poster at the Chemical Research Society of India 28th National Symposium in Chemistry conducted by IIT, Guwahati (2022).

3. Presented poster at the Research and Industrial Conclave Integration conducted by IIT, Guwahati (2022).

4. Presented poster at the Theoretical Chemistry Symposium conducted jointly by IISER Kolkata, IACS Kolkata, Kalyani University and SNBNCBS Kolkata (2021).

5. Presented a flash lecture at the Physical Chemistry Physical Biology conference conducted by IISc, Bangalore (2021).

6. Attended the Advanced Molecular Dynamics Simulations: A Summer School conducted by IISER, Pune (2021).

7. Attended the 22nd Conference of the National Magnetic Resonance Society of India, organized by the Department of Chemistry, IIT Kharagpur (2016).